Collective dynamics, self-ordering and quantum optimization of cold atoms in multi-mode cavities

Dissertation
zur Erlangung des akademischen Grades
Doctor of Philosophy

eingereicht an der
Fakultät für Mathematik, Informatik und Physik
der Leopold-Franzens-Universität Innsbruck

von
Valentin Torggler, MSc

Betreuung der Dissertation:
Univ.-Prof. Dr. Helmut Ritsch,
Institut für Theoretische Physik,
Universität Innsbruck

Innsbruck, August 2019

Zusammenfassung

Auf Atome in Lichtfeldern wirken Kräfte, die ihren Ursprung im Impulsübertrag der gestreuten Photonen haben. Von Lasern verursachte Lichtkräfte sind besonders stark und werden in vielen Experimenten zum Fangen und Kühlen von Atomen verwendet. In einem Gas mit niedriger Dichte ist es normalerweise unwahrscheinlich, dass ein gestreutes Photon auf ein weiteres Atom trifft. Daher erfolgt die Wechselwirkung zwischen Atomen und dem Lichtfeld auf individueller Basis. Das ändert sich drastisch, wenn sich die Atome in einem optischen Resonator hoher Güte bewegen. Durch die Reflexion an den Spiegeln durchläuft ein Photon die Atomwolke mehrere Male, sodass die Rückwirkung der Atome auf das Lichtfeld nicht mehr vernachlässigbar ist. In der daraus resultierenden Atom-Licht-Dynamik dominiert der kollektive den individuellen Anteil.

Das dynamische Wechselspiel von Atomen und Lichtfeldern resultiert oft in kollektivem Kühlen der Atome. Doch auch wenn die Resonatorfelder der Atombewegung adiabatisch folgen, gibt es langreichweitige Atom-Atom-Wechselwirkungen, welche sich oft durch ein kollektives, von der Position aller Atome abhängiges Potential beschreiben lassen. Interessanterweise führt die Beleuchtung der Atomwolke mit einem ausreichend starken Laserstrahl orthogonal zur Resonatorachse dadurch zu einem Phasenübergang von einer homogenen zu einer periodisch geordneten Atomverteilung.

In dieser Arbeit betrachten wir theoretische Modelle zur Beschreibung von kalten Atomen in Viel-Moden-Resonatoren. Die Atome werden transversal zur Resonatorachse von mehreren Laserstrahlen mit verschiedenen Frequenzen, welche quasi-resonant in eine jeweilige Resonatormode gestreut werden, beleuchtet. Aufgrund der im Ort variierenden Struktur der Resonator- und Lasermoden entsteht eine Vielzahl von meta-stabilen Atom-Mustern. Diese entsprechen einem Minimum in der potentiellen Energie der Atome. Im Gegensatz zum Fall von nur einer Mode ist wegen den lokalen Energieminima die Minimierung der Energie nicht mehr trivial. Durch numerische Simulationen der semiklassischen Atom-Lichtfeld-Dynamik von Zwei- und Viel-Moden-Modellen mit äquidistanten Moden untersuchen wir, welche quasi-stationären Zustände erreicht werden. Das hängt sehr stark von der Geschwindigkeit mit der die Laserintensität erhöht wird und von der Anfangstemperatur ab. Wenn die Laser abrupt angeschaltet werden, bleiben die Atome leicht in einem lokalen Energieminimum stecken.

Darauf folgend diskutieren wir die mögliche Anwendung von ultra-kalten Bosonen in optischen Gittern in solchen Viel-Moden-Resonatoren als analoger Quantensimulator, der schwierige Optimierungsprobleme lösen soll. Die Lösung eines solchen Problems kann als globale Minimierung einer von vielen Variablen abhängigen Kostenfunktion formuliert werden. Dazu assoziieren wir die Kostenfunktion mit dem vom Licht kreierten Potential. Die Freiheit bei der Wahl von verschiedenen Moden und dazugehörigen Laser-Intensitäten ermöglicht die Realisierung eines dem Optimierungsproblem angepassten

Potentials. Der Grundzustand des Systems entspricht der Lösung des Problems und wird dynamisch dadurch erreicht, dass die Laserintensität langsam erhöht wird. Diese Methode ähnelt dem bekannten Quantum-Annealing-Protokoll. Wir zeigen, dass man mit $N(N+1)/2$ Moden mit sich genügend voneinander unterscheidender räumlicher Struktur beliebige Atom-Atom Wechselwirkungen erzeugen kann. Als Beispiel bestimmen wir die zu einem Hopfield-Modell passende Modenkonfiguration.

Weiters wenden wir uns einem spezifischen Optimierungsproblem zu und diskutieren eine mögliche Implementierung des sogenannten Damenproblems, einer schachmathematischen Aufgabe, im Detail. Das Damenproblem kann folgendermaßen formuliert werden: Platziere N Schachdamen auf einem N mal N Schachbrett so, dass sich keine dieser Damen schlagen kann, wenn sie sich nach den Schachregeln bewegen dürfen. Wenn auf ausgesuchten Diagonalen keine Damen platziert werden dürfen, entspricht die Frage, ob dann immer noch ein Lösungsmuster existiert, einem Problem der Komplexitätsklasse NP-complete. Weiters gibt es praktisch schwierige Instanzen des Problems für relativ kleine Schachbretter. Die experimentelle Realisierung eines solchen Quantensimulators würde es ermöglichen, den potentiellen Geschwindigkeitsvorteil gegenüber einem klassischen Computer zu testen. Die Implementierung basiert auf ultra-kalten Atomen in einem zwei-dimensionalen optischen Gitter, welche die Damen auf einem Miniatur-Schachbrett repräsentieren. Diese Wahl vermeidet den sonst üblichen Qubit-Overhead. Die Bedingung, dass sich zwei Damen nicht schlagen dürfen, wird durch transversale Beleuchtung mit Frequenzkämmen oder gepulsten Lasern aus drei Richtungen geltend gemacht. Durch Ausnützen der charakteristischen Geometrie des Problems ist die Kopplung an eine nur relativ kleine Anzahl von Moden nötig, welche linear mit N skaliert. Zusätzlich induziert die Beleuchtung kollektive, nicht-lokale Quantenfluktuationen während des Annealing-Protokolls, was darauf hindeutet, dass das System nicht effizient mit Quanten-Monte-Carlo Methoden auf einem klassischen Computer simuliert werden kann.

Abstract

Atoms in light fields experience forces due to the momentum transfer from scattered photons. These light forces are especially strong in laser fields and are routinely used to trap and cool atoms in experiments. Since in a dilute gas it is typically unlikely that a photon which has been scattered by one atom hits another atom, several atoms in a cloud interact with the light field individually. This behavior drastically changes when the atoms are placed in a high finesse optical resonator. Here, photons complete multiple round-trips before leaving the resonator, which renders the back-action of the atoms on the field substantial. Hence in the arising coupled atom-field dynamics the collective dominates the individual part.

The dynamical interplay between atoms and fields can give rise to collective cooling effects. Infinite-range atom-atom interactions emerge even when the resonator fields adiabatically follow the atomic motion and often simplify to a collective potential depending on all atom positions. Prominently, these features bring about a phase transition from homogeneous to ordered atomic patterns, which is driven by the intensity of a laser beam illuminating the atomic cloud within the transversal plane of the resonator.

In this thesis we study theoretical models for the dynamics of cold atoms in a multi-mode resonator. The atoms are transversally pumped by several laser beams with distinctive frequencies, which are quasi-resonantly scattered into different resonator modes. Due to the non-uniform spatial structure of different resonator and pump modes, a multitude of meta-stable patterns emerges. These correspond to a minimum of the atomic potential energy. As opposed to the single-mode case, the energy minimization is not trivial anymore due to the existence of local energy minima. We investigate which quasi-stationary states are attained by numerically simulating the semi-classical atom-field dynamics for a simple two-mode and a multi-mode model with equidistant modes. We find a strong dependence on the pump intensity ramp speed and the initial temperature. Particularly, for fast intensity quenches the atoms are likely to get stuck in a local minimum.

Subsequently, we consider the potential application of ultra-cold lattice bosons in a multi-mode resonator as an analog quantum simulator aiming to solve hard optimization problems. Solving such a problem amounts to the global minimization of a multi-variate cost function. We associate the cost function with the collective light-mediated potential. In this vein the freedom to use different mode shapes and relative laser intensities for each resonator-pump mode pair allows for tailoring the collective potential to fit a desired optimization problem. The ground state representing the solution is dynamically attained by slowly ramping up the pump intensity, which implements a quantum annealing protocol. We demonstrate that by driving $N(N+1)/2$ modes with a sufficiently diverse spatial structure, arbitrary atom-atom interactions can be created. As an

example we numerically find a mode configuration to simulate the annealing dynamics for a Hopfield model.

Shifting to a specific optimization problem, we propose a detailed implementation of the N-queens problem, where the task is to place N queens on an N by N chess board such that no queens attack each other according to the chess rules. When the queens are forbidden to occupy some chosen diagonals, answering the question whether there still exists such a solution is proven to be NP-complete and practically hard instances occur for relatively small problem sizes. Thus the experimental realization of such a quantum simulator would allow for probing for a potential quantum advantage. The implementation is based on ultra-cold atoms in a 2D optical lattice representing the queens on a miniaturized chess board, avoiding any qubit overhead. The non-attacking condition is enforced by transverse illumination with frequency combs from three directions. Exploiting the characteristic geometry of the problem enables to pump only a moderate amount of modes scaling linearly with N. In addition, the illumination induces collective non-local quantum fluctuations during the annealing protocol, which suggests that the system cannot be straightforwardly simulated with quantum Monte Carlo methods on a conventional computer.

Danksagung

Viele Menschen waren mir bei der Erstellung dieser Arbeit in direkter oder indirekter Weise behilflich. Es folgt der Versuch einige von ihnen direkt oder indirekt dankend zu erwähnen.

Vor allem bedanke ich mich bei meinem Betreuer Helmut Ritsch, unter anderem für seine physikalischen Ideen, die dezenten Kurskorrekturen und für seine Faszination an der Physik inklusive ihrer kleineren Details. Außerdem war ich in seiner Arbeitsgruppe immer in ausgezeichneter Gesellschaft. Dazu gehören meine teils ehemaligen Bürokollegen Stefan Ostermann, Sebastian Krämer, Elvia Colella, Daniela Holzmann und Arthur Jungkind, und weiters David Plankensteiner, Wolfgang Niedenzu, Laurin Ostermann, Matthias Sonnleitner, Farokh Mivehvar, Claudiu Genes, Christoph Hotter, Raphael Holzinger, Prasanna Venkatesh und Julian Cremer, und natürlich auch die immer wiederkehrenden Gäste Dominik Winterauer, Karol Gietka, Christiane Ebongue und Natalia Masalaeva. Danke für die unterhaltsame, angenehme und interessante Zeit!

Auch will ich die Menschen vom Institut für Theoretische Physik dankend erwähnen, besonders die uralten Studienkollegen Clemens Dlaska, Katharina Schwaiger und Michael Schuler und die Administrativen Birgit Laimer, Nicole Jorda und Hans Embacher.

Weiters bedanke ich mich für die gute Zusammenarbeit bei Wolfgang Lechner, Philipp Aumann, Konstantin Friebe und Moonjoo Lee in Innsbruck, bei Giovanna Morigi, Simon Jäger, Tim Keller und Stefan Schütz in Saarbrücken und bei Ivor Krešić und Ticijana Ban in Zagreb. Für seine Gastfreundlichkeit in Zürich danke ich Tobias Donner.

Ein großer Dank gilt auch meinen Freunden und lieben Menschen, die ich nicht alle namentlich erwähnen kann. Sie haben sicherlich einen riesengroßen, unsichtbaren, positiven Beitrag zur Erstellung dieser Arbeit erbracht. Und zum Schluss danke ich meinen Eltern für ihre dauernde Unterstützung und vieles mehr!

Contents

1. Introduction

Understanding the fundamentals of the interaction of matter with a radiation field has been a longstanding endeavor in physics. Many aspects can be very well described by classical statistical mechanics combined with electrodynamics based on Maxwell's equations. This theoretical edifice started to collapse after Planck had to discretize the energy of oscillating particles in order to derive the black-body radiation law in 1900 [1.1] and thereby unwillingly introduced quantum mechanics. In the following decades the implications on physics were taken seriously by Einstein and Bohr among others. While Bohr is mainly known for his atom model with which he was able to explain the spectral emission lines, Einstein developed the revolutionary concept of quanta of the radiation field, which are nowadays known as photons. In this picture Maxwell's equations describe wave-like probability functions guiding the photons, but when interacting with matter the energy can be transferred in discrete quanta only – a particle-like behavior. Using these light particles Einstein could explain the photo-electric effect [1.2] and derive Planck's radiation law in various ways, both of which were known from experiments at this time. Moreover, photon statistics paved the way to the theory of the ideal quantum gas [1.3]. The particle-wave duality was also found to exist for matter as initially conceptualized in de Broglie's PhD thesis in 1925 and finally put into a thorough framework by Schrödinger's wave equation [1.4] in 1926. Later, the fully-fledged theory of quantum electrodynamics was formulated by Dirac, Fermi and Feynman [1.5–1.7] among others. Quantum mechanics and electrodynamics proved as outstandingly successful to predict phenomena on the microscopic scale up to the present. The experiments at this time were based on relatively hot gases and solid bodies interacting with thermal radiation, and did not allow for direct observation of the new concepts appearing so abstruse from the macroscopic viewpoint. And people did not think that this was possible. This should change with the development of the laser.

The invention of the maser [1.8] in 1955 and the laser [1.9, 1.10] in 1960 provided a monochromatic optical radiation source with a long phase coherence allowing for tight focusing and high accuracy. On the one hand, this lead to many practical applications of the laser as an indispensable tool for research, medicine, industry and everyday life. On the other hand, it permitted the direct observation of quantum mechanical systems as experimentalists gained control over single or few atoms by making use of laser cooling and trapping of atoms [1.11]. Moreover, the quantum nature of the laser light itself became a subject of experimental and theoretical research known as quantum optics [1.12]. Finally, the fully quantized interaction of both light and atoms was realized in optical and microwave cavities, entering the so-called strong coupling regime of cavity quantum electrodynamics (CQED) [1.13, 1.14].

A striking demonstration of the control of atomic gases was the realization of a Bose-

Einstein condensate [1.15, 1.16] – the degenerate quantum gas predicted by Einstein [1.3] – in 1995. The creation of this ultra-cold atomic cloud relies heavily (but not only) on the use of laser trapping and cooling. Moreover, placing these ultra-cold atoms in an optical lattice created by interfering laser beams [1.17, 1.18] allows for emulating condensed matter models such as the Bose-Hubbard model. So finally Feynman's idea to simulate quantum physical systems with a simpler quantum physical system [1.19] became experimental truth.

Several Nobel prices were awarded for related research. Recently, these were in 1997 for cooling and trapping (Chu, Cohen-Tannoudji, Phillips), in 2001 for Bose-Einstein condensates (Cornell, Ketterle, Wieman), in 2005 for optical coherence and frequency combs (Glauber, Hall, Hänsch), in 2012 for methods to manipulate quantum systems (Haroche, Wineland) and in 2018 for optical tweezers (Ashkin among others).

1.1. Light forces and optical resonators

The fundamental processes of the quantum interaction of radiation and matter were hypothesized by Einstein as early as 1917 [1.20]. The first process consists of the transition of the internal state of an atom to a higher level accompanied by the absorption of a photon from the radiation field, and its inverse, i.e. the transition to a lower internal state and emission of a photon into the radiation field. Since for this purpose the atom has to be driven by radiation it is called *stimulated* emission and absorption. In the second process photons are uniformly emitted in all directions, even when no field is present. This so-called *spontaneous* emission is a visible consequence of the quantum nature of the electric field.

Since photons carry momentum the recoil kick upon emission or absorption induces mechanical forces onto the atom. Let us now consider an atom in one dimension which is illuminated by a laser beam. Photons are absorbed from the beam giving rise to a kick in the beam's propagation direction. As explained above, the emission process can be twofold: Firstly, if the photon is emitted spontaneously, the atom feels a kick in a random uniform direction such that no net force arises. The atom will thus be pushed away by the radiation due the kick upon absorption, so this dissipative force is aptly called *radiation pressure*. Secondly, the photon can be emitted by stimulated emission back into the laser beam. Since its propagation direction is the same as that of the absorbed photon one would expect that there is no net force. This is true for a beam with a uniform intensity distribution. An inhomogeneous intensity such as in the focus of a beam, however, leads to the *dipole force* proportional to the intensity gradient. It pushes the atoms towards the intensity maxima or minima, depending on whether the laser frequency is lower or higher than the atomic resonance frequency, respectively.

Further effects can be identified by considering an atom in two counter-propagating laser beams. The interference in counter-propagating beams leads to an intensity pattern creating a conservative potential for the atoms due to the dipole force. Because of their regular structure these potentials are called *optical lattices* [1.21]. Obviously, the net radiation pressure forces cancel for an atom at rest. For moving atoms, however, the

Doppler effect leads to different absorption rates from the co- and counter-propagating beams, respectively. Applying red-detuned laser light results in a velocity-dependent friction force, which is called Doppler cooling [1.22].

With increasing atom-field coupling strengths, single photon scattering events become more relevant and this granularity leads to quantum noise in addition to the description based on averaged net forces. Finally, the so-called strong-coupling regime is attained when the coherent interaction dominates over dissipative processes. Atom and field can not be seen as single entities anymore, but are rather described by the dressed states of the Jaynes-Cummings model [1.23]. Strong coupling can be realized by placing the atom in an optical resonator, where a photon travels several round-trips increasing the chance of hitting the atom. Strikingly, in such a set-up an atom can be trapped in the field of a single photon [1.24].

Even when scattering itself can be considered classical, the back-action of the atoms on the resonator field is not negligible, which leads to a non-linear coupled atom-field dynamics [1.25]. The reason for this is that the presence of atoms in a resonator dispersively shifts the cavity resonance closer to or further away from the pump laser frequency, which affects the intra-cavity intensity. For moving atoms the optical lattice in the cavity thus dynamically depends on all the atom positions, resulting in a collective cavity-mediated atom-atom interaction. When the pump laser frequency is lower than the cavity frequency, photons leaking out through the mirrors dissipate energy, which gives rise to cavity cooling [1.26, 1.27]. The collective velocity-dependent friction force arises due to the finite time the cavity field needs to adapt to a changed atomic distribution. As opposed to Doppler cooling and most other cooling schemes, cavity cooling does not rely on spontaneous emission and the internal level structure of the particles, and can thus be as well applied to molecules and nano-particles. Moreover, measuring the cavity output fields gives insight into the atomic state in the cavity [1.28, 1.29]. Pumping a ring cavity from one side results in a collective instability coined collective atomic recoil lasing (CARL) [1.30, 1.31].

The collective effects are further enhanced, when the driving field illuminates the atoms directly from a transversal direction. Then the atoms collectively scatter light into the cavity and the intra-cavity intensity crucially depends on their spatial distribution. In turn, the interference between pump field and self-created cavity field induces trapping forces for red cavity detuning. Prominently, this interplay between atoms and fields results in a phase transition from a homogeneous to a self-ordered configuration of the atoms, depending on the pump laser power [1.32, 1.33]. For ordered distributions the scattering into the cavity is super-radiantly enhanced and scales quadratically with the number of particles [1.34]. When several resonator modes are quasi-resonantly pumped, the atoms aim for finding the atomic configuration which is optimally adapted to all modes [1.35].

A Bose-Einstein condensate in such a transversally pumped resonator set-up can be used to realize the Dicke Hamiltonian [1.36]. Moreover, with the help of an external optical lattice, a generalized Bose-Hubbard model with infinite-range interactions [1.37] has been experimentally implemented [1.38]. These extended models exhibit rich phase diagrams [1.39–1.41] and are suitable to simulate exotic states of matter [1.42]. Quantum properties of the atomic state can be non-destructively read off from the cavity output [1.43].

Let us finally note that when the density of the gas and the pump power are high enough, the back-action of the atoms on the field can be significant also in free space. This results for instance in super-radiant Rayleigh scattering [1.44] and spontaneous crystallization [1.45, 1.46]. Atoms moving along optical fibers (nano-fibers, hollow core fibers, etc.) pose an alternative where the tight radial confinement of the light enhances the coupling, while the dimension along the fiber is open as in free space. Also in such a set-up collective ordering phenomena for monochromatic [1.47] and broadband radiation [1.48] occur.

1.2. Solving optimization problems with a physical system

Optimization is to find the best configuration according to some rules and constraints. This is often difficult when the number of configurations is large and the constraints are conflicting. Optimization problems are abundant in economy and engineering, as well as in computer science, social sciences and biology among other research fields. A classic example is the traveling salesman problem, where the task is to visit specified cities with the shortest possible total travel distance. There are also mathematical riddles and games which can be formulated as an optimization problem, for instance the N-queens problem [1.49]. Moreover, chemical or physical problems like the folding of proteins, finding the structure of atomic and molecular clusters, or the behavior of glasses correspond to a continuous optimization problem [1.50].

Optimization problems can be recast into the task of minimizing a *cost function* which typically depends on many variables. The cost function quantifies how well a configuration is adapted to the constraints given by the problem and assigns a real value to each configuration of the variables, which can be discrete or continuous. If there is a finite amount of configurations (implying a discrete configuration space), we talk about combinatorial optimization problems.

For difficult problems with conflicting constraints the cost function is usually rugged and contains many local minima, thus a local search by following the steepest gradient gets easily stuck in one of those minima. So the demanding task is to find the *global minimum* of the cost function. Since the configuration space is typically large, trying out all configurations is not a viable option. Having detailed knowledge of the cost function sometimes allows for finding problem specific deterministic algorithms, but such algorithms are not available in general and often demand formidable resources. An alternative are stochastic methods, where for instance the initial states are sampled from a uniform distribution (global phase) and then local minima are found by a local search (local phase) [1.51]. Note that with these methods there is no absolute guarantee of success and each algorithm is a trade-off between efficiency and reliability.

Interestingly, the inspiration for many stochastic algorithms comes from physics, where the cost function typically corresponds to a fictitious potential energy landscape. A well-known example is the simulated annealing algorithm introduced in 1983 [1.52]. In this algorithm, the distribution of a thermal ensemble of atoms is numerically sampled using a Metropolis algorithm [1.53]. Large thermal fluctuations at the initial stage allow the fictitious particle to explore the space and jump out of local minima. Reducing the fictitious temperature and hence the fluctuations yields distributions which are closer and closer to the global minimum. If this temperature decrease is slow enough, the global minimum is found with an arbitrarily high probability [1.54]. The algorithm thus smoothly transits from a global phase with large fluctuations to a local phase with small fluctuations.

A more recent idea is to exchange the thermal fluctuations with quantum fluctuations close to zero temperature, a method called quantum annealing [1.55, 1.56]. Intuitively speaking, a quantum particle can tunnel through potential barriers while a thermal particle has to jump over them. For spiky barriers one thus naively expects that a quantum particle could be less likely to get stuck in potential minima. The annealing procedure is the same as in the classical case: Initially large quantum fluctuations are slowly decreased such that the system can adiabatically follow [1.57].

Unfortunately, large quantum systems cannot be straightforwardly simulated on a classical computer, since the wave function alone contains as many coefficients as state configurations of the problem – a number growing exponentially with the system size. The precise control of quantum systems in the framework of superconducting qubits, trapped ions, Rydberg atoms or ultra-cold atoms in optical lattices opens a different route: One can envisage to set up a (different) quantum system and let nature do the calculation as proposed by Feynman already in 1981 [1.19]. While there are efforts to realize universal quantum computers [1.58], the task of optimization is thought to be easier using analog special-purpose quantum annealers. Commercial devices implementing quantum annealing are already available since 2011: The D-Wave device [1.59] shows evidence for quantum dynamics [1.60].

Note that it is not clear if these have any advantage on fundamental grounds, because simulating quantum systems on a conventional computer is not always hard. Quantum Monte Carlo algorithms were shown to have the same scaling with system size as real quantum tunneling [1.61]. Thus when Monte Carlo algorithms are applicable, there is no quantum speed-up. For this reason recent effort goes into classifying Hamiltonians into those which can be sampled with Monte Carlo methods, so-called stoquastic Hamiltonians, and those which can not [1.57]. Consequently, quantum speed-up can only exist in the latter class of non-stoquastic Hamiltonians.

1.3. Outline

This thesis deals with the coupled atom-field dynamics in transversally pumped multimode optical resonators and their potential application as a system implementing quantum annealing with the goal to solve optimization problems.

In Chapter 2, we introduce the physical background used in the later chapters. After the introduction of light quantization, we consider the shape and spectral properties of light fields in standing wave optical resonators. The theory of the interaction of these light fields with atoms is reviewed subsequently. Thereby, we focus on the dispersive limit, where the light fields create potentials for the atoms. Finally, these concepts are used for describing the physics of ultra-cold atoms in optical lattices.

Chapter 3 deals with atoms in a transversally pumped optical resonator. The purpose of this chapter is to introduce the basic physics and different approximations for the set-up we consider in the following publications. We motivate the arising coupled atom-field dynamics for the open quantum system from the viewpoint of dynamical optical potentials, and connect to an insightful semi-classical approximation. Moreover, departing from the coupled atom-field dynamics we adiabatically eliminate the cavity fields from the dynamics, shedding light on the effective interactions between atoms themselves. Finally, the last section deals with the description of ultra-cold atoms in lattices placed in the optical resonator.

The next chapter, Chapter 4, introduces the annealing procedure as a method for solving optimization problems. By means of formulating thermal annealing within a Langevin particle model we motivate the basic features and point out the similarities to classical atoms in cavities. Going to the quantum realm, cavities can be used to create a platform for quantum annealing with ultra-cold atoms. In both cases we motivate how to generically create tailored interactions to encode an optimization problem.

In the publication in Chapter 5 we treat the semi-classical physics of particles in a two-mode cavity, which can be understood as a minimal example where a local minimum exists. We investigate the dynamics induced by sudden intensity quenches and slow sweeps, where slower ramp speeds tend to favor a quasi-stationary state globally minimizing the energy predicted by a phase diagram from Ref. [1.62]. This chapter was published in Ref. [1.63].

Chapter 6 introduces quantum annealing with ultra-cold lattice atoms in a multi-mode cavity. Specifically, it is discussed how an arbitrary interaction matrix can be created using a number of modes on the order of N^2, where N is the problem size. As an example a Hopfield neural network is treated. It was published in Ref. [1.64].

A specific problem for quantum annealing in multi-mode cavities is introduced in Chapter 7, where a special set-up for solving the N-queens problem is introduced. The number of mode resources scales only linearly with the problem size here. Variation of the N-queens are proven to be NP-complete and hard instances exist even for small problem sizes. Thus, the problem poses a viable candidate for testing quantum advantage. This chapter was published in Ref. [1.65].

In Chapter 8 we present the ordering and cooling of thermal atoms in an optical resonator which is pumped by a frequency comb. These preliminary results will be published in near future. We conclude the main part of the thesis in Chapter 9.

The appendix includes some more calculations for reference in the main text in Appendix A: Hermite-Gaussian mode shapes, an alternative classical derivation of the steady state field amplitude for transversally pumped atoms in a resonator, details on the quantum Brownian motion master equation and an analysis of collective cooling effects for two particles. A further publication in Appendix B describes an experiment implementing an ion-based quantum sensor of optical cavity photon numbers published in Ref. [1.66], where the author contributed as theoretical support.

2. Physical background

In this chapter we review the physical background for the later chapters in this thesis. After introducing quantized light fields, we investigate the spectral and spatial properties of light in optical resonators. Subsequently, we describe light interacting with atoms in the dispersive limit of large laser-atom detuning, where light creates an optical potential and atoms act as refractive index. Finally, ultra-cold atoms trapped in such an optical potential are introduced.

2.1. Classical and quantum light

From Maxwell's equations without sources it follows that the electric field obeys the wave equation [2.1]

$$\Delta E - \frac{1}{c^2}\frac{\partial^2}{\partial t^2}E = 0, \tag{2.1}$$

where $\Delta = \partial^2/\partial x^2 + \partial^2/\partial y^2 + \partial^2/\partial z^2$ is the Laplacian. For simplicity we choose one specific polarization which makes the electric field a scalar.

The field can be written as a Fourier decomposition in terms of positive and negative frequency parts[*]

$$E(t,\boldsymbol{x}) = i\sum_{\boldsymbol{k}}\left[\mathcal{E}_{\boldsymbol{k}}\mathcal{G}_{\boldsymbol{k}}(\boldsymbol{x})e^{-i\omega_k t} - \mathcal{E}^*_{\boldsymbol{k}}\mathcal{G}^*_{\boldsymbol{k}}(\boldsymbol{x})e^{i\omega_k t}\right] \tag{2.2}$$

with the Fourier coefficients $\mathcal{E}_{\boldsymbol{k}}$ and the normalized mode functions $\mathcal{G}_{\boldsymbol{k}}$. The wave vectors $\boldsymbol{k}$ are connected to the frequencies $\omega_k = ck = c|\boldsymbol{k}|$ via the speed of light c. Note that by writing a discrete sum instead of an integral, we implicitly assumed that the light field is confined to a finite box. The general case is recovered in the limit where the edges go to infinity.

In order to facilitate the formal connection to quantum electrodynamics, we rewrite the Fourier coefficients as dimensionless fields $\alpha_{\boldsymbol{k}}$ normalized to the field of one photon

$$\mathcal{E}_{0,\boldsymbol{k}} = \sqrt{\hbar\omega_k/(2\epsilon_0 V_{\boldsymbol{k}})}, \tag{2.3}$$

with the mode volume $V_{\boldsymbol{k}}$, the vacuum permittivity ϵ_0 and the Planck constant $\hbar$. Note that here the finite box is important since otherwise the mode volume would be infinite

---

[*] With a separation ansatz $E(t,\boldsymbol{x}) = T(t)\mathcal{G}(\boldsymbol{x})$ the wave equation yields a harmonic oscillator equation for the time part $\ddot{T}(t) + c^2k^2T(t) = 0$ with positive and negative frequency solutions $T(t) = e^{\pm i\omega_k t}$ and $\omega_k = ck$. The spatial part obeys the Helmholtz equation in Eq. (2.7). The square of the wave vector enters mathematically as a separation constant [2.1].

and the single-photon field zero. The resulting expression equivalent to Eq. (2.2)

$$E(t,\boldsymbol{x}) = i\sum_{\boldsymbol{k}} \mathcal{E}_{0,\boldsymbol{k}} \left[\alpha_{\boldsymbol{k}}\mathcal{G}_{\boldsymbol{k}}(\boldsymbol{x})e^{-i\omega_k t} - \alpha^*_{\boldsymbol{k}}\mathcal{G}^*_{\boldsymbol{k}}(\boldsymbol{x})e^{i\omega_k t}\right] \tag{2.4}$$

allows for canonical quantization by replacing the dimensionless coefficients $\alpha_{\boldsymbol{k}}$ and $\alpha^*_{\boldsymbol{k}}$ with the bosonic creation and annihilation operators $a_{\boldsymbol{k}}$ and $a^\dagger_{\boldsymbol{k}}$ fulfilling the commutation relations $[a_{\boldsymbol{k}}, a^\dagger_{\boldsymbol{k}'}] = \delta_{\boldsymbol{k}\boldsymbol{k}'}$. This substitution yields the quantized electromagnetic field operator in the Heisenberg picture

$$\hat{E}(t,\boldsymbol{x}) = i\sum_{\boldsymbol{k}} \mathcal{E}_{0,\boldsymbol{k}} \left[a_{\boldsymbol{k}}\mathcal{G}_{\boldsymbol{k}}(\boldsymbol{x})e^{-i\omega_k t} - a^\dagger_{\boldsymbol{k}}\mathcal{G}^*_{\boldsymbol{k}}(\boldsymbol{x})e^{i\omega_k t}\right]. \tag{2.5}$$

For later correspondence, we define the negative frequency part of the field as

$$\hat{E}^-_{\boldsymbol{k}}(\boldsymbol{x}) = \mathcal{E}_{0,\boldsymbol{k}} a_{\boldsymbol{k}} \mathcal{G}_{\boldsymbol{k}}(\boldsymbol{x}) \tag{2.6}$$

and the positive frequency part as $\hat{E}^+_{\boldsymbol{k}}(\boldsymbol{x}) = [\hat{E}^-_{\boldsymbol{k}}(\boldsymbol{x})]^\dagger$, and analogously so for the classical case $E^-_{\boldsymbol{k}}(\boldsymbol{x}) = \mathcal{E}_{0,\boldsymbol{k}}\alpha_{\boldsymbol{k}}\mathcal{G}_{\boldsymbol{k}}(\boldsymbol{x})$ and $E^+_{\boldsymbol{k}} = (E^-_{\boldsymbol{k}})^*$.

In quantum as well as classical case, the spatial shape of the modes is obtained by plugging Eq. (2.2) or (2.5) into the wave equation. This yields the Helmholtz equation for the mode functions

$$\Delta\mathcal{G}_{\boldsymbol{k}}(\boldsymbol{x}) + k^2\mathcal{G}_{\boldsymbol{k}}(\boldsymbol{x}) = 0. \tag{2.7}$$

A free space solution are running plane waves $\mathcal{G}_{\boldsymbol{k}}(\boldsymbol{x}) = e^{i\boldsymbol{k}\boldsymbol{x}}$. Mirrors, instead, add boundary conditions to the Helmholtz equations, so the mode functions depend on their shape. This leads to the mode shapes in optical resonators treated in the next section.

2.2. Fabry-Pérot resonators

Optical resonators are a versatile tool for controlling light fields. They function as a filter allowing for the oscillation of certain frequencies only. Moreover, the shape of the oscillating modes depends on the geometry of the resonator. Finally, the intensity per photon in the resonator can be strongly enhanced such that the interaction between an atom and the light field becomes substantially strong. In the following we will use the expressions optical resonator and cavity interchangeably.

A Fabry-Pérot resonator consists of two mirrors at a distance of L, where light is bouncing back and forth building up a standing wave. The properties of the mirrors are modeled with their amplitude reflection and transmission coefficient r and iq, respectively, where $r^2 + q^2 = 1$. We assume that the mirrors are highly reflective, thus $q^2 \ll 1$.

2.2.1. Spectral properties of the field

Let us now go to the one-dimensional case. The cavity is probed through the mirror with a mono-chromatic laser beam with amplitude $\mathcal{E}_{\text{in}}$, frequency ω and wave number k.

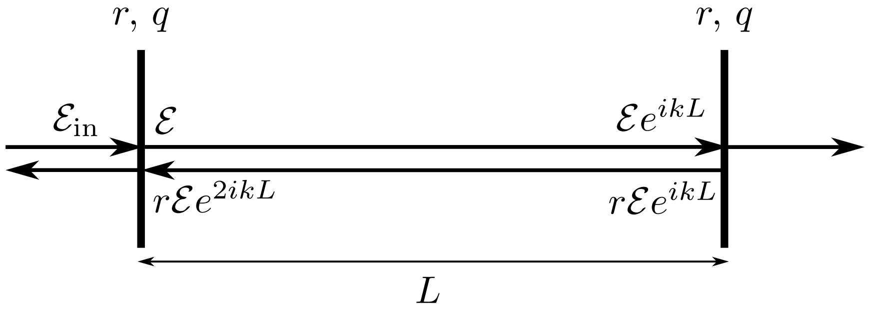

Figure 2.1.: One round trip of the electric field in a Fabry-Pérot resonator with reflection and transmission coefficients r and t, respectively. Starting with a field $\mathcal{E}$, the field after one round trip is given by $r^2e^{2ikL}\mathcal{E} + iq\mathcal{E}_{\rm in}$, where the first part is the twice reflected circulated field and the second part is the probe field.

We are interested in the steady state amplitude of the field in the cavity as a function of k, that is the spectrum of the optical resonator.

The steady state spectrum can be easily derived by considering the fields circulating in the cavity. Since at steady state the field does not change, it has to be unchanged after one round trip [2.2]. With the help of Fig. 2.1, we see that the field after one round trip is given by the reflected part with phase shift $2kL$ and the input field. This yields the steady state condition

$$\mathcal{E} \overset{!}{=} r^2e^{2ikL}\mathcal{E} + iq\mathcal{E}_{\rm in} \tag{2.8}$$

and the steady state cavity field

$$\mathcal{E}_{\rm st}(k) = \frac{iq}{1-r^2e^{2ikL}}\mathcal{E}_{\rm in} \tag{2.9}$$

is obtained by solving for $\mathcal{E}$.

The intra-cavity intensity at steady state is the input intensity multiplied by the factor

$$\mathcal{I}(k) = \left|\frac{\mathcal{E}_{\rm st}(k)}{\mathcal{E}_{\rm in}}\right|^2 = \frac{q^2}{(1-r)^2 + 4r^2\sin^2(kL)}, \tag{2.10}$$

which is depicted in Fig. 2.2. One observes resonances at a distance of the free spectral range $\omega_{\rm FSR} = \pi c/L$. In a high-Q cavity, r approaches unity and the peaks become narrow and finally converge to delta peaks for perfectly reflecting mirrors. In this limit the cavity acts as a filter singling out very narrow frequency lines, where the intensity is strongly enhanced.

Close to a specific resonance at ω_c, the steady state cavity field can be rewritten in terms of the cavity detuning $\Delta_c = \omega - \omega_c$ and the cavity line width or amplitude decay rate $\kappa = q^2c/(2L)$. For $|\Delta_c| \ll \omega_{\rm FSR}$ we can do the approximation $r^2e^{2ikl} \approx 1 - q^2 + iq^2\Delta_c/\kappa$ [2.2] and the steady state field becomes

$$\mathcal{E}_{\rm st} = \frac{iq\mathcal{E}_{\rm in}}{q^2}\frac{1}{1-i\Delta_c/\kappa} = -\frac{\sqrt{\kappa c/(2L)}}{\Delta_c + i\kappa}\mathcal{E}_{\rm in}. \tag{2.11}$$

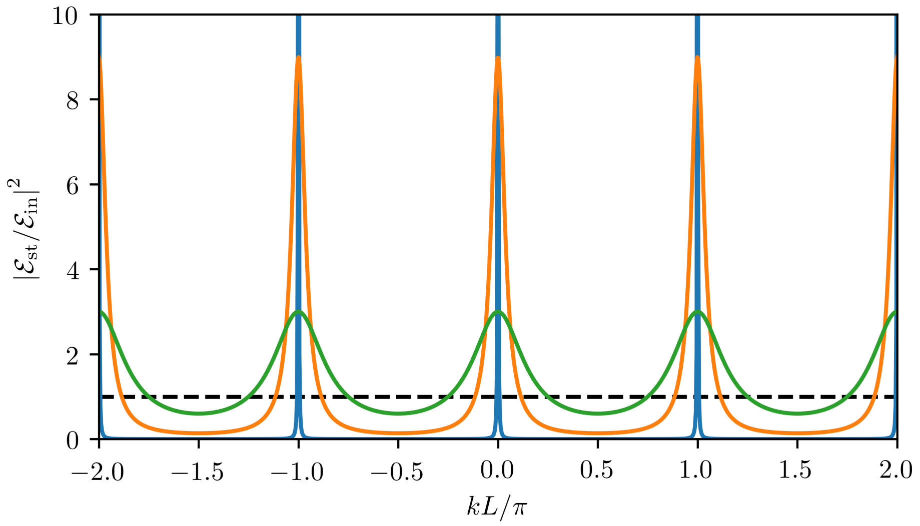

Figure 2.2.: Enhancement of the intensity in an empty Fabry-Pérot resonator for different reflection coefficients $r = 0.5$ (green), $r = 0.8$ (orange) and $r = 0.999$ (blue) from Eq. (2.10). The resonances are peaked at $k_n = n\pi/L$ and for highly reflective mirrors we have $|\mathcal{E}_{\mathrm{st}}(k_n)/\mathcal{E}_{\mathrm{in}}|^2 \gg 1$.

On resonance ($\Delta_c = 0$) the steady state amplitude is the ratio of input and output field, while off resonance it decreases according to the function $(1 - i\Delta_c/\kappa)^{-1}$.

2.2.2. Electric field modes in high-Q cavities

We have seen that in high-Q cavities the intra-cavity intensity at steady state is significantly enhanced only close to a resonance and suppressed otherwise. To obtain the mode functions of the resonator it is thus a good approximation to assume a closed cavity with perfectly reflecting mirrors $r = 1$. Since then the field on the perfectly conducting mirror surfaces has to be zero, the presence of the cavity simply adds boundary conditions to the Helmholtz equation in Eq. (2.7). This way the form of the mirrors influences the shape of the mode functions.

In the one-dimensional case, a general real solution of the Helmholtz equation can be written as a linear combination of sines and cosines. Placing the origin $x = 0$ into the center of the cavity, the boundary conditions impose that $\mathcal{G}_n(\pm L/2) = 0$ for all modes indexed by n (in the 1D case a single index is sufficient). This yields the resonance condition for the wave number k

$$k_n = n\frac{\pi}{L}, \tag{2.12}$$

which exactly correspond to the peaks in Fig. 2.2. The mode functions can be written as

$$\mathcal{G}_n(x) = \cos(k_n x + \phi_n), \tag{2.13}$$

where $\phi_n = 0$ for odd n and $\phi_n = \pi/2$ for even n.

An important special case in three dimensions are optical resonators with spherical mirrors of curvature R. In the limit of weak focusing, the resonant modes can be expanded in the set of Hermite-Gaussian mode functions. The resonator geometry is summarized by the so-called stability parameter $g = 1 - L/R$, where special cases are the confocal ($g = 0$), planar ($g = 1$) and concentric ($g = -1$) configuration [2.3]. The resonant wave numbers

$$k_{nlm} = n\frac{\pi}{L} + (l + m + 1)\frac{\arccos(g)}{L} \tag{2.14}$$

are derived in Sec. A.1 by imposing the boundary conditions due to the mirrors [2.4]. Thereby the transversal indices l and m denote different Hermite-Gaussian shapes, so-called TEM_{lm} modes. The index n distinguishes different longitudinal modes as in the 1D case. Correspondingly, the shift with respect to the 1D resonant wave numbers vanishes for the (quasi-1D) planar geometry since $\arccos(1) = 0$.

2.3. Atom-light interaction

The interaction of atoms with light is at the heart of this theses. We are in the following particularly interested in the trapping of the atoms due to the dipole force. In the dispersive limit, where the light frequency is far from any atomic resonance frequency and internal degrees of freedom can be eliminated, the dissipative part can often be neglected and light fields with a fixed amplitude create a conservative optical potential.

2.3.1. Jaynes-Cummings model - the dipole approximation and fundamental aspects

Let us start by modeling an atom as a system with only two electronic energy eigenstates, the ground state $|g\rangle$ and the excited state $|e\rangle$. Their energy difference is given by $\hbar\omega_a$ with the atomic resonance frequency ω_a. Atoms are usually small (a few Angstoms) compared to optical wave lengths (400-800 nm), and thus the electric field can be approximated as spatially uniform within the atom's extension. If this is valid, the atom behaves like a dipole [2.5] leading to the interaction energy

$$H_{\text{int}} = -\hat{d}\hat{E}, \tag{2.15}$$

which is well-known from electrostatics [2.6]. The dipole is aligned parallel to the electric field's polarization. The dipole operator is given by $\hat{d} = \mu(\sigma + \sigma^\dagger)$ with the transition operator $\sigma = |g\rangle\langle e|$ and the dipole moment μ of the transition.

Inserting a single-mode field with frequency ω_p in the Schrödinger picture $\hat{E}(x) = i(\hat{E}^-(x) - \hat{E}^+(x))$ (dropping the index) we obtain

$$H_{\text{int}} = -i\mu[\hat{E}^-(x) - \hat{E}^+(x)][\sigma + \sigma^\dagger] \overset{\text{RWA}}{\approx} -i\mu[\sigma^\dagger\hat{E}^-(x) - \hat{E}^+(x)\sigma]. \tag{2.16}$$

In the second step we made the rotating wave approximation (RWA) neglecting non-resonant terms oscillating rapidly with $\omega_a + \omega_p$ over resonant terms oscillating with $\omega_a - \omega_p$ [2.5]. Inserting the expression for the fields from Eq. (2.6) the Hamiltonian takes the form of the well-known Jaynes-Cummings model [2.7]

$$H_{\mathrm{JC}} = -i\hbar g(\sigma^\dagger a \mathcal{G}(x) - a^\dagger \sigma \mathcal{G}^*(x)), \tag{2.17}$$

with the single-photon Rabi frequency $g = \mu \mathcal{E}_0/\hbar$. Note that usually this Hamiltonian is expressed for a fixed position $\mathcal{G}(x_0) = 1$.

Physically, the atom-light interaction within the dipole approximation can be described by stimulated emission ($a^\dagger \sigma$) and absorption ($\sigma^\dagger a$) of photons. Moreover, atoms can always spontaneously emit photons into any of the other modes in a random direction. This is an incoherent process, since all other modes are traced out from the dynamics and considered as a bath [2.8]. Because photons carry the momentum $\hbar \boldsymbol{k}$, both processes induce forces onto the particles. The coherent part is called dipole force, while the incoherent contribution is called radiation pressure [2.9].

2.3.2. Optical potentials - a moving atom in the dispersive limit

A mobile atom with position and momentum operators $\hat{x}$ and $\hat{p}$ and a mass m_a in a single-mode quantum field has the Hamiltonian

$$H = \frac{\hat{p}^2}{2m_a} - \hbar\Delta_a \sigma^\dagger \sigma - i\mu[\sigma^\dagger \hat{E}^-(\hat{x}) - \hat{E}^+(\hat{x})\sigma] + H_{\mathrm{field}}, \tag{2.18}$$

with the Hamiltonian of the free field H_{field} and the atomic detuning $\Delta_a = \omega_p - \omega_a$. Here it is written in a frame of reference rotating with ω_p. Spontaneous emission with the rate γ must in principle be taken into account via a master equation, but in the far detuned limit $|\Delta_a| \gg \gamma$ it can often be neglected. The Heisenberg equation for the σ operator is given by

$$\dot{\sigma} = i\Delta_a \sigma - \frac{\mu}{\hbar}\sigma^z \hat{E}^-. \tag{2.19}$$

If the dynamics of the dipole is much faster than the time scale of the atomic motion, we can assume that the dipole follows the field instantaneously and set $\dot{\sigma} = 0$. The atomic dipole is thus slaved to the electric field, and can be approximated by [2.9]

$$\sigma \overset{\dot{\sigma}=0}{\approx} -i\frac{\mu}{\hbar\Delta_a}\sigma^z \hat{E}^- \overset{\sigma^z=-1}{\approx} i\frac{\mu}{\hbar\Delta_a}\hat{E}^-. \tag{2.20}$$

In the first expression, the polarizability is non-linear since it depends on the energy level occupation via σ^z. For a low saturation of the atom, i.e. not too strong light fields, the polarizability becomes linear and is given by $\mathcal{P} = -\mu^2/(\hbar\Delta_a)$. The dipole operator can then be effectively expressed as $\hat{d} = \mathcal{P}\hat{E}$.

Using the result for σ yields the effective Hamiltonian in the far-detuned and low-saturation limit

$$H = \frac{\hat{p}^2}{2m_a} + \hat{V}(\hat{x}) + H_{\mathrm{field}} \tag{2.21}$$

where the quantum potential is given by

$$\hat{V}(\hat{x}) = \frac{\mu^2}{\hbar\Delta_a}(\hat{E}^+\hat{E}^-)(\hat{x}) = \frac{\hbar\hat{\Omega}^\dagger(\hat{x})\hat{\Omega}(\hat{x})}{\Delta_a}, \tag{2.22}$$

with the operator $\hat{\Omega} = \mu\hat{E}^-/\hbar$. Note that for quantum fields $\hat{V}$ is an operator on the joint Hilbert space of field and external atomic degrees of freedom and is just called potential here due the correspondence to the classical case. For classical fields it becomes a real potential and Ω becomes the Rabi frequency (within the RWA). The emergence of a potential arises from a position-dependent AC-Stark shift of the lower atomic level, which can also be obtained within the Jaynes-Cummings model in the low saturation limit. Note that the conservative force due to the potential is the aforementioned dipole force, while radiation pressure was neglected by not considering spontaneous emission.

This result can also be motivated from classical electrostatics [2.6]. The energy of an induced dipole $d = \mathcal{P}E$ in a field is given by $V(x) = -d(x)E(x) \approx -\mathcal{P}E^-(x)E^+(x)$ within the RWA. The polarizability of a classical dipole oscillator in the far-detuned limit is given by $\mathcal{P} = -6\pi\epsilon_0\gamma/(c^3\omega_a^3\Delta_a)$ [2.2]. In classical physics the decay rate γ is a phenomenological quantity. In order to connect to the result above, we insert the analytical expression from the (quantum) Wigner-Weisskopf theory $\gamma = c^3\omega_a^3\mu^2/(6\pi\epsilon_0\hbar)$ [2.10], and see that the polarizability corresponds to the one derived in the quantum case. Thus the $\hbar$ as quantum signature enters only via the expression of γ. For a more detailed discussion see Sec. A.2.

Let us consider two simple examples. Two counter-propagating laser beams create a classical standing wave $E^+ = E^- \propto \cos(kx)$, which effects in a periodic potential $V(x) \propto \cos^2(kx)$ with a lattice constant $a = \lambda/2 = \pi/k$. We will discuss these so-called optical lattices in Sec. 2.4 coming up next. For a running wave $E^- \propto e^{ikx}$ the potential is uniform and induces no dipole force. Remember that radiation pressure was neglected by going to the dispersive limit.

2.4. Ultracold atoms in optical lattices

We have seen in Eq. (2.22) that classical light fields create a potential for the atoms due to the ground state AC-Stark shift. Since strong counter-propagating laser beams give rise to a (classical) standing wave, they constitute a periodic potential often coined optical lattice. Trapped ultracold atoms at zero temperature in a deep optical lattice are well described by the Bose-Hubbard model. This relatively simple model yields a toolbox for theory and experiment allowing for the investigation and explanation of a plethora of quantum many-body phenoma [2.11, 2.12]. We now derive the Bose-Hubbard model following Ref. [2.13].

2.4.1. Band structure

We now aim to derive an approximate wave function of a quantum particle in a (classical) periodic potential with period (or lattice constant) a obeying the Hamiltonian

$$H_1 = \frac{\hat{p}^2}{2m_a} + V(\hat{x}). \tag{2.23}$$

Due to the Bloch theorem the eigenfunctions of this Hamiltonian are Bloch waves

$$\phi_q^n(x) = e^{iqx} u_q^n(x) \tag{2.24}$$

where the functions $u_q^n(x) = u_q^n(x+a)$ have the same period as the lattice.

Inserting into the Hamiltonian H_1 yields the eigenvalue equation $H_q u_q^n = E_q^n u_q^n$ with $H_q = (p + \hbar q)^2/(2m_a) + V(x)$. One can now diagonalize H_q for $q \in [-1/a, 1/a]$ to obtain the energy bands E_q^n and the corresponding wave functions ϕ_q^n for different quasi-momenta q and bands n. Numerically, it is easiest to rewrite the equation for the Fourier coefficients of the Bloch waves [2.13].

The Bloch waves are delocalized over the whole lattice, which is a meaningful basis for nearly free particles in shallow lattices. As the lattice depth increases, however, particles become localized close to potential minima. A more suitable basis is then provided by Wannier functions [2.14], which are given by a localized linear superposition of Bloch waves

$$w_n(x - x_j) = \sqrt{\frac{a}{2\pi}} \int_{-\pi/a}^{\pi/a} \phi_q^n(x) e^{-iqx_j} \mathrm{d}q. \tag{2.25}$$

Note that instead of the quasi-momentum index, they are now distinguished by the lattice site location of their maximum. This definition is not unique since the phases of the Bloch functions are arbitrary. But for each band there exists only one maximally localized Wannier function per lattice site, which has the properties that it is real, symmetric or anti-symmetric around x_j and exponentially decaying. These maximally localized Wannier functions can be obtained by fixing the phase of the Bloch waves at the origin: For even n the $\phi_q^n(x_j)$ need to be real, while for odd n they need to be purely imaginary [2.14].

2.4.2. Bose-Hubbard model

So far we treated a single particle. To describe many indistinguishable quantum particles at zero temperature we introduce bosonic field operators $\hat{\Psi}(x)$ fulfilling the bosonic commutation relations $[\hat{\Psi}(x), \hat{\Psi}^\dagger(x')] = \delta(x - x')$. The many-body Hamiltonian then takes the form [2.11]

$$H = \int \mathrm{d}x \hat{\Psi}^\dagger(x) H_1 \hat{\Psi}(x) + \frac{g_{1\mathrm{D}}}{2} \int \mathrm{d}x \hat{\Psi}^\dagger(x) \hat{\Psi}^\dagger(x) \hat{\Psi}(x) \hat{\Psi}(x), \tag{2.26}$$

where the second term introduces the contact interaction quantified with $g_{1\mathrm{D}}$. It is now useful to expand the bosonic field operators in the Wannier basis introduced above as

$\hat{\Psi}(x) = \sum_i \sum_n b_i^n w_n(x - x_i)$ with the bosonic annihilation operator b_i^n of the ith site and nth band. If the energy bands are well separated and the atoms are cold enough, only the lowest band is populated and the expansion can be truncated. This yields the tight-binding Hamiltonian

$$H = -\sum_{ij} J_{ij} b_i^\dagger b_j + \frac{1}{2} \sum_{ijkl} U_{ijkl} b_i^\dagger b_j^\dagger b_k b_l \tag{2.27}$$

with the overlaps

$$J_{ij} = -\int \mathrm{d}^3x \, w(x - x_i) \left(-\frac{\hbar^2}{2m_a} \nabla^2 + V(x) \right) w(x - x_j) \tag{2.28a}$$

$$U_{ijkl} = g_{1D} \int \mathrm{d}^3x \, w(x - x_i) w(x - x_j) w(x - x_k) w(x - x_l), \tag{2.28b}$$

where $b_i = b_i^1$ and $w = w_1$. These describe the motion in the lattice (tunneling) and the contact interactions, respectively.

Already for moderately deep lattices $V_\mathrm{L} \geq 5E_\mathrm{R}$ all overlaps are small compared to the on-site interactions $U = U_{0000}$ and the nearest-neighbor tunneling amplitudes $J = J_{i,i+1}$ [2.15]. Neglecting all but these two matrix elements, we obtain the standard Bose-Hubbard Hamiltonian

$$H = -J \sum_{\langle i,j \rangle} b_i^\dagger b_j + \frac{U}{2} \sum_i \hat{n}_i (\hat{n}_i + 1) \tag{2.29}$$

with the site occupation operator $\hat{n}_i = b_i^\dagger b_i$ and the sum over nearest neighbors denoted by $\langle i, j \rangle$.

Note that for strong trapping the potential wells can be approximated by harmonic traps with some characteristic length a_T and trapping frequency ω_T[†]. The band structure converges to the harmonic oscillator energies in this limit and the bandwidth goes to zero ("flat bands"). Hence also J goes to zero, since it is given the bandwidth of the lowest band divided by 4 in the case of an ideal gas $U = 0$ [2.15]. The lowest-band Wannier function converges to the ground state wave function of a harmonic oscillator

$$w_\mathrm{har}(x) = \pi^{-1/4} a_\mathrm{T}^{-1/2} \exp\left(-\frac{x^2}{2a_\mathrm{T}^2} \right). \tag{2.30}$$

Within this approximation, we can roughly estimate that the lowest-band approximation is valid when the energy gap $\hbar\omega_\mathrm{T}$ is much larger than the thermal energy $k_\mathrm{B}T$ and the interaction energy U.

The Bose-Hubbard Hamiltonian has two important limits: In the ideal gas limit $U \ll J$ the ground state is the so-called super-fluid state $|\mathrm{SF}\rangle \propto (\sum_i b_i^\dagger)^N |0\rangle$ with the (many-body) vacuum state $|0\rangle$ and the atom number N. This state contains all superpositions

---

[†] For a typical standing wave potential $V(x) = V_\mathrm{L} \cos^2(k_\mathrm{L} x)$ created by counter-propagating lasers with wave number k_L, they are given by $\omega_\mathrm{T} = \sqrt{4V_\mathrm{L}E_\mathrm{R}}/\hbar$ and $a_\mathrm{T} = (E_\mathrm{R}/V_\mathrm{L})^{1/4}/k_\mathrm{L}$, with the recoil energy $E_\mathrm{R} = \hbar^2 k_\mathrm{L}^2/(2m_a)$.

of occupation number states and the atoms are thus delocalized over the whole lattice. For $U \gg J$ the ground state becomes a Mott insulator, which is given by $|\mathrm{MI}\rangle = \prod_i b_i^\dagger |0\rangle$, in this case of commensurate filling $N/K = 1$ with the number of lattice sites K. This state is local and has no number fluctuations. The phase diagram of the Bose-Hubbard Hamiltonian was first calculated by Fisher et al. [2.16], while the first experimental realization of the superfluid to Mott insulator transition was published in Ref. [2.17].

As mentioned before, the periodic potential is created by (classical) standing wave laser light via the Stark potential in Eq. (2.22). Using standing waves from different directions allows for realizing many different lattice types, rendering atoms in optical lattices a versatile platform for testing many-body physics and quantum simulation. The standard setup consists of three perpendicular standing waves, leading to a regular three dimensional cubic lattice. If tunneling in one direction is frozen out by increasing the light intensity, one obtains several slaps (or pan cakes) of two dimensional optical lattices [2.12]. Finally, freezing out the motion in all but one direction creates 1D tubes [2.18].

3. Atoms in a tranversally pumped multi-mode cavity

In this chapter we consider the dynamics of laser-illuminated atoms in optical resonators. Most of the work so far dealt with optical resonators driven by a single laser pump [3.1]. Here we consider the case of a non-degenerate multi-mode cavity consisting of M pump-cavity mode pairs with pump and cavity mode functions $\mathcal{H}_m(\boldsymbol{x})$ and $\mathcal{G}_m(\boldsymbol{x})$, respectively. One pair is detuned from each other with the cavity detunings $\Delta_{c,m} = \omega_{p,m} - \omega_{c,m}$ and the pump mode field is denoted by $\mathcal{E}_{\text{in},m} = \mathcal{E}_{0,m}\alpha_{\text{in},m}$. A schematic illustration of the system is depicted in Fig. 3.1. We assume that the modes are far enough apart in frequency, such that light is only redistributed within a pump-cavity mode pair, while there is no cross-scattering between adjacent modes. All of these modes, however, interact with the same atomic cloud. When the mode shapes differ for each m this can introduce frustration and metastable states for the atoms, since it might not be clear for the atoms according to which shape they should order. This introduces a wealth of new physics beyond the single-mode case. Particularly, there is a deep connection between systems of this kind and optimization problems, which will be treated in the next chapter. For now we derive the central formulas describing the dynamics of atoms and fields for dispersive atom-light coupling in multi-mode cavities.

3.1. Coupled atom-field dynamics

The dynamics of the coupled atom-field system can be split into a coherent part described by a Hamiltonian and an incoherent part including cavity losses. For simplicity, we consider only one-dimensional motion along some axis x of the atoms in this section, since the models can be straightforwardly generalized to the 3D case.

3.1.1. Coherent part - dynamical quantum potentials

In order to derive a Hamiltonian describing the above mentioned coupled atom-field dynamics, we first write down the electric field at the position of the atoms. The negative frequency part of the mth mode pair in the Heisenberg picture is given by

$$\hat{E}_m^-(t,x) = \mathcal{E}_{0,m}\left(\alpha_{\text{in},m}\mathcal{H}_m(x)e^{-i\omega_{p,m}t} + a_m\mathcal{G}_m(x)e^{-i\omega_{c,m}t}\right), \tag{3.1}$$

and the total field $\hat{E}^-(t,x) = \sum_m \hat{E}_m^-(t,x)$ is a simple sum over all modes.

The (quantum) optical potential in Eq. (2.22) was derived for a single mode. Since here several frequencies are involved, the atomic detuning Δ_a will also depend on m (and

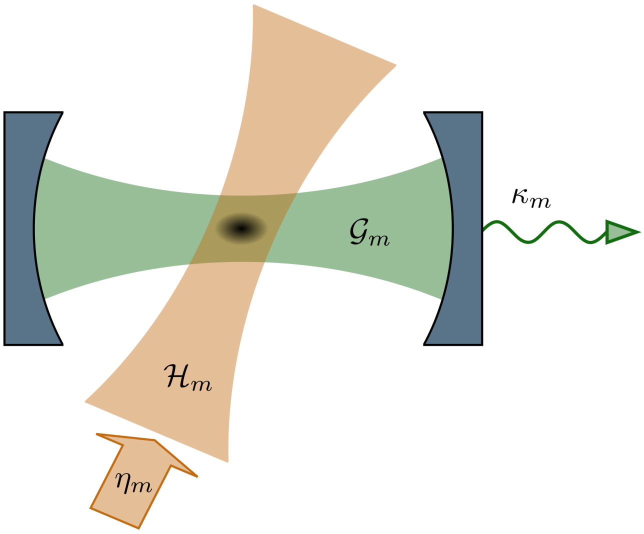

Figure 3.1.: Schematic illustration of the mth pump-cavity mode pair. Atoms (black cloud) in an optical Fabry-Perót resonator are directly illuminated from the side with the pump strength η_m and the mode function $\mathcal{H}_m$. The atomic cloud collectively scatters light from the pump mode into the cavity mode with the shape $\mathcal{G}_m$ and decay rates κ_m (and vice versa).

in principle also slightly on the pump-cavity detuning for a given m). We now assume that the spread of the mode frequencies is small compared to the atomic detuning, in which case the atomic detuning does not vary much and can be taken independent of m. An alternative would be to assume that each mode couples to a different atomic transition with the same Δ_a. In this case we can use Eq. (2.22) and obtain

$$\hat{V}(x) = \frac{\mu^2}{\hbar\Delta_a}\sum_{mn}\mathcal{E}_{0,m}\mathcal{E}_{0,n}\Big(\mathcal{G}_m^*\mathcal{G}_n a_m^\dagger a_n e^{i(\omega_{c,m}-\omega_{c,n})t} + \mathcal{H}_m^*\mathcal{H}_n\alpha_{\mathrm{in},m}^*\alpha_{\mathrm{in},n}e^{i(\omega_{p,m}-\omega_{p,n})t} + \\ + \mathcal{G}_m^*\mathcal{H}_n a_m^\dagger\alpha_{\mathrm{in},n}e^{i(\omega_{c,m}-\omega_{p,n})t} + \mathcal{H}_m^*\mathcal{G}_n\alpha_{\mathrm{in},m}^* a_n e^{i(\omega_{p,m}-\omega_{c,n})t}\Big)\,. \tag{3.2}$$

Since in high-Q cavities the mode spacing (i.e. the free spectral range) is typically much larger than $|\Delta_c|$ and the coupling, the fast rotating terms with $n \neq m$ can be neglected over the slowly rotating terms with $n = m$. This rotating wave approximation for adjacent modes physically means that different modes do not interfere. The result is a simple total potential $\hat{V}(x) = \sum_m \hat{V}_m(x)$ where the mth pump-cavity mode pair contributes

$$\hat{V}_m(x) = \hbar\Big(U_{0,m}|\mathcal{G}_m|^2 a_m^\dagger a_m + U_{p,m}|\mathcal{H}_m|^2 + \eta_m\mathcal{G}_m^*\mathcal{H}_m a_m^\dagger + \eta_m^*\mathcal{H}_m^*\mathcal{G}_m a_m\Big)\,. \tag{3.3}$$

The new quantities are the depth of the cavity potential $U_{0,m} = g_m^2/\Delta_a$, the effective pump-cavity mode coupling strength via the atoms $\eta_m = \Omega_m g_m/\Delta_a$ and the pump lattice depth $U_{p,m} = |\Omega_m|^2/\Delta_a$ for the mth mode pair. They are written in terms of the single cavity photon Rabi frequency $g_m = \mu\mathcal{E}_{0,m}/\hbar$ and the pump laser Rabi frequency $\Omega_m = g_m\alpha_{\mathrm{in},m}$.

Knowing this we can generalize Eq. (2.21) in order to obtain the Hamiltonian for N particles

$$\begin{aligned} H =& \sum_{j=1}^{N} \frac{\hat{p}_j^2}{2m_a} - \hbar \sum_{m=1}^{M} \Delta_{c,m} a_m^\dagger a_m \\ &+ \hbar N \sum_{m=1}^{M} \left[U_{0,m}\hat{\mathcal{B}}_m a_m^\dagger a_m + \eta_m(\hat{\Theta}_m^\dagger a_m + a_m^\dagger \hat{\Theta}_m) + U_{p,m}\hat{\mathcal{K}}_m \right], \end{aligned} \tag{3.4}$$

where we introduced the collective atomic operators

$$\hat{\Theta}_m = \frac{1}{N}\sum_j \mathcal{H}_m(\hat{x}_j)\mathcal{G}_m^*(\hat{x}_j) \tag{3.5}$$

$$\hat{\mathcal{B}}_m = \frac{1}{N}\sum_j |\mathcal{G}_m(\hat{x}_j)|^2 \tag{3.6}$$

$$\hat{\mathcal{K}}_m = \frac{1}{N}\sum_j |\mathcal{H}_m(\hat{x}_j)|^2. \tag{3.7}$$

In most parts of the thesis we will do one further approximation: Often one can neglect the back-scattering within the cavity mode, only keeping scattering from the pump mode to the cavity mode. As a more classical argument, it means that the optical potential created by the cavity field is neglected with respect to the terms containing the pump field. It is valid when $|\Delta_{c,m}| \gg N|U_{0,m}|$, when we can neglect the term containing $\hat{\mathcal{B}}_m$. Moreover, due to geometry, in the rest of this thesis we encounter the case where $|\mathcal{H}_m(x)|^2 = 1$ for all possible atomic positions x. The cavity Hamiltonian then simplifies to

$$H = \sum_j \frac{\hat{p}_j^2}{2m_a} - \hbar\sum_m \Delta_{c,m}a_m^\dagger a_m + \hbar N\sum_m \eta_m(\hat{\Theta}_m^\dagger a_m + a_m^\dagger\hat{\Theta}_m), \tag{3.8}$$

which is given here for future reference. The operator coupling the atomic position to the fields is hence the order operator $\hat{\Theta}_m$, whose form comes from the interference of each pump-cavity field pair.

3.1.2. Incoherent part - decay of the fields

Now we turn to the incoherent part of the dynamics due to light leaking out of the cavity with the field amplitude damping rate κ_m. As detailed in text books [3.2, 3.3], this damping can be described by a master equation obtained from coupling the cavity modes to the modes outside the cavity, which form a zero temperature bath, and tracing them out. In quantum optics it typically takes the form

$$\dot{\rho} = -\frac{i}{\hbar}[H,\rho] + \sum_m \kappa_m(2a_m\rho a_m^\dagger - a_m^\dagger a_m\rho - \rho a_m^\dagger a_m), \tag{3.9}$$

with the density matrix ρ and the Hamiltonian H [Eq. (3.8)] describing the coherent part from the previous section.

As an alternative representation, from this master equation we can derive Heisenberg-Langevin equations [3.3] for the operators $\hat{x}_j$, $\hat{p}_j$ and a_m

$$\dot{\hat{x}}_j = \frac{\hat{p}_j}{m_a} \tag{3.10a}$$

$$\dot{\hat{p}}_j = - iN \sum_m \eta_m([\hat{p}_j, \hat{\Theta}_m^\dagger] a_m + a_m^\dagger [\hat{p}_j, \hat{\Theta}_m]) \tag{3.10b}$$

$$\dot{a}_m = (i\Delta_{c,m} - \kappa_m) a_m - i\eta_m N \hat{\Theta}_m + \sqrt{2\kappa_m}\hat{\xi}_m, \tag{3.10c}$$

where we used $[\hat{x}, \hat{p}^2] = 2i\hbar\hat{p}$ and introduced the quantum noise operator fulfilling $[\hat{\xi}_m(t), \hat{\xi}_n^\dagger(t')] = \delta(t-t')\delta_{mn}$ [3.3]. Interpreting these equations, we see that the fields decay with κ_m, get pumped with $\eta_m N \hat{\Theta}_m$ and are subject to input noise $\hat{\xi}_m$, which makes sure that the commutation relations of a_m are preserved.

3.1.3. Semi-classical limit

The master equation [Eq. (3.9) with the Hamiltonian Eq. (3.8)] can be rewritten as a partial differential equation using a joint Wigner function for atoms and fields [3.4]. This partial differential equation can be approximated by a Fokker-Planck equation for a cloud of atoms with a temperature much larger than the recoil energy $k_B T \gg E_R$ with $E_R = \hbar^2 k^2/(2m_a)$ for all k's involved. Finally, the Fokker-Planck equation corresponds to a set of coupled stochastic differential equations. For a uniform pump field intensity $|\mathcal{H}_m(x)|^2 = 1$ the equations take the form [3.5]

$$\dot{x}_j = \frac{p_j}{m_a} \tag{3.11a}$$

$$\dot{p}_j = -\hbar N \sum_m \eta_m([\partial_{x_j} \Theta_m^*] \alpha_m + \alpha_m^* [\partial_{x_j} \Theta_m]) \tag{3.11b}$$

$$\dot{\alpha}_m = (i\Delta_{c,m} - \kappa_m)\alpha_m - i\eta_m N \Theta_m + \sqrt{\kappa_m}\xi_m \tag{3.11c}$$

with the order parameters

$$\Theta_m = \frac{1}{N} \sum_j \mathcal{H}_m(x_j) \mathcal{G}_m^*(x_j) \tag{3.12}$$

as the classical pendant of the order operator in Eq. (3.5). The complex white noise processes with the only non-vanishing moments $\langle \xi_m(t) \xi_n^*(t') \rangle = \delta(t-t')\delta_{mn}$ are the sum of two real white noise processes $\xi_m = (\zeta_m^1 + i\zeta_m^2)/\sqrt{2}$ with $\langle \zeta_m^{\{1,2\}}(t) \zeta_n^{\{1,2\}}(t') \rangle = \delta(t-t')\delta_{mn}$. We used the shorthand notation $\partial_{x_j} = \partial/\partial x_j$.

Note that the commutators in the quantum version Eqs. (3.10) can be written as $[\hat{p}_j, \hat{\Theta}_m] = -i\hbar\partial_{x_j}\hat{\Theta}_m$. Then the equations have a similar form as the semi-classical equations introduced here, containing quantum operators of course.

3.2. Adiabatic elimination of the cavity fields

We now shift to the regime of a bad or far detuned cavity, where the cavity fields follow (almost) instantaneously the atomic movement and can thus be eliminated from the dynamics. This has several advantages: First, it leads to a simplified description allowing for more analytical insight. For instance, the effect of the light fields can be described by infinite-range atom-atom interactions leading to a collective potential. Moreover, in the quantum case the full system often becomes intractable for numerical simulations since the size of the Hilbert space increases exponentially with the number of modes by the factor $(n_{\text{cutoff}} + 1)^M$, where n_{cutoff} is the numerical cutoff of the Fock space of the field oscillators. In the eliminated regime one can thus treat larger ensembles of particles. The bad cavity regime is realized in the experiment from Ref. [3.6] for instance.

3.2.1. Semi-classical elimination of the fields

Let us start in the semi-classical regime using Eqs. (3.11). For simplicity we treat here the case of real mode functions leading to real order parameters. While this is not the most general case, it conveys the basic idea of a systematic adiabatic elimination based on the separation of time scales including first (and possibly higher) order corrections in the particle momenta.

Coarse grained time grid

The field can be eliminated when it reaches a steady state before the atoms move significantly. Formally this means that there exists an intermediate time scale Δt, which fulfills (i) $\Delta t \gg \kappa_m^{-1}$ and (ii) $\Delta t \ll \Gamma$, where $\Gamma = m_a/(k_m p)$ is the typical time scale of the atomic motion. This has to be fulfilled for all m of course.

Formally integrating Eq. (3.11c) from t_0 to t with $\Delta t = t - t_0$ yields

$$\alpha_m(t) = e^{(i\Delta_{c,m} - \kappa_m)\Delta t}\alpha(t_0) + iN\eta_m \int_0^{\Delta t} \mathrm{d}s\, e^{(i\Delta_{c,m} - \kappa_m)s}\Theta_m(t-s) + \Sigma_m(t). \tag{3.13}$$

The averaged noise

$$\Sigma_m(t) = \sqrt{\kappa_m} \int_0^{\Delta t} \mathrm{d}s\, e^{(i\Delta_{c,m} - \kappa_m)s}\xi_m(t-s) \tag{3.14}$$

is colored and has the two-time correlation function [3.7]

$$\langle \Sigma_m(t)\Sigma_n^*(t')\rangle = \frac{1}{2}\exp\left(-\kappa_m|t-t'| - i\Delta_{c,m}(t-t')\right)\delta_{mn}. \tag{3.15}$$

Due to assumption (i) all correlations decay to zero within the time Δt and the noise can be approximated by white noise

$$\langle \Sigma_m(t)\Sigma_n^*(t')\rangle \approx \frac{\kappa_m}{\Delta_{c,m}^2 + \kappa_m^2}\delta(t-t')\delta_{mn} = \frac{\kappa_m}{\Delta_{c,m}^2 + \kappa_m^2}\langle \xi_m(t)\xi_n^*(t')\rangle. \tag{3.16}$$

The deterministic integral can be expanded into a sum by integrating by parts several times

$$\int_0^{\Delta t} \mathrm{d}s\, e^{(i\Delta_{c,m}-\kappa_m)s}\Theta_m(t-s) = \sum_{n=0}^{\infty} \frac{\Theta_m^{(n)}(t) - e^{(i\Delta_{c,m}-\kappa_m)\Delta t}\Theta_m^{(n)}(t_0)}{(i\Delta_{c,m}-\kappa_m)^{n+1}} \tag{3.17}$$

with

$$\Theta_m^{(n)}(t) = \frac{\mathrm{d}^n}{\mathrm{d}s^n}\Theta_m(s)\Big|_{s=t}. \tag{3.18}$$

Note that we do not care about convergence here since we will limit ourselves to the first terms only. The cavity field is then given by

$$\alpha_m(t) \approx \frac{N\eta_m}{\Delta_{c,m}+i\kappa_m}\sum_{n=0}^{\infty}\frac{\Theta^{(n)}(t)}{(i\Delta_{c,m}-\kappa_m)^n} + \sqrt{\frac{\kappa_m}{\Delta_{c,m}^2+\kappa_m^2}}\xi_m. \tag{3.19}$$

The atomic motion is now assumed slow compared to the time scale Δt due to assumption (ii). Then we can take into account the parameter $\epsilon = (k_m p/m_a)/|i\Delta_{c,m}-\kappa_m|$ only up to first order, yielding

$$\alpha_m \approx \frac{N\eta_m}{\Delta_{c,m}+i\kappa_m}\Theta_m + \frac{iN\eta_m}{(i\Delta_{c,m}-\kappa_m)^2}\dot{\Theta}_m + \sqrt{\frac{\kappa_m}{\Delta_{c,m}^2+\kappa_m^2}}\xi_m. \tag{3.20}$$

Effective Langevin equations

Plugging the first order approximation of the field into the momentum equation in the SDEs we obtain Langevin equations for the atoms only [3.8]

$$\dot{x}_j = \frac{p_j}{m_a} \tag{3.21a}$$

$$\dot{p}_j = -\frac{\partial U(x_1,...,x_N)}{\partial x_j} + \sum_{i=1}^{N}\beta_{ij}p_i + \sum_{m=1}^{M} B_{jm}\zeta_m. \tag{3.21b}$$

with the real white noise process $\zeta_m = (\xi_m + \xi_m^*)/\sqrt{2}$. The adiabatic (zeroth order) contribution of the force can be derived from a collective potential

$$U(x_1,...,x_N) = \hbar\sum_m \frac{\eta_m^2\Delta_{c,m}}{\Delta_{c,m}^2+\kappa_m^2}N^2\Theta_m^2. \tag{3.22}$$

Linear collective friction stems from the first order contribution of the force and is given by the matrix

$$\beta_{ij} = \frac{\hbar}{m_a}\sum_m 4\frac{\eta_m^2\Delta_{c,m}\kappa_m}{(\Delta_{c,m}^2+\kappa_m^2)^2}[\partial_{x_i}N\Theta_m][\partial_{x_j}N\Theta_m]. \tag{3.23}$$

Finally the $N \times M$ noise matrix is given by

$$B_{jm} = -\hbar\eta_m\sqrt{\frac{2\kappa_m}{\Delta_{c,m}^2+\kappa_m^2}}[\partial_{x_j}N\Theta_m]. \tag{3.24}$$

Both friction and noise affect the particles in a collective manner. That is for instance, the position of atom i influences the friction on atom j. Physically, this behavior emerges since the atoms collectively couple to the same mode m.

Similar equations were derived in Ref. [3.9] without a semi-classical approximation of the light fields, which were consequently used in Refs. [3.10, 3.11] and Chapter 5. They obtain an additional noise term in the position equation which is correlated with the momentum noise (a position-momentum cross-derivative term in the Fokker-Planck equation).

Stationary solution from Fokker-Planck equation

In order to find the stationary state we rewrite the Langevin equations Eqs. (3.21) into a Fokker-Planck equation for the probability distribution $P(t, x_1, ..., x_N, p_1, ..., p_N)$ [3.12]

$$\begin{aligned}\frac{\partial P}{\partial t} = &-\sum_j \frac{\partial}{\partial x_j}\left(\frac{p_j}{m_a}P\right) - \sum_j \frac{\partial}{\partial p_j}\left(-\frac{\partial U}{\partial x_j}P\right) \\ &-\sum_j \frac{\partial}{\partial p_j}\left(\sum_i \beta_{ij} p_i P\right) + \frac{1}{2}\sum_{ij}\frac{\partial^2}{\partial p_i \partial p_j}\left([BB^T]_{ij}P\right).\end{aligned} \tag{3.25}$$

The stationary distribution is given by

$$P_{\mathrm{st}} \propto \exp[-E/(k_{\mathrm{B}}T)] \tag{3.26}$$

with the energy

$$E(x_1, ..., x_N, p_1, ..., p_N) = U(x_1, ..., x_N) + \sum_j \frac{p_j^2}{2m_a} \tag{3.27}$$

and the self-consistent stationary temperature

$$k_{\mathrm{B}}T = \hbar\frac{\Delta_{c,m}^2 + \kappa_m^2}{-4\Delta_{c,m}}. \tag{3.28}$$

This can be verified by checking that the stationary equation $\partial P_{\mathrm{st}}/\partial t = 0$ is satisfied. In detail, the first term cancels with the second term (adiabatic force), while the friction term cancels with the noise term in Eq. (3.25). Note that the stationary state only exists when there is only one temperature in the system, i.e. Eq. (3.28) does not depend on m [3.13]. Moreover, for the existence of a steady state the pump lasers need to be red detuned $\Delta_{c,m} < 0$ with respect to the cavity resonances, such that the field retardation leads to friction.

3.2.2. Quantum elimination of the fields

In principle, a very similar derivation via the Heisenberg-Langevin equations from Eqs. (3.10) can be done in the quantum case, but one has to additionally take care of the ordering of the operators and mind an extra factor 2. Unfortunately, we are not aware of a direct way for obtaining a Lindblad master equation from the effective Heisenberg-Langevin equations for $\hat{x}_j$ and $\hat{p}_j$.

Master equation neglecting retardation

A simple result can be obtained by totally neglecting retardation effects, i.e. the terms containing the time derivative of $\hat{\Theta}_m$, and keeping only the adiabatic contribution and the noise. The field operators are then expressed by atomic operators and input noise

$$a_m^{\mathrm{st}} = \frac{N\eta_m}{\Delta_{c,m} + i\kappa_m}\hat{\Theta}_m + \sqrt{\frac{2\kappa_m}{\Delta_{c,m}^2 + \kappa_m^2}}\hat{\xi}_m, \tag{3.29}$$

where we note the additional factor $\sqrt{2}$ compared to the classical case. Inserting this expression into the momentum equation in Eq. (3.10b) yields effective Heisenberg-Langevin equations. They correspond to the effective atomic master equation [3.14]

$$\dot{\rho} = -\frac{i}{\hbar}[H_{\mathrm{atom}} + H_{\mathrm{cav}}^{\mathrm{eff}}, \rho] + N^2 \sum_m \eta_m^2 \frac{\kappa_m}{\Delta_{c,m}^2 + \kappa_m^2}\left(2\hat{\Theta}_m \rho \hat{\Theta}_m^\dagger - \hat{\Theta}_m^\dagger \hat{\Theta}_m \rho - \rho \hat{\Theta}_m^\dagger \hat{\Theta}_m\right) \tag{3.30}$$

with

$$H_{\mathrm{cav}}^{\mathrm{eff}} = \hbar \sum_m \eta_m^2 \frac{\Delta_{c,m}}{\Delta_{c,m}^2 + \kappa_m^2} N^2 \hat{\Theta}_m^\dagger \hat{\Theta}_m. \tag{3.31}$$

and $H_{\mathrm{atom}} = \sum_j \hat{p}_j^2/(2m_a)$. This equation is also valid for complex interference fields.

Note that this master equation always converges to the infinite temperature steady state and is thus only suitable for the dynamics long before the steady state is reached. This is expected since we omitted the retardation term and thus friction, which is the only process to counteract the heating from the noise. It is not trivial to include retardation effects, but a high temperature correction can be obtained by a quantum Brownian motion master equation [3.3] for the special case of Hermitian order operators (or real interference fields)

$$\begin{aligned}\dot{\rho} = &-\frac{i}{\hbar}[H_{\mathrm{atom}} + H_{\mathrm{cav}}^{\mathrm{eff}}, \rho] + N^2 \sum_m \eta_m^2 \frac{\kappa_m}{\Delta_{c,m}^2 + \kappa_m^2}\left(2\hat{\Theta}_m \rho \hat{\Theta}_m - \hat{\Theta}_m^2 \rho - \rho \hat{\Theta}_m^2\right) \\ &+ iN^2 \sum_m \eta_m^2 \frac{2\Delta_{c,m}\kappa_m}{(\Delta_{c,m}^2 + \kappa_m^2)^2}(\hat{\Theta}_m \rho \dot{\hat{\Theta}}_m - \dot{\hat{\Theta}}_m \rho \hat{\Theta}_m + \hat{\Theta}_m \dot{\hat{\Theta}}_m \rho - \rho \dot{\hat{\Theta}}_m \hat{\Theta}_m).\end{aligned} \tag{3.32}$$

Note that due to the additional friction terms the master equation does not have Lindblad-form anymore and thus the positivity of the density operator is not necessarily preserved. More details are discussed in Appendix A.3.

Effective states

By using the method of elimination via operators in the Heisenberg picture, it is not totally clear which atom-field state corresponds to an effective atomic state. The connection is established only by the relation in Eq. (3.29), and not by any assumptions on the states. We now aim to answer the question, which full atom-field state

$$\rho_{\mathrm{tot}} = \sum_{\mu\nu} \rho_{\mu\nu} |\mu_{\mathrm{tot}}\rangle\langle\nu_{\mathrm{tot}}| \tag{3.33}$$

corresponds to the effective atomic state

$$\rho = \sum_{\mu\nu} \rho_{\mu\nu} |\mu\rangle\langle\nu|, \tag{3.34}$$

when both states have the same coefficients $\rho_{\mu\nu}$ in the eigenbasis $\{|\nu\rangle\}_\nu$ of the order operator defined via $\hat{\Theta}_m|\nu\rangle = \theta_m^\nu|\nu\rangle$.

From the Heisenberg-Langevin equation of the fields in Eq. (3.10c) we know that after a time on the order of κ_m^{-1} the expectation values of the fields scattered by $|\nu\rangle$ reach a steady state $\alpha_m^\nu = \langle\nu|a_m^{\mathrm{st}}|\nu\rangle = N\eta_m/(\Delta_{c,m} + i\kappa_m)\theta_m^\nu$. Since the master equation is only valid on the coarse grained time grid $\Delta t \gg \kappa_m^{-1}$, the fields are always assumed to be in this steady state in our effective description.

We now impose that the expectation values of the actual field operators a_m have to be the same as the ones of the steady state operators a_m^{st} from the correspondence Eq. (3.29)

$$\langle a_m\rangle_{\mathrm{tot}} \overset{!}{=} \langle a_m^{\mathrm{st}}\rangle \Leftrightarrow \langle\nu_{\mathrm{tot}}|a_m|\mu_{\mathrm{tot}}\rangle \overset{!}{=} \langle\nu|a_m^{\mathrm{st}}|\mu\rangle, \tag{3.35}$$

where we used the properties of the trace for the equivalence. Moreover, also normally ordered products of field operators as e.g. $a_m^\dagger a_m$ should give rise to the same expectation value when we neglect the noise in Eq. (3.29). One can check that this is fulfilled for coherent field states, leading to the atom-field state

$$|\nu_{\mathrm{tot}}\rangle = |\nu\rangle \otimes |\alpha_1^\nu\rangle \otimes \ldots \otimes |\alpha_M^\nu\rangle. \tag{3.36}$$

For both we have $\langle\mu_{\mathrm{tot}}|\nu_{\mathrm{tot}}\rangle = \langle\mu|\nu\rangle = \delta_{\mu\nu}$. Note however that the expectation values do not necessarily agree for an atomic operator $\hat{\mathcal{O}}$: the matrix element $\langle\nu|\hat{\mathcal{O}}|\mu\rangle$ should be equal to $\langle\nu_{\mathrm{tot}}|\hat{\mathcal{O}}|\mu_{\mathrm{tot}}\rangle = \langle\nu|\hat{\mathcal{O}}|\mu\rangle \prod_m \langle\alpha_m^\nu|\alpha_m^\mu\rangle$, but the overlaps of coherent states are only close to one when the fields are similar. This can lead to non-physical behavior like tunneling between potential wells created by two fields α and $-\alpha$. It becomes resonant because the potential depth depends only on the intensity $|\alpha|^2$ and not on the field phases. Physically however, the tunneling should be suppressed for larger $|\alpha|$, because the overlap of the two field states goes to zero due to the opposite phase of α [3.15].

3.3. Transversally pumped ultracold atoms in an optical lattice

In this section we introduce a model describing ultracold atoms in an optical lattice in a cavity. We consider an optical lattice, which is created by external laser beams which are not resonant with the cavity. Since in general the cavity fields are dynamical and even operator-valued, also the Wannier functions have to be determined self-consistently from the dynamical field and are in principle also operator-valued [3.1]. Here we assume however, that the cavity-created potentials are much weaker than the external lattice, and can thus be treated as a perturbation of the Bose-Hubbard model introduced in Sec. 2.4. In this vein we make the approximation that the Wannier functions are solely determined by the external lattice and the mode functions of the cavity enter only via the on-site and off-site nearest-neighbor overlaps

$$v_m^i = \int \mathrm{d}x\, w^2(x - x_i)\mathcal{H}_m(x)\mathcal{G}_m^*(x) \tag{3.37a}$$

$$u_m^{ij} = \int \mathrm{d}x\, w(x - x_i)\mathcal{H}_m(x)\mathcal{G}_m^*(x)w(x - x_j). \tag{3.37b}$$

The lattice order operators then take the form

$$\hat{\Theta}_{\mathrm{L},m} = \frac{1}{N}\left(\sum_i v_m^i \hat{n}_i + \sum_{\langle i,j\rangle} u_m^{ij} b_i^\dagger b_j\right) \tag{3.38}$$

where the first diagonal term is dominant since off-site nearest-neighbor overlaps u_m^{ij} are exponentially smaller than v_m^i. This quantity obviously depends on the mode functions, but also on the position and depth of the lattice wells via the Wannier functions.

The lattice Hamiltonian is then formally very similar to Eq. (3.8) where the kinetic term is substituted by the tunneling term

$$H_\mathrm{L} = -J\sum_{\langle i,j\rangle} b_i^\dagger b_j + \frac{U}{2}\sum_i \hat{n}_i(\hat{n}_i + 1) - \hbar\sum_m \Delta_{c,m} a_m^\dagger a_m + \hbar N\sum_m \eta_m(\hat{\Theta}_{\mathrm{L},m}^\dagger a_m + a_m^\dagger \hat{\Theta}_{\mathrm{L},m}). \tag{3.39}$$

It poses a generalized Bose-Hubbard model, which has been extensively studied theoretically [3.16–3.19] and experimentally tested [3.6].

The atom-atom coupling mediated via the cavity becomes visible by adiabatically eliminating the field, which can be done analogously to Sec. 3.2.2. Instead of the Heisenberg-Langevin equation for the momentum operator of the jth atom we have to consider the annihilation operator of the ith site b_i. The result is an effective Hamiltonian as in Eq. (3.31), but with the lattice order operator from Eq. (3.38). Different types of infinite range interactions can be seen: the term $\hat{\Theta}_{\mathrm{L},m}^\dagger \hat{\Theta}_{\mathrm{L},m}$ gives rise to density-density interactions $\hat{n}_i\hat{n}_j$, a modified tunneling amplitude due to occupation of a site elsewhere $\hat{n}_i b_j^\dagger b_{j+1}$ and tunneling-tunneling interactions $b_i^\dagger b_{i+1} b_j^\dagger b_{j+1}$. The implications of these non-local fluctuations are discussed in more detail in Chapter 7.

3.4. Geometries

Here we briefly mention some special cases which are well-known from literature to give some concrete form of the order parameters. The standard set-up for self-organization is a cavity which is pumped orthogonally to its axis [3.20], applying one standing wave pump laser scattering into a single cavity mode. Defining the cavity direction as x and the pump direction as z, the mode functions are given by $\mathcal{H}(x,z) = \cos(kz)$ and $\mathcal{G}(x,z) = \cos(kx)$. This yields the order parameter $\Theta = \sum_i \cos(kz_i)\cos(kx_i)/N$. It is maximized (minimized) when the atoms form a checkerboard pattern, where the occupation of even (odd) sites correspond to the value 1 (-1). Most of the physics can be understood from a simple 1D model restricted to $z = 0$ and thus $\mathcal{H}(x) = 1$ and $\Theta = \sum_i \cos(kx_i)/N$.

Using this mode configuration in a lattice with wave length $k_{\mathrm{L}} = k$ and lattice constant $a = \pi/k$, the order parameter is $\hat{\Theta} = v \sum_i (-1)^i \hat{n}_i = v(\hat{N}_{\text{even}} - \hat{N}_{\text{odd}})$, where $0 < v < 1$ is the overlap of the Wannier function and the mode function depending on the lattice depth. Note that the off-diagonal overlaps Eq. (3.37b) are exactly zero in this case because the mode function changes the sign and the integral cancels to zero. The order parameter thus measures the imbalance between even and odd sites [3.6].

4. Simulated annealing with atoms in optical resonators

The physical properties of many materials like metals or glass can be altered by a heat treatment. An example is the so-called *annealing* procedure, where the material is heated above its recrystallization temperature and then slowly cooled in air or liquid. Thereby, it is crucial that a long time is spent close to the transition point. The result is that the materials have less defects, which removes stress and increases the durability and ductility. In the language of thermodynamics the system's configuration moves from some meta-stable state closer to the thermodynamic equilibrium, i.e. the energetic minimum. Note that this approach to equilibrium would also happen spontaneously without annealing, but usually very slow compared to human time scales.

Solving an optimization problem corresponds to finding the global minimum in an extensive and rugged potential landscape, and can thus be conceptually connected with thermodynamics. Transferring the methods from material science, one can simulate the annealing procedure on a computer in order to find the global minimum [4.1] by reducing a fictitious temperature. Moreover, one can envisage to build a simple well-controllable model system consisting of cold atoms, where the information is stored in the position of the atoms. The configuration of atoms with the minimal energy then corresponds to the solution of the optimization problem. Hence the minimization or solving is done by a real physical dynamics.

In this chapter we investigate the physical Langevin dynamics of the annealing schedule for thermal annealing and connect it to cold particles in transversally pumped optical resonators. Moreover, we discuss to what extend one can tailor the cost function (or physically: the collective potential) in order to encode optimization problems. Quantum annealing is proposed to be implemented using ultra-cold atoms in optical lattices, where the site-to-site interactions are mediated by cavity fields.

4.1. Thermal annealing

4.1.1. Standard Langevin dynamics

We consider a one-dimensional system of N classical point particles moving in a collective potential energy landscape $U(x_1, ..., x_N)$, where x_i are the particle positions. The jth particle is hence subject to the force $-\partial U(x_1, ..., x_N)/\partial x_j$. For now we assume the limit of large friction μ, where the motion is overdamped. Lacking inertia the particles will always fall into the closest local minimum along the steepest gradient

$$\dot{x}_j = -\frac{1}{m_a\mu}\frac{\partial}{\partial x_j}U(x_1, ..., x_N). \tag{4.1}$$

In order to find the global minimum the particles have to be able to leave a local minimum and climb up the walls again (see Fig. 4.1). This happens for instance when they have a non-zero temperature T, which introduces random noise. The overdamped dynamics is then described by the Langevin equations[*]

$$\dot{x}_j = -\frac{1}{m_a\mu}\frac{\partial}{\partial x_j}U(x_1, ..., x_N) + \sqrt{\frac{2k_\mathrm{B}T}{m_a\mu}}\zeta_j \tag{4.2}$$

with $\langle\zeta_j(t)\rangle = 0$ and $\langle\zeta_i(t)\zeta_j(t')\rangle = \delta(t-t')\delta_{ij}$. The stationary state ($t \to \infty$) is given by the Boltzmann distribution [4.2]

$$\Pi_T(x_1, ..., x_2) \propto \exp\left(-\frac{U(x_1, ..., x_N)}{k_\mathrm{B}T}\right). \tag{4.3}$$

For $T \to 0$ the particles should thus be distributed arbitrarily close to the global minimum. Unfortunately, the time to reach the steady state from an arbitrary initial state increases exponentially for $T \to 0$ ($\propto \exp(T^{-1})$) [4.3] and thus getting closer to the global minimum soon takes prohibitively long. A way out is to use an annealing schedule: The temperature $T(t)$ is slowly decreased from a high value to zero. In the early high temperature stage the stationary distribution is nearly uniform and the whole configuration space can be explored. During the slow temperature decrease finer and finer features of the energy landscape are resolved until for $T \to 0$ the distribution becomes localized at the global minimum. If the temperature curve fulfills $T(t) \geq l/(\ln(t+2))$ for large enough l, it can be shown that the system's state gets arbitrarily close to the thermodynamic ground state (i.e. the global minimum) for any initial state [4.3, 4.4].

The simulated annealing algorithm [4.1] was inspired by this physics. Instead of simulating the physical dynamics leading to a Boltzmann distribution, however, the final distribution is numerically sampled with a Metropolis algorithm [4.5]. The annealing is done by decreasing a now fictitious temperature $T(t)$. A very similar condition on the temperature curve for convergence is known [4.6]. There are several variations to the standard Metropolis algorithm aiming for faster convergence, some of which use a pseudo-dynamics inspired by overdamped particle motion [4.7].

Let us go back to physical particles. Leaving the overdamped limit, the dynamics more generally follows[†]

$$\dot{x}_j = \frac{p_j}{m_a} \tag{4.4a}$$

$$\dot{p}_j = -\frac{\partial}{\partial x_j}U(x_1, ..., x_N) - \mu p_j + \sqrt{2\mu m_a k_\mathrm{B}T}\,\zeta_j. \tag{4.4b}$$

---

[*] Note that the Langevin equations correspond to a Smoluchowski FPE for one particle in $\mathbb{R}^N$.

[†] The corresponding FPE is a Kramers equation [4.8] for one particle in $\mathbb{R}^N$.

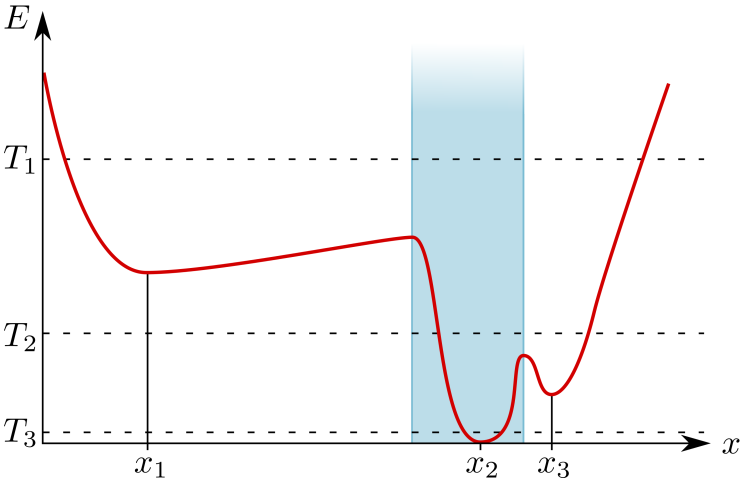

Figure 4.1.: A one-dimensional potential with one global minimum x_2 and two local minima x_1 and x_3. Gradient descent dynamics of a particle in this potential [Eq. (4.1)] would lead to the final position x_2 only when starting in the blue region. An annealing schedule helps to find the global minimum from any initial position. Starting with a high temperature T_1 the particle can move nearly freely over the three minima. Slowly decreasing the temperature leads to a distribution which is localized around x_2 and x_3 for T_2. Finally, if the temperature decrease was slow enough the particle probably ends up in the global minimum x_2 for $T = T_3 \to 0$.

In the stationary limit $t \to \infty$ position and momentum factorize and one obtains [4.2]

$$P_{\mathrm{st}}(x_1, ..., x_N; p_1, ..., p_N) \propto \exp\left(-\frac{U(x_1, ..., x_N)}{k_{\mathrm{B}}T}\right) \prod_{j=1}^{N} \exp\left(-\frac{p_j^2}{2m_a k_{\mathrm{B}}T}\right). \tag{4.5}$$

So the particles' positions are again distributed according to Boltzmann as before.

For a reasonably large friction, the arguments from the overdamped case are thus still expected to apply and the annealing schedule can still lead to a distribution close to the thermodynamic ground state. Of course, the way how this equilibrium is approached is more complicated compared to the overdamped dynamics (and also compared to simulated annealing pseudo-dynamics), for instance limit cycles can occur. The particles oscillate around minima or even leave the minimum again solely due to their inertia instead of diffusion.

4.1.2. Classical dynamics in a transversally pumped cavity

The dynamics of classical point particles in a cavity have a similar, yet more complicated form compared to Brownian particles in potentials as described by Eqs. (4.4) [4.9]. In order to identify similarities and differences we consider the Langevin equations obtained in Eqs. (3.21) in Sec. 3.2.1 describing the particles' positions and momenta after adiabatic elimination of the fields.

A crucial similarity is that the light-mediated atom-atom interactions give rise to a collective potential depending on all atom positions, corresponding to the cost function. Moreover, within the adiabatic approximation of the fields the stationary state for red detuning $\Delta_c < 0$ is again a Boltzmann distribution with a stationary temperature given by $k_{\mathrm{B}}T = \hbar(\Delta_c^2 + \kappa^2)/(-4\Delta_c)$ [see Eq. (3.26)]. The collective character of friction and noise instead is more complicated – they do not only act individually on each atom but depend on all other atom positions. A further difference is that the temperature is not an external parameter and not fixed but determined self-consistently by the dynamics.

To obtain the minimum of the collective potential U, we can still apply an annealing schedule. A possible parameter sweep can be an increase of all pump strengths η_m, which ramps up the collective potential. The stationary temperature instead remains unchanged within the first order approximation in the momentum. Only for larger pump strengths there is a correction proportional to the square of the trap frequency [4.10]. Since the Boltzmann distribution depends only on the ratio $U/(k_{\mathrm{B}}T)$, ramping up the potential is equivalent to decreasing the temperature for the stationary state. Note that this is not necessarily true for the dynamical evolution leading to the stationary state.

How likely the atoms get stuck in local minima then depends on the intensity ramp speed. This is discussed in Chapter 5, which treats a simple two mode model already containing local minima. A detailed numerical discussion of the influence of ramp speed and initial temperature on the final state reveals that slower ramp speeds yield states closer to the minimum.

In such a system for $\Delta_{c,m} < 0$, a minimization of the collective potential goes hand in hand with a maximization of the scattered intensity. The device can thus be interpreted as an adaptive light harvesting system [4.11], which always adapts in order to maximize the total scattering into all modes.

Encoding a problem. In order to solve the desired optimization problem the potential landscape needs to be tailored, such that the global minimum corresponds to a solution of the problem. The form of the cost function depends on the order parameters and thus on the form of the interference fields $\mathcal{H}_m(x)\mathcal{G}_m^*(x)$.

The collective potential in Eq. (3.22) can be re-written by exchanging the sum over the fields with the sum over the atoms

$$U(x_1,...,x_N) = \sum_{i,j=1}^{N}\sum_{m=1}^{M} \frac{\hbar\eta_m^2\Delta_{c,m}}{\Delta_{c,m}^2+\kappa_m^2}\mathrm{Re}\left[\mathcal{H}_m^*(x_i)\mathcal{H}_m(x_j)\mathcal{G}_m(x_i)\mathcal{G}_m^*(x_j)\right]. \tag{4.6}$$

We made use of fact that an index exchange $i \leftrightarrow j$ corresponds to a complex conjugation. This expression reveals the atom-atom interaction energy between ith and jth atom

$$\mathcal{U}_{\mathrm{int}}(x_i,x_j) = \sum_m \frac{\hbar\eta_m^2\Delta_{c,m}}{\Delta_{c,m}^2+\kappa_m^2}\mathrm{Re}\left[\mathcal{H}_m^*(x_i)\mathcal{H}_m(x_j)\mathcal{G}_m(x_i)\mathcal{G}_m^*(x_j)\right] = \sum_m c_m\mathcal{V}_m(x_i,x_j). \tag{4.7}$$

The second expression forms a series expansion with the real functions $\mathcal{V}_m(x_i,x_j) = \mathrm{Re}\left[\mathcal{H}_m^*(x_i)\mathcal{H}_m(x_j)\mathcal{G}_m(x_i)\mathcal{G}_m^*(x_j)\right]$ and the coefficients $c_m = \hbar\eta_m^2\Delta_{c,m}/(\Delta_{c,m}^2+\kappa_m^2)$. One can mathematically create any shape of the interaction energy by adjusting the coefficients c_m, when the $\mathcal{V}_m$'s form a basis of the functions of two real variables (and m ranging to infinity). Of course in practice, there is no infinite number of modes available and thus the shape of $\mathcal{U}_{\mathrm{int}}(x_i,x_j)$ is always limited for continuous interactions. However, with a finite number of modes a potential can be approximated with reasonable accuracy. How well this works is of course dependent on the problem.

Since the interference field $\mathcal{H}_m(x)\mathcal{G}_m^*(x)$ typically has a periodic shape, the series expansion often takes the form of a Fourier series, and well-known results from Fourier analysis can be applied. For instance, for running wave pump modes $\mathcal{H}_m(x) = \exp(ik_mx)$ and $\mathcal{G}_m(x) = 1$ one obtains $\mathcal{V}_m(x_i,x_j) = \cos(k_m(x_i-x_j))$, an interaction which depends only on distance in this case. The interaction energy is then an even Fourier series for the distance (see Chapters 7 and 8).

Note that in general the sign of the coefficients is determined by the cavity detunings $\Delta_{c,m}$. So when intrinsic cavity cooling is desired one is less flexible due to the restriction $\Delta_{c,m} < 0$. This can in principle be circumvented by employing extra cooling (e.g. Doppler cooling) not relying on dissipation through the cavity mirrors.

4.2. Quantum annealing

4.2.1. Quantum annealing in a tight-binding model

In the previous section we reduced the temperature to values close to zero, but we still remained in the classical regime $k_{\mathrm{B}}T \gg E_{\mathrm{R}}$. Using temperatures lower than the recoil energy E_{R} results in quantum dynamics. While in this limit the thermal fluctuations disappear, a particle's spatial wave function is so large that quantum fluctuations on the order of the length scale of the potential (i.e. the laser wave length) arise[‡]. The fluctuations allow the atom to tunnel through the potential barriers. This zero-temperature tunneling might allow the particles to more efficiently leave local minima than with classical thermal hopping. Moreover, a quantum particle can be in a superposition state and thus see the whole potential landscape at once, while classically the multitude of states has to be run through sequentially [4.12].

In the framework of a tight-binding model for ultra-cold atoms as introduced in Sec. 2.4, a quantum annealing Hamiltonian can have the form

$$H(t) = -J(t) \sum_{\langle i,j \rangle} b_i^\dagger b_j + U_I(t) \sum_{i,j} A_{ij} \hat{n}_i \hat{n}_j. \tag{4.8}$$

The first term describes quantum tunneling with the amplitude J and gives rise to quantum fluctuations. The second term creates site-to-site interactions specified by the interaction matrix A and is diagonal in the computational basis, which here corresponds to the occupation basis (eigenbasis of $\hat{n}_i$). This latter term corresponds to the collective potential with the interaction matrix encoding the (classical) optimization problem. Note that in the tight-binding model the space was rendered discrete and the degrees of freedom were significantly reduced by using the lowest band approximation [4.13]. This also leads to a simpler configuration space and makes it more straightforward to encode problems in the Hamiltonian.

In contrast to the classical case, annealing is done by reducing the quantum fluctuations via reducing $J(t)$ from $J(0) > 0$ to $J(\tau) \approx 0$ while increasing the interaction Hamiltonian by ramping up the site-to-site interactions $U_I(t)$ from $U_I(0) \approx 0$ to $U_I(\tau) = U_I^f$. If the system is prepared in the ground state of the Hamiltonian at $t = 0$, the adiabatic theorems for Schrödinger time evolutions [4.14] guarantee that the system stays in its ground state as long as the sweep is slow enough. Thus the system ends up in the ground state of the interaction Hamiltonian, which is the solution of the problem.

The decisive question whether quantum annealing has an advantage in speed over classical annealing is not easy to answer in general since it depends crucially on the specific problem and thus on the potential landscape. As an intuitive rule of thumb, quantum tunneling tends to work better when the potential barriers are high and narrow [4.12], as it is often the case for infinite-range interacting systems such as the Sherrington-Kirkpatrick model. Figure 4.2 shows a toy model potential, the parabolic washboard, where quantum tunneling performs better [4.15]. When quantum annealing outperforms thermal annealing, we talk about a "limited speed-up" [4.14].

The more relevant question for real life applications is if quantum annealing has a speed-up over *any* known classical device or algorithms for some problem [4.16]. Since a (pure) quantum state is specified by as many coefficients as configuration states (the

---

[‡] For free particles the size of the wave function corresponds to the thermal de Broglie wave length $\lambda_{\mathrm{th}} = \hbar\sqrt{2\pi/(m_a k_{\mathrm{B}} T)}$. The condition for the classical regime $k_{\mathrm{B}}T \gg E_{\mathrm{R}}$ translates to $\lambda_{\mathrm{th}} \ll \lambda/\sqrt{\pi}$.

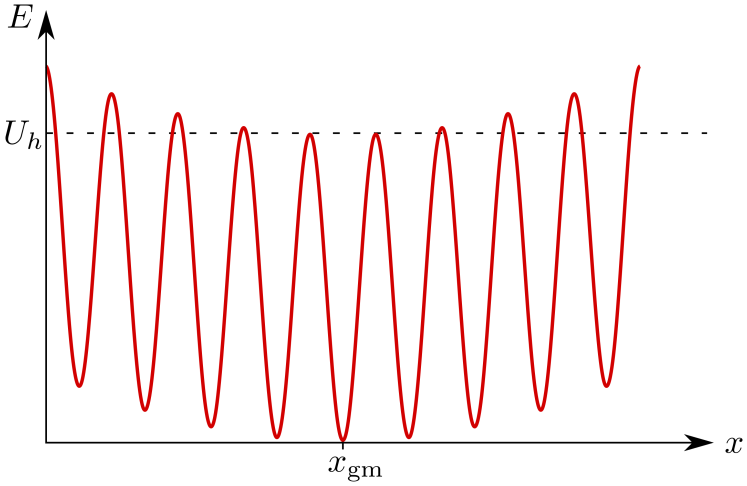

Figure 4.2.: A one dimensional potential, where quantum annealing is advantageous over thermal annealing [4.15]. Thermal hopping would require temperatures on the order of the barrier height U_{h}, while quantum particles can tunnel through the barriers.

size of the Hilbert space), it cannot be directly implemented in a computer with polynomial overhead. However, for many Hamiltonians the ground state (or a thermal mixed state with very small temperature) can be sampled using quantum Monte Carlo methods [4.12]. Just as in the classical simulated annealing algorithm, simulated quantum annealing consists in reducing quantum fluctuations in course of such a sampling procedure. With these quantum physics inspired algorithms tunneling can be simulated efficiently on a classical computer for so-called stoquastic Hamiltonians [4.17, 4.18], whose off-diagonal elements are all negative in the computational basis [such as the one in Eq. (4.8)]. For non-stoquastic Hamiltonians instead, the question of the existence of quantum speed-up is still open [4.14, 4.16].

Note that in literature typically Ising spin models are considered instead of the tight-binding model coming from ultra-cold atoms in Eq. (4.8). However, the tight-binding model can be mapped on such models when only single excitations occur, for example when large contact interactions make doubly occupied sites energetically unfavorable (as in Chapter 6) or by single atom filling (as in Chapter 7).

4.2.2. Ultra-cold atoms in a cavity

Ultra-cold atoms in an optical lattice placed in a transversally pumped cavity as described in Sec. 3.3 obey a similar Hamiltonian as in Eq. (4.8). The atom-atom interaction becomes revealed when considering again the case of adiabatically eliminated cavity fields. As in the classical case, the crucial effect of the cavity beyond standard optical lattice physics are the infinite-range all-to-all interactions stemming from collective scattering. The annealing is then simply done via increasing the pump strength, as in the classical case. Note that since the light fields also change the tunneling, the resulting

Hamiltonian is not stoquastic, and thus can in principle support quantum speed-up.

Since the realistic open system is described by a master equation [Eq. (3.9)], we have to take into account more effects than those coming from the coherent Schrödinger dynamics. On the one hand, cavity cooling (or heating) can arise, which comes from the time lag between atomic motion and fields as in the classical case. This effect could in principle be used to amend quantum annealing and cool excitations due to unwanted non-adiabatic transfers back to the ground state. On the other hand, quantum superpositions get destroyed by dephasing due to photon loss, which reduces the coherence time and creates an upper bound to the annealing time. This is briefly treated in Chapter 7 by using a master equation of the form Eq. (3.30).

Tailor the interaction matrix. In the tight-binding lattice model the effective Hamiltonian can be written as (see Sec. 3.3)

$$H_{\text{eff}} = \sum_{i,j=1}^{K} \sum_{m=1}^{M} \frac{\hbar \eta_m^2 \Delta_{c,m}}{\Delta_{c,m}^2 + \kappa_m^2} \text{Re}[(v_m^i)^* v_m^j] \hat{n}_i \hat{n}_j + \text{cavity-induced tunneling.} \tag{4.9}$$

with the on-site Wannier-mode overlaps v_m^i from Eq. (3.37a). In order to simplify this discussion we do not consider the off-diagonal cavity-induced tunneling terms. The indices i, j run over lattice sites now. Due to the lattice the single-mode site-to-site interaction is discrete and given by the real and symmetric matrices $V_m^{ij} = \text{Re}[(v_m^i)^* v_m^j]$. This yields the total site-to-site interaction

$$U_{\text{int}}^{ij} = \sum_m c_m V_m^{ij}. \tag{4.10}$$

As in the classical case, it can be interpreted as a series expansion with coefficients c_m. With a proper choice of mode and lattice geometry, $K(K+1)/2$ matrices V_m can span a basis and an arbitrary interaction matrix can be obtained (see Chapter 6).

To gain more insight to the interaction matrices, we note that in the limit of deep lattice depths $V_{\text{L}} \to \infty$ we obtain $V_m^{ij} \to \mathcal{V}_m(\tilde{x}_i, \tilde{x}_j)$ and $U_{\text{int}}^{ij} \to \mathcal{U}_{\text{int}}(\tilde{x}_i, \tilde{x}_j)$ with the lattice site positions $\tilde{x}_i$. Thus in this limit the additional lattice simply discretizes the interaction energy $\mathcal{U}_{\text{int}}$. For (realistic) finite lattice depths, they are not evaluated at the point but rather blurred by the finite width Wannier functions to yield v_m^i. It is this finite width which also leads to cavity-induced tunneling.

There are interesting problems where the interaction matrix can be created with much less modes. As shown in Chapter 7, the N-queens problem can be implemented using $\mathcal{O}(K)$ modes. The series expansion also allows for systematically approximating the interaction up to some target accuracy by omitting summands (or physically modes), reducing the complexity of the implementation.

5. Publication

NEW JOURNAL OF PHYSICS **20**, 025004 (2018)

Quenches across the self-organization transition in multimode cavities*

T. Keller[1,4], V. Torggler[2,4], S. B. Jäger[1], S. Schütz[1,3], H. Ritsch[2] and G. Morigi[1]

[1] *Theoretische Physik, Universität des Saarlandes, D-66123 Saarbrücken, Germany*
[2] *Institut für Theoretische Physik, Universität Innsbruck, Austria*
[3] *icFRC, IPCMS (UMR 7504) and ISIS (UMR 7006), University of Strasbourg and CNRS, 67000 Strasbourg, France*
[4] *First authors*

A cold dilute atomic gas in an optical resonator can be radiatively cooled by coherent scattering processes when the driving laser frequency is tuned close but below the cavity resonance. When sufficiently illuminated, moreover, the atoms' steady state undergoes a phase transition from homogeneous density to crystalline order. We characterize the dynamics of this self-ordering process in the semi-classical regime when distinct cavity modes with commensurate wavelengths are quasi-resonantly driven by laser fields via scattering by the atoms. The lasers are simultaneously applied and uniformly illuminate the atoms, their frequencies are chosen so that the atoms are cooled by the radiative processes, their intensity is either suddenly switched or slowly ramped across the self-ordering transition. Numerical simulations for different ramp protocols predict that the system exhibits long-lived metastable states, whose occurrence strongly depends on initial temperature, ramp speed, and number of atoms.

doi: 10.1088/1367-2630/aaa161

---

[*] The author of the present thesis performed the numerical simulations of Eqs. (5.19) [in parallel with T. K. and S. S. simulating Eqs. (5.1)], prepared the manuscript together with S. J., G. M. and H. R. and did some analytical calculations. The phase diagram was obtained by T. K., S. J., and G. M. in Ref. [5.1]. The results were discussed and interpreted by all authors.

5.1. Introduction

Laser light creates an attractive optical potential for cold atoms when far detuned below an optical transition. Such potential can be significantly enhanced if the light is confined by an optical resonator [5.2–5.5]. In addition, if the laser illuminates the atoms, trapping is induced by a dynamical optical potential emerging from the interference between the scattered light and the laser, which tends to order the particles at the maxima of the intensity [5.5, 5.6]. The interference contrast, and thus the trapping depends on the relative positions of the scattering atoms. Therefore, this phenomenon can be also understood in terms of an effective long-range force, which is mediated by the collectively scattered photons [5.6–5.10]. This force has also a dissipative component, which is due to the dissipative nature of the resonator and which cools the atoms when the pump is tuned below the cavity resonance [5.4, 5.11]. Theoretical studies with single-mode resonators predicted that this dissipation can establish long-range correlations and support the onset of metastable ordered structures [5.12, 5.13].

In a multimode cavity and for several illumination frequencies, competing ordering processes are present and lead to a richer phase dynamics. In a two-mode cavity, like the one depicted in Fig. 5.1(a), the transition to self-organization can be a phase-transition of first or second order depending on the laser intensities and on their relative strength [5.1]. The corresponding self-ordered phases can exhibit superradiant scattering either in one or in both cavity modes, as illustrated in Fig. 5.1(b), while the asymptotic distribution of the atoms can be thermal provided that the lasers' frequencies are suitably chosen [5.1]. In our example the particles can order in a lattice at a given length scale λ and/or on a lattice with half the period $\lambda/2$. For these settings we numerically analyze the semi-classical dynamics following sudden quenches or slow ramps of the laser intensities across the thresholds separating the homogeneous from one of the self-organized phases. We describe the evolution by stochastic differential equations, which correspond to the Fokker-Planck equation derived in Ref. [5.14] for a similar system. We find that even at very long times the atoms' spatial distribution strongly depends on the initial temperature, ramp speeds, and on the quench protocol, such that the system gets trapped in long-lived metastable states. In particular, for quenches starting with ensembles at low temperatures, the buildup of long-range order requires longer times when compared to higher initial temperatures.

Our work is organized as follows: In Section 5.2 we introduce the system and the semi-classical equations describing the dynamics. The atoms' stationary properties are then summarized in a phase diagram, which was derived in Ref. [5.1]. In Sec. 5.3 we numerically study the real time dynamics when the parameters are varied within the phase diagram according to different quench protocols. In Sec. 5.4 we analyze the crystallization dynamics starting from spatially homogeneous distributions with different momentum widths. In Sec. 5.5 we compare the predictions of the stochastic differential equations we employ with an extended approach including the dynamical evolution of the field modes introduced in Refs. [5.15, 5.16]. The conclusions are drawn and future perspectives are discussed in Sec. 5.6.

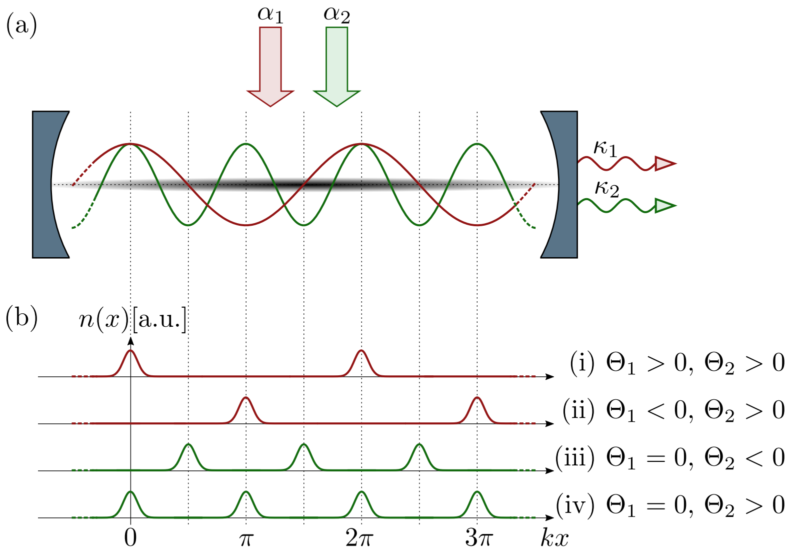

Figure 5.1.: **(a)** Cold atoms are confined within an optical cavity and move along the cavity axis (x axis). They coherently scatter photons from transverse lasers with rescaled amplitudes α_1 and α_2 into the (correspondingly) resonant cavity modes with spatial mode functions $\cos(kx)$ (red) and $\cos(2kx)$ (green) and loss rates κ_1 and κ_2, respectively. **(b)** Sketch of the atomic density distribution $n(x)$ along the cavity axis (in units of $1/k$) for the four possible stationary self-organized orders. On the right we report the corresponding values of the quantities Θ_1 and Θ_2, signaling Bragg order in the mode 1 and 2, respectively. See text and Ref. [5.1] for details.

5.2. Semiclassical dynamics

The system we consider consists of a gas of N cold atoms with mass m, which are trapped inside a high-finesse optical resonator and coherently scatter laser light into the cavity modes. The atomic motion is confined along the cavity axis (here the x axis) by a tight external dipole trap [5.17, 5.18] and is here described in the semi-classical limit.

The geometry of the setup is illustrated in Fig. 5.1. Lasers with (rescaled) intensities α_n propagate in a direction orthogonal to the cavity axis and are quasi resonant with the standing wave cavity modes $\cos(nkx)$ with frequency $\omega_{c,n}$ and wave number nk ($n = 1, 2$) [5.19] †. The lasers have frequency $\omega_{p,n}$ and linear polarization which is parallel to the one of the corresponding cavity mode. Each pair of laser and cavity mode couples to an atomic dipolar transition at frequency $\omega_{a,n}$, where $\Omega_{p,n}$ and g_n are the laser and the vacuum Rabi frequency, respectively. Spontaneous scattering processes are suppressed when the absolute value of the detuning $\Delta_{a,n} = \omega_{p,n} - \omega_{a,n}$ exceeds the coupling strengths and the detuning $\Delta_n = \omega_{p,n} - \omega_{c,n}$ between laser and cavity mode by

---

†This can be realised by assuming $\omega_{c,2} = 2\omega_{c,1} \equiv 2\omega_c$, giving $k_2 = 2k_1 \equiv 2k$. Another possible realisation, where $\omega_{c,1} \approx \omega_{c,2}$, has been discussed in Ref. [5.1], and uses two optical single-mode cavities crossing at an angle of 60°. For a similar experimental setup see also Ref. [5.19]

orders of magnitude: $|\Delta_{a,n}| \gg \Omega_{pn,}, g_n, |\Delta_n|$. The relevant dissipative process are given by cavity decay, and we denote by κ_n the loss rate of cavity mode $n = 1, 2$.

In the so-called bad cavity limit, assuming that the cavity field loss rates are faster than the rate of the dynamics of the atomic motion, one can eliminate the cavity field variables from the equations of motion of the atoms by means of a coarse graining in time. This gives rise to an effective model, where the atoms experience a long-range interaction mediated by the cavity photons, while retardation effects and fluctuations of the cavity field are responsible for friction forces and diffusion. In the semi-classical limit one can derive a Fokker-Planck equation for the atoms' position and momentum distribution, assuming that the single-atom momentum distribution has a width Δp which, at all instants of time, is orders of magnitude larger than the photon recoil $\hbar k$: $\Delta p \gg \hbar k$ [5.1, 5.14, 5.20]. The corresponding stochastic differential equations read

$$dx_j = \frac{p_j}{m} dt \,, \tag{5.1a}$$

$$dp_j = (F_{j,\mathrm{ad}} + F_{j,\mathrm{ret}})dt + dW_j^{(1)} + dW_j^{(2)} \,, \tag{5.1b}$$

where

$$F_{j,\mathrm{ad}} = - \sum_{n=1,2} 2\hbar nk \frac{\alpha_n}{\hbar \beta_n} \sin(nkx_j)\Theta_n \,, \tag{5.2}$$

$$F_{j,\mathrm{ret}} = - \sum_{n=1,2} \frac{\hbar (nk)^2}{m} \alpha_n \frac{\kappa_n}{-\Delta_n} \sin(nkx_j) \frac{1}{N} \sum_{l=1}^{N} p_l \sin(nkx_l) \,, \tag{5.3}$$

and

$$\alpha_n = \frac{4NS_n^2\Delta_n^2}{(\Delta_n^2 + \kappa_n^2)^2} \,, \tag{5.4}$$

$$\beta_n = \frac{-4\Delta_n}{\hbar(\Delta_n^2 + \kappa_n^2)} \,. \tag{5.5}$$

Here, $S_n = g_n\Omega_n/\Delta_{an}$ is the amplitude of coherent scattering by a single atom and has the dimension of a frequency, while $dW_j^{(1)}$ and $dW_j^{(2)}$ in Eq. (5.1b) describe Wiener processes, which fulfill $\langle dW_i^{(n)} \rangle = 0$ and $\langle dW_i^{(n)} dW_j^{(m)} \rangle = 2D_{ij}^n \delta_{nm} dt$ ($n, m = 1, 2$ and $i, j = 1, ..., N$). Here,

$$D_{ij}^n = (\hbar nk)^2 \frac{\alpha_n}{\hbar \beta_n} \frac{\kappa_n}{-\Delta_n} \sin(nkx_i) \sin(nkx_j) \,. \tag{5.6}$$

Finally, the parameter

$$\Theta_n = \frac{1}{N} \sum_{i=1}^{N} \cos(nkx_i) \tag{5.7}$$

quantifies Bragg ordering of the atoms in the cavity mode with wave number nk. In particular, $|\Theta_n| = 1$ when the atoms are localized either at the maxima or at the minima of $\cos(nkx)$, which is the configuration which maximizes the intracavity field intensity. We identify Θ_n with the order parameter for self-organization in the corresponding cavity mode [5.1]. Below, we will denote by "long-wavelength order" a configuration with non-vanishing value of Θ_1, corresponding to a Bragg grating with period $\lambda = 2\pi/k$. Similarly, "short-wavelength order" refers to a configuration with $\Theta_2 \neq 0$, corresponding to a Bragg grating with $\lambda/2$. Note that here and in the rest of the paper we discard the dynamical Stark shift of the cavity frequency assuming that this is much smaller than the cavity mode linewidth $Ng_n^2/|\Delta_{a,n}| \ll \kappa_n$. For details we refer to Ref. [5.1].

5.2.1. Stationary states

An analysis of the Fokker-Planck equation at the basis of Eq. (5.1) allows to identify the conditions for the existence of a stationary state. The latter exists provided that $\Delta_n < 0$ and $\beta_1 = \beta_2 \equiv \beta$, see Eq. (5.5). In this case the atoms' distribution at steady state reads [5.1]

$$f_{\text{st}}(x_1, p_1, \ldots, x_N, p_N) = \frac{\exp(-\beta H_{\text{eff}})}{\mathcal{Z}(\beta)} \tag{5.8}$$

where H_{eff} is the effective Hamiltonian derived after eliminating the cavity field variables,

$$H_{\text{eff}} = \sum_{j=1}^{N} \frac{p_j^2}{2m} - \sum_{n=1,2} N \frac{\alpha_n}{\beta_n} \Theta_n^2 \,, \tag{5.9}$$

while $\mathcal{Z}(\beta)$ denotes the partition function:

$$\mathcal{Z}(\beta) = \frac{1}{\Delta^N} \int_{-\infty}^{\infty} dp_1 \ldots \int_{-\infty}^{\infty} dp_N \int_0^{\lambda} dx_1 \ldots \int_0^{\lambda} dx_N \, e^{-\beta H_{\text{eff}}} \,, \tag{5.10}$$

with $\lambda = 2\pi/k$ and with $\Delta = 2\pi\hbar$ the single particle unit phase space volume. In the following we will assume that the cavity decay rates are equal,

$$\kappa_1 = \kappa_2 =: \kappa \,, \tag{5.11}$$

so that the condition for the existence of the stationary state in Eq. (5.8) becomes

$$\Delta_1 = \Delta_2 =: \Delta_c < 0 \,. \tag{5.12}$$

The phase diagram of the system can be determined by using that the steady state, Eq. (5.8), has the form of a thermal state. On the basis of this observation we introduce the temperature T of the stationary state, which is defined as

$$k_B T = \beta^{-1} = \frac{\hbar(\Delta_c^2 + \kappa^2)}{-4\Delta_c} \,, \tag{5.13}$$

with the Boltzman constant k_B. The steady-state temperature T has the same functional dependence on Δ_c and κ as for a single-mode cavity [5.8, 5.14]. We can further define the free energy per particle $\mathcal{F}$ using the formal equivalence with the canonical ensemble of equilibrium statistical mechanics [5.8]:

$$\mathcal{F} = -\frac{1}{N\beta} \ln(\mathcal{Z}(\beta)) \,. \tag{5.14}$$

Following the procedure detailed in Refs. [5.1, 5.8, 5.13] we determine the global minima of $\mathcal{F}$ in an appropriately defined thermodynamic limit, which consists in keeping α_n constant for $N \to \infty$. The global minima are the resulting stationary phases. The corresponding order parameters Θ_1 and Θ_2, in particular, are determined by α_1 and α_2. When the fields are sufficiently weak, then $\Theta_1 = \Theta_2 = 0$ the density is homogeneous and there is no structural order. We denote this phase by paramagnetic, borrowing the notation of the generalized Hamiltonian mean-field model (GHMF) [5.21–5.23] to which this model can be mapped. The possible ordered phases at steady state are illustrated in Fig. 5.1(b) and take one of four set of values. In particular, the ferromagnetic phase is characterized by (i) $\Theta_1 > 0$, $\Theta_2 > 0$ and (ii) $\Theta_1 < 0$, $\Theta_2 > 0$, exhibiting Bragg order in both cavity modes. The nematic phases (iii) and (iv), instead, are characterized by no order in the long-wavelength mode, $\Theta_1 = 0$ while Θ_2 can be either negative or positive.

The resulting phase diagram in the $\alpha_1 - \alpha_2$ plane is shown in Fig. 5.2 and reproduces the one of Ref. [5.1]. The phases are separated by either first- or second-order transitions, which have been determined using Ehrenfest's criterion [5.23]. The shaded areas show stability regions in which the free energy has a local minimum that corresponds to the paramagnetic (dark gray region) and nematic (light gray region) phase. Examples of the free-energy landscape in the $\Theta_1 - \Theta_2$ plane are shown in subplots (b) and (c). Subplot (b) corresponds to the parameters of the red bullet labeled by (b) in subplot (a): Here, the free energy exhibits two symmetric global minima which correspond to the ferromagnetic phase. In subplot (c), corresponding to the parameters of the red bullet labeled by (c), there is an additional local minimum corresponding to a nematic phase. In the latter there is only ordering in the short-wavelength lattice, while $\Theta_1 = 0$. We denote this region by *bistable* referring to the existence of a second, metastable state in which the system can be dynamically trapped.

5.3. Dynamics of self-organization

We now examine the dynamics of the system when the values of α_1 and α_2 are varied as a function of time. Experimentally, this corresponds to vary the pump laser intensities or their detuning with respect to the cavity mode frequencies. At time $t = 0$ we assume that the system is prepared in the stationary state of a paramagnetic phase, described by the distribution in Eq. (5.8) by setting $\alpha_n = \alpha_{ni} \ll 1$ in Eq. (5.9) ($n = 1, 2$). The values α_n appearing in the equations of motion (5.1) are then varied in time, by performing either (i) a sudden quench, i.e. suddenly switching the two values of α_{1f} and α_{2f}, or (ii) a slow quench, consisting in varying $\alpha_n(t)$ monotonously and continuously in time towards the final values α_{1f} and α_{2f}. We choose the final values α_{nf} in the ferromagnetic phase. The quench protocols we consider are illustrated by the green lines in Fig. 5.2(a): for

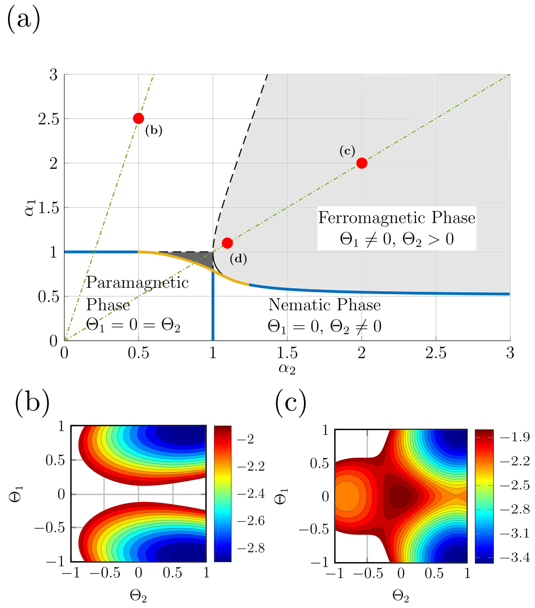

Figure 5.2.: (a) Phase diagram of the stationary phases, corresponding to the global minima of Eq. (5.14), in the plane $\alpha_1 - \alpha_2$. Blue (yellow) lines mark second (first) order phase transitions. The light gray area (dark gray area) within the ferromagnetic phase indicate the parameter region where the nematic (paramagnetic) phase are local minima of the free energy. The red circles labeled by (b) and (c) indicate the parameters to which the contour plots of free energy in subplots (b) and (c) are shown in the $\Theta_1 - \Theta_2$ landscape. The free energy in subplot (b) exhibits two global minima at $\Theta_1 = \pm 0.92$ and $\Theta_2 = 0.73$; in (c) the two global minima of the ferromagnetic phase are at $\Theta_1 = \pm 0.97$ and $\Theta_2 = 0.88$, the local minimum in the nematic phase is at $\Theta_1 = 0$ and $\Theta_2 = -0.83$ (the contour of $\mathcal{F}$ is reported below a convenient threshold). The green dash-dotted lines in subplot (a) illustrate the paths of the quench protocols discussed in Sec. 5.3. Circle (d) indicates the parameters of the quench discussed in Sec. 5.3.3.

sudden quenches, the initial and final values are two points connected by the green line. A slow quench sweeps across the intermediate points along the line. We are interested in determining the dynamics leading to the steady state.

In what follows we perform numerical simulations of Eq. (5.1) using the parameters of a gas of ^{85}Rb atoms. In particular, we take $k = 2\pi/\lambda$ with $\lambda = 780$nm the wavelength of the D_2 line. The corresponding recoil frequency is $\omega_r = 2\pi \times 3.86$kHz. The cavity linewidth is taken to be $\kappa = 2\pi \times 1.5$MHz, so that $\kappa \approx 388.6\omega_r$. A possible realization of the two-mode setup here considered has been discussed in Refs. [5.1, 5.19].

5.3.1. Sudden quench into the ferromagnetic phase

We first consider sudden quenches from α_{1i}, α_{2i} in the paramagnetic phase to α_{1f}, α_{2f} in the ferromagnetic phase, keeping $\alpha_{1i}/\alpha_{2i} = \alpha_{1f}/\alpha_{2f} = 5$. The initial values are vanishingly small and the atoms are at the corresponding stationary distribution, which is a thermal distribution at the temperature determined by the corresponding detuning, Eq. (5.13), with homogeneous density. The detuning before and after the quench is taken to be equal, thus it is expected that the atoms reach a thermal distribution with the same temperature as the initial state.

Figure 5.3 displays the distribution $\mathcal{P}_t(\Theta)$ for the order parameters Θ_1 and Θ_2 as a function of time for $(\alpha_{1f}, \alpha_{2f}) = (2.5, 0.5)$. It is defined as a time sequence of normalized histograms

$$\mathcal{P}_t(\Theta) = \frac{\#\text{ trajectories with } \Theta(t) \in [\Theta - \Delta_\Theta/2, \Theta + \Delta_\Theta/2]}{\#\text{ trajectories} \times \Delta_\Theta}, \tag{5.15}$$

where Θ is calculated on each trajectory of the simulations with the stochastic different equations and its value is determined according to the precision Δ_Θ of the grid in Θ. We observe that at a given time scale of the order of $10^2/\kappa$, $\mathcal{P}_t(\Theta_1)$ splits into two branches corresponding to two possible orders in the long-wavelength lattice. This symmetry breaking is well known from the single mode case [5.6]. The order parameter of the short-wavelength mode Θ_2, which is weakly pumped, substantially grows to a positive value long after the symmetry breaking. The fact that $\mathcal{P}_t(\Theta_2)$ vanishes for negative Θ_2 values comes from the ordering of the atoms close to the anti-nodes of the dominant long-wavelength mode field $\cos(kx)$ (see Fig. 5.1).

The distributions $\mathcal{P}(\Theta_n)$ at the asymptotics are reported in the right panels of Fig. 5.3. They are obtained by averaging $\mathcal{P}_t(\Theta_n)$ over times $t \geq 10^6/\kappa$, where a stable configuration has been reached. Formally

$$\mathcal{P}(\Theta) = \sum_{i=1}^{N_t} \mathcal{P}_{t_i}(\Theta)/N_t\,, \tag{5.16}$$

where N_t is the number of instants of times at which the distribution is sampled in the interval $[t_1, t_\mathrm{f}]$, with $t_1 = 10^6/\kappa$ and $t_\mathrm{f} = t_{N_t} > t_1$. Comparing the widths of the distributions in the right panel of Fig. 5.3 one observes that after sufficiently long times the long-wavelength order parameter fluctuates less than the short-wavelength order parameter.

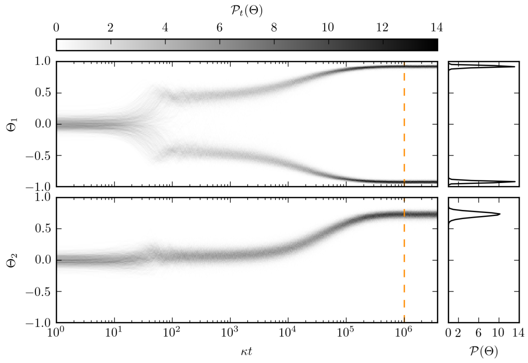

Figure 5.3.: Dynamics following a sudden quench from $\alpha_{1i}, \alpha_{2i} \ll 1$ to $\alpha_{1f} = 2.5$, $\alpha_{2f} = 0.5$ keeping constant the detuning $\Delta_c = -\kappa$. The left panel displays the contour plot of distribution $\mathcal{P}_t(\Theta)$ (Eq. (5.15)) for $\Theta = \Theta_1$ and $\Theta = \Theta_2$ as a function of time (in units of $1/\kappa$). The distribution has been extracted from the numerical simulations using Eq. (5.1) for $N = 100$ atoms and 1000 trajectories. The grid in Θ for the left panel has minimum step $\Delta_\Theta = 2/111$, the grey scale gives the relative weight. The right panels display the distributions $\mathcal{P}(\Theta_1)$ and $\mathcal{P}(\Theta_2)$ as a function of Θ_1 and Θ_2, respectively, see Eq. (5.16). Here, the time average has been performed for $N_t = 113$ instants of time chosen between $t_1 = 10^6/\kappa$ and $t_\mathrm{f} = 3.77 \times 10^6/\kappa$. The vertical dashed line in the left panels marks the instant of time $t_1 = 10^6/\kappa$.

Figures 5.4(a)-(b) display the dynamics of the mean absolute value of the order parameters for different values of N. Figure 5.4 (c) shows the time evolution of the fluctuations of the order parameters $\delta\Theta_n = \sqrt{\langle\Theta_n^2\rangle - \langle|\Theta_n|\rangle^2}$ for $N = 100$ particles. The order parameters asymptotically tend to the values predicted by the free energy, indicated by the horizontal dashed line, for a time scale of the order of $10^6/\kappa$. Meanwhile the fluctuation $\delta\Theta_1$ relaxes to a much smaller value than the asymptotic value of $\delta\Theta_2$ reproducing the widths of the distributions in the right panel in Fig. 5.3. The time evolution of $\langle|\Theta_1|\rangle$, in particular, is reminiscent of the one observed for quenches into the ferromagnetic phase in a single-mode resonator [5.12]. It can be separated into three stages which we denote by (in order of their temporal appearance) (i) violent relaxation, corresponding to an exponential increase of the absolute value of the order parameter $\langle|\Theta_1|\rangle$; (ii) transient dynamics, corresponding to power-law scaling with time, and (iii) relaxation phase, where the mean values tend exponentially towards the asymptotic value. The violent relaxation can be described by a mean-field model [5.13], in the transient stage the coherent dynamics is prevailing, while the relaxation stage is dominated by dissipation [5.12]. The transient and relaxation stages are characterized by time scales which increase with N but with different functional dependence [5.13]. The time scale $10^6/\kappa$ can here be identified as the one at which the asymptotic state is reached for $N \lesssim 200$, while for larger numbers of particles longer time scales shall be considered.

Interestingly, in the transient phase there is ordering only in the long-wavelength mode

(a)

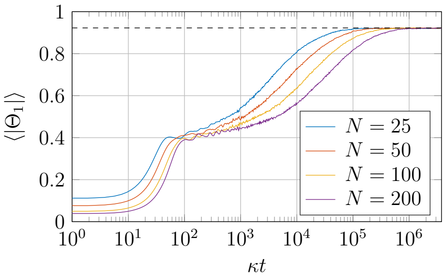

(b)

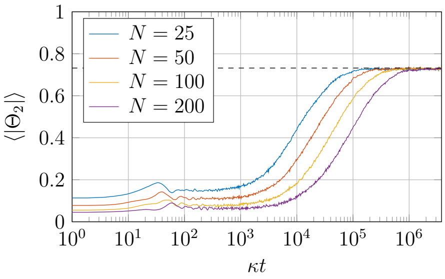

(c)

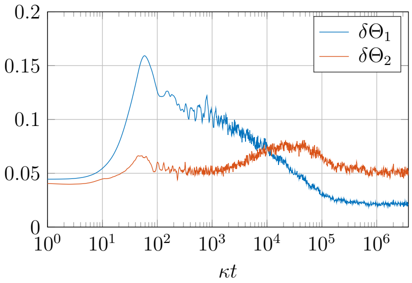

Figure 5.4.: Dynamics of (a) $\langle|\Theta_1|\rangle$, (b) $\langle|\Theta_2|\rangle$, and (c) their fluctuations $\delta\Theta_n = \sqrt{\langle\Theta_n^2\rangle - \langle|\Theta_n|\rangle^2}$ as a function of time (in units of $1/\kappa$). The parameters and quench protocol are the same as in Fig. 5.3, the curves are however evaluated for different numbers of atoms and of trajectories. In (a) and (b) the data correspond to $N = 25, 50, 100, 200$ particles (see legenda for color code) and respectively $1000, 500, 250, 125$ trajectories. The horizontal dashed lines indicate the value predicted by the global minimum of the free energy in Eq.(5.14). The finite values of the order parameters at $t = 0$ are due to finite size effects, $\langle|\Theta_n(0)|\rangle = 1/\sqrt{\pi N}$. The curves in (c) are calculated for $N = 100$ and 250 trajectories.

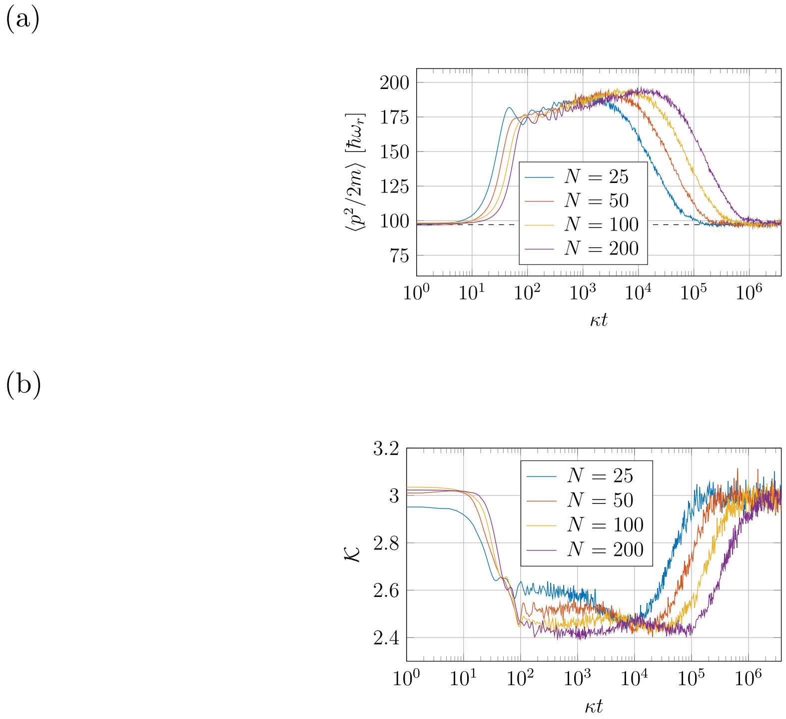

Figure 5.5.: Dynamics of (a) the single-particle kinetic energy $\langle p^2/2m \rangle$ (in units of $\hbar\omega_r$) and (b) the Kurtosis $\mathcal{K} = \langle p^4 \rangle / \langle p^2 \rangle^2$, for $N = 25, 50, 100, 200$ particles (see legenda) and correspondingly $1000, 500, 250, 125$ trajectories. The other parameters and quench protocol are the same as in Fig. 5.4. The horizontal dashed line in (a) indicates the asymptotic value predicted by Eq. (5.13).

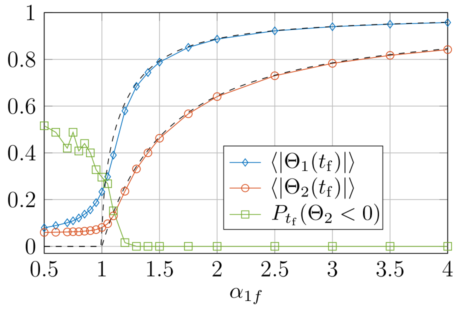

Figure 5.6.: Asymptotic values of $\langle |\Theta_1(t_\mathrm{f})| \rangle$, $\langle |\Theta_2(t_\mathrm{f})| \rangle$, and $P_{t_\mathrm{f}}(\Theta_2 < 0)$, Eq. (5.17), as a function of α_{1f}. The quenches start all from the same initial values in the paramagnetic phase ($\alpha_{1i}, \alpha_{2i} \ll 1$ and $\Delta_c = -\kappa$) and end up in different values α_{1f}, α_{2f} with $\alpha_{1f} = 5\alpha_{2f}$ (lying along the left green line in Fig. 5.2(a)) and $\Delta_c = -\kappa$. The circles correspond to the results of the numerical simulations at $t_\mathrm{f} = 3.77 \times 10^6/\kappa$ with $N = 100$ particles and 250 trajectories. The dashed lines indicate the predictions of the global minima of Eq. (5.14).

of the cavity, while ferromagnetic order is finally established by dissipation on a longer timescale. The metastable phase of the transient dynamics can be therefore denoted by "nematic", its lifetime increases with N and for $N \sim 200$ it is of the order of $t \sim 10^4/\kappa$. However, this metastable "nematic" state cannot be understood in terms of the landscape of the free energy, but rather seems to exhibit the features of the quasi-stationary state due to the long-range coherent dynamics analogous to the ones reported in Ref. [5.22]. This conjecture is also supported by the behaviour of the single-particle kinetic energy and of the kurtosis $\mathcal{K} = \langle p^4 \rangle / \langle p^2 \rangle^2$, which are shown in Fig. 5.5. The latter quantifies the deviation of the momentum distribution from a Gaussian, for which it takes the value $\mathcal{K}_{\text{Gauss}} = 3$. For these quantities we observe that in the metastable nematic phase the kinetic energy grows, while the distribution is non-thermal. Ordering in the second, short-wavelength lattice is accompanied by cooling into a thermal distribution.

We now compare the numerical results with the analytic theory for different quenches starting from the same initial values of $\alpha_{1i}, \alpha_{2i} \ll 1$ but with different endpoints α_{1f}, α_{2f}. We take different endpoints ranging from the paramagnetic to the ferromagnetic phase, under the constrain $\alpha_{1f}/\alpha_{2f} = 5$. The circles in Fig. 5.6 correspond to the numerical results for 100 particles at time $t_{\text{f}} > 10^6/\kappa$, where we expect that the system has reached the steady state. These are in good agreement with the analytical results (dashed lines) based on evaluating the corresponding observables at the global minimum of the free energy. The interval where $\langle |\Theta_n| \rangle$ grows monotonically from $\sim 1/\sqrt{N}$ to the value of the ferromagnetic phase is expected to shrink as N is increased, in agreement with a second order phase transition at the thermodynamic limit. Further information on the onset of this ferromagnetic order can be gained by the probability $P_t(\Theta_2 < 0)$ that Θ_2 is negative at t:

$$P_t(\Theta_2 < 0) = \int_{-1}^{0} \mathrm{d}\Theta_2 \mathcal{P}_t(\Theta_2) \,. \tag{5.17}$$

We note that in the paramagnetic phase (homogeneous spatial distribution) we expect $P_t(\Theta_2 < 0) \simeq 0.5$. In contrast, due to the given mode structure we expect that $P_t(\Theta_2 < 0) \simeq 0$ for long-wavelength ordering in the ferromagnetic phase. Indeed, as α_{1f} increases across the critical value, $P_t(\Theta_2 < 0)$, quickly drops down to zero.

5.3.2. Sudden quenches into the bistable phase

We now turn to the dynamics following sudden quenches from the paramagnetic to the ferromagnetic phase but following the right path of Fig. 5.2(a), which consists in equal effective pumping $\alpha_{1i}/\alpha_{2i} = \alpha_{1f}/\alpha_{2f} = 1$. In this parameter region (bistable phase) the free energy exhibits a local minimum, which is nematic. As in the previous case, the initial values α_{1i}, α_{2i} are vanishingly small and the atoms are at the corresponding stationary distribution, whose temperature is determined by the detuning Δ_c and whose spatial density is homogeneous. The quench is performed by switching the laser power keeping the detuning constant, thus the atoms should reach a thermal distribution with the same temperature as the initial state.

Figure 5.7 displays the time evolution of the trajectories' Θ-distribution for $\alpha_{1f} = \alpha_{2f} = 2$ and $\Delta_c = -\kappa$. As opposed to the previous section, here a finite fraction of

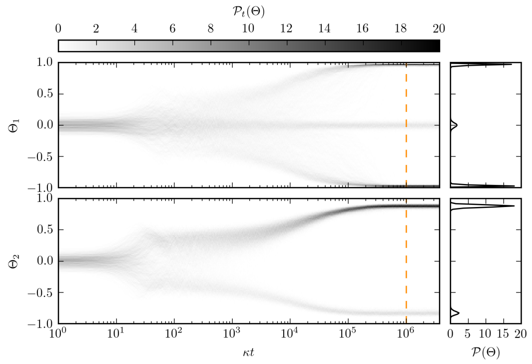

Figure 5.7.: Dynamics following a sudden quench from $\alpha_{1i}, \alpha_{2i} \ll 1$ to $\alpha_{1f} = \alpha_{2f} = 2$ keeping constant the detuning $\Delta_c = -\kappa$ (red circle (c) in Fig. 5.2(a)). The left panel displays the contour plot of the distribution $\mathcal{P}_t(\Theta)$ (Eq. (5.15)) for $\Theta = \Theta_1$ and $\Theta = \Theta_2$ as a function of time (in units of $1/\kappa$). The distribution has been extracted from the numerical simulations using Eq. (5.1) for $N = 100$ atoms and 1000 trajectories. The right panels display the distributions $\mathcal{P}(\Theta_1)$ and $\mathcal{P}(\Theta_2)$ as a function of Θ_1 and Θ_2, respectively, see Eq. (5.16). See Fig. 5.3 for further details.

trajectories gets trapped in the nematic phase with vanishing value of Θ_1 and finite probability that Θ_2 takes negative values. This is visible in the small extra peaks in $\mathcal{P}(\Theta_1)$ and $\mathcal{P}(\Theta_2)$ (right panels). The trapping occurs at the time scale of the violent relaxation, and it seems stable over times of the order of $10^6/\kappa$. We conjecture that it persists also at asymptotic times. In Fig. 5.8 the time evolution of the mean absolute value of the order parameters is shown for different numbers of particles. While $\langle|\Theta_2|\rangle$ reaches the same stationary value (in reality its value decreases slightly with N), instead the asymptotic value of $\langle|\Theta_1|\rangle$ decreases as N grows. This suggests that the probability that the dynamics gets trapped in the local minimum increases with the number of particles. The asymptotic value of $\delta\Theta_1 = \sqrt{\langle\Theta_1^2\rangle - \langle|\Theta_1|\rangle^2}$ in subplot (c) reflects the contribution of these trajectories.

Mean single-particle kinetic energy and kurtosis are shown in Fig. 5.9. From their behaviour we infer that the metastable nematic state does not significantly deviate from a thermal distribution with the expected asymptotic temperature (Eq. (5.13)).

Peculiar features of these dynamics become visible when inspecting the probability $P_t(\Theta_2 < 0)$ at the asymptotics and as a function of α_{1f} in Fig. 5.10. As in Fig. 5.6, it vanishes identically upon leaving the paramagnetic phase, but increases again as α_{1f}, α_{2f} are chosen deeper in the bistable phase of Fig. 5.2(a). Correspondingly, $\langle|\Theta_1|\rangle$ starts to decrease as α_{1f} increases, which suggests that from this point on the depth of the local minimum grows. The value of the order parameter $\langle|\Theta_2|\rangle$ at which $P_t(\Theta_2 < 0)$ starts to grow again identifies a threshold, above which the local minimum is sufficiently deep to stably trap particles.

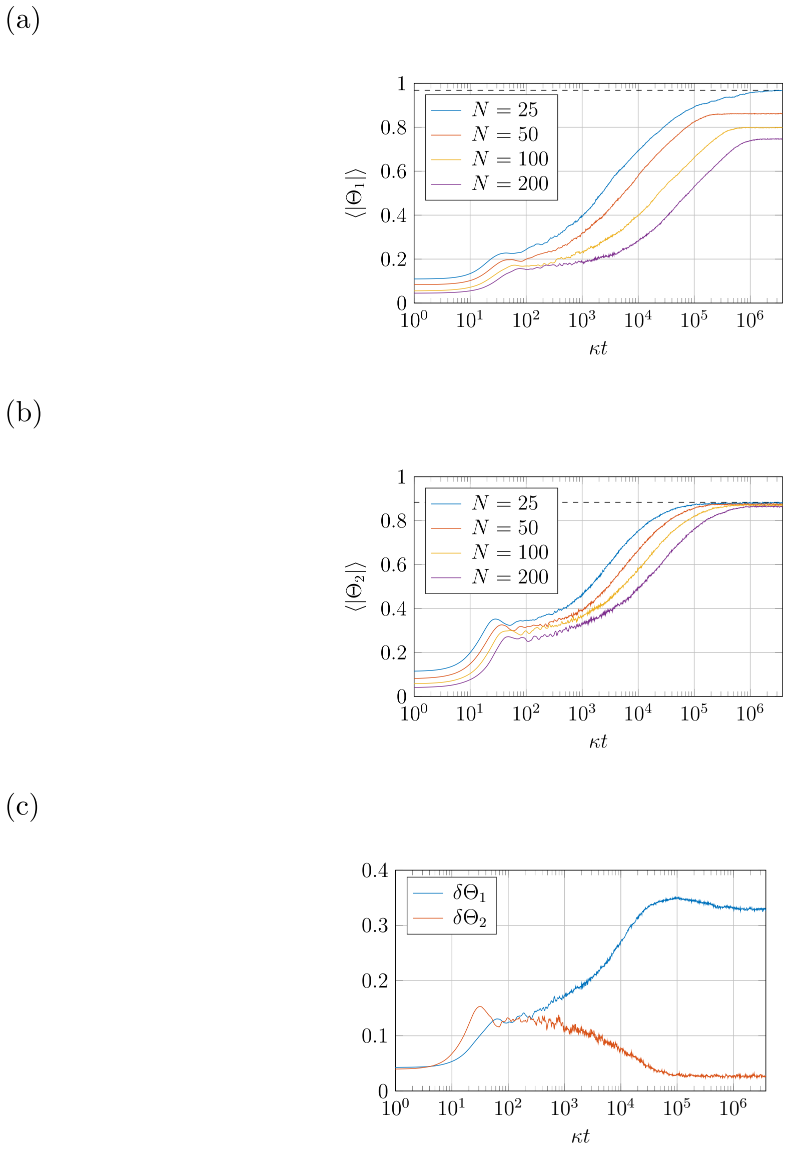

Figure 5.8.: Dynamics of (a) $\langle|\Theta_1|\rangle$, (b) $\langle|\Theta_2|\rangle$, and (c) their fluctuations $\delta\Theta_n = \sqrt{\langle\Theta_n^2\rangle - \langle|\Theta_n|\rangle^2}$ as a function of time (in units of $1/\kappa$). The parameters and quench protocol are the same as in Fig. 5.7, the curves are evaluated for different numbers of atoms and of trajectories. In (a) and (b) the data correspond to $N = 25, 50, 100, 200$ particles (see legenda for color code) and respectively $1000, 500, 250, 125$ trajectories. The horizontal dashed lines indicate the value predicted by the global minimum of the free energy in Eq. (5.14). The finite values of the order parameters at $t = 0$ are due to finite size effects, $\langle|\Theta_n(0)|\rangle = 1/\sqrt{\pi N}$. The curves in (c) are calculated for $N = 100$ and 250 trajectories.

(a)

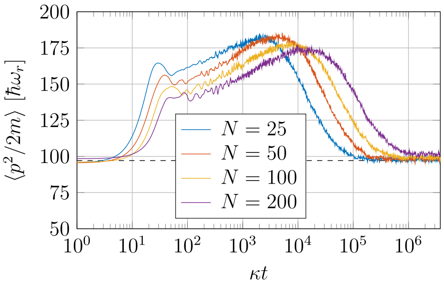

(b)

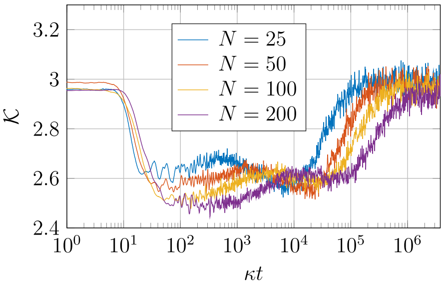

Figure 5.9.: Dynamics of (a) the single-particle kinetic energy $\langle p^2/2m \rangle$ (in units of $\hbar\omega_r$) and (b) the Kurtosis $\mathcal{K} = \langle p^4 \rangle / \langle p^2 \rangle^2$, for $N = 25, 50, 100, 200$ particles (see legenda) and correspondingly $1000, 500, 250, 125$ trajectories. The other parameters and initial conditions are the same as in Fig. 5.8. The horizontal dashed line in (a) indicates the asymptotic value predicted by Eq. (5.13).

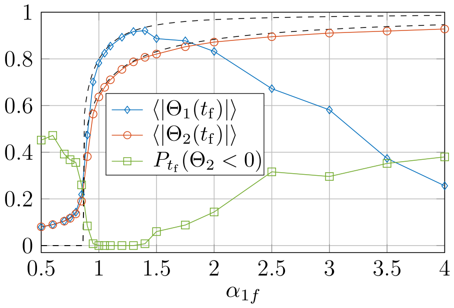

Figure 5.10.: Asymptotic values of $\langle |\Theta_1(t_\mathrm{f})| \rangle$, $\langle |\Theta_2(t_\mathrm{f})| \rangle$, and $P_{t_\mathrm{f}}(\Theta_2 < 0)$, Eq. (5.17), as a function of α_{1f}. The quenches start all from the same initial values in the paramagnetic phase ($\alpha_{1i}, \alpha_{2i} \ll 1$ and $\Delta_c = -\kappa$) and end up in different values α_{1f}, α_{2f} with $\alpha_{1f} = \alpha_{2f}$ (lying along the right green line in Fig. 5.2(a)) and $\Delta_c = -\kappa$. The circles correspond to the results of the numerical simulations at $t_\mathrm{f} = 3.77 \times 10^6/\kappa$ with $N = 100$ particles and 250 trajectories. The dashed lines indicate the predictions of the global minima of Eq. (5.14).

(a)

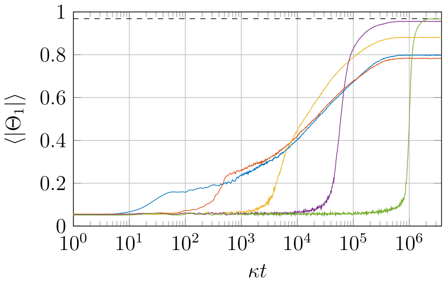

(b)

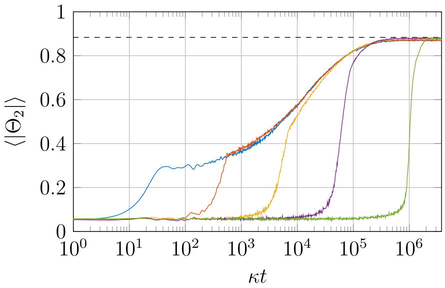

Figure 5.11.: Mean value of the order parameters, (a) $\langle|\Theta_1|\rangle$ and (b) $\langle|\Theta_2|\rangle$ as a function of time (in units of $1/\kappa$) for $N = 100$ and $\Delta_c = -\kappa$, evaluated numerically with 250 trajectories. The curves are the time evolution during and after linear ramps of duration $\tau = 0$ (blue); $\tau = 5.5 \times 10^2/\kappa$ (red), $\tau = 6.8 \times 10^3/\kappa$ (yellow), $\tau = 8.5 \times 10^4/\kappa$ (purple), $\tau = 2 \times 10^6/\kappa$ (green). The ramps are from the paramagnetic to the bistable phase, specifically, from $\alpha_{1i} = \alpha_{2i} = \varepsilon \ll 1$ to $\alpha_{1f} = \alpha_{2f} = 2$. As before, at $t = 0$ the initial state of the atoms is the steady state, Eq. (5.8), for $\alpha_n = \alpha_{ni}$ and $\Delta_c = -\kappa$. The dashed horizontal lines show the steady state values of the global minima of the free energy, Eq. (5.14).

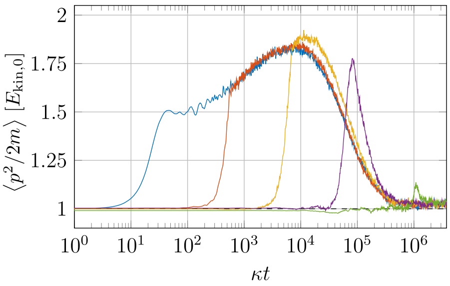

Figure 5.12.: Mean value of the single-particle kinetic energy, $\langle p^2/(2m)\rangle$ (in units of $E_{\text{kin},0} = \hbar\kappa/4$) as a function of time (in units of $1/\kappa$) for the same parameters and color codes as in Fig. 5.11.

5.3.3. Slow ramp into the bistable phase

We now consider linear ramps of $\alpha_n(t)$ across the transition region separating the paramagnetic from the bistable region. The ramps protocols have duration τ and sweep between the values $[\varepsilon, \alpha_{nf}]$, with $\varepsilon \ll 1$. In particular, $\alpha_n(t) = \varepsilon + \alpha_{nf}\frac{t}{\tau}$ if $t \in [0, \tau]$, while for $t > \tau$ then $\alpha_n(t)$ is constant and equal to α_{nf}. Note that a sudden quench is the limit $\tau \to 0$ of a linear quench. We choose to vary the values of $\alpha_n(t)$ along the rightmost green line in Fig. 5.2(a), so that $\alpha_1(t) = \alpha_2(t)$ at all instants of time, with α_{nf} in the bistable phase. We further keep Δ_c constant, and solely vary the pump intensity. This means that the asymptotic temperatures at each value of α_n are equal.

Figure 5.11 displays the dynamics of the mean absolute value of the order parameters for $\alpha_{1f} = \alpha_{2f} = 2$ for linear ramps with different durations τ. The dynamics following the sudden quench (cif. Fig. 5.8 (a) and (b)) is shown for comparison (blue curve). We observe that the dynamics of the order parameters exhibits an exponential increase which occurs almost simultaneously for both $\langle|\Theta_1|\rangle$ and $\langle|\Theta_2|\rangle$. This behaviour seems to be initiated at the instant of time when the parameters $\alpha_n(t)$ cross the critical point of the phase diagram. Moreover, for sufficiently slow ramps $\langle|\Theta_1|\rangle$ approaches the asymptotic value of the free energy's global minimum, signaling stationary long-wavelength order.

We further note that for $\tau \lesssim 10^3/\kappa$ the orders parameters undergo a three-stage dynamics, as for the sudden quench (we attribute the fluctuations to the statistics of trajectories). For slower ramps, instead, the mean value of the order parameter tends exponentially towards the steady state, which approaches the free energy's global minimum of Eq. (5.14) for $\tau > 10^4/\kappa$. We believe that this behaviour is determined by the ramp duration τ with respect to the time scale of the transient dynamics, and thus by the time the parameters $\alpha_n(t)$ spend close to the transition point. This conjecture is supported by the analysis of the time evolution of the single-particle kinetic energy shown in Fig. 5.12, corresponding to the curves in Fig. 5.11. For faster ramps it is similar to the sudden quench, exhibiting first a violent relaxation followed by a time interval where the dynamics is prevailingly coherent, and finally an exponential decay to the steady state

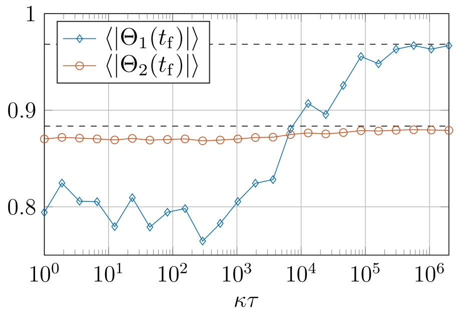

Figure 5.13.: Values of $\langle|\Theta_1(t_\mathrm{f})|\rangle$ (blue) and $\langle|\Theta_2(t_\mathrm{f})|\rangle$ (red) at $t_\mathrm{f} = 3.77 \times 10^6/\kappa$ and as a function of the ramp duration τ (in units of $1/\kappa$), for the same parameters as in Fig. 5.11. The dashed horizontal lines show the steady state value predicted by the free energy, Eq. (5.14).

(a)

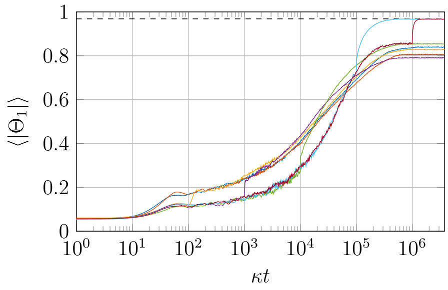

(b)

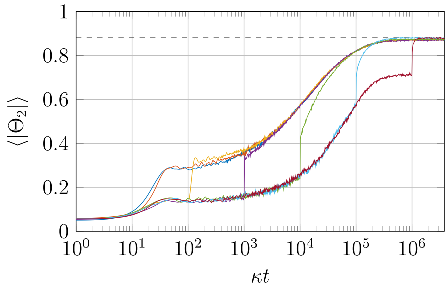

Figure 5.14.: Dynamics of (a) $\langle|\Theta_1|\rangle$ and (b) $\langle|\Theta_2|\rangle$ as a function of time (in units of $1/\kappa$) for the two-step quench protocol. Here, the parameters α_n are suddenly ramped at $t = 0$ from the initial values $\alpha_{1i}, \alpha_{2i} \ll 1$ to $\alpha_{1\text{int}} = \alpha_{2\text{int}} = 1.1$; After a time interval τ, there is a second quench from $\alpha_{1\text{int}} = \alpha_{2\text{int}} = 1.1$ to $\alpha_{1f} = \alpha_{2f} = 2$. The parameters are $\Delta_c = -\kappa$, $N = 100$ with 250 trajectories, and $\tau = 1/\kappa$ (blue), $10/\kappa$ (red), $10^2/\kappa$ (yellow), $10^3/\kappa$ (purple), $10^4/\kappa$ (green), $10^5/\kappa$ (light blue) and $10^6/\kappa$ (dark red). The dashed horizontal lines show the value predicted by global minimum of the free energy, Eq. (5.14), at $\alpha_1 = \alpha_2 = 2$ and $\Delta_c = -\kappa$.

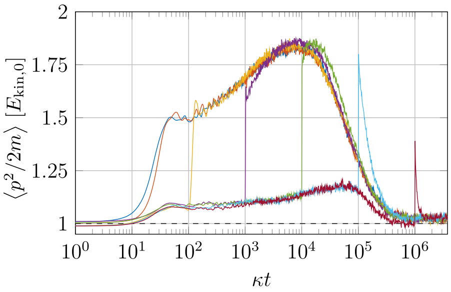

Figure 5.15.: Mean kinetic energy per particle, $\langle p^2/2m\rangle$ (in units of the asymptotic value $E_{\text{kin},0} = \hbar\kappa/4$) as a function of time (in units of $1/\kappa$) for the same parameters and colour codes as in Fig. 5.14.

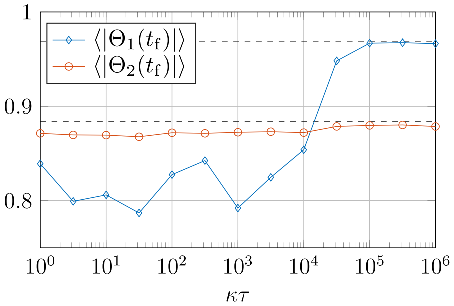

Figure 5.16.: The symbols correspond to $\langle|\Theta_1(t_f)|\rangle$ (blue) and $\langle|\Theta_2(t_f)|\rangle$ (red) at $t_f = 3.77 \times 10^6/\kappa$ as a function of the time elapsed between the two quenches, τ (in units of $1/\kappa$), for the same parameters as in Fig. 5.14. The dashed horizontal lines show the steady state value predicted by the global minimum of the free energy, Eq. (5.14) at $\alpha_1 = \alpha_2 = 2$ and $\Delta_c = -\kappa$.

value due to cavity cooling. In contrast, upon increasing the ramp duration towards slower ramps this transient regime disappears. Particularly, for the slowest ramp considered here, dissipation leads to quasi-adiabatic dynamics. Figure 5.13 shows the order parameters $\langle|\Theta_1(t)|\rangle$ and $\langle|\Theta_2(t)|\rangle$ at $t = 3.77 \times 10^6/\kappa$, where the curves of Fig. 5.11 have reached an asymptotic behaviour. Self-organization in the long-wavelength grating depends on the ramp duration τ and is found for $\tau > 10^4/\kappa$. Note that short-wavelength order quantified by $\langle|\Theta_2(t)|\rangle$, in contrast, only slightly depends on the ramp duration.

On a microscopic scale, it seems that the reason for better long-wavelength ordering after slower ramps is that more time is spent close to the transition line ($\alpha_1 = \alpha_2 \sim 1$), where the local minimum of the free energy is not deep enough to stably trap the system. In order to test this conjecture, we consider a two-step quench protocol which splits the sudden quench of Sec. 5.3.2 into two subsequent quenches: one at $t = 0$ from a paramagnetic to a ferromagnetic bistable phase, but close to the transition line: $\alpha_{1\mathrm{int}} = \alpha_{2\mathrm{int}} = 1.1$. This quench shows a vanishing value of $P_t(\Theta_2 < 0)$ for sufficiently long times as in Fig. 5.10. The second sudden quench occurs after an elapsed time τ and goes from this intermediate point into $\alpha_{1f} = \alpha_{2f} = 2$. The detuning Δ_c is kept constant during the evolution.

Figure 5.14 displays the time evolution of the mean absolute values of the order parameters for different time intervals τ elapsed between the two quenches. The order parameters undergo a first violent relaxation at $t = 0$, when the first sudden quench occurs, and a second one immediately after the second quench (which looks like a jump in logarithmic scale). As expected, the larger the time elapsed between the two quenches, the closer the asymptotic value is to the one of the global minimum. Inspecting the dynamics of the kinetic energy in Fig. 5.15 we observe that for large τ the atoms are cooled into the stationary state at $\alpha_n \sim 1$. At this point of the phase diagram the free energy has two ferromagnetic global minima, while the nematic local minimum is very shallow. The system thus gets cooled close to the global minima of the free energy at

$\alpha_n = 2$, and remains trapped there after the second quench.

Figure 5.16 displays the mean absolute value of the order parameters, as extracted from the numerical data at $t = 3.77 \times 10^6/\kappa$, as a function of the time elapsed between the two quenches. Their value is compared to the predictions of the global minimum of the free energy at $\alpha_1 = \alpha_2 = 2$ and $\Delta_c = -\kappa$. The behaviour is quite similar to the one observed when performing a linear ramp of corresponding duration, Fig. 5.13. Dynamical ordering in the long-wavelength mode seems thus to require that the atoms are initially cooled close to the global minima. This is realised by means of the sufficiently large time τ spent close to the transition point.

5.4. Cooling into crystalline order

We now analyse sudden quenches of the parameter α_n starting with different initial single-particle momentum widths. A possible realization is a quench in the detuning since Δ_c controls the steady state temperature, see Eq. (5.13). By these means we consider quenches which could either lead to heating or cooling of the system to the stationary temperature T_0,

$$k_B T_0 = \frac{\hbar\kappa}{2}, \tag{5.18}$$

namely, the minimal temperature achieved by cavity cooling, corresponding to setting $\Delta_c = -\kappa$. Thereby we also consider initial thermal distributions which are spatially uniform and with temperature $T_{\text{ini}} < T_0$. The initial momentum distribution we consider are Gaussian and their width is $\Delta p^2 = m k_B T_{\text{ini}}$.

Figure 5.17 shows the time evolution of the mean absolute values of the order parameters for different values of T_{ini} ranging from $0.1 T_0$ up to $5T_0$. The asymptotic value of $\langle|\Theta_1|\rangle$ increases with the initial temperature: The hotter is initially the system, the smaller is the fraction of trajectories which remain trapped in the metastable, nematic state. The corresponding time evolution of mean kinetic energy per particle is displayed in Fig. 5.18 and shows that for $T_{\text{ini}} = 2T_0$ (and even more for $T_{\text{ini}} = 5T_0$) the system stays relatively hot over time scales of the order of $10^4/\kappa$. For lower initial temperatures, instead, the system is heated by the energy released by the sudden quench before relaxation cools the atoms.

As visible in Fig. 5.17, for samples initially cold a long-wavelength Bragg grating is formed faster than for hotter samples. In this case we recognize a three-stage dynamics like the one observed for the sudden quenches of the laser intensity, when a transient long-range order is established for times $t > 10/\kappa$ and $t < 10^3/\kappa$. For $t > 10^3/\kappa$ dissipation becomes important and $\langle|\Theta_1|\rangle$ increases to a stationary value. This relaxation stage is also present for samples with initial temperatures larger than T_0, however, in this hotter case it is significant faster. Taking a threshold value $\langle|\Theta_1|\rangle|_{\text{thres}} = 0.5$, we observe that buildup of long-wavelength order can take up to a hundred times shorter than for a cold initial state. This is reminiscent of the Mpemba effect in supercooled water [5.24–5.28]. Its origin could be traced to a suppression of long-wavelength order if short-wavelength order is already established on a much faster time scale, visible in Fig. 5.17(b).

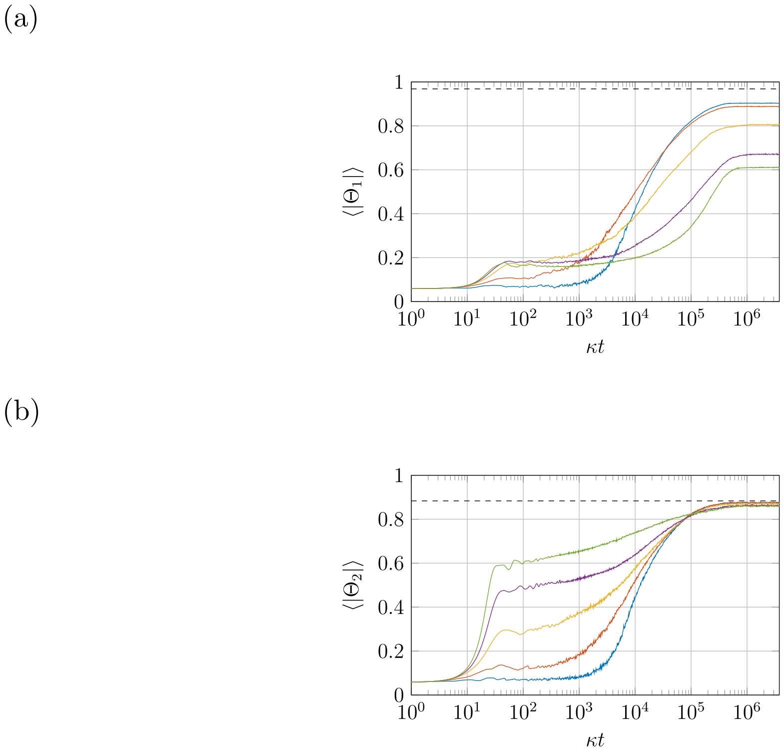

Figure 5.17.: Dynamics of (a) $\langle|\Theta_1|\rangle$ and (b) $\langle|\Theta_2|\rangle$ as a function of time (in units of $1/\kappa$) after a sudden quench at $t = 0$ from $\alpha_{1i} = \alpha_{2i} = 0$ and temperature T_{ini} to $\alpha_{1f} = \alpha_{2f} = 2$ and $\Delta_c = -\kappa$ (corresponding to the asymptotic temperature T_0), for $N = 100$ and 250 trajectories. The different curves correspond to $T_{\text{ini}} = 5T_0$ (blue), $2T_0$ (red), T_0 (yellow), $0.5T_0$ (purple) and $0.1T_0$ (green). The dashed horizontal lines show the steady state value predicted by the global minimum of the free energy, Eq. (5.14).

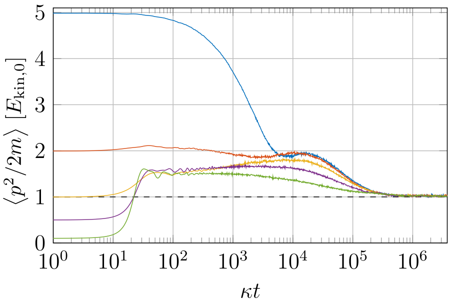

Figure 5.18.: Mean kinetic energy per particle, $\langle p^2/2m\rangle$ (in units of $E_{\text{kin},0} = \hbar\kappa/4$) as a function of time (in units of $1/\kappa$), for the same parameters and colour codes as in Fig. 5.17. The horizontal dashed line corresponds to the asymptotic value $\langle p^2/2m\rangle = E_{\text{kin},0}$.

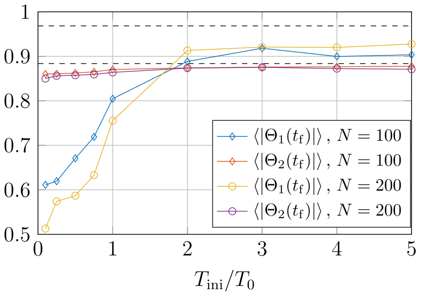

Figure 5.19.: The symbols correspond to the values of $\langle|\Theta_1(t_{\text{f}})|\rangle$ (blue) and $\langle|\Theta_2(t_{\text{f}})|\rangle$ (red) at $t_{\text{f}} = 3.77 \times 10^6/\kappa$ as a function of T_{ini} (in units of T_0), for the same parameters as in Fig. 5.14, but for $N = 200$ particles (125 trajectories). See box for the color code. The dashed horizontal lines show the steady state value predicted by the global minimum of the free energy, Eq. (5.14).

In Fig. 5.17 (a) we observe that the final value of $\langle|\Theta_1|\rangle$ does not coincide with its predicted stationary value even after very long cooling times. This can also be seen in Fig. 5.19, which shows the mean absolute value of the order parameters at $t = 3.77 \times 10^6/\kappa$ as a function of the initial temperature for $N = 100, 200$. One would expect that $\langle|\Theta_1|\rangle$ should have reached a constant value corresponding to the stationary state. Apparently this is not the case and even for finite N a significant fraction of trajectories converges to and remains in the local minimum. This behavior gets much less pronounced, if the initial temperature lies above a certain threshold set by the energy released by the quench itself.

5.5. Comparison between different numerical approaches

The discussion of this paper has been based on results obtained by numerical integration of the stochastic differential equations (5.1) and on their comparison with the corresponding analytical model. Both rely on the validity of the so-called bad cavity limit, where cavity damping is the fastest time scale, and in particular on treating retardation as a small parameter in the dynamics. This regime allows one to systematically describe the quantum fluctuations of the cavity degrees of freedom by eliminating the cavity variables from the equations of motion of the external degrees of freedom. We now compare these predictions with the ones of stochastic differential equations derived in Ref. [5.15] where the cavity degrees of freedom are treated in the semi-classical limit but included at all orders of the retardation expansion. These stochastic differential equations are here extended to our setup composed of two cavity modes [5.16] and read:

$$dx_j = \frac{p_j}{m}dt\,, \tag{5.19a}$$

$$dp_j = \sum_{n=1,2} 2\hbar nkS_n\mathcal{E}_{n,r}\sin(nkx_j)dt\,, \tag{5.19b}$$

$$d\mathcal{E}_{n,r} = (-\Delta_n\mathcal{E}_{n,i} - \kappa_n\mathcal{E}_{n,r})dt + d\xi_{n,r}\,, \tag{5.19c}$$

$$d\mathcal{E}_{n,i} = (\Delta_n\mathcal{E}_{n,r} - \kappa_n\mathcal{E}_{n,i} - NS_n\Theta_n)dt + d\xi_{n,i}\,, \tag{5.19d}$$

where $\mathcal{E}_{n,r} = \mathrm{Re}\{\mathcal{E}_n\}$ and $\mathcal{E}_{n,i} = \mathrm{Im}\{\mathcal{E}_n\}$ are the real and imaginary part of the positive-frequency component of the cavity field mode $n = 1, 2$. The Wiener processes $d\xi_{n,i}, d\xi_{n,r}$ have vanishing first moment, $\langle d\xi_{n,i}\rangle = 0 = \langle d\xi_{n,r}\rangle$, while the second moments fulfill $\langle d\xi_{n,i}d\xi_{m,i}\rangle = \delta_{nm}\kappa/2dt$, $\langle d\xi_{n,r}d\xi_{m,r}\rangle = \delta_{nm}\kappa/2dt$, and $\langle d\xi_{n,r}d\xi_{m,i}\rangle = 0$.

The results of the simulations based on the two approaches for a single-mode cavity show good agreement. For the two-mode cavity we generally find qualitative agreement. Quantitative discrepancies are found in general for the momentum distribution: The simulations based on Eq. (5.19) predict for certain parameters samples whose temperature is 10% hotter than the one obtained with Eq. (5.1). Small differences are found also for the order parameters after the quenches into the bistable phase.

Figure 5.20 shows a representative result of the discrepancies found after the quench protocol discussed in Sec. 5.3.2. The two simulations predict different stationary values for both kinetic energy and the order parameters. We believe that this discrepancy is due to retardation effects, which are neglected in the approach of Eq. (5.1) and become relevant when the atoms are trapped at tight minima.

In order to test our conjecture we use the prediction of the kinetic theory of Refs. [5.29, 5.30], where the temperature of the stationary thermal distribution was corrected by the contribution due to the atoms' localization at the minima of the self-organized lattice,

$$k_B\tilde{T} = \hbar\frac{\Delta_c^2 + \kappa^2}{4|\Delta_c|} + \hbar\frac{\omega_0^2}{|\Delta_c|}\,. \tag{5.20}$$

Here, ω_0 is the frequency of oscillation about the lattice minima in the harmonic approximation. It can be estimated using Eq. (5.19b) and imposing the equality

$$dp_j \approx \sum_{n=1,2} 2\hbar(nk)^2S_n\mathcal{E}_{n,r}x_jdt \equiv -m\omega_0^2x_jdt\,.$$

This delivers an analytic estimate of the frequency

$$\omega_0^2 = \omega_r\frac{\Delta_c^2 + \kappa^2}{-\Delta_c}\left(\alpha_1\Theta_1 + 4\alpha_2\Theta_2\right),$$

where we used Eq. (5.4). For the parameters of the quench in Fig. 5.20, with $\Delta_c = -\kappa$ and $\alpha_1 = \alpha_2 = 2$, we obtain $k_B\tilde{T} \approx 1.1k_BT_0$, where T_0 is the temperature given in Eq. (5.18). Indeed, this corrected value of the final temperature is in good agreement with the discrepancy observed in Fig. 5.20 (a).

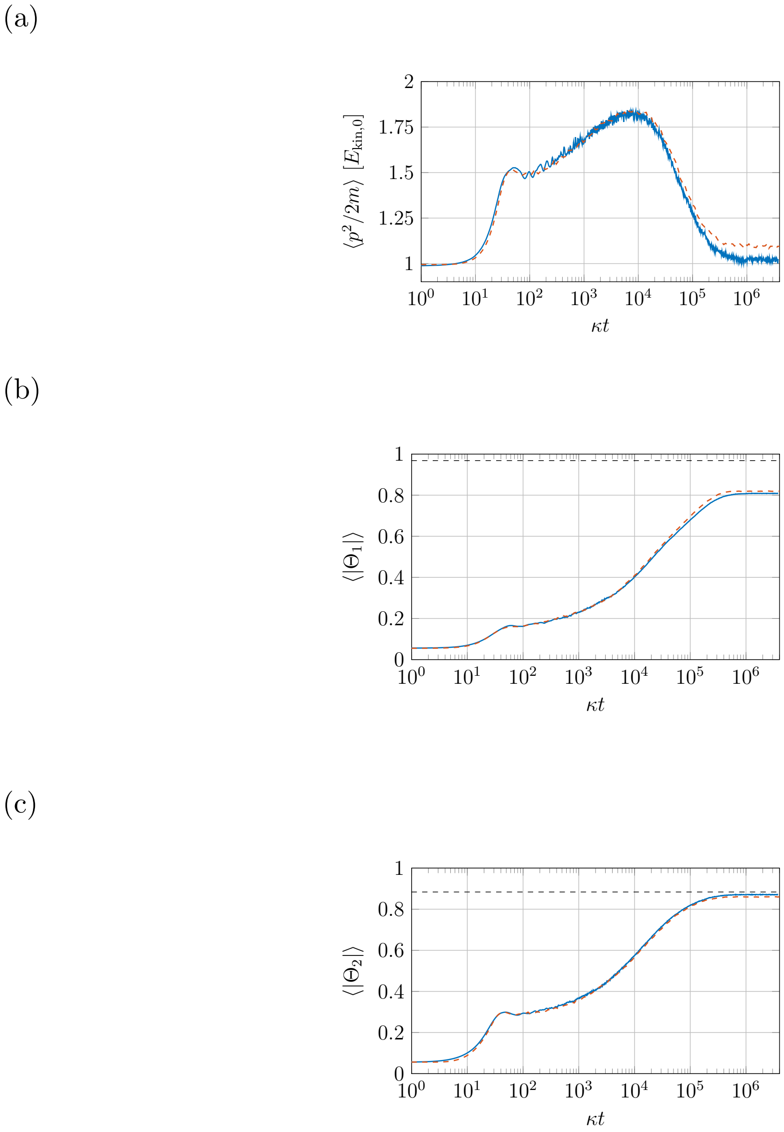

Figure 5.20.: Dynamics of (a) single-particle kinetic energy (in units of $E_{\mathrm{kin},0}$), (b) $\langle|\Theta_1|\rangle$, and (c) $\langle|\Theta_2|\rangle$ as a function of time (in units of $1/\kappa$) following a quench at $t = 0$ from $\alpha_{1i} = \alpha_{2i} \ll 1$ to $\alpha_1 = \alpha_2 = 2$, for $\Delta_c = -\kappa$ and $N = 100$. The blue (red) lines correspond to the simulations using Eq. (5.1)(Eq. (5.19)). The black dashed lines mark the values of the order parameters obtained by the free energy, Eq. (5.14). In (a) the blue (red) line corresponds to 250 (500) trajectories. In (b) and (c) the blue and red lines correspond to 1000 (500) trajectories. Note, that a quench from α_1, α_2 as performed in Sec. 5.3.2 for fixed $\Delta_c = -\kappa$ corresponds for the simulation of Eq. (5.19) to a quench in the pumping strengths S_n such that $NS_n^2 = \alpha_n \kappa^2$. At time $t_{\mathrm{f}} = 3.77 \times 10^6/\kappa$ we observe that 16.9% (15.4%) of the trajectories are in nematic phase using Eq. (5.1) (Eq. (5.19)).

This hypothesis is also consistent with the discrepancy observed in the asymptotic values of the order parameters. In fact, stationary temperature and the final values of the order parameters are related: the stationary values of the order parameters are determined by the parameters α_1, α_2 (cif. [5.1]) and thus depend on both field intensities as well as detunings, see Eq. (5.4). According to this hypothesis, the asymptotic values of the order parameters for the simulation using Eq. (5.19) should be the ones corresponding to the system's parameters with the corrected temperature $\tilde{T}$, hence we shall minimize the free energy of Eq. (5.14) using $\tilde{\beta} = 1/(k_B\tilde{T})$, Eq. (5.20), instead of $1/(k_BT_0)$. This is equivalent to rescale the phase diagram in Fig. 5.2(a) using the prescription $\tilde{\alpha}_n = \alpha_n T_0/\tilde{T} < \alpha_n$, and results in a smaller stationary value of the order parameter which is consistent with the discrepancies visible in Fig. 5.20 (b) and (c).

5.6. Conclusions

In this work we have studied the semi-classical dynamics of atoms interacting with two cavity modes after quenches of the intensity and/or frequency of the pumping lasers. In the quench protocols the laser parameters were varied across transition lines separating a disordered from an ordered self-organized phase. We could verify numerically that the states reached at the asymptotics of the dynamics correspond to the minima of the free energy of a corresponding thermodynamic description developed in Ref. [5.1]. This picture is further confirmed by the comparison with numerical simulations based on different initial assumptions. This analysis shows, in particular, that trapping of the system in local minima of the free energy crucially depends on the initial temperature and on the cooling rate.

We observe, in addition, that the system can be trapped in metastable configurations for transient times which cannot be understood in terms of the effective thermodynamic description. For hundreds of particles the lifetime of these states is about four orders of magnitude longer than the cavity lifetime, and is expected to increase with N. They share analogies with metastable configurations found in the GHMF when performing quenches in the microcanonical ensemble [5.22]. Since the phase diagrams of GHMF and the model here considered can be formally mapped into one another [5.1], we conjecture that these metastable configurations could be due to the coherent dynamics. This conjecture can be tested by means of a mean-field analysis as the one performed in Ref. [5.13] for a single mode cavity.

Interestingly, when the initial temperature of the atomic ensemble is different from the stationary temperature of cavity cooling, we observe that the final magnitude of asymptotic order changes. In particular when the initial temperature is even lower than the predicted cavity cooling temperature, the probability that the systems remains trapped in metastable configurations is further increased. This reminds of the behavior of supercooled water [5.24–5.28].

Here we have considered the very special case of two commensurate modes. While this already highlights many generic properties of the dynamics, future considerations certainly should include the case in which the wavelength of the cavity modes are incommensurate [5.31], so that the ordering mechanisms are much more strongly competing and a multitude of meta-stable states can form. A further interesting direction is operation with much colder temperatures or in the side-band resolved cooling regime [5.32]. Here it is intriguing to consider in which form meta-stable states survive deep in the quantum regime. Besides diffusion they could be depleted via tunneling and atom-field entanglement plays an important role in this dynamics [5.33], a process which should also be relevant in closely related schemes of simulated quantum annealing [5.34].

Acknowledgments

The authors thank Tobias Donner, Sebastian Krämer, and Francesco Rosati for stimulating and helpful discussions. This work was supported by the German Research Foundation (DFG, DACH project "Quantum crystals of matter and light") and by the European Commission (ITN network "ColOpt"). V. T. and H. R. are supported by Austrian Science Fund Project No. I1697-N27. T. K. and V. T. contributed equally to this work.

6. Publication

Physical Review A **95**, 032310 (2017)

Quantum annealing with ultracold atoms in a multimode optical resonator[*]

V. Torggler, S. Krämer, and H. Ritsch

Institut für Theoretische Physik, Universität Innsbruck, A-6020 Innsbruck, Austria

A dilutely filled N-site optical lattice near zero temperature within a high-Q multimode cavity can be mapped to a spin ensemble with tailorable interactions at all length scales. The effective full site to site interaction matrix can be dynamically controlled by the application of up to $N(N+1)/2$ laser beams of suitable geometry, frequency and power, which allows for the implementation of quantum annealing dynamics relying on the all-to-all effective spin coupling controllable in real time. Via an adiabatic sweep starting from a superfluid initial state one can find the lowest energy stationary state of this system. As the cavity modes are lossy, errors can be amended and the ground state can still be reached even from a finite temperature state via ground state cavity cooling. The physical properties of the final atomic state can be directly and almost non-destructively read off from the cavity output fields. As example we simulate a quantum Hopfield associative memory scheme.

doi: 10.1103/PhysRevA.95.032310

---

[*] The author of the present theses did numerical as well as analytical calculations and prepared the manuscript together with H. R. All authors discussed the results. S. K. provided substantial numerical support in co-developing the algorithm selecting the optimal modes.

6.1. Introduction

The realization of strong collective coupling between ultracold atoms and the electromagnetic field in a Fabry-Pérot cavity [6.1] opens a unique test ground to study the real time dynamics of quantum phase transitions in open systems of mesoscopic size [6.2–6.9]. Cavity field mediated interactions induce a variety of self-ordered phases where the particles break the translational symmetry by forming complex spatial patterns [6.1, 6.10–6.13]. In a seminal experiment at ETH the first controllable quantum simulation of the superradiant Dicke phase transition was demonstrated as predicted for the Tavis-Cummings model several decades ago [6.6, 6.14]. By adding an extra optical lattice in the cavity, the complex phase diagram of a Bose-Hubbard Hamiltonian with tailorable short and infinite range interactions was then experimentally studied in great detail, exhibiting superfluid, insulator and supersolid regions [6.15]. The experiment shows very good agreement with theoretical models using various approximate numerical methods like dynamical mean field approaches, predicting a supersolid phase region [6.16, 6.17].

In recent work we exhibited that versatility and complexity of the lattice cavity system strongly increase by adding extra pump laser frequencies close to resonance with different cavity modes [6.18]. For classical point particles one finds that the coupled atom-cavity dynamics can be designed as a self-optimizing light collection system with learning and memory capacity [6.19]. Similarly, generalizing the system to fixed multilevel atoms and using degenerate modes, Gopalakrishnan and coworkers previously proposed to simulate a quantum version of the Hopfield model [6.20–6.22]. Applications to study the physics of a Bose glass were also suggested [6.23].

As the scattered light contains information on the atoms' quantum statistical properties, one can perform minimally perturbing observations in real time and use quantum measurement back action and feedback to further control the system [6.24, 6.25]. First experimental studies of multimode systems were also reported recently [6.26].

For a single laser frequency the interaction between the atoms induced by a single cavity mode is spatially periodic and infinite range [6.1]. In contrast, we show that by help of several pump laser frequencies and tailored illumination geometries, the coupling strengths and light shifts at different sites can be individually modified in such a form as to implement a full connectivity matrix between all lattice sites. In the limit of strong on-site repulsion and low density one gets only zero or one atom per site mimicking a pseudo spin lattice. At least in principle any coupling matrix can be realized using order N^2 cavity modes [6.27]. In contrast to current implementations [6.28], which use minor embedding [6.29], and alternative architectures [6.30], our approach does not need auxiliary qubits to realize long-range coupling.

As power and frequency of the pump lasers can be externally controlled in real time, we have a natural and straightforward way to implement quantum annealing [6.31, 6.32]. One simply slowly increases the strength of the pump lasers in the system to adiabatically reach the ground state of the coupled spin Hamiltonian. As we have a genuine open system, our implementation also suggests a new route towards quantum simulation in a driven-dissipative system as small errors during the sweep process can be amended via cavity ground state cooling [6.33] when we operate the lasers red detuned. This is the

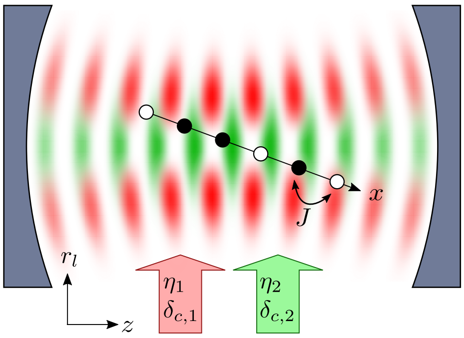

Figure 6.1.: A partially filled optical lattice with N sites inside a multimode optical resonator is pumped from the side by several lasers with frequencies close to cavity resonances.

more effective the more laser modes we have available for coupling and cooling.

This work is organized as follows: after introducing the general multimode atom-field Hamiltonian and its truncated Bose-Hubbard form, we map it to a coupled spin model in the strong on-site interaction limit in Section 6.2. Spin-spin coupling arises from cavity enhanced light scattering and we exhibit how any desired coupling matrix can be found by proper choice of laser parameters in Section 6.3. By employing an adiabatic passage described in 6.4 we finally simulate a Hopfield associative memory model via quantum annealing [6.34] as generic nontrivial example in Section 6.5.

6.2. Model

We study a 1D optical lattice with N_A atoms trapped in N sites ($N > N_\mathrm{A}$), which is placed inside an optical resonator supporting several non-degenerate modes (see Figure 6.1). The atoms are directly illuminated by M lasers with frequencies close to the resonance of the corresponding cavity modes. For sufficient mode spacing, light from each laser is scattered into one specific mode only and scattering between different modes is suppressed. Thus the number of relevant modes equals the number of pump lasers. Furthermore, the laser frequencies are far away from any internal atomic resonance which allows for the elimination of the inner atomic degrees of freedom, resulting in an effective Hamiltonian, coupling modes and atomic motion [6.1]. In addition to the coherent processes described so far, photons leak out through the mirrors. Note that lattice and cavity orientation can be chosen independently.

The single particle Hamiltonian for an atom with mass m_A then reads [6.35]

$$H_0 = \frac{\hat{p}^2}{2m_\mathrm{A}} + V_\mathrm{L}\cos^2(k_\mathrm{L}\hat{x}) - \hbar\sum_{m=1}^{M}\Delta_{c,m}a_m^\dagger a_m + \hbar\sum_{m=1}^{M}\eta_m(u_{p,m}^*(\hat{x})u_{c,m}(\hat{x})a_m + \text{h.c.}), \tag{6.1}$$

where h.c. denotes the Hermitian conjugate. The operators $\hat{x}$ and $\hat{p}$ are position and momentum operators along the lattice axis x, while a_m ($a_m^\dagger$) denotes the annihilation (creation) operator of a photon in the m-th cavity mode. The normalized mode functions of pump and cavity modes are $u_{p,m}(x)$ and $u_{c,m}(x)$, respectively, which are evaluated on the lattice axis. The cavity parameters consist of the effective pump strengths η_m and the detuning between pump laser and cavity mode frequency $\Delta_{c,m}$ of the m-th mode. The optical lattice of depth V_{L} is created by an extra standing wave with wave number k_{L}. Here we neglect the atomic state dependent dispersive shifts of the cavity modes [6.1], which is valid if they are much smaller than the detunings $|\Delta_{c,m}|$.

The many-particle Hamiltonian including contact interactions between atoms can be deduced in the framework of second quantization. In the tight binding limit and neglecting cavity modifications of the tunneling we obtain a generalized intra-cavity Bose-Hubbard Hamiltonian [6.35–6.37]

$$H = H_{\mathrm{BH}} - \hbar \sum_m \Delta_{c,m} a_m^\dagger a_m + \hbar \sum_m \eta_m \sum_i ((v_m^i)^* a_m + v_m^i a_m^\dagger) \hat{n}_i \tag{6.2}$$

with the standard Bose-Hubbard Hamiltonian

$$H_{\mathrm{BH}} = -J \sum_i (b_{i+1}^\dagger b_i + b_i^\dagger b_{i+1}) + \frac{U}{2} \sum_i \hat{n}_i (\hat{n}_i - 1). \tag{6.3}$$

Here b_i and $b_i^\dagger$ are bosonic annihilation and creation operators, whereas $\hat{n}_i = b_i^\dagger b_i$ gives the number of atoms at site i. The matrix elements J and U are the nearest neighbor tunneling rate and the on-site repulsion energy [6.38], respectively, which depend on the optical lattice only. The geometry of the modes (i.e. the mode functions and laser illumination directions) only enters via the N-dimensional coupling amplitude vectors $\boldsymbol{v}_m$ given by

$$v_m^i = \int \mathrm{d}x\, w^2(x - x_i) u_{p,m}(x) u_{c,m}^*(x), \tag{6.4}$$

where $w(x-x_i)$ is the Wannier function for an atom at site i. Thereby we assume that the external optical lattice is much deeper than the potential created by the dynamical cavity field intensity and the pump intensity. In this limit the Wannier functions exclusively depend on the external lattice and are obtained from its Bloch waves in the standard way [6.39].

Additionally to the coherent dynamics treated so far, the cavity fields decay to a steady state with the rates $2\kappa_m$. If these rates are much larger than the rate of change of the atomic motion $J/\hbar$, the state of the cavity fields instantaneously reacts on an altered atomic state and is thus totally determined by the latter. This can be formally expressed by substituting the field operators by atomic operators

$$a_m \equiv \eta_m \sum_i v_m^i \hat{n}_i / (\Delta_{c,m} + i\kappa_m), \tag{6.5}$$

which amounts to an adiabatic elimination of the cavity field operators [6.23, 6.35, 6.40] (see Appendix 6.C for details). Note that this a realistic regime: Already for moderately deep lattices $V_{\mathrm{L}} \sim 10 E_{\mathrm{R}}$ the matrix elements $J \sim 10^{-2} E_{\mathrm{R}}$ are much smaller than realistic cavity decay rates $\hbar\kappa_m \gtrsim E_{\mathrm{R}}$ [6.6, 6.41], where $E_{\mathrm{R}} = (\hbar k_{\mathrm{L}})^2/(2m_{\mathrm{A}})$ is the recoil energy.

In this so-called bad cavity limit the coherent dynamics is described by an effective atomic Hamiltonian

$$H_{\mathrm{ad}} = H_{\mathrm{BH}} - \zeta \sum_{i,j} A_{ij} \hat{n}_i \hat{n}_j. \tag{6.6}$$

The interesting part of the physics is encoded in the real and symmetric interaction matrix

$$A = \sum_m (f_m/\zeta) V_m \tag{6.7}$$

with an effective interaction strength $\zeta = \|\sum_m f_m V_m\|$ and the trace norm $\|M\| = \mathrm{Tr}(\sqrt{M^\dagger M})$ for some matrix M. Thereby each single mode contributes to A with the single mode interaction matrix

$$V_m = \mathrm{Re}(\boldsymbol{v}_m \otimes \boldsymbol{v}_m^*), \tag{6.8}$$

where $\otimes$ denotes the outer product. The strength and sign are controlled by the input parameters $f_m = -\hbar\Delta_{c,m}\eta_m^2/(\Delta_{c,m}^2 + \kappa_m^2)$. Since these parameters depend on detuning and amplitude of the pump lasers, one can externally manipulate A without any change of the setup.

So far we have a quite general coupled quantum oscillator implementation in which the state of each oscillator is given by the occupation number at a lattice site. By increasing the on-site repulsion the oscillators get nonlinear and the extra energy required for multiple occupation of a site becomes large. Consequently, for low enough densities only zero or single occupations occur and the bosonic creation and annihilation operators can be mapped to spin-1/2 operators, identifying an occupied site with spin-up and an empty site with spin-down. In this so-called Tonks-Girardeau limit ($U \gg J, \zeta$) the system reduces to a coupled spin model

$$H_{\mathrm{sp}} = -J \sum_i (\sigma_{i+1}^\dagger \sigma_i + \sigma_i^\dagger \sigma_{i+1}) - \frac{\zeta}{4}\left(\sum_{i,j} A_{ij}\sigma_i^z \sigma_j^z + \sum_i \left[2\sum_j A_{ij}\right]\sigma_i^z\right), \tag{6.9}$$

which amounts to the substitutions $b_i \equiv \sigma_i$ and consequently $\hat{n}_i \equiv \frac{1}{2}(\sigma_i^z + 1)$, where σ_i^α are Pauli matrices and $\sigma_i = \frac{1}{2}(\sigma_i^x - i\sigma_i^y)$. Formally it is a projection of H_{ad} onto the zero and single occupation subspace, which is valid within first order perturbation theory in the small parameters J/U and ζ/U [6.42]. Note that this limit is already reached for moderate lattice depths $V_{\mathrm{L}} \approx 10E_{\mathrm{R}}$ [6.43]. An equivalent model appears for polarized fermions in the lattice.

Since H_{sp} commutes with $\sum_i \sigma_i^z$ the accessible Hilbert space reduces to the $\binom{N}{N_{\mathrm{A}}}$-dimensional subspace with fixed number of spin-up particles. However, for $N_{\mathrm{A}} = N/2$ the subspace still grows exponentially with N.

6.3. Constructing an interaction matrix

Let us now investigate how to realize a general interaction matrix A. While its off-diagonal elements determine the interaction between two pseudo-spins, the diagonal elements specify the local field strengths in the second line of Equation (6.9). Specifically, a local field strength on the i-th spin $h_i = 2\sum_j A_{ij}$ corresponds to the diagonal element $A_{ii} = h_i/2 - \sum_{j\neq i} A_{ij}$ in the matrix. Hence, in order to have full control over interactions and local fields we have to specify up to $N(N+1)/2$ elements, which in the worst case requires as many lasers. Fortunately, these are classical fields with fixed amplitude and frequency.

Formally, the interaction matrix (6.7) appears as linear combination of matrices V_m with coefficients f_m/ζ. Thus if we manage to choose mode functions $u_{c,m}$, pump fields $u_{p,m}$ and lattice location such that $\{V_m\}_{m=1,\ldots,N(N+1)/2}$ forms a basis of the real symmetric matrices, Equation (6.7) can be inverted to fix the required input parameters

$$f_m(A) = \zeta \sum_n (G^{-1})_{mn} \langle V_n, A \rangle. \tag{6.10}$$

Here G is the Gram matrix $G_{mn} = \langle V_m, V_n \rangle$ with inner product $\langle A, B \rangle = \mathrm{Tr}(AB^\dagger)$. In other words, once a set of modes forming a basis is found, we can directly determine the pump laser properties to realize an arbitrary interaction matrix A. While $N(N+1)/2$ lasers are needed to get a complete basis set, many interesting interaction matrices can be constructed with a lot less modes.

6.4. Quantum annealing

In principle our setup realizes an effective spin Hamiltonian with general time dependent all-to-all spin interactions and local fields. This allows for quantum simulation and encoding classical optimization problems in its ground state. The numerically non-trivial task of finding the ground state of a Hamiltonian H_{pr} is tackled by quantum annealing [6.31, 6.32, 6.44], which might promise a speedup over classical methods [6.45–6.47]. To this end one adiabatically evolves the system with a time-dependent Hamiltonian

$$H_{\mathrm{QA}}(t) = a(t)H_{\mathrm{kin}} + b(t)H_{\mathrm{pr}}. \tag{6.11}$$

The kinetic term H_{kin} is chosen simple enough to posses a known gapped ground state. Initially at $t = 0$, the first term is dominant, i.e. $a(0) \gg b(0)$ and the system is prepared in this ground state of H_{kin}. By slowly decreasing $a(t)$ and increasing $b(t)$ the second term becomes dominant after an annealing time τ, i.e. $a(\tau) \ll b(\tau)$. Due to the adiabatic theorem [6.48] the system approximately stays in its instantaneous eigenstate and thus finally ends up in the ground state of H_{pr}, provided τ is large enough, i.e. the adiabatic passage is slow.

The Hamiltonian H_{sp} given in Equation (6.9) with time-dependent coefficients $\zeta(t)$ and $J(t)$ already has the genuine form of a quantum annealing Hamiltonian H_{QA}, where the first line corresponds to H_{kin} and the second line to H_{pr}. For an adiabatic transfer we ramp up $\zeta(t)$ from $\zeta(0) = 0$ until the kinetic term becomes negligible $\zeta(\tau) \gg J$. This can be achieved by uniformly increasing all $|f_m|$'s, which physically amounts to increasing the strengths η_m of all pump lasers or, alternatively, tuning them from $|\Delta_{c,m}| \gg \kappa_m$ to $|\Delta_{c,m}| \sim \kappa_m$ at some fixed pump strength. The uniformity guarantees that A and thus the structure of H_{pr} is not changed during the sweep. A simultaneous increase of the lattice depth to reduce tunneling J helps further.

Note that instead of adiabatic transfer one could implement cavity cooling for the full interacting Hamiltonian to cool towards the ground state starting from a thermal state. This has proven successful for the single mode case [6.33, 6.41] and cooling profits from more modes [6.1].

Readout

The final state readout can be done by analyzing the light leaking out from the cavity [6.24, 6.37], where the quantities of interest are the (classical) spins $\langle \sigma_i^z \rangle \equiv 2\langle \hat{n}_i \rangle - 1$, which can be calculated from the occupations $\langle \hat{n}_i \rangle$.

Measuring the output fields $\propto \langle a_m \rangle$ (e.g. by homodyne detection) one has to approximately solve the expectation value version of Equations (6.5) for $\langle \hat{n}_i \rangle$, which is an overdetermined $M \times N$ linear system of equations, e.g. by using a least mean square method. Alternatively, by measuring the output intensities $\propto \langle a_m^\dagger a_m \rangle$ one has to invert

$$\langle a_m^\dagger a_m \rangle = \frac{\eta_m^2}{\Delta_{c,m}^2 + \kappa_m^2} \sum_{i,j} V_m^{ij} \langle \hat{n}_i \hat{n}_j \rangle \tag{6.12}$$

to obtain the $N(N+1)/2$ correlations $\langle \hat{n}_i \hat{n}_j \rangle$. Since in the large-$U$ limit it holds that $\hat{n}_i^2 \equiv \hat{n}_i \equiv (\sigma_i^z + 1)/2$, the occupations correspond to the diagonal elements $\langle \hat{n}_i^2 \rangle$.

6.5. Associative memory

As a generic example we consider a Hopfield associative memory network with a quantum annealing recall [6.34, 6.49, 6.50]. A Hopfield net consists of N binary state units (so-called neurons), which can be represented by (classical) Ising spins s_i interconnected by real symmetric weights W_{ij}. For their dynamics Hopfield proposed an iterative update rule, which locally minimizes an energy function $E(\boldsymbol{s}) = -\sum_{i<j} W_{ij} s_i s_j$ of the system state vector $\boldsymbol{s} = (s_1, ..., s_N)$. In combination with a learning rule determining the weights W_{ij} the network works as an associative memory, which can memorize a set of P states $\mathcal{M} = \{\boldsymbol{w}_p\}_{p=1,...,P}$. That is, the system converges to the stored state in P having maximal overlap with an initial (input) state. A proven standard choice of weights is provided by the Hebbian learning rule [6.51]

$$W_{ij} = \frac{1}{P} \sum_{p=1}^{P} w_p^i w_p^j. \tag{6.13}$$

Each associative memory of size N has a limited capacity, i.e. a maximal number of stored states which can be reliably recalled. This capacity grows proportional to N using the aforementioned update rule [6.52]. Thus convergence to a particular memory state is not guaranteed to succeed for an input state with too strong deviations or if too many states are stored.

This capacity is suggested to scale much more favorable in a quantum simulator version of the model [6.34]. In such a setup one replaces Hopfield's classical spin update dynamics by quantum annealing to find the ground state of the Hamiltonian

$$H_{\mathrm{AM}} = -\sum_{i<j} W_{ij}\sigma_i^z\sigma_j^z - \nu\sum_i \chi_i\sigma_i^z. \tag{6.14}$$

A state of the network $\boldsymbol{s}$ now corresponds to eigenstates $|\boldsymbol{s}\rangle$ of the σ_i^z-operators. Obviously, the first term is the pendant to the energy function $E(\boldsymbol{s})$, which lowers the energy of memory states $|\boldsymbol{w}_p\rangle$. The input state $\boldsymbol{\chi}$ is encoded in the local fields (as opposed to the classical case, where it is the initial state), such that the energy of a state $|\boldsymbol{s}\rangle$ is lowered proportionally to its similarity to $|\boldsymbol{\chi}\rangle$ quantified by the inner product $\boldsymbol{\chi}\cdot\boldsymbol{s} = \sum_i \chi_i s_i$. The ground state then corresponds to the memorized state with maximal overlap with $\boldsymbol{\chi}$ for a not too large ν as discussed in [6.34] (see also Appendix 6.D).

In our system H_{AM} can be realized with the interaction matrix

$$A_{ij} = W_{ij} + \nu\chi_i\delta_{ij} \tag{6.15}$$

in the coupled spin Hamiltonian of Equation (6.9), where δ_{ij} denotes the Kronecker delta. Physically each lattice site corresponds to a neuron with the two states 'occupied' and 'not occupied' and weights are determined by the pump lasers and cavity modes.

Example

Let us now consider a specific problem with 8 sites ($N = 8$) filled with 4 particles resulting in $\binom{8}{4} = 70$ possible states. We want to store two memory states

$$\begin{aligned}\boldsymbol{w}_1 &= (1,1,-1,-1,1,-1,1,-1)\\ \boldsymbol{w}_2 &= (1,1,-1,1,1,-1,-1,-1).\end{aligned}$$

Recalling the input patterns

$$\begin{aligned}\boldsymbol{\chi}_1 &= (1,1,1,-1,-1,-1,1,-1)\\ \boldsymbol{\chi}_2 &= (1,1,-1,1,-1,-1,-1,1)\end{aligned}$$

and choosing $\nu = 0.7$ amounts to specifying the interaction matrices A_{χ_1} and A_{χ_2} (see Appendix 6.A). The similarities between the states are summarized by $\boldsymbol{\chi}_i \cdot \boldsymbol{w}_j = 4\delta_{ij}$. Thus we can already anticipate the expected results: Upon recalling $\boldsymbol{\chi}_1$ ($\boldsymbol{\chi}_2$) the ground state of the system should converge to $\boldsymbol{w}_1$ ($\boldsymbol{w}_2$) for large ζ/J.

In the following we go through the steps for implementing such a problem in our system: Firstly, we search for a 'good' choice of modes and geometry for this system size. Secondly, we implement the stated problem, i.e. the interaction matrices for $\boldsymbol{\chi}_1$ and $\boldsymbol{\chi}_2$. Finally, we simulate the coherent annealing dynamics which should yield the solution to the problem.

A specific set-up.—We consider a cavity supporting several Hermite-Gaussian modes denoted by the longitudinal mode index n and the transverse mode indices l and m, which define the transverse cavity axes r_l and r_m. The external 1D optical lattice has a depth of $V_{\mathrm{L}} = 10E_{\mathrm{R}}$ and a spacing $d = 1.2\lambda_{n=100}/2$ and is located in the z-r_l-plane of the cavity (see Figure 6.1). The standing wave pump lasers are approximated by plane waves and are applied orthogonally to the lattice axis such that each has an anti-node at the lattice location and consequently $u_{p,m}(x) = 1$. Thus the form of the couplings between lattice and modes only depends on which cavity modes (indexed by n, l, m) are addressed and where the lattice is positioned, i.e. where the cavity mode functions are evaluated. The ratio of radius of curvature of the mirrors and cavity length is chosen as $R/L = 2/3$.

Finding the best suitable modes.—In order to invert Equation (6.7) one has to choose $N(N+1)/2 = 36$ linearly independent single-mode coupling matrices V_m forming a basis $\mathcal{B}$ of the matrix space. Due to the different spatial shape of the mode functions this is generally fulfilled for most mode choices in principle. However, if the V_m's are too similar, in practice an unrealistically high precision for the input laser parameters f_m is needed to reliably implement the most general interaction matrix. Therefore, to reduce the experimental restrictions on laser control, one should find a set of modes, which gives rise to a distinct set of single-mode coupling matrices. As a figure of merit one can use the determinant of the Gram matrix of the normalized V_m's (i.e. the squared volume spanned by those vectors), which should be maximized (orthogonal vectors would lead to the maximal value of 1). Additionally, we optimize over different lattice orientations (for more details see Appendix 6.B). Here we restrict ourselves to modes from the candidate set $n \in \{100, 199\}$, $l \in \{0, 1, 2\}$ and $m = 0$.

Let us emphasize that this step is only needed due to the finite precision available and crucially depends on the specific implementation. The modes do not have to be optimal, but only sufficiently ‘good’ for the given precision of the input parameters.

Input parameters.—Choosing the modes (and thus fixing $\mathcal{B}$) has to be done only once for a certain system size N. Afterwards any specific interaction matrix can be realized by changing the input parameters $f_m(A)$. We calculate these parameters from Equation (6.10) for A_{χ_1} and A_{χ_2} and subsequently round to one decimal place yielding $\tilde{f}_m^{\chi_i}$, mimicking some finite maximally possible experimental accuracy. The recovered interaction matrix $\tilde{A}_{\chi_i} = A(\tilde{f}_1^{\chi_i}, ..., \tilde{f}_M^{\chi_i})$ will then approximate A_{χ_i} depending on how well we select the modes and how accurately we impose the input parameters. The upper plot in Figure 6.2 shows the input parameters for $\tilde{A}_{\chi_1}$ and $\tilde{A}_{\chi_2}$, which can be realized by the pump strengths η_m shown in the lower plot, assuming the same $|\Delta_{c,m}|$ for each mode.

Adiabatic passage.—Let us now have a look at the adiabatic passage realized by a slow increase of ζ. The eigenvalue spectrum of the spin Hamiltonian H_{sp} for the interaction matrix $\tilde{A}_{\chi_1}$ is shown in Figure 6.3. With increasing ζ/J the ground state converges to $|\boldsymbol{w}_1\rangle$ since the inner product $\boldsymbol{\chi}_1 \cdot \boldsymbol{w}_1 = 4$ is larger than $\boldsymbol{\chi}_1 \cdot \boldsymbol{w}_2 = 0$. This can be already seen at $\zeta/J = 2$, where the overlap between ground state and target state is $|\langle\phi_0(\zeta = 2J)|\boldsymbol{w}_1\rangle|^2 = 0.976$. We observe that the minimum gap between ground and first excited state is $\delta_{\min} = 0.56J$ at $\zeta = 0.28J$. During a time evolution with increasing ζ this is the most likely region for Landau-Zener tunneling from ground state to excited states.

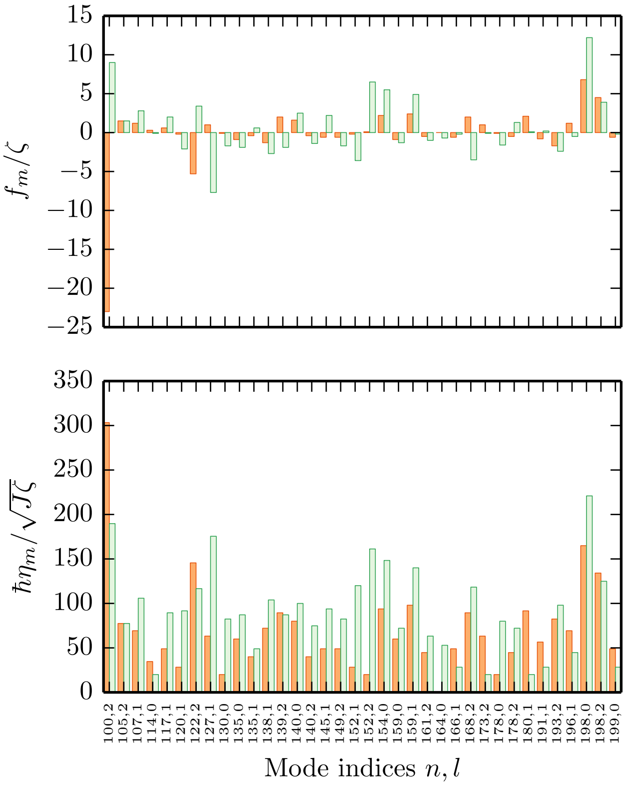

Figure 6.2.: **Top:** Input parameters for the two input states $\boldsymbol{\chi}_1$ (dark/orange) and $\boldsymbol{\chi}_2$ (light/green) given in the main text for a chosen set of modes $\mathcal{B}$, where the second transverse mode index $m = 0$. **Bottom:** These input parameters can be realized by the pump strengths $\eta_m = \sqrt{-f_m(\Delta_{c,m}^2 + \kappa_m^2)/(\hbar\Delta_{c,m})}$, where $\kappa_m = 1000J/\hbar$ and $\Delta_{c,m} = \mathrm{sgn}(-f_m)\kappa_m$. Due to weak coupling e.g. the first mode needs to be pumped strong in both cases.

The typical behavior of the time-dependent solution of the Schrödinger equation for a linear sweep and different annealing times τ is shown in Figure 6.4, where we see that for $J\tau \gtrsim 50$ the system stays close to the ground state in this specific example. Especially, the final overlap with the target state $\boldsymbol{w}_1$ for $J\tau = 50$ is $|\langle\psi(\tau)|\boldsymbol{w}_1\rangle|^2 = 0.959$. This can also be seen from the time evolution of the individual spins $\langle\sigma_i^z\rangle$ as depicted in Figure 6.5: From an initially unpolarized configuration, they evolve to a value close to 1 or -1 corresponding to $\boldsymbol{w}_1$. The annealing time $J\tau = 50$ translates to $\tau = 100\,\mathrm{ms}$ for $^{87}\mathrm{Rb}$ with $E_\mathrm{R}/\hbar \approx 24\,\mathrm{kHz}$ and $J \approx 0.02E_\mathrm{R}$, which is a realistic ramp time [6.15].

At the end of the ramp when we have prepared the final state, it can be directly determined in a non-destructive way by measuring the output intensities shown in Figure 6.6. This is a crucial advantage of our open system architecture compared close atomic lattice implementation, where site resolved atomic detection is required at the end.

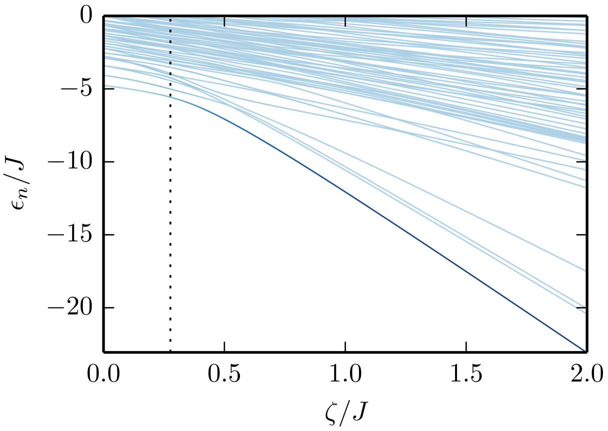

Figure 6.3.: Spectrum of the lowest few eigenvalues ϵ_n of H_{sp}, Equation (6.9), as function of ζ for a recall of the input pattern $\boldsymbol{\chi}_1$, leading to the recovered interaction matrix $\tilde{A}_{\chi_1}$. The dotted line at $\zeta/J = 0.28$ shows the position of the smallest gap between ground state and first excited state, while the brightness of the lines encodes the overlap of the target memory state with the eigenstates $|\langle\phi_n(\zeta)|\boldsymbol{w}_1\rangle|^2$ from light ($= 0$) to dark ($= 1$). Already at $\zeta/J = 2$, the ground state is very close to the target state: $|\langle\phi_0(\zeta = 2J)|\boldsymbol{w}_1\rangle|^2 = 0.976$.

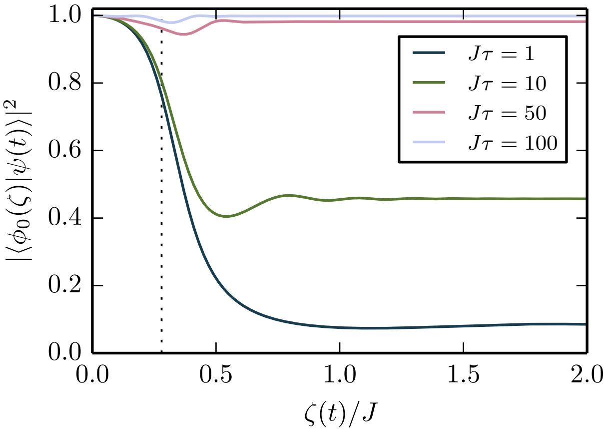

Figure 6.4.: Time evolution of the overlap between the instantaneous ground state $|\phi_0(\zeta)\rangle$ and the solution of the time-dependent Schrödinger equation $|\psi(t)\rangle$ for the linear ramp $\zeta(t) = 2Jt/\tau$ and different annealing times τ. The vertical dotted line shows the location of the smallest gap, as in Figure 6.3.

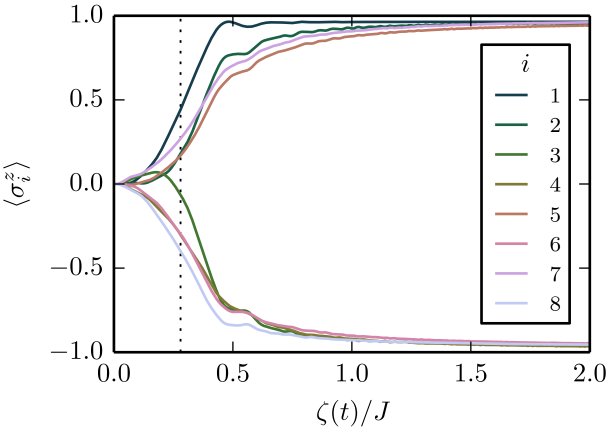

Figure 6.5.: Time evolution of the expectation values $\langle \sigma_i^z \rangle$ for each lattice site i for an annealing time of $J\tau = 50$ and a linear ramp $\zeta \propto t$ (see Figure 6.4). The overlap with the target state in the end is $|\langle \psi(\tau)|\boldsymbol{w}_1\rangle|^2 = 0.959$. Due to the finite annealing time there is a fraction in the excited states and thus the curves do not converge to 1 and -1 exactly.

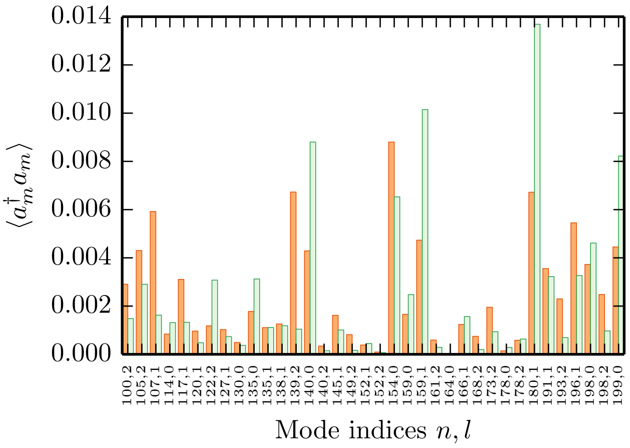

Figure 6.6.: Different atomic states give rise to distinct intensity patterns, which can be measured. Here they are shown for the states $\boldsymbol{w}_1$ (dark/orange) and $\boldsymbol{w}_2$ (light/green) at $\zeta/J = 2$. The parameters are as given in Figure 6.2.

6.6. Conclusions

We demonstrated how to obtain a coupled Ising spin model from a dilutely filled optical lattice within a multimode cavity with the help of transverse pump lasers. The interactions and local fields of the spins can be tuned by changing the power and detuning of the lasers allowing for real time control. This can be used to slowly ramp up the spin-spin interactions, implementing a quantum annealing dynamics. The final atomic state can be nearly non-destructively read out by measuring the cavity output fields.

Let us point out that the system studied here is technologically not far from current available experimental configurations as used at ETH [6.15] and Hamburg [6.8]. These need to be extended by adding extra laser frequencies, as provided by existing frequency comb and amplifier technology. As cavity and comb modes are equidistant, a single lock would be sufficient to bring all modes to resonance. While the general quadratic scaling of the number of lasers with the lattice sites number seems to be rather restrictive at first, the lasers are just a classical resource here. It also turns out that the required number of laser frequencies for a specific problem can be strongly reduced by applying the same laser from different angles.

In our example we found the desired state via adiabatic transfer. As said, for our open system, adiabatic transfer is not the only possibility as the ground state can also be reached via cavity side band cooling [6.33, 6.41] generalized to the multimode case. In this case the scan time can be reduced as errors are corrected by cooling at a later stage.

Acknowledgments

We thank W. Lechner, T. Donner, J. Leonard and G. De las Cuevas for helpful discussions. This work is supported by the Austrian Science Fund Project I1697-N27.

Appendix

6.A. Interaction matrices

Recalling the pattern $\boldsymbol{\chi}_1 = (1,1,1,-1,-1,-1,1,-1)$ and choosing $\nu = 0.7$ results in an interaction matrix $A_{\chi1}$ given by

$$A_{\chi1} = \begin{pmatrix} 1.7 & 1.0 & -1.0 & 0.0 & 1.0 & -1.0 & 0.0 & -1.0 \\ 1.0 & 1.7 & -1.0 & 0.0 & 1.0 & -1.0 & 0.0 & -1.0 \\ -1.0 & -1.0 & 1.7 & 0.0 & -1.0 & 1.0 & 0.0 & 1.0 \\ 0.0 & 0.0 & 0.0 & 0.3 & 0.0 & 0.0 & -1.0 & 0.0 \\ 1.0 & 1.0 & -1.0 & 0.0 & 0.3 & -1.0 & 0.0 & -1.0 \\ -1.0 & -1.0 & 1.0 & 0.0 & -1.0 & 0.3 & 0.0 & 1.0 \\ 0.0 & 0.0 & 0.0 & -1.0 & 0.0 & 0.0 & 1.7 & 0.0 \\ -1.0 & -1.0 & 1.0 & 0.0 & -1.0 & 1.0 & 0.0 & 0.3 \end{pmatrix}.$$

Using the above modes this matrix can be realized by the following laser input parameters

$$\begin{aligned} \tilde{\boldsymbol{f}}^{\chi1}/\zeta = (&- 23., 1.5, 1.2, 0.3, 0.6, -0.2, -5.3, 1., -0.1, \\ &- 0.9, -0.4, -1.3, 2., 1.6, -0.4, -0.6, -0.6, \\ &- 0.2, 0.1, 2.2, -0.9, 2.4, -0.5, 0., -0.6, 2., 1., \\ &- 0.1, -0.5, 2.1, -0.8, -1.7, 1.2, 6.8, 4.5, -0.6), \end{aligned}$$

which are already rounded to one position after the decimal point. We see that all parameters have similar magnitude, which is due to the proper choice of the modes. The recovered interaction matrix from the rounded input parameters $\tilde{A}_{\chi_1}$ is (rounded up to 2 positions after decimal point)

$$\tilde{A}_{\chi_1} = \begin{pmatrix} 1.72 & 1.01 & -1.01 & 0.02 & 0.99 & -1.00 & 0.00 & -0.97 \\ 1.01 & 1.67 & -0.91 & -0.02 & 0.99 & -0.99 & 0.00 & -1.01 \\ -1.01 & -0.91 & 1.66 & 0.03 & -1.00 & 0.98 & 0.01 & 1.01 \\ 0.02 & -0.02 & 0.03 & 0.27 & 0.05 & 0.03 & -1.00 & -0.00 \\ 0.99 & 0.99 & -1.00 & 0.05 & 0.33 & -0.97 & -0.03 & -1.00 \\ -1.00 & -0.99 & 0.98 & 0.03 & -0.97 & 0.29 & 0.01 & 0.96 \\ 0.00 & 0.00 & 0.01 & -1.00 & -0.03 & 0.01 & 1.70 & 0.02 \\ -0.97 & -1.01 & 1.01 & -0.00 & -1.00 & 0.96 & 0.02 & 0.30 \end{pmatrix}$$

which is similar to $A_{\chi1}$.

Recalling another pattern $\boldsymbol{\chi}_2 = (1,1,-1,1,-1,-1,-1,1)$ results in an interaction matrix which differs from A_{χ_1} only in the diagonal (since the memory is the same), i.e.

$$A_{\chi 2} = \begin{pmatrix} 1.7 & 1.0 & -1.0 & 0.0 & 1.0 & -1.0 & 0.0 & -1.0 \\ 1.0 & 1.7 & -1.0 & 0.0 & 1.0 & -1.0 & 0.0 & -1.0 \\ -1.0 & -1.0 & 0.3 & 0.0 & -1.0 & 1.0 & 0.0 & 1.0 \\ 0.0 & 0.0 & 0.0 & 1.7 & 0.0 & 0.0 & -1.0 & 0.0 \\ 1.0 & 1.0 & -1.0 & 0.0 & 0.3 & -1.0 & 0.0 & -1.0 \\ -1.0 & -1.0 & 1.0 & 0.0 & -1.0 & 0.3 & 0.0 & 1.0 \\ 0.0 & 0.0 & 0.0 & -1.0 & 0.0 & 0.0 & 0.3 & 0.0 \\ -1.0 & -1.0 & 1.0 & 0.0 & -1.0 & 1.0 & 0.0 & 1.7 \end{pmatrix}.$$

Analogously, it can be implemented by the rounded input parameters

$$\begin{aligned}\tilde{\boldsymbol{f}}^{\chi_2}/\zeta = (&9., 1.5, 2.8, -0.1, 2., -2.1, 3.4, -7.7, -1.7, -1.9,\\ &0.6, -2.7, -1.9, 2.5, -1.4, 2.2, -1.7, -3.6, 6.5,\\ &5.5, -1.3, 4.9, -1., -0.7, -0.2, -3.5, -0.1,\\ &-1.6, 1.3, 0.1, 0.2, -2.4, -0.5, 12.2, 3.9, -0.2).\end{aligned}$$

6.B. Selecting the modes

Here we explain how we select the modes for the set-up with 8 sites ($N = 8$) and 4 particles ($N_A = 4$) discussed in Section 6.5. As mentioned in the main text, in this specific example the single-mode coupling matrices V_m depend on the cavity modes only. Thus in order to find good modes we choose a candidate set of $K = 300$ Hermite-Gauss cavity modes with longitudinal mode indices $n \in \{100, 199\}$ and transverse mode indices $l \in \{0, 1, 2\}$ and $m = 0$. Now we aim to find a subset of $M = N(N + 1)/2 = 36$ modes which results in a large determinant of the Gram matrix created by the normalized V_m's for one specific lattice location (it does not have to be the optimum). Since the number of M-combinations out of the candidate set of size K is huge, $\binom{K}{M} \sim 10^{46}$, we cannot try out all, but have to use some algorithm which still scales polynomially. We use one possible choice which is given by:

(i) Compare all pairs of modes and choose the best ($K(K - 1)$ steps).

(ii) Subsequently add the best mode until ending up with M modes ($< MK$ steps).

(iii) Tentatively replace each selected mode by one mode of the remaining candidate set and take the best replacement, but only if the new Gram matrix determinant is larger. Repeat this for all selected modes ($M(K - M)$ steps).

In each step, the Gram matrix determinant has to be calculated. We repeat this procedure for different lattice locations and angles to the cavity axes. In addition to that, we post-select sets of modes where the norms $\sqrt{\langle V_m, V_m\rangle}$ are relatively uniform in order to guarantee uniform input parameters.

A resulting 'good' lattice location is given by the coordinates of the first lattice site $z^0 = -5d$, $r_l^0 = -2d$ and $r_m^0 = 0$ in a coordinate system with origin at the cavity center and has an angle $\phi = 47°$ with respect to the cavity z-axis (see Figure 6.7). The set

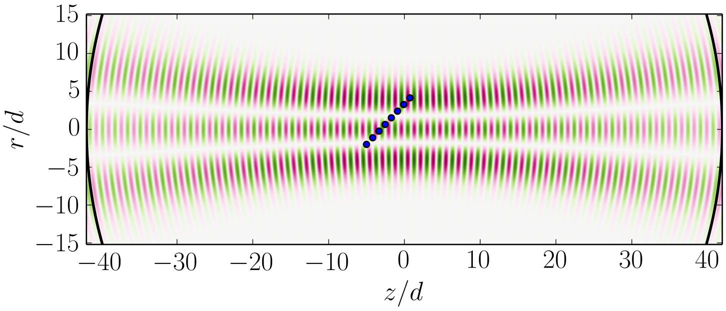

Figure 6.7.: The lattice location within the cavity used in the example in Section 6.5. The (blue) dots indicate positions of individual lattice sites. The depicted cavity mode is $(n, l) = (100, 2)$. The (black) arcs depict the cavity mirrors.

of selected modes for this lattice location, defining the basis $\mathcal{B}$, is given as mode index tuples (n, l)

$$\begin{aligned}\mathcal{B} = \{&(100,2),(105,2),(107,1),(114,0),(117,1),(120,1),\\ &(122,2),(127,1),(130,0),(135,0),(135,1),(138,1),\\ &(139,2),(140,0),(140,2),(145,1),(149,2),(152,1),\\ &(152,2),(154,0),(159,0),(159,1),(161,2),(164,0),\\ &(166,1),(168,2),(173,2),(178,0),(178,2),(180,1),\\ &(191,1),(193,2),(196,1),(198,0),(198,2),(199,0)\}.\end{aligned}$$

This configuration results in a Gram matrix determinant of 3.21×10^{-11}.

6.C. Adiabatic elimination of the cavity modes

The adiabatic elimination of the cavity modes has already been discussed in similar set-ups, see e.g. [6.23, 6.35, 6.40]. The Heisenberg-Langevin equation of the cavity field operators is

$$\dot{a}_m = \frac{1}{i\hbar}[a_m, H] = (i\delta_{c,m} - \kappa_m)a_m - i\eta_m \sum_i v_m^i \hat{n}_i + \hat{\xi}_m. \tag{6.16}$$

Including the coupling of the cavity modes with the vacuum field gives rise to field decay and an input noise operator $\hat{\xi}_m$ with $\langle \hat{\xi}(t) \rangle = 0$ and $\langle \hat{\xi}(t), \hat{\xi}(t') \rangle = 2\kappa_m \delta(t - t')$. Formal integration from t_0 to t leads to

$$a_m(t) = e^{(i\delta_{c,m}-\kappa_m)\Delta t} a_m(t_0) - i\eta_m \sum_i v_m^i \int_0^{\Delta t} \mathrm{d}s\, e^{(i\delta_{c,m}-\kappa_m)s} \hat{n}_i(t-s) + \hat{\Sigma}_m(t) \tag{6.17}$$

with the new noise operator

$$\hat{\Sigma}_m(t) = \int_0^{\Delta t} \mathrm{d}s\, e^{(i\delta_{c,m}-\kappa_m)s}\hat{\xi}_m(t-s). \tag{6.18}$$

The time step $\Delta t = t - t_0$ defines an intermediate time scale: One the one hand it is (i) much larger than the cavity time scale $\kappa_m^{-1} \ll \Delta t$, and on the other hand (ii) much smaller than the time scale of the atomic motion $\Delta t \ll (J/\hbar)^{-1}$.

Due to (i) we can neglect the first term in (6.17). Moreover, because of (ii) the atomic operator $\hat{n}_i$ does not vary much in the time Δt and can hence be approximated by $\hat{n}_i(t)$, which allows us to evaluate the integral. This approximation amounts to truncating an expansion in the small parameter $\dot{\hat{n}}_i/|\delta_{c,m} + i\kappa_m| \propto J/(\hbar|\delta_{c,m} + i\kappa_m|)$ at zeroth order. It yields

$$a_m(t) = \frac{\eta_m}{\delta_{c,m} + i\kappa_m}\sum_i v_m^i \hat{n}_i(t) + \hat{\Sigma}_m(t). \tag{6.19}$$

Within the limit (i), the noise operator has the properties $\langle\hat{\Sigma}_m(t)\rangle = 0$ and $\langle\hat{\Sigma}_m(t)\hat{\Sigma}_m^\dagger(t')\rangle = \frac{2\kappa_m}{\delta_{c,m}^2+\kappa_m^2}\delta(t-t')$ [6.40].

The interaction part of the Heisenberg equation of a the bosonic annihilation operator is

$$\dot{b}_i = -i\sum_m \eta_m(v_m^i a_m^\dagger b_i + (v_m^i)^* b_i a_m) + ..., \tag{6.20}$$

where a specific order of atomic and cavity operators was chosen and the dots stand for terms containing atomic operators only. The ordering freedom leads to ambiguities [6.35]. Plugging in (6.19) without the noise term yields

$$\begin{aligned}\dot{b}_i =& -i\sum_m \frac{\delta_{c,m}\eta_m^2}{\delta_{c,m}^2 + \kappa_m^2}(v_m^i (v_m^j)^* \hat{n}_j b_i + (v_m^i)^* v_m^j b_i \hat{n}_j) \\ &+ \sum_m \frac{\kappa_m \eta_m^2}{\delta_{c,m}^2 + \kappa_m^2}(v_m^i (v_m^j)^* \hat{n}_j b_i - (v_m^i)^* v_m^j b_i \hat{n}_j) + ...\end{aligned} \tag{6.21}$$

Using the identity $[b_i, \sum_{j,k} M_{jk}\hat{n}_j\hat{n}_k] = \sum_j (M_{ij}\hat{n}_j b_i + M_{ji} b_i \hat{n}_j)$ we realize that the first term can be obtained from $\dot{b}_i = 1/(i\hbar)[b_i, H_{\mathrm{ad}}^{\mathrm{int}}]$ with a purely atomic Hamiltonian

$$H_{\mathrm{ad}}^{\mathrm{int}} = \hbar\sum_{i,j}\sum_m \frac{\delta_{c,m}\eta_m^2}{\delta_{c,m}^2 + \kappa_m^2} v_m^i (v_m^j)^* \hat{n}_i\hat{n}_j = \hbar\sum_{i,j}\sum_m \frac{\delta_{c,m}\eta_m^2}{\delta_{c,m}^2 + \kappa_m^2}\mathrm{Re}(v_m^i (v_m^j)^*)\hat{n}_i\hat{n}_j, \tag{6.22}$$

where we used $[\hat{n}_i, \hat{n}_j] = 0$ in the second expression.

The incoherent dynamics coming from Lindblad terms $\mathcal{L}\rho = \sum_m (2C_m\rho C_m - C_m^2\rho - \rho C_m^2)$ with the Hermitian operators

$$C_m = \sqrt{2\kappa_m}\frac{\eta_m}{\sqrt{\delta_{c,m}^2 + \kappa_m^2}}\sum_i v_m^i \hat{n}_i \tag{6.23}$$

gives rise to the second term in (6.21) and the noise (which we did not explicitly consider). In the main text we neglect this incoherent contribution, which well describes the physics in current experiments [6.6, 6.15].

6.D. Detailed analysis of the associative memory Hamiltonian

We discuss the structure of the Hamiltonian H_{AM}, which is described in [6.34]. Since this Hamiltonian is diagonal in the occupation number basis (it only contains σ^z-operators), the analysis can be reduced to a classical energy function. The energy of an arbitrary state $\boldsymbol{s}$ evaluates to

$$E_{\mathrm{AM}}(\boldsymbol{s}) = \langle \boldsymbol{s}|H_{AM}|\boldsymbol{s}\rangle = -\frac{1}{2P}\sum_{q=1}^{P}\langle \boldsymbol{s}, \boldsymbol{w}_q\rangle^2 - \nu\langle \boldsymbol{s}, \boldsymbol{\chi}\rangle. \tag{6.24}$$

The goal is that the lowest energy state

(i) is a memory state and

(ii) has maximum similarity to the input pattern $\boldsymbol{\chi}$,

i.e. $\boldsymbol{w}_k = \max_p\langle \boldsymbol{w}_p, \boldsymbol{\chi}\rangle$ with $\boldsymbol{w}_p \in \mathcal{M}$. Formally we require

$$E_{\mathrm{AM}}(\boldsymbol{w}_k) < E_{\mathrm{AM}}(\boldsymbol{s}) \text{ for } \boldsymbol{s} \neq \boldsymbol{w}_k := \max_p\langle \boldsymbol{w}_p, \boldsymbol{\chi}\rangle. \tag{6.25}$$

While the first term in E_{AM} is responsible for requirement (i), the second term should come up for (ii).

6.D.1. Memory term

Let us now consider the first term ($\nu = 0$), which lowers the energy of memory states to

$$E_{\mathrm{AM}}(\boldsymbol{w}_p) = -\frac{1}{2P}\sum_{q=1}^{P}\langle \boldsymbol{w}_p, \boldsymbol{w}_q\rangle^2 = -\frac{N}{2} - \frac{1}{2P}\sum_{q\neq p}\langle \boldsymbol{w}_p, \boldsymbol{w}_q\rangle^2. \tag{6.26}$$

We observe that all memory states are degenerate, i.e. $E_{\mathrm{AM}}(\boldsymbol{w}_p)$ is independent of p, if the dot product of all memory pattern pairs is the same: $\langle \boldsymbol{w}_p, \boldsymbol{w}_q\rangle = a$ for all $p \neq q$ and $a \in \mathbb{Z}$. This is guaranteed e.g. for pairwise orthogonal memory states $\langle \boldsymbol{w}_p, \boldsymbol{w}_q\rangle = N\delta_{pq}$ (i.e. $a = 0$) and for $P = 2$ due to the commutativity of the dot product ($\langle \boldsymbol{w}_1, \boldsymbol{w}_2\rangle = \langle \boldsymbol{w}_2, \boldsymbol{w}_1\rangle$).

6.D.2. Recall term

The second term in (6.24) lowers the energy of states close to an input pattern $\boldsymbol{\chi}$. Now we clarify the bounds on the size of this term ν.

Lower bound.—If the memory states are degenerate an arbitrarily small $\nu > 0$ is sufficient to bias the memory state with maximum overlap to $\boldsymbol{\chi}$. In other words, the lower bound on the local field strength is zero, $\nu_{\min} = 0$, in case of degenerate memory states.

For non-degenerate memories in general we need a lower bound $\nu_{\min} > 0$ in order to get the right solution, since certain memory patterns will be preferred over others.

Upper bound.—Moreover, we have to make sure that the input pattern is not over-biased, i.e. that the input pattern itself does not become the ground state in order to meet requirement (i). That is

$$\min_p E_{\mathrm{AM}}(\boldsymbol{w}_p) < E_{\mathrm{AM}}(\boldsymbol{\chi}), \tag{6.27}$$

which leads to an upper bound for ν:

$$\nu < \max_p \frac{1}{2P(N - \langle \boldsymbol{\chi}, \boldsymbol{w}_p \rangle)} \sum_{q=1}^{P} \left(\langle \boldsymbol{w}_p, \boldsymbol{w}_q \rangle^2 - \langle \boldsymbol{\chi}, \boldsymbol{w}_q \rangle^2 \right). \tag{6.28}$$

However, there is a caveat: Calculating this bound amounts to evaluating all inner products $\langle \boldsymbol{\chi}, \boldsymbol{w}_q \rangle$, which solves the problem of finding the most similar memory state to $\boldsymbol{\chi}$ and thus renders the whole annealing procedure superfluous.

For the special case of degenerate memories however, one can simply choose the smallest possible $\nu > 0$ (depending on the available precision). This situation is depicted in Figure 6.8. Having non-degenerate memories, one could repeat for different values of ν. For large values of ν, the resulting ground state should be $\boldsymbol{\chi}$. Upon lowering ν we should arrive at a point where the ground state changes to some other state, which is the right memory state, assuming $\chi \notin \mathcal{M}$ and enough precision.

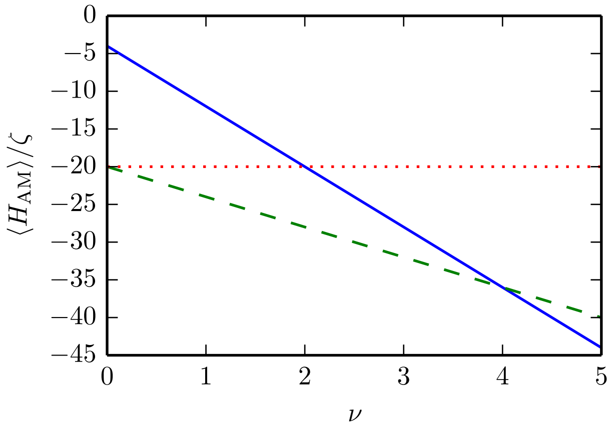

Figure 6.8.: The energies depending on the choice of ν when recalling $\boldsymbol{\chi}_1$. The recall bias $E_{\mathrm{AM}}(\boldsymbol{\chi}_1)$ (solid blue) has to be smaller than $E_{\mathrm{AM}}(\boldsymbol{w}_1)$ (dashed green), hence we need to choose $0 < \nu < 4$. $E_{\mathrm{AM}}(\boldsymbol{w}_2)$ (dotted red) is not affected by ν due to $\langle \boldsymbol{\chi}_1, \boldsymbol{w}_2 \rangle = 0$. Here $P = 2$ such that the memory patterns are degenerate.

7. Publication

Quantum **3**, 149 (2019)

A Quantum N-Queens Solver*

V. Torggler[1], P. Aumann[1], H. Ritsch[1], and W. Lechner[1,2]

[1] *Institute for Theoretical Physics, University of Innsbruck, Austria*
[2] *Institute for Quantum Optics and Quantum Information of the Austrian Academy of Sciences, A-6020 Innsbruck, Austria*

The N-queens problem is to find the position of N queens on an N by N chess board such that no queens attack each other. The excluded diagonals N-queens problem is a variation where queens cannot be placed on some predefined fields along diagonals. This variation is proven NP-complete and the parameter regime to generate hard instances that are intractable with current classical algorithms is known. We propose a special purpose quantum simulator that implements the excluded diagonals N-queens completion problem using atoms in an optical lattice and cavity-mediated long-range interactions. Our implementation has no overhead from the embedding allowing to directly probe for a possible quantum advantage in near term devices for optimization problems.

doi: 10.22331/q-2019-06-03-149

---

[*] The author of the present thesis did most numerical and analytical calculations and prepared the main part of the manuscript. P. A. did the parameter optimization. All authors discussed and checked the results.

7.1. Introduction

Quantum technology with its current rapid advances in number, quality and controllability of quantum bits (qubits) is approaching a new era with computational quantum advantage for numerical tasks in reach [7.1–7.11]. While building a universal gate-based quantum computer with error-correction is a long-term goal, the requirements on control and fidelity to perform algorithms with such a universal device that outperform their classical counterparts are still elusive. Building special purpose quantum computers with near-term technology and proving computational advantage compared to classical algorithms is thus a goal of the physics community world wide [7.12]. Quantum simulation with the aim to solve Hamiltonian systems may serve as a building block of such a special purpose quantum computer [7.13–7.15]. In particular, adiabatic quantum computing [7.16–7.18] has been proposed to solve computationally hard problems by finding the ground state of Ising spin glasses [7.19]. Despite considerable theoretical [7.18] and experimental [7.20] efforts, quantum speedup in adiabatic quantum computing has not been demonstrated in an experiment yet [7.21]. Thus, demonstrating quantum advantage by solving optimization problems using quantum simulation tools is a crucial step towards the development of general programmable quantum optimizers [7.22, 7.23].

Here we present a scheme that aims at solving the N-queens problem, and variations of it, using atoms with cavity-mediated long-range interactions [7.24–7.28]. We note that the N-queens problem is not just of mathematical interest but also has some applications in computer science [7.29]. In this work, variations of the problem are used as a testbed [7.30] to study a possible quantum advantage in solving classical combinatorial problems in near term quantum experiments.

Our proposed setup consists of N ultracold atoms in an optical lattice that represent the queens on the chess board [7.31]. The non-attacking conditions are enforced by a combination of restricted hopping [7.32] and interactions between the atoms stemming from collective scattering of pump laser light into a multi-mode cavity [7.33–7.40] (see Fig. 7.1). For the excluded diagonals variation of the N-queens problem, additional repulsive optical potentials are introduced. The solution of the problem (or the ground state of the many-body quantum system) is attained via a superfluid-to-solid transition. From the measurement of photons that leave the cavity [7.41] it can be determined if a state is a solution to the N-queens problem. The position of the atoms can in addition be read out with single site resolved measurement. The final solution is a classical configuration and thus easy to verify. We show that a full quantum description of the dynamics is required to find this solution.

Following Ref. [7.1], we identify a combination of several unique features of the proposed model that makes it a viable candidate to test quantum advantage in near term devices. (a) The completion and excluded diagonals problem is proven to be NP-complete and hard instances for the excluded diagonals variant are known from computer science literature [7.30], (b) the problem maps naturally to the available toolbox of atoms in cavities and thus can be implemented without intermediate embedding and no qubit overhead, (c) the verification is computationally simple and (d) the number of qubits required to solve problems which are hard for classical computers ($N > 21$ for the solvers

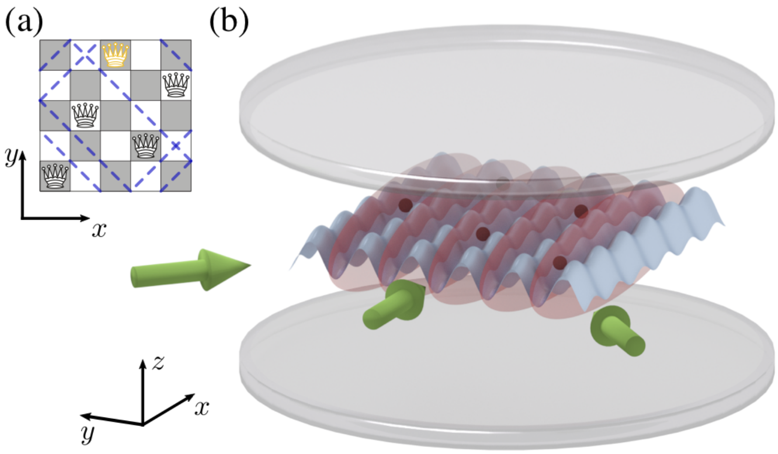

Figure 7.1.: *Sketch of the setup.* (a) The N-queens problem is to place N non-attacking queens on an N by N board. A variation thereof is the N-queens completion problem where some of the queens are already placed (yellow). In addition, some excluded diagonals are introduced (dashed blue lines) on which no queen can be placed. (b) Each queen is represented by an atom which is trapped in an anisotropic optical potential (blue) allowing for tunneling in x-direction only. Collective scattering of pump laser light (green arrows) into an optical resonator induces atom-atom interactions, preventing atoms from aligning along the y-axis and along the diagonals. After initial preparation in superposition states delocalized in x-direction (red tubes), increasing the interactions transfers the system into its solid phase, which is the solution of the queens problem (black balls).

used in Ref. [7.30]) is available in the lab.

Methods such as minor embedding [7.23, 7.42], LHZ [7.22, 7.43, 7.44] or nested embedding [7.45] always cause a qubit overhead. Here the intermediate step of embedding the optimization problem in an Ising model is removed by implementing the infinite-range interactions with cavity-mediated forces tailored to the problem's geometry in combination with constrained tunneling [7.32]. Hence there is no qubit overhead and the mode resources scale linearly with N. The required number of qubits is reduced from several hundreds to below 50, which is available in current experiments. By implementing our scheme with less than 50 atoms the problem is already hard to tackle with current classical algorithms [7.30].

Light-mediated coupled tunneling gives rise to non-local quantum fluctuations across the whole lattice in the intermediate stage of the transition [7.46, 7.47]. Their non-uniform signs stemming from the relative phases of the cavity fields from site to site indicate that the system's Hamiltonian is non-stoquastic and can thus not be efficiently simulated with path integral Monte Carlo methods on a classical computer [7.48]. The question of a quantum speed-up is thus open unless a local transformation to a stoquastic Hamiltonian is found [7.49, 7.50].

In our model implementation the non-local qubit interactions are mediated via the field modes of an optical resonator, which will attain non-classical atom-field superposition states during the parameter sweep. This appears to be an essential asset of the system as we find that the ground-state is reached only with a very low probability, when the full quantum dynamics of the fields is replaced by a classical mean-field approximation.

As a final feature let us point out here that the verification of a solution is computationally trivial as the final state is classical and no quantum tomography is needed. In principle the convergence to a solution can be simply deduced from the cavity outputs at the end of the sweep. With this, the proposed setup may serve as a platform to demonstrate combinatorial quantum advantage in near-term experiments.

This work is organized as follows: In Sec. 7.2 we introduce a quantum model based on coupled quantum harmonic oscillators simulating the N queens problem. A proposed physical implementation using ultracold atoms in optical lattices and light-mediated atom-atom interaction is described in Sec. 7.3. In Sec. 7.4 we present a numerical comparison between model and implementation including photon loss. Finally we discuss in Sec. 7.5 how light leaking out of the cavity can be used for read-out and we conclude in Sec. 7.6.

7.2. Quantum simulation of the N-queens problem

Following the idea of adiabatic quantum computation [7.16–7.18], we construct a classical problem Hamiltonian H_{pr} such that its ground state corresponds to the solutions of the N-queens problem. In order to find this ground state, the system is evolved with the time-dependent Hamiltonian

$$H(t) = H_{\text{kin}} + \frac{t}{\tau} H_{\text{pr}} \tag{7.1}$$

from $t = 0$ to $t = \tau$. Initially at $t = 0$, the system is prepared in the ground state of $H(0) = H_{\text{kin}}$. During the time evolution, the second term is slowly switched on. If this parameter sweep is slow enough, the system stays in the instantaneous ground state and finally assumes the ground state of $H(\tau)$ at $t = \tau$. If the lowest energy gap of H_{pr} is much larger than the one of H_{kin}, this state is close to the ground state of H_{pr} and thus the solution of the optimization problem.

In the following we construct the problem Hamiltonian H_{pr} and the driver Hamiltonian H_{kin}. The system is modeled as a 2D Bose-Hubbard model with annihilation (creation) operators b_{ij} ($b_{ij}^{\dagger}$) on the sites (i, j). A position of a queen is represented by the position of an atom in an optical lattice with the total number of atoms being fixed to N. The non-attacking condition between queens, which amounts to interactions between two sites (i, j) and (k, l), is implemented with four constraints: There can not be two queens on the same line along (i) the x-direction $j = l$, (ii) the y-direction $i = k$, the diagonals (iii) $i + j = k + l$ and (iv) $i - j = k - l$.

Condition (i) is implemented by using an initial state with one atom in each horizontal line at y_j and restricting the atomic movement to the x-direction [see Fig. 7.1(b)].

Thereby we use the a priori knowledge that a solution has one queen in a row, which reduces the accessible configuration space size from $\binom{N^2}{N}$ to N^N configurations. In this vein the restricted tunneling Hamiltonian [7.32] is given by

$$H_{\text{kin}} = -J \sum_{i,j=1}^{N} \hat{B}_{ij}, \tag{7.2}$$

where J is the tunneling amplitude and $\hat{B}_{ij} = b^\dagger_{i,j} b_{i+1,j} + b^\dagger_{i+1,j} b_{i,j}$ with $\hat{B}_{Nj} = 0$ are the tunneling operators.

Constraints (ii), (iii) and (iv) are enforced by infinite range interactions between the atoms with

$$H_{\text{Q}} = U_{\text{Q}} \sum_{ijkl=1}^{N} A_{ijkl}\ \hat{n}_{ij}\hat{n}_{kl}, \tag{7.3}$$

where $\hat{n}_{i,j} = b^\dagger_{i,j} b_{i,j}$ and $U_{\text{Q}} > 0$. The interaction matrix is

$$A_{ijkl} = \begin{cases} 3 & \text{if } (i,j) = (k,l) \\ 1 & \text{if } i = k \vee i + j = k + l \vee i - j = k - l \\ 0 & \text{otherwise,} \end{cases} \tag{7.4}$$

where in the first case all three constraints are broken.

In order to implement variations of the N-queens problem, we need to exclude diagonals (for the excluded diagonals problem) and pin certain queens (for the completion problem). These additional conditions are implemented by local energy offsets of the desired lattice sites

$$H_{\text{pot}} = U_{\text{D}} \sum_{i,j=1}^{N} D_{ij}\ \hat{n}_{ij} - U_{\text{T}} \sum_{i,j=1}^{N} T_{ij}\ \hat{n}_{ij}. \tag{7.5}$$

For $U_{\text{D}} > 0$ the first term renders occupations of sites on chosen diagonals energetically unfavorable. Each diagonal (in $+$ and $-$ direction) has an index summarized in the sets $\mathcal{D}_+$ and $\mathcal{D}_-$, respectively, and the coefficients are

$$D_{ij} = \begin{cases} 2 & \text{if } i + j - 1 \in \mathcal{D}_+ \wedge i - j + N \in \mathcal{D}_- \\ 1 & \text{if } i + j - 1 \in \mathcal{D}_+ \vee i - j + N \in \mathcal{D}_- \\ 0 & \text{otherwise.} \end{cases} \tag{7.6}$$

For $U_{\text{T}} > 0$, the second term favors occupations of certain sites. The sites where queens should be pinned to are pooled in the set $\mathcal{T}$ and therefore the coefficients are given by

$$T_{ij} = \begin{cases} 1 & \text{if } (i,j) \in \mathcal{T} \\ 0 & \text{otherwise.} \end{cases} \tag{7.7}$$

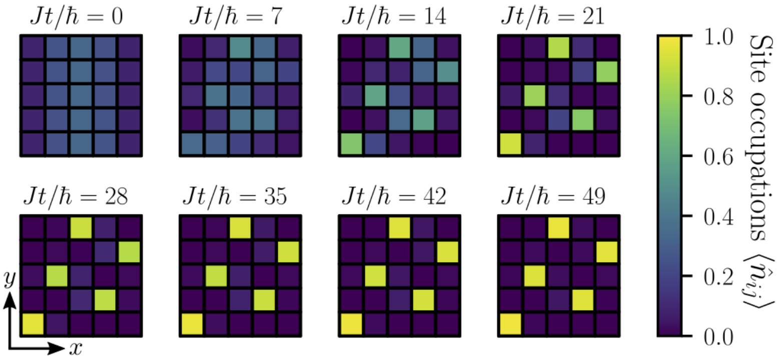

Figure 7.2.: *Time evolution of site occupations.* Each subplot shows a snapshot of the site occupations $\langle \hat{n}_{ij} \rangle$ for the parameter sweep in Eq. (7.1) and a sweep time $J\tau/\hbar = 49$. This is the instance shown in Fig. 7.1a, where the excluded diagonals are indexed by $\mathcal{D}_+ = \{2, 3, 6, 9\}$ and $\mathcal{D}_- = \{1, 2, 8, 9\}$ and one queen is pinned at site $(3, 5)$, i.e. $\mathcal{T} = \{(3, 5)\}$ (see text). The final values of the sweep are $U_\mathrm{Q} = J$, $U_\mathrm{D} = 5J$, $U_\mathrm{T} = 2J$ while J is kept constant. Since the sweep time is large enough, the state of the system adiabatically converges to the unique solution of the problem, which can be easily verified.

The problem Hamiltonian of the N-queens problem with excluded diagonals is then

$$H_\mathrm{pr} = H_\mathrm{Q} + H_\mathrm{pot}. \tag{7.8}$$

Note that due to the initial condition atoms never meet and sites are occupied by zero or one atom only. Hence the system can be effectively described by spin operators [7.31, 7.40], also without large contact interactions.

Let us illustrate the parameter sweep in Eq. (7.1) for a specific example instance with $N = 5$ queens (see Fig. 7.1). The excluded diagonals chosen here restrict the ground state manifold to two solutions, and by biasing site $(3, 5)$ one of these solutions is singled out. The time evolution of the site occupations $\langle \hat{n}_{ij} \rangle$ from numerically solving the time-dependent Schrödinger equation is shown in Fig. 7.2. Initially, the atoms are spread out in x-direction since the ground state of $H(0) = H_\mathrm{kin}$ is a superposition of excitations along each tube. After evolving for a sufficiently large time $J\tau/\hbar = 49$, the system is in the ground state of H_pr and thus assumed the solution of the optimization problem.

The energy spectrum of the given instance is shown in Fig. 7.3(a). The minimal gap between ground state (orange) and first excited state (green) determines the minimum sweep time τ to remain in the ground state according to the Landau-Zener formula. At the end of the sweep, the ground state closely resembles the solution to the excluded diagonals problem shown in Fig. 7.1.

The Hilbert space for the atomic state corresponding to the configuration space mentioned above grows exponentially as N^N and thus, as usual for quantum systems, the

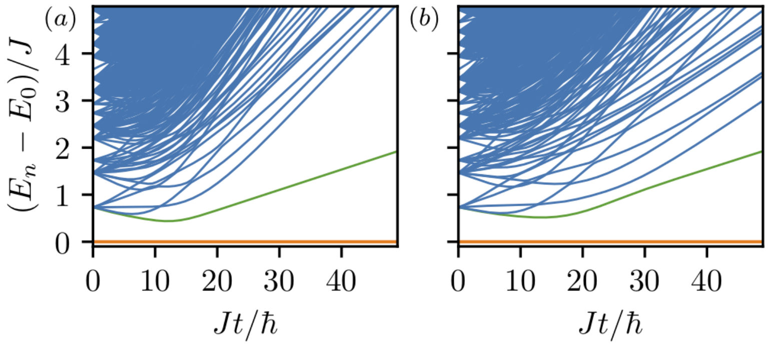

Figure 7.3.: *Energy spectrum.* Eigenvalue spectrum of $H(t)$ for (a) the model Hamiltonian [Eq. (7.1)] and (b) the Hamiltonian created by the field-atom interactions [Eq. (7.10)] for the instance described in Fig. 7.2. The orange and green lines show ground state and first excited state, respectively. The blue lines depict higher energy eigenstates. The low energy sector, and especially the minimal gap, are qualitatively similar.

computational costs get large for rather small systems. Simulations with significantly larger systems are hence not easily tractable.

7.3. Implementation

Here we propose a specific and at least conceptionally simple and straightforward physical implementation of Eq. (7.1), where the N queens are directly represented by N ultracold atoms in an NxN two-dimensional optical lattice. Assuming tight binding conditions the atoms are confined to the lowest band of the lattice. They can coherently tunnel between sites [7.51] and interact via collective light scattering within an optical resonator. To implement the required queens interactions via light scattering we make use of a set of optical field modes in a multi-mode standing-wave resonator [see Fig. 7.1(b)]. It was shown before that this configuration in principle allows to implement arbitrary site to site interactions [7.40] if a sufficient number of modes is used.

To reduce the necessary Hilbert space without loss of generality, it is sufficient to enable tunneling only along one dimension (x), e.g. the rows of the lattice and increase the lattice depth in the column (y) direction. This confines the atoms (queens) to move only along tubes in the x-direction forming a parallel array of N 1D optical lattices as routinely used to study 1D physics with cold atoms [7.52].

Luckily, for the special case of the infinite range queens interactions, one can find a strikingly simple and intuitive example configuration requiring only few field modes for each of the three remaining queens interaction directions. For this we consider the optical lattice to be placed in the center symmetry plane of the optical resonator, where one has a common anti-node of all symmetric eigenmodes. The trapped atoms are then illuminated by running plane wave laser beams from three different directions within the lattice plane with frequencies matched to different longitudinal cavity modes.

Depending on the size of the problem we need to add more laser frequencies in each direction to avoid a periodic recurrence of the interaction within the lattice. Note that all frequencies can be easily derived and simultaneously stabilized from a single frequency comb with a spacing matched to the cavity length. Since all light frequencies are well separated compared to the cavity line width, each is scattered into a distinct cavity mode and as the cavity modes are not directly coupled no relative phase stability is needed [7.40]. The resulting position-dependent collective scattering into the cavity then introduces the desired infinite-range interactions between the atoms. Choosing certain frequencies and varying their relative pump strengths allows for tailoring these interactions to simulate the three non-attacking conditions in the queens problem discussed in the previous section. Additional light sheets and local optical tweezers can be used to make certain diagonals energetically unfavorable (for the excluded diagonal problem) or pin certain queens. Alternatively pinning can be achieved by selective cavity mode injection.

In the first part (Sec. 7.3.1) we will now introduce a Bose-Hubbard-type Hamiltonian for the trapped atoms interacting via collective scattering for general illumination fields in more detail. For this we first consider the full system of coupled atoms and cavity modes and later adiabatically eliminate the cavity fields to obtain effective light-mediated atom-atom interactions.

In the second part (Sec. 7.3.2) we discuss how to implement the non-attacking conditions of the N-queens problem with such light-mediated atom-atom interactions. Specifically, we consider the limit of a deep optical lattice leading to simple analytical expressions. These formulas allow us to find a specific pump configuration of wave numbers and pump strengths leading to the ideal queens interaction Hamiltonian in Eq. (7.3). As a deep lattice depth slows down atomic tunneling it requires long annealing times. Luckily, it turns out that the pump configuration derived for a deep lattice still gives the same ground state for moderate lattice depth with faster tunneling. We show this by numerical simulations in Sec. 7.4. While the details of the interaction are altered it still sufficiently well approximates the N-queens interaction.

7.3.1. Tight-binding model for atoms interacting via light

Driving far from any atomic resonance the internal degrees of freedom of the atoms can be eliminated. In this so-called dispersive limit the resulting effective Hamiltonian couples the atomic motion to the light fields [7.53].

Single-particle Hamiltonian. For a single particle of mass m_A, the motion of the atoms in the x-y-plane is described by [7.25, 7.54]

$$\begin{aligned} H_1 =& \frac{\hat{p}_x^2 + \hat{p}_y^2}{2m_A} + V_\mathrm{L}^x \cos^2(k_\mathrm{L}\hat{x}) + V_\mathrm{L}^y \cos^2(k_\mathrm{L}\hat{y}) + V_\mathrm{bias}|\mathcal{F}(\hat{x},\hat{y})|^2 \\ &- \hbar \sum_{m=1}^{M_\mathrm{tot}} \tilde{\Delta}_{c,m} a_m^\dagger a_m + \hbar \sum_{m=1}^{M_\mathrm{tot}} \eta_m \left(h_m^*(\hat{x},\hat{y}) a_m + a_m^\dagger h_m(\hat{x},\hat{y}) \right). \end{aligned} \tag{7.9}$$

The first line contains the kinetic term with the momentum operators $\hat{p}_x$ and $\hat{p}_y$. Classical electric fields create optical potentials with depths V_{L}^{x}, V_{L}^{y} and V_{bias}. The first two create the optical lattice with wave number k_{L} and lattice spacing $a = \pi/k_{\mathrm{L}}$, while V_{bias} is much smaller and only responsible for a bias field on certain sites, for instance for excluding diagonals. Thereby $\mathcal{F}(x, y)$ is an electric field distribution whose maximum is normalized to one.

The last two terms describe the free evolution of the cavity fields and atom-state-dependent scattering of the pump fields into the cavity, the atom-light interaction. The quantized electric cavity fields are described by a_m ($a_m^{\dagger}$), the annihilation (creation) operators of a photon in the m-th mode. These fields are coupled to the classical pump fields with mode functions $h_m(x, y)$ via the effective scattering amplitudes $\eta_m = g_m \Omega_m/\Delta_{a,m}$, with the pump laser Rabi frequencies Ω_m, the atom-cavity couplings g_m and the detunings between pump lasers and atomic resonance frequency $\Delta_{a,m}$. The effective cavity detunings $\tilde{\Delta}_{c,m} = \Delta_{c,m} - NU_{0,m}$ are given by the detunings between pump laser and cavity mode frequencies $\Delta_{c,m}$ and the dispersive shifts of the cavity resonance due to the presence of the atoms in the cavity $NU_{0,m}$ [7.24].

Note that, for example by placing the optical lattice (x-y-plane) in a common anti-node of the standing wave cavity modes and exciting only TEM_{00} modes, the atom-cavity coupling is uniform in space in our model. Thus the only spatial dependence in the cavity term is due to the pump fields.

Generalized Bose-Hubbard Hamiltonian. The atom-atom interactions are taken into account by introducing bosonic field operators $\hat{\Psi}(\boldsymbol{x})$ with $\tilde{H} = \int \mathrm{d}^2x \hat{\Psi}^{\dagger}(\boldsymbol{x}) H_1 \Psi(\boldsymbol{x})$ [7.25, 7.55]. Note that we do not include contact interactions since atoms never meet due to the initial condition we will use. We assume that the optical lattice with depths V_{L}^{x} and V_{L}^{y} is so deep, that the atoms are tightly bound at the potential minima and only the lowest vibrational state (Bloch band) is occupied. Moreover, the optical potential created by bias and cavity fields is comparably small, such that the form of the Bloch wave functions only depends on the optical lattice [7.54]. In this limit we can expand the bosonic field operators in a localized Wannier basis $\hat{\Psi}(\boldsymbol{x}) = \sum_{i,j} w_{2D}(\boldsymbol{x} - \boldsymbol{x}_{ij}) b_{ij}$ with the lowest-band Wannier functions $w_{2D}(\boldsymbol{x})$ coming from Bloch wave functions of the lattice [7.56]. We split the resulting Hamiltonian in three terms

$$\tilde{H} = H_{\mathrm{kin}} + H_{\mathrm{cav}} + H_{\mathrm{pot}}, \tag{7.10}$$

which will be explained in the following.

As in the standard Bose-Hubbard model, one obtains a tunneling term H_{kin} as in Eq. (7.2). Tunneling in y-direction is frozen out by ensuring $V_{\mathrm{L}}^{y} \gg V_{\mathrm{L}}^{x}$. The other terms H_{cav} and H_{pot} originate from the weak cavity-pump interference fields and the bias fields introduced above and should resemble H_{pr} [Eq. (7.8)]. In order to realize the sweep Eq. (7.1), the relative strength of these terms and the kinetic term has to be tuned, e.g. by ramping up the pump laser and bias field intensity (make H_{cav} and H_{pot} larger) or the lattice depth (make H_{kin} smaller).

The cavity-related terms in Eq. (7.9) give rise to

$$H_{\mathrm{cav}} = -\hbar \sum_m \tilde{\Delta}_{c,m} a_m^{\dagger} a_m + \hbar \sum_m N \eta_m \left(\hat{\Theta}_m^{\dagger} a_m + a_m^{\dagger} \hat{\Theta}_m \right) \tag{7.11}$$

with the order operator of cavity mode m

$$\hat{\Theta}_m = \frac{1}{N} \sum_{i,j=1}^{N} \left(v_m^{ij} \hat{n}_{ij} + u_m^{ij} \hat{B}_{ij} \right). \tag{7.12}$$

The structure of the fields enters in the on-site and nearest neighbor atom-mode overlaps

$$v_m^{ij} = \int dx\, w^2(x - x_i) h_m(x, y_j) \tag{7.13}$$

$$u_m^{ij} = \int dx\, w(x - x_i) h_m(x, y_j) w(x - x_{i+1}) \tag{7.14}$$

where $y_j = ja$ with $j = 0, ..., N-1$ are the tube positions and $w(x)$ the one-dimensional Wannier functions in x-direction. This is because for $V_\mathrm{L}^y \gg V_\mathrm{L}^x$ we can approximate the y-dependence of the Wannier functions by a Dirac delta: $w_{2D}(\boldsymbol{x}) = w(x)\delta(y)$.

The last term H_pot describes all extra fields responsible for local energy off-sets at certain sites that stem from the weak classical fields with the distribution $\mathcal{F}(x, y)$ ($V_\mathrm{bias} \ll V_\mathrm{L}^x$). The off-sets ought to be calculated from the overlaps of fields and Wannier functions, analogously to v_m^{ij}. Thus the fields have to be chosen such that the resulting Hamiltonian resembles Eq. (7.5). We do not detail the derivation further here and use H_pot for numerical simulations.

Atom-atom interaction Hamiltonian. The main focus of this work is to show how to create the tailored all-to-all particle interactions via collective scattering. We derive this interaction by eliminating the cavity fields introduced in the previous section [7.54, 7.57, 7.58]. This can be done because the cavity fields decay through the mirrors with the rates κ_m and thus end up in a particular steady-state for each atomic configuration. Assuming that the atomic motion is much slower than the cavity field dynamics, i.e. $J/\hbar \ll |\tilde{\Delta}_{c,m} + i\kappa_m|$, this steady-state is a good approximation at all times. The stationary cavity field amplitudes are given by

$$a_m^\mathrm{st} \equiv \frac{\eta_m}{\tilde{\Delta}_{c,m} + i\kappa_m} N \hat{\Theta}_m \tag{7.15}$$

and thus replaced by atomic operators (see Appendix 7.B).

In the coherent regime $|\tilde{\Delta}_{c,m}| \gg \kappa_m$, the atom-light interaction is then described by an effective interaction Hamiltonian for the atoms [7.28]

$$H_\mathrm{cav}^\mathrm{eff} = \hbar \sum_m \frac{\tilde{\Delta}_{c,m} \eta_m^2}{\tilde{\Delta}_{c,m}^2 + \kappa_m^2} N^2 \hat{\Theta}_m^\dagger \hat{\Theta}_m. \tag{7.16}$$

The collective, state-dependent scattering induces interactions between each pair of sites (i, j) and (k, l): Density-density interactions due to the terms containing $\hat{n}_{ij}\hat{n}_{kl}$ and a modified tunneling amplitude due an occupation or a tunneling event somewhere else in the lattice due to $\hat{n}_{ij}\hat{B}_{kl}$, $\hat{B}_{ij}\hat{n}_{kl}$ and $\hat{B}_{ij}\hat{B}_{kl}$. While the density-density interactions constitute the problem Hamiltonian [see Eq. (7.3)], the latter cavity-induced tunneling terms lead to non-local fluctuations which might help to speed up the annealing process [7.46].

Since the Wannier functions are localized at the lattice sites, the on-site overlaps v_m^{ij} tend to be much larger than the nearest-neighbor overlaps u_m^{ij}. Thus density-density interactions are expected to be the dominant contribution to $H_{\text{cav}}^{\text{eff}}$. As intuitively expected, the atoms localize stronger for deeper lattices, where analytical expressions for the overlaps can be obtained within a harmonic approximation of the potential wells leading to Gaussian Wannier functions with a width $\propto (V_{\text{L}}^{x})^{-1/4}$. Apart from a correction factor due to this width, the on-site overlaps are given by the pump fields at the lattice sites. The nearest-neighbor overlaps correspond to the pump fields in between the lattice sites, but are exponentially suppressed (see Appendix 7.C). Consequently, in the deep lattice limit (large V_{L}^{x}) when the width tends to zero we get $v_m^{ij} = h_m(x_i, y_j)$ and $u_m^{ij} = 0$ [7.28], and an interaction Hamiltonian [from Eq. (7.16)]

$$H_{\text{cav}}^{\text{dl}} = \hbar \sum_m \frac{\tilde{\Delta}_{c,m}\eta_m^2}{\tilde{\Delta}_{c,m}^2 + \kappa_m^2} \sum_{ijkl} h_m^*(x_i, y_j) h_m(x_k, y_l) \hat{n}_{ij} \hat{n}_{kl}, \tag{7.17}$$

which only depends on density operators, and hence does not include cavity induced-tunneling.

7.3.2. N-queens interaction

In this section we aim to find pump fields $h_m(x, y)$ such that the interaction Hamiltonian in the deep lattice limit Eq. (7.17) corresponds to the desired queens Hamiltonian H_{Q} [Eq. (7.3)] containing the non-attacking conditions. Using these pump fields we later show numerically in Sec. 7.4, that the atom-atom interaction for realistic lattice depths [Eq. (7.16)], although slightly altered, still well resembles the queens interaction.

We consider three sets of M parallel running wave laser beams with different propagation directions, each of which could be created by a frequency comb. The three directions are perpendicular to the lines along which queens should not align, that is along the x-direction and along the diagonals. We denote the corresponding wave vectors with $\boldsymbol{k}_m^x = (k_m^0, 0)^T$, $\boldsymbol{k}_m^+ = (k_m^0, k_m^0)^T$ and $\boldsymbol{k}_m^- = (k_m^0, -k_m^0)^T$, respectively, with the wave numbers k_m^0. Therefore the pump fields are given by

$$h_m(x, y) = e^{i\boldsymbol{k}_m \boldsymbol{x}}, \tag{7.18}$$

where $\boldsymbol{x} = (x, y)^T$ is the position vector and $\boldsymbol{k}_m$ is a wave vector in any of the three directions.

With running wave pump fields, Eq. (7.17) can be written as

$$H_{\text{cav}}^{\text{dl}} = U_{\text{Q}} \sum_{ijkl} \tilde{A}_{ijkl} \hat{n}_{ij} \hat{n}_{kl}. \tag{7.19}$$

This formally corresponds to H_{Q} [Eq. (7.3)], where the quantities now have a physical meaning: The interaction matrix is given by

$$\tilde{A}_{ijkl} = \sum_m f_m \cos(\boldsymbol{k}_m(\boldsymbol{x}_{ij} - \boldsymbol{x}_{kl})) \tag{7.20}$$

with lattice site connection vectors $\boldsymbol{x}_{ij} - \boldsymbol{x}_{kl}$ and

$$f_m U_\mathrm{Q} = \hbar \frac{\tilde{\Delta}_{c,m} \eta_m^2}{\tilde{\Delta}_{c,m}^2 + \kappa_m^2} \tag{7.21}$$

with $\sum_{m=0}^{M-1} f_m = 1$. The dimensionless parameters f_m capture the relative strengths of the modes, determining the shape of the interaction. They have to be chosen such that $\tilde{A}$ approximates A [Eq. (7.4)]. The overall strength of the interaction term is captured by the energy U_Q, which can be easily tuned by the cavity detunings or the pump intensities to implement the parameter sweep in Eq. (7.1). For the following discussion we define an interaction function

$$\tilde{\mathcal{A}}(\boldsymbol{r}) = \sum_m f_m \cos(\boldsymbol{k}_m \boldsymbol{r}) \tag{7.22}$$

which returns the interaction matrix when evaluated at lattice site connection vectors $\tilde{A}_{ijkl} = \tilde{\mathcal{A}}(\boldsymbol{x}_{ij} - \boldsymbol{x}_{kl})$.

We note that one set of parallel $\boldsymbol{k}_m^\mu$ ($\mu \in \{x, +, -\}$) creates an interaction $\tilde{\mathcal{A}}$ which is constant and infinite range (only limited by the laser beam waist) in the direction perpendicular to the propagation direction $\boldsymbol{r} \perp \boldsymbol{k}_m^\mu$. Along the propagation direction $\boldsymbol{r} \parallel \boldsymbol{k}_m^\mu$ instead, the interaction is shaped according to the sum of cosines, and can be modified by the choice of wave numbers $k_m^\mu = |\boldsymbol{k}_m^\mu|$ and their relative strengths f_m.

In the following we will use the example wave numbers

$$k_m^0 = k_\mathrm{L} \left(1 + \frac{2m+1}{2M}\right) \tag{7.23}$$

with $m = 0, ..., M-1$ and uniform $f_m = 1/M$. Taking into account $\boldsymbol{k}_m^x$ only, the interaction along the x-direction $\boldsymbol{r} \parallel \boldsymbol{k}_m^x$ at lattice site distances $r_j = j\pi/k_\mathrm{L} = ja$ has the values

$$\tilde{\mathcal{A}}(r_j) = \begin{cases} (-1)^l & \text{for } j = 2Ml,\ l \in \mathbb{Z} \\ 0 & \text{otherwise,} \end{cases} \tag{7.24}$$

as shown in Appendix 7.D. If we guarantee that $-2M < j < 2M$ this results in an interaction which is zero everywhere apart from $j = 0$, i.e. at zero distance. So for repulsive interactions ($U_\mathrm{Q} > 0$ and thus $\tilde{\Delta}_{c,m} > 0$), the wave vectors $\boldsymbol{k}_m^x$ create the non-attacking interaction along the y-direction ($\tilde{A}_{ijkl} = 1$ if $i = k$ and 0 otherwise) as long as $N \leq 2M$. This is illustrated in Fig. 7.4(a) for $M = N = 5$. Analogously, $\boldsymbol{k}_m^\pm$ cause the non-attacking interactions along the diagonals. In a square lattice the diagonals have the distance $r_j/\sqrt{2}$, which is compensated by $k_m^\pm = |\boldsymbol{k}_m^\pm| = \sqrt{2} k_m^0$. Since there are $2N - 1$ diagonals, one has to make sure that $2N - 1 \leq 2M$. Upon combining all wave vectors from three directions we finally obtain the full queens interaction, as shown in Fig. 7.4(b), which is realized with $M_\mathrm{tot} = 3M = 3N$ frequencies in our example.

Note that there are several combinations of wave numbers and mode strengths which, at least approximately, create the desired line-shaped interactions perpendicular to the light propagation direction. For this it is insightful to reformulate the interaction as a Fourier transform. To deal with continuous functions, we define an envelope $f(k)$ with

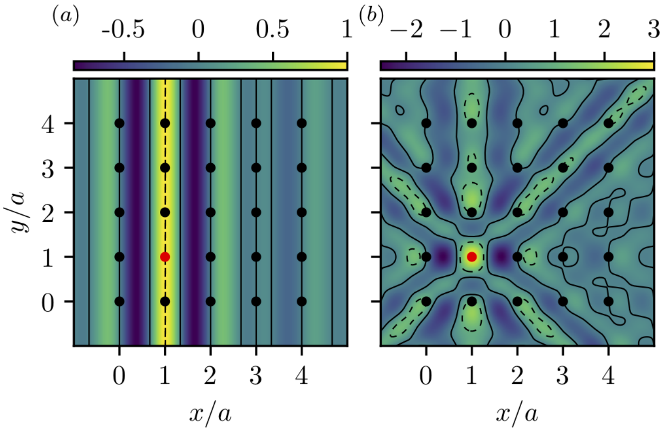

Figure 7.4.: *Energy penalty created by one atom.* These density plots show the energy penalty $\tilde{\mathcal{A}}(\boldsymbol{x}-\boldsymbol{x}_a)$ for an atom at position $\boldsymbol{x}=(x,y)^T$ created by an atom at position $\boldsymbol{x}_a=(a,a)^T$ (red dot) for $N=M=5$ [see Eq. (7.22)]. The dots indicate lattice site positions and the solid (dashed) contour lines indicate where $\tilde{\mathcal{A}}(\boldsymbol{x}-\boldsymbol{x}_a)=0$ ($\tilde{\mathcal{A}}(\boldsymbol{x}-\boldsymbol{x}_a)=1$) is fulfilled. (a) Pumping along the x-axis with the wave vectors $\boldsymbol{k}_m^x=(k_m^0,0)^T$ with $k_m^0/k_\mathrm{L}=1.1,1.3,1.5,1.7,1.9$ [according to Eq. (7.23)] creates interactions along y. (b) Additionally including diagonal pump lasers $\boldsymbol{k}_m^+=(k_m^0,k_m^0)^T$ and $\boldsymbol{k}_m^-=(k_m^0,-k_m^0)^T$ implements the full queens interaction along diagonals and vertical lines [Eq. (7.3)].

$f(k_m)=f_m$, which is sampled at the wave numbers $n\Delta k$ with $n\in\mathbb{Z}$ containing all k_m^μ. Considering one illumination direction for simplicity, the interaction [Eq. (7.22)] along $\boldsymbol{r}\parallel\boldsymbol{k}_m^\mu$ with $r=|\boldsymbol{r}|$ can be written as

$$\begin{aligned}\tilde{\mathcal{A}}(r)&=\mathrm{Re}\left[\sqrt{2\pi}\mathcal{F}\left\{f(k)\sum_{n=-\infty}^{\infty}\delta(k-n\Delta k)\right\}(r)\right]\\&=\sum_{l=-\infty}^{\infty}\mathrm{Re}\left[\sqrt{2\pi}\mathcal{F}\{f\}\left(r-l\frac{2\pi}{\Delta k}\right)\right],\end{aligned}\tag{7.25}$$

where $\mathcal{F}\{f\}(r)=\int_{-\infty}^{\infty}\mathrm{d}k f(k)e^{ikr}/\sqrt{2\pi}$ is the Fourier transform of $f(k)$ and $\delta(x)$ is a Dirac delta at $x=0$. See Appendix 7.D for a detailed derivation.

The last line allows for a simple interpretation: The interaction consists of peaks repeating with a spatial period $R=2\pi/\Delta k$. Each of these peaks has the shape of the real part of the Fourier transform of the envelope function $f(k)$ with a width corresponding to the inverse of the mode bandwidth $\sigma\sim 2\pi/\Delta k_\mathrm{BW}$.

For the (approximate) non-attacking condition ($\tilde{\mathcal{A}}(ja)\approx 1$ for $j=0$ and $|\tilde{\mathcal{A}}(ja)|\ll 1$ otherwise) there are two conditions. Firstly, at most one peak should be within the region of the atoms. Thus the period has to be larger than the (diagonal) size of the optical lattice $R\geq Na$ ($R\geq\sqrt{2}Na$). Secondly, the width of one peak has to be smaller than the lattice spacing $\sigma \lesssim a$. Combining these conditions to $R \gtrsim N\sigma$, we see that the minimum number of modes per direction M scales linearly with N

$$M \approx \Delta k_{\mathrm{BW}}/\Delta k \gtrsim N. \tag{7.26}$$

Therefore, with only $\sim N$ modes this quite generically allows for creating an interaction along lines perpendicular to the light propagation. Note however, that the second condition also implies that the spatial frequency spread has to be at least on the order of the lattice wave number $\Delta k_{\mathrm{BW}} \gtrsim k_{\mathrm{L}}$.

7.4. Numerical justification of assumptions

We compare the ideal model Hamiltonian described in Sec. 7.2 [Eq. (7.1)] to the physically motivated tight-binding Hamiltonian for finite lattice depths introduced in Sec. 7.3 [Eq. (7.10)]. As for the ideal model in Fig. 7.2, we consider the time evolution during a slow linear sweep of U_{Q}, U_{T} and U_{D} by numerically integrating the time-dependent Schrödinger equation. Physically, this sweep can be realized by ramping up the pump and the bias field intensities. Moreover, we show that evolving the system using a classical approximation for the cavity mode fields does not result in a solution to the N-queens problem, and address the effect of dephasing by photon loss with open system simulations.

In the following we use a realistic lattice depth of $V_{\mathrm{L}}^{x} = 10E_{\mathrm{R}}$ with the recoil energy $E_{\mathrm{R}} = \hbar^2 k_{\mathrm{L}}^2/(2m_{\mathrm{A}})$. For example, for rubidium ^{87}Rb and $\lambda_{\mathrm{L}} = 785.3\,\mathrm{nm}$ it is $E_{\mathrm{R}}/\hbar = 23.4\,\mathrm{kHz}$ [7.26]. The chosen lattice depth leads to a tunneling amplitude $J \approx 0.02E_{\mathrm{R}}$, which can be obtained from the band structure of the lattice. We consider our cavity model in Eq. (7.10) for $N = 5$. The pump modes are as in Sec. 7.3.2 and Fig. 7.4. While in the limit of a deep lattice this would result in the ideal model interactions, here they depend on the overlaps between Wannier functions and pump modes [Eq. (7.13)] and are thus altered. In the following the overlaps are calculated with Wannier functions which where numerically obtained from the band structure of the lattice. It turns out, that the deviation from the ideal overlaps does not qualitatively change the interaction for the realistic parameters used.

7.4.1. Coherent dynamics

The energy spectrum of the Hamiltonian for finite lattice depths in Eq. (7.16) is shown in Fig. 7.3(b) and is qualitatively of the same form as for the ideal model in Fig. 7.3(a). In comparison the eigenvalue gaps tend to be smaller at the end of the sweep. This is because the on-site atom-mode overlaps decrease for shallower lattices and less localized atoms due to a smoothing of the mode functions by the finite width Wannier functions (see Appendix 7.C). Moreover, we consider the time evolution during the nearly adiabatic sweep for $J\tau/\hbar = 49$ for the same parameters by integrating the time-dependent Schrödinger equation. Snapshots of the site occupations $\langle \hat{n}_{ij} \rangle$ for several times are shown in Fig. 7.5(a), where we observe a similar behavior as for the model in Fig. 7.2. This

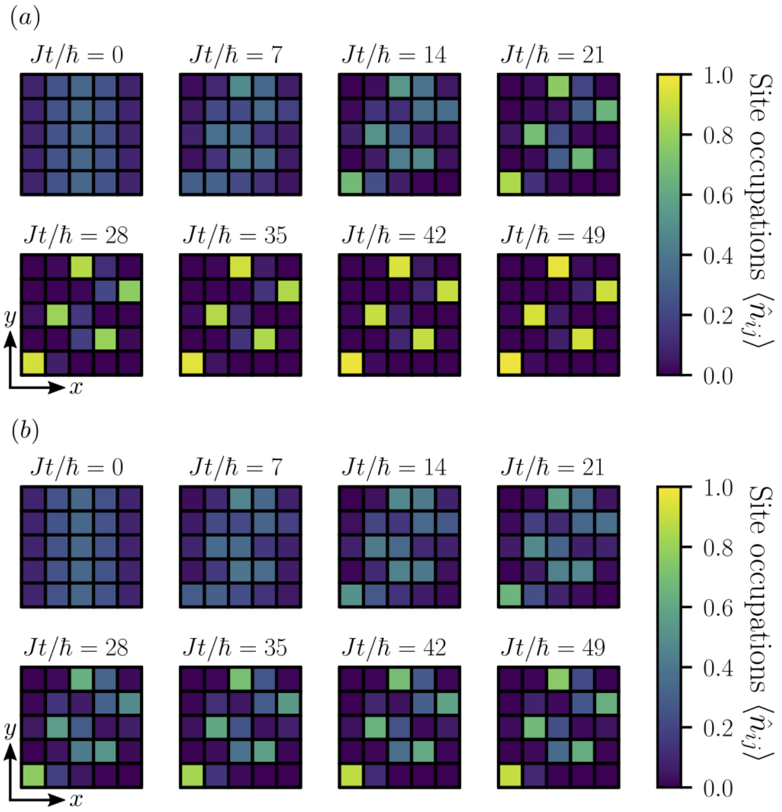

Figure 7.5.: *Comparison of the time evolution with quantum and classical fields.* Lattice site occupations for a time evolution during a nearly adiabatic sweep using the cavity Hamiltonian including cavity-assisted tunneling for the same parameters as in Fig. 7.2. Subplot (a) shows the dynamics using the full quantum interaction Hamiltonian [Eq. (7.16)]. It closely resembles the results from the model Hamiltonian in Fig. 7.2. Subplot (b) shows the time evolution with the classical approximation of the cavity fields [Eq. (7.27)]. The state does not converge to the solution, also not for much larger sweep times. The modes for both cases where chosen as in Fig. 7.4(b).

suggests that the system is robust against the errors introduced by the moderate lattice depth. Note that the physical Hamiltonian used here is non-stoquastic in the occupation basis due to cavity-induced tunneling.

7.4.2. Classical cavity fields

In the following we show that quantum correlations are crucial for the efficiency of the sweep. In particular, if we substitute the field operators a_m^{st} by its expectation values representing classical cavity fields the solution is not found. We consider the semi-classical Hamiltonian

$$H_{\mathrm{cav}}^{\mathrm{class}} = \hbar \sum_m \frac{N^2 \tilde{\Delta}_{c,m} \eta_m^2}{\tilde{\Delta}_{c,m}^2 + \kappa_m^2} \left(\hat{\Theta}_m^\dagger \langle \hat{\Theta}_m \rangle + \langle \hat{\Theta}_m^\dagger \rangle \hat{\Theta}_m - |\langle \hat{\Theta}_m \rangle|^2 \right), \tag{7.27}$$

where the expectation values have to be calculated self-consistently with the current atom state vector. This substitution amounts to considering only first order fluctuations around the mean of $\hat{\Theta}_m$ in Eq. (7.16).

Consequently, the dynamics are described by a differential equation which is non-linear in the state vector $|\psi\rangle$. We numerically solve this equation by self-consistently updating the expectation value in each time step. It turns out that even for very long sweep times, using classical fields does not lead to a solution of the queens problem. The time evolution for $J\tau/\hbar = 49$ is depicted in Fig. 7.5(b). The discrepancy shows the necessity of entangled light-matter states in our procedure.

7.4.3. Dephasing due to cavity field loss

Finally, motivated by experimental considerations, we consider the open system including photon decay through the cavity mirrors. This system can be described by a master equation for the atoms [7.54]

$$\dot{\rho} = -\frac{i}{\hbar}[H_{\mathrm{kin}} + H_{\mathrm{cav}}^{\mathrm{eff}}, \rho] + \sum_m \frac{N^2 \eta_m^2 \kappa_m}{\Delta_{c,m}^2 + \kappa_m^2} \left(2\hat{\Theta}_m \rho \hat{\Theta}_m^\dagger - \{\hat{\Theta}_m^\dagger \hat{\Theta}_m, \rho\} \right), \tag{7.28}$$

where curly brackets denote the anti-commutator (see Appendix 7.B). The model is suitable for analyzing the dephasing close to the coherent regime before any steady state is reached.

More insight can be gained by rewriting it in the basis of scattering eigenstates $|\nu\rangle$ with $\hat{\Theta}_m|\nu\rangle = \theta_m^\nu|\nu\rangle$, which scatter a field $\alpha_m^\nu = \frac{N\eta_m}{\tilde{\Delta}_{c,m}+i\kappa_m}\theta_m^\nu$. These states converge to the occupation states in the deep lattice limit. The time evolution for the matrix elements $\rho_{\mu\nu} = \langle\mu|\rho|\nu\rangle$ reads

$$\dot{\rho}_{\mu\nu} = (-\Gamma_{\mu\nu} - i\Omega_{\mu\nu})\rho_{\mu\nu} - i\frac{J}{\hbar}\sum_k \left(\langle\mu|\hat{B}|k\rangle\rho_{k\nu} - \langle k|\hat{B}|\nu\rangle\rho_{\mu k} \right) \tag{7.29}$$

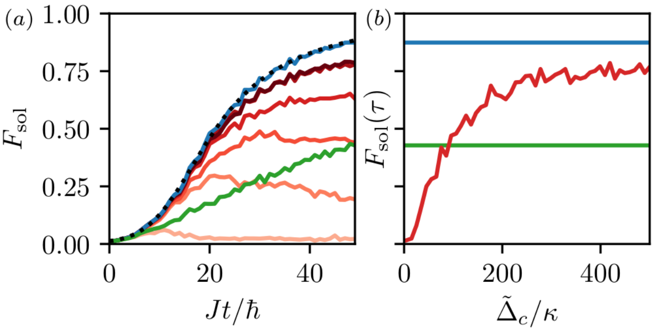

Figure 7.6.: *Comparison to open system dynamics.* (a) The figure shows the fidelity F_{sol} between the solution and the instantaneous eigenstate (black dotted), and between solution and dynamical state from the time evolution using the Schrödinger equation (blue), classical fields (green) and the open system (red). The open system fidelity depends on $\tilde{\Delta}_c/\kappa$, where we present results for the values $5, 50, 100, 200, 500, 1000$ (from light red to dark red). (b) The fidelity between solution and the final state after the sweep as a function of $\tilde{\Delta}_c/\kappa$ for the curves of (a), where the colors are the same as in (a). The parameters used here are as in Fig. 7.5.

with the rates

$$\Omega_{\mu\nu} = \sum_m \tilde{\Delta}_{c,m}(|\alpha_m^\mu|^2 - |\alpha_m^\nu|^2) \tag{7.30}$$

$$\Gamma_{\mu\nu} = \sum_m \kappa_m |\alpha_m^\mu - \alpha_m^\nu|^2. \tag{7.31}$$

While the energy gaps $\hbar\Omega_{\mu\nu}$ describe the coherent dynamics we considered up to now, the dephasing rates $\Gamma_{\mu\nu}$ stem from photon loss. Hence a superposition of two scattering eigenstates $|\mu\rangle$ and $|\nu\rangle$ looses its coherence depending on the difference of the scattered fields, or how distinguishable the states are by field measurement.

We now return to the example we had before, using uniform mode strengths $f_m = 1/M$, decay rates κ and detunings $\tilde{\Delta}_c$. Figure 7.6 compares the coherent Schrödinger time evolution from Sec. 7.4.1, the mean-field approximation with classical cavity fields from Sec. 7.4.2 and the open system dynamics with dephasing. For the latter the master equation is approximated by using Monte-Carlo wave function simulations. As a measure of similarity between states we use the fidelity. For two mixed states it is defined as $F(\rho,\sigma) = \mathrm{Tr}(\sqrt{\sqrt{\rho}\sigma\sqrt{\rho}})$ and reduces to the overlap $|\langle\psi|\phi\rangle|$ for pure states.

The open system dynamics is depicted for different detunings $\tilde{\Delta}_c/\kappa$ while keeping U_{Q} fixed. This can be achieved by adjusting the pump strength η correspondingly. In this case the dephasing rates

$$\frac{\hbar\Gamma_{\mu\nu}}{U_{\mathrm{Q}}} = \frac{\kappa}{\tilde{\Delta}_c} N^2 \sum_m |\theta_m^\mu - \theta_m^\nu|^2 \tag{7.32}$$

go to zero for $\tilde{\Delta}_c/\kappa \gg 1$. Thus, as expected, the open system converges to the coherent Schrödinger dynamics in this limit (see Fig. 7.6(b)).

Note that the coherence between states creating similar fields is preserved much longer than for other states, which is expected to be important at the late stage of the sweep. For states with fixed similarity (e.g. one atom moved), $|\theta_m^\mu - \theta_m^\nu|^2$ is on the order of N^{-2}, and thus the dephasing rates do not scale with N for such states.

7.5. Read-out

After the parameter sweep we need to determine if the obtained state is a solution or not. This can in principle be done by reading out the final atomic state with single site resolution using a quantum gas microscope [7.59, 7.60]. However, as we consider an open system with the cavity output fields readily available, we will show that by proper measurements on the output light we can directly answer this question without further additions. Note that after the sweep at the stage of the read-out, quantum coherences do not have to be preserved since the solution is a classical state. This gives the freedom to increase the lattice depth to some high value in the deep lattice regime to suppress further tunneling, and to increase the pump power or decrease the detunings in order to get a stronger signal at the detector.

7.5.1. Intensity measurement

For uniform cavity detunings, a state corresponding to the solution of the N-queens problem scatters less photons than all other states. Thus the measurement of the total intensity in principle allows one to distinguish a solution from other states. To illustrate this we consider the total rate of photons impinging on a detector scattered by an atomic state $|\psi\rangle$

$$\begin{aligned} P(|\psi\rangle) =& \sum_m 2\kappa_m \langle (a_m^{\mathrm{st}})^\dagger a_m^{\mathrm{st}}\rangle = \sum_m \frac{2\kappa_m}{\tilde{\Delta}_{c,m}} \frac{\tilde{\Delta}_{c,m}\eta_m^2 N^2}{\tilde{\Delta}_{c,m}^2 + \kappa_m^2} \langle \hat{\Theta}_m^\dagger \hat{\Theta}_m\rangle \\ \approx& U_{\mathrm{Q}} \frac{\zeta}{\hbar} \sum_{ijkl} \tilde{A}_{ijkl} \langle \hat{n}_{ij}\hat{n}_{kl}\rangle = \frac{\zeta}{\hbar}\langle H_{\mathrm{cav}}^{\mathrm{dl}}\rangle. \end{aligned} \tag{7.33}$$

In the last line we assumed that $\zeta = 2\kappa_m/\tilde{\Delta}_{c,m}$ does not depend on m and a deep lattice.

Since P is proportional to the energy expectation value, the ground state, i.e. the solution of the queens problem, causes a minimal photon flux at the detector $P_0 = 3NU_{\mathrm{Q}}\zeta$. It stems from the on-site terms $(i,j) = (k,l)$, where the factor 3 comes from the three pump directions. In contrast, each pair of queens violating the non-attacking condition in $\tilde{A}$ leads to an increase of the photon flux by $\Delta P = 2U_{\mathrm{Q}}\zeta$. The two atoms create an energy penalty for one another, explaining the factor 2. The relative difference of the photon flux due to a state with L attacking pairs and a solution is given by

$$\frac{L\Delta P}{P_0} = \frac{2L}{3N}. \tag{7.34}$$

As this scales with $1/N$ it is difficult to distinguish solutions from other states via measurement of the intensity for large N. Note that for non-uniform $\kappa_m/\tilde{\Delta}_{c,m}$, photons from different modes have to be distinguished.

7.5.2. Field measurement

Measurement of the output field quadratures, for example by homodyne detection, gives insight about the absolute position of the atoms projected onto the pump laser propagation direction. For the three directions used in our setup, this yields the occupations of each column $\langle \hat{N}_i^x \rangle$ and each diagonal $\langle \hat{N}_i^+ \rangle$ and $\langle \hat{N}_i^- \rangle$. Since a solution of the queens problem has maximally one atom on each diagonal and exactly one atom on each column, it must fulfill

$$\langle \hat{N}_i^x \rangle = 1 \wedge \langle \hat{N}_i^+ \rangle \leq 1 \wedge \langle \hat{N}_i^- \rangle \leq 1. \tag{7.35}$$

The output field quadratures can thus be used to determine if a classical final state is a solution or not, which is the answer to the blocked diagonals decision problem we aim to solve. The signatures of two example states in the cavity fields are depicted in Fig. 7.7.

Let us illustrate the measurement by considering only light scattered from the x-direction with incident wave vectors $\boldsymbol{k}_m^x$. Since these plane waves are constant in y-direction, the atom-field overlaps do not depend on j. Neglecting cavity-induced tunneling, the field quadratures for a phase difference ϕ are

$$\mathrm{Re}(\langle a_m^{\mathrm{st}} \rangle e^{-i\phi}) = \sum_i \mathrm{Re}\left(\frac{\eta_m e^{-i\phi}}{\tilde{\Delta}_{c,m} + i\kappa_m} v_m^{i1} \right) \langle \hat{N}_i^x \rangle, \tag{7.36}$$

revealing that cavity fields are determined by the total occupations of the columns $\hat{N}_i^x = \sum_j \hat{n}_{ij}$.

For at least N modes ($M \geq N$) this system of equations can be inverted yielding the column occupations $\langle \hat{N}_i^x \rangle$. By measuring the cavity output field quadratures scattered from the diagonal pump light we obtain the occupations of each diagonal $\langle \hat{N}_i^+ \rangle$ and $\langle \hat{N}_i^- \rangle$. Inverting the system of equations for diagonals demands at least as many pump modes as diagonals, that is $2N-1$. Inversion can also be done efficiently and intuitively by using a discrete Fourier transform and its inverse. To reveal the Fourier relation, one has to express the v_m^{ij}'s in Eq. (7.36) within the harmonic (or in the deep lattice) approximation (see Appendix 7.C). The so obtained approximate inversion formula also works well for realistic lattice depths.

Strictly speaking the condition in Eq. (7.35) is sufficient only for classical configurations, like occupation number basis states $|\phi_\nu\rangle$. Some superpositions $|\psi\rangle = \sum_\nu c_\nu |\phi_\nu\rangle$ which are no solutions might also fulfill the above criterion, because summands in the field expectation values $\langle a_m^{\mathrm{st}} \rangle = \sum_\nu |c_\nu|^2 \langle \phi_\nu | a_m^{\mathrm{st}} | \phi_\nu \rangle$ can cancel each other. For instance, for $U_\mathrm{T} = 0$ the solution from our example in Fig. 7.2 $|\psi_{\mathrm{sol}}\rangle = |1, 4, 2, 5, 3\rangle$ scatters the same fields $\langle a_m^{\mathrm{st}} \rangle$ as the superposition $|\psi_{\mathrm{nosol}}\rangle = (|\psi_{\mathrm{nosol}}^1\rangle + |\psi_{\mathrm{nosol}}^2\rangle)/\sqrt{2}$ with $|\psi_{\mathrm{nosol}}^1\rangle = |1, 3, 2, 5, 4\rangle$ and $|\psi_{\mathrm{nosol}}^2\rangle = |1, 4, 5, 2, 3\rangle$, both of which are no solution. In this notation the state $|i_1, i_2, ..., i_N\rangle$ has one atom on each site (i_j, j). However, these

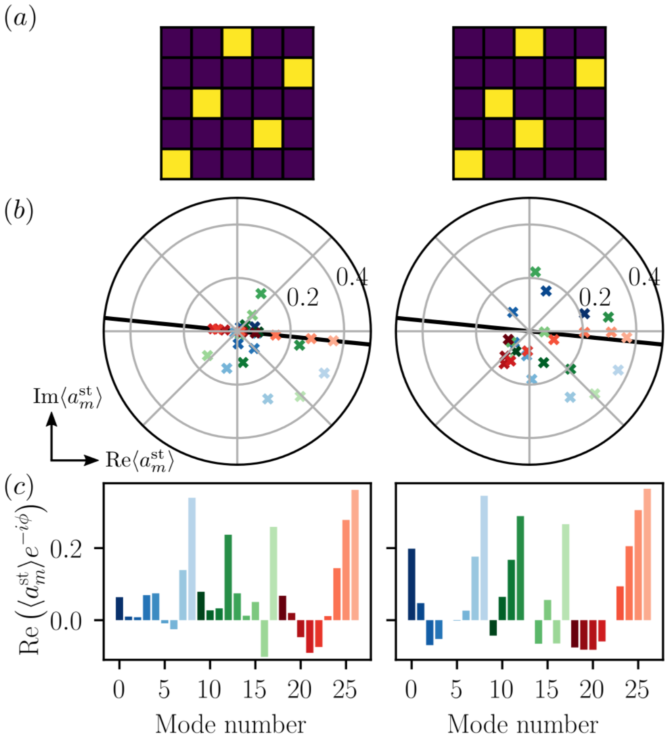

Figure 7.7.: *Signature of an atomic state in the cavity output.* In left and right column the signature of two different atomic (pure) states are compared, whose occupations are shown on the top (a). On the left there is a solution to the N-queens problem, while on the right one atom was moved. (b) The polar plot shows the cavity field expectation value $\langle a_m^{\mathrm{st}} \rangle$ in the complex plane. Measuring the fields by homodyne detection yields a certain quadrature of the field depending on the phase angle ϕ. An example is illustrated by the black line. (c) The measurable quadratures are shown for the example angle. The sequences can be Fourier transformed to obtain the occupations of columns and of the diagonals. The parameters used here are $U_{\mathrm{Q}} = 5$ and $\tilde{\Delta}_c/\kappa = 10$. We used $M = 2N - 1 = 9$ modes per direction with wave numbers as in Eq. (7.23). Different colors encode the different directions of the pump modes: $\boldsymbol{k}_m^x$ (blue), $\boldsymbol{k}_m^+$ (green) and $\boldsymbol{k}_m^-$ (red). The lighter the color the larger the wave number $|\boldsymbol{k}_m^{x,\pm}|$.

macroscopic superpositions are highly unstable. Even theoretically the measurement back-action [7.41, 7.61] projects superpositions of states scattering different fields (such as $|\psi_{\mathrm{nosol}}\rangle$) to one of its constituents. The inclusion of measurement back-action due to continuous measurement might thus lead to intriguing phenomena beyond those presented here and is subject to future work.

We emphasize again that the measurements described above answer the question if we found a solution or not, which is the answer to the combinatorial decision problem. The exact configuration of the final state can be measured with single site resolution as demonstrated in several experiments [7.59, 7.60].

7.6. Conclusions

We present a special purpose quantum simulator with the aim to solve variations of the N-queens problem based on atoms in a cavity. This combinatorial problem may serve as a benchmark to study a possible quantum advantage in intermediate size near term quantum experiments. From the algorithmic point of view, the problem is interesting for quantum advantage as it is proven NP-hard and instances can be found that are not solvable with current state-of-the-art algorithms. From the implementation point of view, the proposed quantum simulator implements the queens problem without overhead and thus a few tens of atoms are sufficient to enter the classically intractable regime. The proposed setup of atoms in a cavity fits the queens problem naturally as the required infinite range interactions arise there inherently. We find that by treating the light field classically the simulation does not find the solutions suggesting that quantum effects like atom-field entanglement cannot be neglected. Moreover, we investigate the influence of photon loss on the coherence time.

The queens problem is formulated as a decision problem, asking whether there is a valid configuration of queens or not given the excluded diagonals and fixed queens. Remarkably, to answer the decision problem, a read-out of the atom positions is not required as the necessary information is encoded in the light that leaves the cavity. To determine the position of the queens requires single site resolved read-out, which is also available in several current experimental setups [7.59].

In this work we concentrated on the coherent regime. The driven-dissipative nature of the system provides additional features which can be exploited for obtaining the ground state. For certain regimes, cavity cooling [7.24, 7.62] can help to further reduce sweep times and implement error correction. Moreover, the back action of the field measurement onto the atomic state can be used for preparing states [7.41].

Note that an implementation of the N-queens problem for a gate-based quantum computer was proposed in Ref. [7.63] aiming to find a solution of the unconstrained N-queens problem. Our work in contrast employs an adiabatic protocol and intends to answer the question if a solution exists given constraints of blocked diagonals or already placed queens, which was shown to be NP-complete and numerically hard [7.30].

Acknowledgments. We thank I. Gent, C. Jefferson and P. Nightingale for fruitful discussions. Simulations were performed using the open source QuantumOptics.jl framework in Julia [7.64] and we thank D. Plankensteiner for related discussions. V. T. and H. R. are supported by Austrian Science Fund Project No. I1697-N27. W. L. acknowledges funding by the Austrian Science Fund (FWF) through a START grant under Project No. Y1067-N27 and the SFB BeyondC Project No. F7108-N38, the Hauser-Raspe foundation, and the European Union's Horizon 2020 research and innovation program under grant agreement No. 817482 PasQuanS.

Appendix

7.A. Instance parameters

Table 7.1 provides an overview of the chosen parameters for the exemplary linear parameter sweep in the main text (Figs. 7.2, 7.3 and 7.5).

Parameter	Symbol	Value
System size	N	5
Final queens interaction energy	U_{Q}	J
Final excluded diagonals penalty	U_{D}	$5J$
Final trapping energy	U_{T}	$2J$
Sweep time	τ	$49\hbar/J$
Excluded sum-diagonals		$\{2,3,6,9\}$
Excluded difference-diagonals		$\{1,2,8,9\}$
Trapping sites		$\{(3,5)\}$
Number of modes per direction	M	5

Table 7.1.: Parameters of the exemplary instance used in the figures in the main text.

We now describe how we choose the parameters used in our example. For this we calculate the minimal gap and the overlap with the final solution for several parameters to find a region with large minimal gap and large overlap. Note that this is only done to find good parameters for our small example, where we already know the solution. For large systems such a calculation would beyond classical numerical capabilities, which is why the problem poses a potential application for a quantum simulator.

The minimal gap in the spectrum (e.g. the one shown in Fig. 7.3) depends on the final queens interaction energy U_{Q}, the final trapping energy U_{T}, the tunneling amplitude J and the final excluded diagonals penalty U_{D}. To find proper values for these parameters we determine the minimal gap in a wide parameter range. In order to get the minimal gap, some of the Hamiltonian's lowest eigenenergies are calculated for discrete time steps during the sweep. Subsequently, the minimum of the difference between the groundstate and the first exited state at all time steps is taken to be the minimal gap. The values of the minimal gap have to be scrutinized carefully since its accuracy depends on the resolution of the discrete time steps. Therefore a more detailed analysis of the minimal gap might require a more careful analysis, especially for high interaction strengths.

To analyze how well the quantum system reproduces the solution of the N-queens problem we study the overlap

$$F = |\langle\phi|\psi\rangle| \tag{7.37}$$

between the state $|\phi\rangle$ that corresponds to the solution of the chosen instance of the queens problem introduced in Fig. 7.1 and the state at the end of an adiabatic sweep $|\psi\rangle$ (i.e. the ground state of our spectrum on the right side). This is necessary because we do not switch off the kinetic Hamiltonian in our example, and thus the "perfect" solution is only obtained in the limit of large energy penalties U_{Q}, U_{D} and U_{T}.

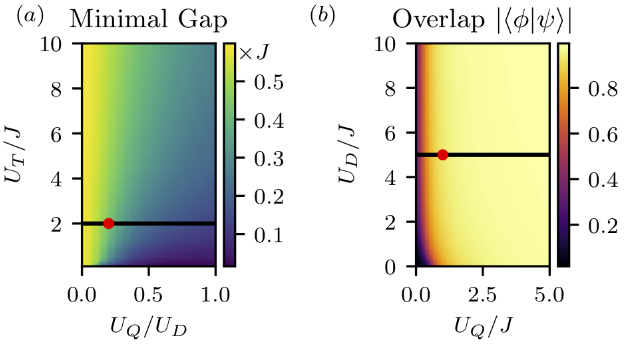

Figure 7.8.: *Discussion of the impact of parameter values.* (a) The minimal gap of the energy spectrum for the sweep as a function of the final parameters. U_{D} is fixed to $5J$ and U_{Q} is varied. For the discussion on fidelity [subplot (b)] we choose $U_{\mathrm{T}} = 2J$ which is indicated by the black line. The values of U_{T} are non-zero to avoid degenerate ground states. We choose an instance with parameter values denoted by the red dot. (b) The overlap defined in Eq. (7.37). The black line indicates the fixed value of U_{D} for subplot (a) and the red dot indicates the chosen set of parameters as before.

Figure 7.8(a) suggests that in order to increase the minimal gap the ratio $U_{\mathrm{Q}}/U_{\mathrm{D}}$ has to be chosen as small as possible. We vary the ratio by fixing U_{D} and varying U_{Q}. Therewith, Fig. 7.8(a) indicates that U_{Q} should be as small as possible. However, as it can be seen in Fig. 7.8(b), a small U_{Q} also decreases the overlap with the solution and the physical system does not resemble the desired solution of the queens problem anymore. We therefore have to make a compromise between a reasonably large overlap and an optimized minimal gap.

If we set U_{D} to $5J$ and U_{T} to $2J$ we find that for $U_{\mathrm{Q}} = 1J$ the overlap is $F \approx 0.93$ and the minimal gap is around $0.44J$. These values were used for Figs. 7.2 and 7.3.

7.B. Derivation of the effective Hamiltonian

The derivation essentially follows App. C in Ref. [7.40], generalized to two dimensions and additionally including cavity-induced tunneling (see also e.g. Ref. [7.54]). Including the decay of the cavity fields through the mirrors with the rates κ_m, the full open-system dynamics in the tight binding limit is given by the Lindblad equation

$$\dot{\rho} = -\frac{i}{\hbar}[\tilde{H}, \rho] + \sum_m \kappa_m (2a_m \rho a_m^\dagger - a_m^\dagger a_m \rho - \rho a_m^\dagger a_m), \tag{7.38}$$

where $\tilde{H}$ is specified in Eq. (7.10). The important term for the following discussion discussion is the atom-light interaction H_{cav} given in Eq. (7.11).

From this master equation we obtain the Heisenberg-Langevin equations of the cavity fields

$$\dot{a}_m = (i\tilde{\Delta}_{c,m} - \kappa_m)a_m - iN\eta_m\hat{\Theta}_m + \sqrt{2\kappa_m}\hat{\xi}_m \tag{7.39}$$

with the quantum noise operator $\hat{\xi}_m$ obeying $[\hat{\xi}_m(t), \hat{\xi}_m^\dagger(t')] = \delta(t - t')$.

Assuming that the cavity mode fields evolve on a much faster time scale than the atomic motion ($J/(\hbar|\tilde{\Delta}_{c,m} + i\kappa_m|) \ll 1$), they can be approximated by their steady state on a course grained time scale [7.40, 7.54, 7.57, 7.58]. From the Heisenberg-Langevin equation, to zeroth order in $J/(\hbar|\tilde{\Delta}_{c,m} + i\kappa_m|)$, we get

$$a_m^{\rm st} \equiv \frac{\eta_m}{\tilde{\Delta}_{c,m} + i\kappa_m} N\hat{\Theta}_m + \sqrt{\frac{2\kappa_m}{\tilde{\Delta}_{c,m}^2 + \kappa_m^2}}\,\hat{\xi}_m \tag{7.40}$$

with $\hat{\Theta}_m = \frac{1}{N}\sum_{i,j=1}^N \left(v_m^{ij}\hat{n}_{ij} + u_m^{ij}\hat{B}_{ij}\right)$. That is, at steady state the effect of the field can be expressed by atomic operators only.

We now substitute the cavity field operators by their corresponding steady-state approximations in the Heisenberg equation of the atomic annihilation operators

$$\begin{aligned}\dot{b}_{ij} = \frac{1}{i\hbar}[b_{ij}, H_{\rm cav}] + ... = &-i\sum_m \frac{(N\eta_m)^2}{\tilde{\Delta}_{c,m}^2 + \kappa_m^2}\Big[\tilde{\Delta}_{c,m}\Big([b_{ij}, \hat{\Theta}_m^\dagger]\hat{\Theta}_m + \hat{\Theta}_m^\dagger[b_{ij}, \hat{\Theta}_m]\Big)\\ &\qquad\qquad\qquad -i\kappa_m\Big([b_{ij}, \hat{\Theta}_m^\dagger]\hat{\Theta}_m - \hat{\Theta}_m^\dagger[b_{ij}, \hat{\Theta}_m]\Big)\Big]\\ &-i\sum_m \frac{N\eta_m\sqrt{2\kappa_m}}{\sqrt{\tilde{\Delta}_{c,m}^2 + \kappa_m^2}}\Big([b_{ij}, \hat{\Theta}_m^\dagger]\hat{\xi}_m + \hat{\xi}_m^\dagger[b_{ij}, \hat{\Theta}_m]\Big)\end{aligned} \tag{7.41}$$

where we only report terms including the cavity. At this point, ordering of atomic and field operators becomes important, since $a_m^{\rm st} \propto \hat{\Theta}_m$ as opposed to a_m does not necessarily commute with atomic operators. Here we choose normal ordering, as already done in Eq. (7.11). The expression contains coherent terms proportional to $\tilde{\Delta}_{c,m}$ and incoherent terms proportional to κ_m.

For $|\tilde{\Delta}_{c,m}| \gg \kappa_m$ we can neglect the incoherent part and the Heisenberg equation can be obtained from

$$\dot{b}_{ij} = \frac{1}{i\hbar}[b_{ij}, H_{\rm cav}^{\rm eff}] + ... \tag{7.42}$$

Thus the dynamics in the coherent regime is described by the effective Hamiltonian $H_{\rm cav}^{\rm eff}$ given in Eq. (7.16). Otherwise the Heisenberg equation is equivalent to the master equation (7.28).

The results can also be obtained by naively substituting a_m with $a_m^{\rm st}$ directly in the Hamiltonian Eq. (7.11) or the master equation (7.38) with the given ordering.

Note that the effective Hamiltonian can also be written in the form

$$H_{\rm cav}^{\rm eff} = \hbar\sum_m \tilde{\Delta}_{c,m}(a_m^{\rm st})^\dagger a_m^{\rm st}, \tag{7.43}$$

which allows for a simple interpretation: For $\tilde{\Delta}_{c,m} > 0$ the lowest energy states tend to minimize the intensity of the cavity fields $\langle(a_m^{\rm st})^\dagger a_m^{\rm st}\rangle$.

7.C. Harmonic approximation of potential wells

In this section we investigate the limit of a deep lattice in more detail. In Section 7.3.1 we presented results in the "infinitely" deep lattice limit, where the Wannier functions become delta functions. To gain more insight to deep but finite lattice depths, we use a harmonic approximation for the potential wells. The ground state wave function is then an approximation to the lowest-band Wannier function

$$w_{\mathrm{har}}(x) = \pi^{-\frac{1}{4}} a_0^{-\frac{1}{2}} e^{-\frac{x^2}{2a_0^2}} \tag{7.44}$$

with the size $a_0 = (E_{\mathrm{R}}/V_{\mathrm{L}})^{1/4}/k_{\mathrm{L}}$ [7.55].

With this the atom-mode overlap integrals [Eq. (7.13)] can be calculated analytically using running wave mode functions [Eq. (7.18)]. For the on-site term we obtain

$$v_m^{ij} = h_m(x_i, y_j) e^{-\left(\frac{k_m^x}{2k_{\mathrm{L}}}\right)^2 \sqrt{\frac{E_{\mathrm{R}}}{V_{\mathrm{L}}}}}. \tag{7.45}$$

It consists of the mode function at the lattice site and an exponential which reduces the overlap due to Gaussian smoothing of the mode function. As intuitively expected, the smoothing has a stronger effect for large mode wave numbers k_m^x. For $V_{\mathrm{L}}/E_{\mathrm{R}} \gg 1$, we obtain $v_m^{i,j} = h_m(x_i, y_j)$, as in the main text.

For the off-site overlaps we obtain

$$u_m^{ij} = h_m((x_i + x_{i+1})/2, y_j) e^{-\left(\frac{k_m^x}{2k_{\mathrm{L}}}\right)^2 \sqrt{\frac{E_{\mathrm{R}}}{V_{\mathrm{L}}}}} e^{-\frac{\pi^2}{4}\sqrt{\frac{V_{\mathrm{L}}}{E_{\mathrm{R}}}}}. \tag{7.46}$$

The overlap consists of three terms: First, it is the mode function evaluated in between the lattice sites. Second, there is again the Gaussian smoothing term as for the on-site overlap. Lastly, there is an exponential independent of the modes, which comes from the overlap of the two Gaussians. It goes to zero for $V_{\mathrm{L}}/E_{\mathrm{R}} \gg 1$, leading to $u_m^{ij} = 0$.

The order operator is then

$$\hat{\Theta}_m^{\mathrm{har}} = \frac{1}{N} e^{-\left(\frac{k_m^x}{2k_{\mathrm{L}}}\right)^2 \sqrt{\frac{E_{\mathrm{R}}}{V_{\mathrm{L}}}}} \sum_{i,j=1}^{N} \left(h_m(x_i, y_j)\hat{n}_{ij} + h_m((x_i + x_{i+1})/2, y_j)\hat{B}_{ij} e^{-\frac{\pi^2}{4}\sqrt{\frac{V_{\mathrm{L}}}{E_{\mathrm{R}}}}} \right) \tag{7.47}$$

leading to an interaction Hamiltonian [Eq. (7.16)] given by

$$\begin{aligned} H_{\mathrm{cav}}^{\mathrm{har}} = & U_Q \sum_m f_m e^{-2\left(\frac{k_m^x}{2k_{\mathrm{L}}}\right)^2 \sqrt{\frac{E_{\mathrm{R}}}{V_{\mathrm{L}}}}} \sum_{ijkl} \left(h_m^*(x_i, y_j)\hat{n}_{ij} + h_m^*((x_i + x_{i+1})/2, y_j)\hat{B}_{ij} e^{-\frac{\pi^2}{4}\sqrt{\frac{V_{\mathrm{L}}}{E_{\mathrm{R}}}}} \right) \\ & \times \left(h_m(x_k, y_l)\hat{n}_{kl} + h_m((x_k + x_{k+1})/2, y_l)\hat{B}_{kl} e^{-\frac{\pi^2}{4}\sqrt{\frac{V_{\mathrm{L}}}{E_{\mathrm{R}}}}} \right), \end{aligned} \tag{7.48}$$

which in the "infinitely" deep lattice limit simplifies to Eq. (7.17). All cavity-induced tunneling terms are suppressed by the exponential and tend to be smaller than density-density terms. Also, since U_{Q} is maximally on the order of J (at the end of the sweep), cavity-induced tunneling terms are smaller than H_{kin}. However, also the density-density terms can be small for example when $h_m(x_i, y_j) = 0$, which is why we still include cavity-induced tunneling in the simulations.

In the main text we chose uniform $f_m = 1/M$. To compensate for Gaussian smoothing one might want to include the exponential as correction

$$\tilde{f}_m = f_m e^{2\left(\frac{k^x_m}{2k_{\mathrm{L}}}\right)^2 \sqrt{\frac{E_{\mathrm{R}}}{V_{\mathrm{L}}}}}, \tag{7.49}$$

which leads to even better results ($\tilde{A}$ is closer to A for finite lattice depths). Note that this correction does only depend on V_{L} and not on the problem size or number of modes in our implementation, since the range of k^x_m is fixed.

7.D. Shape of the interaction

Here we reformulate the interaction in the infinitely deep lattice limit from Eq. 7.22 with Fourier transforms by defining a real envelope function $f(k)$ such that $f(k_m) = f_m$. To get back the discrete wave numbers, this function is sampled with a Dirac comb at the lines $m\Delta k + k_s$ with $m \in \mathbb{Z}$, where k_s is a constant shift and Δk is the spacing between the pumped modes. In the main text we only consider the case $k_s = 0$ for simplicity. We define the Fourier transform as $\mathcal{F}\{f\}(r) = \int_{-\infty}^{\infty} \mathrm{d}k f(k) e^{ikr}/\sqrt{2\pi}$ and denote the convolution as $(f * g)(t) = \int_{-\infty}^{\infty} f(\tau) g(t-\tau) \mathrm{d}\tau$.

For simplicity, we take parallel wave vectors $\boldsymbol{k}_m$. Along this direction $\boldsymbol{r} \parallel \boldsymbol{k}_m$ we write

$$\begin{aligned}
\tilde{\mathcal{A}}(r) &= \sum_m f_m \cos(k_m r) = \int_{-\infty}^{\infty} \mathrm{d}k\, f(k) \sum_{m=-\infty}^{\infty} \delta(k - m\Delta k - k_s) \cos(kr) \\
&= \mathrm{Re}\left[\sqrt{2\pi}\mathcal{F}\left\{ f(k) \sum_{m=-\infty}^{\infty} \delta(k - m\Delta k - k_s) \right\}(r)\right] \\
&= \mathrm{Re}\left[\sqrt{2\pi}\mathcal{F}\{f\}(r) * \sum_{l=-\infty}^{\infty} \delta\left(r - l\frac{2\pi}{\Delta k}\right) e^{ik_s r}\right] \\
&= \sum_{l=-\infty}^{\infty} \mathrm{Re}\left[\sqrt{2\pi}\mathcal{F}\{f\}\left(r - l\frac{2\pi}{\Delta k}\right) e^{i2\pi l \frac{k_s}{\Delta k}}\right],
\end{aligned} \tag{7.50}$$

where $r = |\boldsymbol{r}|$. We used the convolution and shift theorem from Fourier analysis in the second to last line and evaluated the convolution integrals by pulling out the sum in the last line.

For symmetric envelopes centered around k_c we can further simplify using the shift theorem

$$\tilde{\mathcal{A}}(r) = \sum_{l=-\infty}^{\infty} \sqrt{2\pi}\mathcal{F}\{\tilde{f}\}\left(r - l\frac{2\pi}{\Delta k}\right) \cos\left(k_c\left(r - l\frac{2\pi}{\Delta k}\right) + 2\pi l \frac{k_s}{\Delta k}\right), \tag{7.51}$$

where $\tilde{f}(k) = f(k + k_c)$ is the shifted envelope centered around $k = 0$, whose Fourier transform is real.

Let us apply this to our example described in Section 7.3.2 and find out why the interaction has the desired property given in equation Eq. (7.24). There we had uniform $f_m = 1/M$ and wave numbers

$$k_m^0 = k_\mathrm{L} \left(1 + \frac{2m+1}{2M}\right) \tag{7.52}$$

with $m = 0, ..., M-1$. These have a mode spacing of $\Delta k = k_\mathrm{L}/M$ and are centered around $k_c = 3k_\mathrm{L}/2$. One can see that only the odd modes of the cavity (wave numbers $k_n = n\Delta k_\mathrm{FSR}$ with n odd and free spectral range Δk_FSR) are used. Therefore, $\Delta k = 2\Delta k_\mathrm{FSR}$ and $k_s = \Delta k/2$, because the comb has to be shifted to fit the odd modes. Due to the uniform f_m the envelope is a rectangular function with width k_L and height $1/M$ centered at k_c

$$f(k) = \mathrm{rect}((k - k_c)/k_\mathrm{L})/M = \begin{cases} 1/M & \text{for } k \in [k_c - k_\mathrm{L}/2, k_c + k_\mathrm{L}/2] \\ 0 & \text{otherwise.} \end{cases} \tag{7.53}$$

The Fourier transform of a rectangular function centered around zero with unit width and height is a sinc function $\mathrm{sinc}(x) = \sin(x)/x$. Using the addition theorem for the cosine and noting that $\cos(\pi l) = (-1)^l$ and $\sin(\pi l) = 0$ we obtain an analytical expression for the interaction

$$\tilde{\mathcal{A}}(r) = \sum_{l=-\infty}^{\infty} (-1)^l \mathrm{sinc}\left(\frac{k_\mathrm{L}}{2}\left(r - l\frac{2\pi}{\Delta k}\right)\right) \cos\left(k_c\left(r - l\frac{2\pi}{\Delta k}\right)\right). \tag{7.54}$$

For $l = 0$ and at lattice site spacings $r_j = j\pi/k_\mathrm{L}$ it takes the values

$$\mathrm{sinc}(\pi j/2)\cos(3\pi j/2) = \begin{cases} 1 & \text{for } j = 0 \\ 0 & \text{otherwise,} \end{cases} \tag{7.55}$$

as desired. This comes from well known properties of sinc and cosine

$$\mathrm{sinc}(\pi j/2) = \begin{cases} 1 & \text{for } j = 0 \\ 0 & \text{for } j \text{ even} \\ (-1)^{\frac{j-1}{2}} \frac{2}{\pi j} & \text{for } j \text{ odd} \end{cases}$$

$$\cos(3\pi j/2) = \begin{cases} (-1)^{\frac{j}{2}} & \text{for } j \text{ even} \\ 0 & \text{for } j \text{ odd.} \end{cases}$$

The other summands have the same form, but are shifted by $R = 2\pi/\Delta k = 2\pi M/k_\mathrm{L} = r_{2M}$ ($2M$ lattice sites) and have alternating signs. Since R is an integer multiple of the lattice spacing this adds up to the desired interaction given in Eq. (7.24) in the main text.

Thus for rectangle envelopes the bandwidth Δk_{BW} determines the zeros of the interaction. Taking $\Delta k_{\mathrm{BW}} = 2k_{\mathrm{L}}$ would lead to zeros at all lattice sites. For the smaller bandwidth $\Delta k_{\mathrm{BW}} = k_{\mathrm{L}}$ used here, only even sites become zero. This can be compensated by choosing a central wave number $k_c = nk_{\mathrm{L}}/2$ with n odd, which is responsible for the zeros at odd sites. The mode spacing Δk determines the peak distance. Finally, using odd cavity modes (specifying k_s) leads to alternating peaks, which does not have an effect in our implementation, since $-2M < j < 2M$.

8. Self-ordering and cavity cooling using a femtosecond pulse train

In this chapter we present an analysis of a multi-mode optical resonator filled with a cloud of thermal atoms which is transversally pumped by a pulsed laser. While the dynamics is well described by the already known Eqs. (3.11), which were also employed in Chapter 5, the existence of a large number of modes which are dense in frequency space adds a wealth of new physical effects. First, the dynamics becomes nearly translationally invariant along the cavity axis. Moreover, the bandwidth of the frequency comb adds a new length scale, which renders clustering of atoms on this length scale energetically favorable. We numerically determine the self-organization thresholds. We find that the cooling time can be reduced by using a large number of modes, as we show by numerical integration of Eqs. (3.11).

8.1. Frequency comb and cavity setup

For our purposes, a frequency comb is a laser beam whose frequency spectrum contains many equidistant narrow lines, as for instance a regular pulse train with narrow pulses. Specifically, we say that the lines are at the spatial frequencies $k_s + n\delta k_{\mathrm{FC}}$, where k_s is a shift and δk_{FC} is the distance between the comb lines. The spectrum can be written as a Dirac comb

$$S(k) = \sum_{n=-\infty}^{\infty} f(k)\delta(k - k_s - k_{\mathrm{FC}}), \tag{8.1}$$

where the envelope function $f(k)$ has the characteristic width Δk. We define the central wave number as k_c.

As discussed in Sec. 2.2.2, a Fabry-Pérot cavity with the length L supports only frequencies close to the resonances at $k_n = nk_0$ with $k_0 = \pi/L$. The comb lines match the cavity lines when the ratio of the respective line distances is rational, i.e. can be written as

$$\frac{\delta k_{\mathrm{FC}}}{k_0} = \frac{p}{r} \tag{8.2}$$

with the integers p and r. In words this means that every rth frequency comb line pumps the cavity and every pth cavity resonance is pumped. The mode distance of pumped cavity modes is given by $\delta k = pk_0$.

If the frequency comb is phase locked, the laser beam consists of a regular pulse train. The pulse shape is given by the Fourier transform of the comb envelope and has thus a width $\sim 2\pi/\Delta k$. The distance between two pulses is $d_{\mathrm{FC}} = 2\pi/\delta k_{\mathrm{FC}} = 2Lr/p$, where we used the definition Eq. (8.2). Assuming scattering at a single point (or atom), the pulse distance in the cavity, instead, is $d = 2\pi/\delta k = 2L/p \leq 2L$. That means that p pulses fit into one round trip length $2L$ of the cavity. Since $d \leq d_{\mathrm{FC}}$, the repetition rate in the cavity is always larger than the one of the frequency comb. This intuitively makes sense since in the cavity the pulse comes back after one round trip. A scattering atomic cloud with finite size L_a (instead of a single atom) leads to dephasing and thus widening of the pulse when $L_a > 2\pi/\Delta k$. Qualitatively, the minimum pulse width in the cavity is given by the cloud size L_a.

In the following we assume that a set of adjacent cavity modes is pumped, i.e. $p = 1$ in the above notation, and thus the mode distance is simply the free spectral range $\delta k = k_0$. By choosing the origin in the center of the cavity, the modes are described by alternating cosines and sines as in Eq. (2.13). The order parameters can thus be written as

$$\Theta_m = \frac{1}{N} \sum_i \cos(k_m x_i + \phi_m), \tag{8.3}$$

where $\phi_m = 0$ for odd m and $\phi_m = \pi/2$ for even m. We denote the set of pumped modes by $\mathcal{M}$, i.e. $m \in \mathcal{M}$.

For simplicity, we restrict ourselves to rectangular comb envelopes with the single-mode pump strength η. Moreover, we assume that the cavity detuning Δ_c and the decay rate κ do not depend on the mode index.

8.2. Semi-classical equations

The atomic and electric field motion can be well approximated by the semi-classical equations formulated in Eqs. (3.11). After the adiabatic elimination of the fields up to first order in momentum, we obtain analytical expressions for the effective forces from Eqs. (3.21)

$$F_{\mathrm{ad},j} = \hbar \frac{\eta^2 \Delta_c}{\Delta_c^2 + \kappa^2} \sum_m 2k_m \sum_i \cos(k_m x_i + \phi_m) \sin(k_m x_j + \phi_m) \tag{8.4a}$$

$$F_{\mathrm{ret},j} = \hbar \frac{\eta^2 \Delta_c \kappa}{(\Delta_c^2 + \kappa^2)^2} \sum_m 4 \frac{k_m^2}{m_a} \sum_i p_i \sin(k_m x_i + \phi_m) \sin(k_m x_j + \phi_m). \tag{8.4b}$$

The adiabatic contribution $F_{\mathrm{ad},j}$ can be derived from a suitable potential energy [see Eq. (3.22)]

$$U(x_1, ..., x_N) = u_1 \sum_{i,j} \sum_m \cos(k_m x_i + \phi_m) \cos(k_m x_j + \phi_m) \tag{8.5}$$

with $u_1 = \hbar \eta^2 \Delta_c / (\Delta_c^2 + \kappa^2)$. In the following we assume high-field seeking atoms, i.e. $\Delta_c < 0$ and thus $u_1 < 0$.

For a single cosine mode the potential energy is given by

$$U_{1\mathrm{m}} = u_1 \sum_{i,j} \cos(k x_i) \cos(k x_j), \tag{8.6}$$

which is minimized when all cosines are $+1$ or -1 leading to the well-known self-organized λ-periodic pattern. Note that there are two minimal energy (or "optimal") patterns, where the absolute position of the particles is fixed by the mode structure.

As a second mode configuration we consider a combination of a cosine and a sine mode ($\phi_1 = 0$ and $\phi_2 = \pi/2$) which have the equal wave number k. Using the identity $\cos(\alpha)\cos(\beta) + \sin(\alpha)\sin(\beta) = \cos(\alpha - \beta)$, the potential energy then depends only on the distances of the particles

$$U_{2\mathrm{m}} = u_1 \sum_{i,j} \cos(k(x_i - x_j)). \tag{8.7}$$

We thus expect periodic ordering on a length scale of $\lambda = 2\pi/k$, such that the cosine gets close to 1. As opposed to the single-mode case, this system is translationally invariant here. Note that the terms $i = j$ are included and add a constant shift. Further note that at the cavity center two neighboring longitudinal modes very closely resemble this cosine-sine configuration.

In the multi-mode case, the form of the potential energy depends on the mode distance δk and the bandwidth Δk in relation to the extension of the atomic cloud L_a. Since the extension of the atomic cloud has to be much smaller than the cavity length, it is fulfilled that $L_a/L = L_a\delta k/\pi \ll 1^*$. In this typical case, adjacent sine and cosine modes do not dephase on the length L_a, and thus we can approximate their spatial frequencies to be equal. The system thus consists of $M/2$ sine-cosine pairs and the potential energy resembles the two mode case with an additional sum over the modes

$$U_{\mathrm{mm}} = u_1 \frac{1}{2} \sum_{i,j} \sum_{m} \cos(k_m(x_i - x_j)). \tag{8.8}$$

The factor $1/2$ emerges since we still sum all individual modes, and not pairs of cosines and sines.

The form of the potential depends now on the bandwidth Δk of the k_m's and the spatial interval L_a we consider, leading to different mode regimes (see Figs. 8.1 and 8.2). For $L_a\Delta k/(2\pi) \ll 1$ all modes stay in phase within the interval and the scenario can be approximated by the two-mode case, $U_{\mathrm{mm}} \approx (M/2)U_{2\mathrm{m}}$. Here we expect again a periodic pattern with a period around λ_c anywhere in space (we choose the central wavelength $\lambda_c = 2\pi/k_c$ as representative frequency comb wave length). For $L_a\Delta k/(2\pi) \gtrsim 1$ the bandwidth introduces its own length scale $2\pi/\Delta k$. In addition to the λ_c-periodic modulation, it is energetically favorable for the atoms to cluster. We thus expect an additional envelope with a width $\sim 2\pi/\Delta k$ in the density distribution.

Cooling and heating effects come from the retardation force Eq. (8.4b), which is discussed in more detail in Appendix A.4.

---

[*] In general, we have $L_a\delta k/\pi = pL_a/L$. When not all adjacent cavity modes are pumped and p is large, we can also enter the opposite regime $L_a\delta k/\pi \gg 1$ [see Fig. 8.1]. This is for instance the case in the two-mode model in Chapter 5.

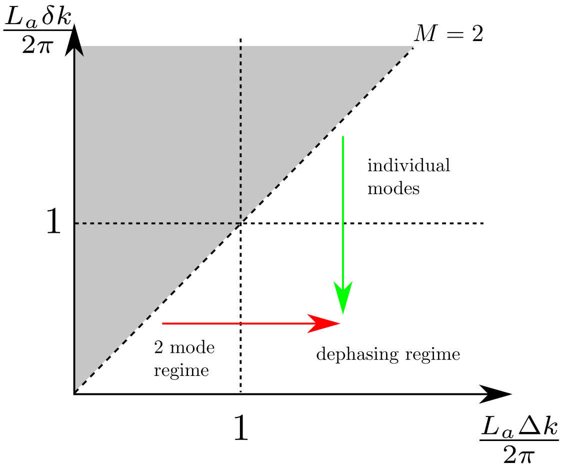

Figure 8.1.: Qualitative depiction of the different regimes. In the two-mode regime all the modes can be approximated to have the same frequency, which effectively leads to one sine and one cosine mode. In the dephasing regime, adjacent modes have approximately the same frequencies, while in general the modes dephase over the interval. In the individual mode regime even adjacent modes dephase and thus have to be taken into account individually. The gray region is forbidden due to $M \geq 2$ and $\delta k = \Delta k/(M-1)$. The red arrow shows the parameter sweep used in Fig. 8.3, where upon increasing M we go from the effective two mode regime to the dephasing regime. The green arrow shows the case of Fig. 8.6, from the region where we have to take into account individual modes to the dephasing regime.

Figure 8.2.: The relevant length scales in the dephasing regime. The central wavelength of the frequency comb $\lambda_c = 2\pi/k_c$ is the length scale of periodic ordering as in the single-mode case. In order to stay in the in-phase region of the modes, it is energetically favorable when atoms cluster on a length scale $2\pi/\Delta k$. This is only relevant when it is smaller than the atomic cloud size L_a, i.e. the light red region exists. When approaching the two-mode regime, this region becomes smaller and finally vanishes. The cavity length L is much larger than all other involved length scales.

8.3. Self-ordering threshold from mean-field theory

In addition to the qualitative theoretical analysis, we will use numerical simulations to obtain the pump power threshold of the phase transition from homogeneous to ordered configurations for $\Delta_c < 0$ for different mode configurations. We employ the mean-field self-consistent iteration used in the single-mode case in Ref. [8.1]. After starting with some initial particle distribution, one calculates all order parameters of the different modes for this distribution. From these one can further obtain the single-particle potential

$$U_1(x) = 2\hbar \frac{\eta^2 \Delta_c}{\Delta_c^2 + \kappa^2} N \sum_m \Theta_m \cos(k_m x + \phi_m), \tag{8.9}$$

which is the potential one atom feels due to all other atoms[†]. The new atomic distribution is then set to the thermal equilibrium Boltzmann distribution at some chosen temperature T, i.e. $P_{\text{new}}(x) \propto \exp(-U_1(x)/(k_B T))$. Now we again calculate the corresponding order parameters and the procedure is iterated until the distribution does not change anymore.

As a figure of merit of the ordering with respect to all pumped modes we introduce the root-mean-square (or total) order parameter

$$\bar{\Theta} = \sqrt{\frac{1}{M} \sum_m \Theta_m^2}. \tag{8.10}$$

Moreover, we introduce the maximum photon number per particle $\bar{n} = N\eta^2/(\Delta_c^2 + \kappa^2)$ in a single mode. It was shown in Refs. [8.2, 8.3], that the critical photon number per particle above which self-organization takes place is given by $\bar{n}_c = (\Delta_c^2 + \kappa^2)/(4\Delta_c^2)$, when the atoms have the steady-state temperature $k_B T = \hbar(\Delta_c^2 + \kappa^2)/(-4\Delta_c)$. We use these quantities to define the pump intensity normalized to the critical intensity

$$\zeta = \frac{\bar{n}}{\bar{n}_c} = \frac{4N\eta^2\Delta_c^2}{(\Delta_c^2 + \kappa^2)^2} \tag{8.11}$$

and thus expect single-mode self-organization for $\zeta > 1$.

In view of the experimental set-up in Zagreb[‡], we define $k_c = 93750 k_0$ as the central wave number and consider the mode interval between $k_{\text{start}}/k_0 = 92750$ and $k_{\text{end}}/k_0 = 94750$. The bandwidth of this interval is

$$\frac{\Delta k_r}{k_c} = \frac{k_{\text{end}} - k_{\text{start}}}{k_c} = \frac{94750 - 92750}{93750} \approx 0.0213 = 2.13\%, \tag{8.12}$$

so about two percent of the central wave number. Physically, this interval fits 2001 cavity modes, and a smaller number can be chosen as long as δk is an integer multiple of k_0 ($\delta k = p k_0$, see Sec. 8.1). But theoretically we may take an arbitrary number of modes

---

[†] It is related to the adiabatic contribution of the force by $F_{\text{ad},j} = -\frac{\mathrm{d}}{\mathrm{d}x} U_1(x)|_{x=x_j}$.

[‡] In the group of T. Ban at the Institut za Fiziku.

M_r equidistantly distributed in the interval. The mode spacing can then be calculated by

$$\frac{\delta k}{k_c} = \frac{1}{M_r - 1}\frac{\Delta k_r}{k_c} \approx \frac{0.0213}{M_r - 1}. \tag{8.13}$$

This defines a ruler for the wave numbers, which we specify by the number of ruler ticks M_r and which has the fixed length Δk_r. In the following we are going to consider different scenarios pumping subsets of the modes with wave numbers taken from the ruler.

The atoms are distributed on the interval $L_a = 300\lambda_c$, physically corresponding to the size of the atomic cloud. The cavity parameters are $\kappa = 400\omega_{\mathrm{R}}^{k_c}$ and $\Delta_c = -\kappa$ with the recoil frequency $\omega_{\mathrm{R}}^{k_c} = \hbar k_c^2/(2m_a)$. The temperature is chosen as $k_{\mathrm{B}}T = \hbar\kappa/2$, which is the self-consistent stationary temperature.

8.3.1. Thresholds for homogeneous initial distributions

In order to enter the regime of high mode density we need to choose a large ruler tick number M_r. Here we take $M_r = 2000$, which yields the mode spacing $\delta k/k_c = 1.067 \times 10^{-5}$ for which adjacent modes do not dephase (since $\delta k L_a/(2\pi) = 300\delta k/k_c \approx 3.2 \times 10^{-3} \ll 1$). For subsets containing a number M of equidistant δk-spaced modes, the bandwidth varies with M and is given by $\Delta k = \delta k(M-1)$. There is thus a linear relation between M and Δk with this choice. Consistently, for $M = 2000$ we get the bandwidth $\Delta k = \Delta k_r$. Note that this variation of parameters corresponds to the red arrow in Fig. 8.1.

In order to find the thresholds we conduct a self-consistent iteration for different pump strengths starting with a homogeneous initial distribution with small fluctuations. In Fig. 8.3(a) the root-mean-square order parameter of the stationary distribution is plotted. Up to a certain threshold ζ_c, the stationary distribution is nearly homogeneous and the total order parameter is close to zero. Above ζ_c the atomic distribution has the characteristic λ_c-periodic density modulation [see Fig. 8.3(c)]. As opposed to the single-mode case, where the order parameter tends to one, the impossibility of simultaneous ordering to cosine and sine modes leads to an asymptotic value of $\sqrt{2}/2$ for all other mode configurations. For $M = 2$ this can be seen from

$$\bar{\Theta} \approx \sqrt{\frac{1}{2}}\sqrt{\frac{1}{N^2}\sum_{i,j}\cos(k(x_i - x_j)} \leq \frac{\sqrt{2}}{2}. \tag{8.14}$$

Interestingly, the thresholds ζ_c depend on the bandwidth Δk (or here M) in a non-trivial way. We discuss this with the help of Fig. 8.3(b), where the extracted thresholds are depicted. Apart from the special case $M = 1$, we again identify two different mode regimes (see red arrow in Fig. 8.1): In the effective two-mode regime $L_a\Delta k/(2\pi) \ll 1$ the total critical pump strength $M\zeta_c$ remains at the constant value 2. Since the modes do not dephase, adding more modes and keeping the total pump strength constant does not qualitatively alter anything. This changes as $L_a\Delta k/(2\pi)$ becomes larger than 1. Then the single-mode critical pump strength ζ_c stays constant, suggesting that adding more

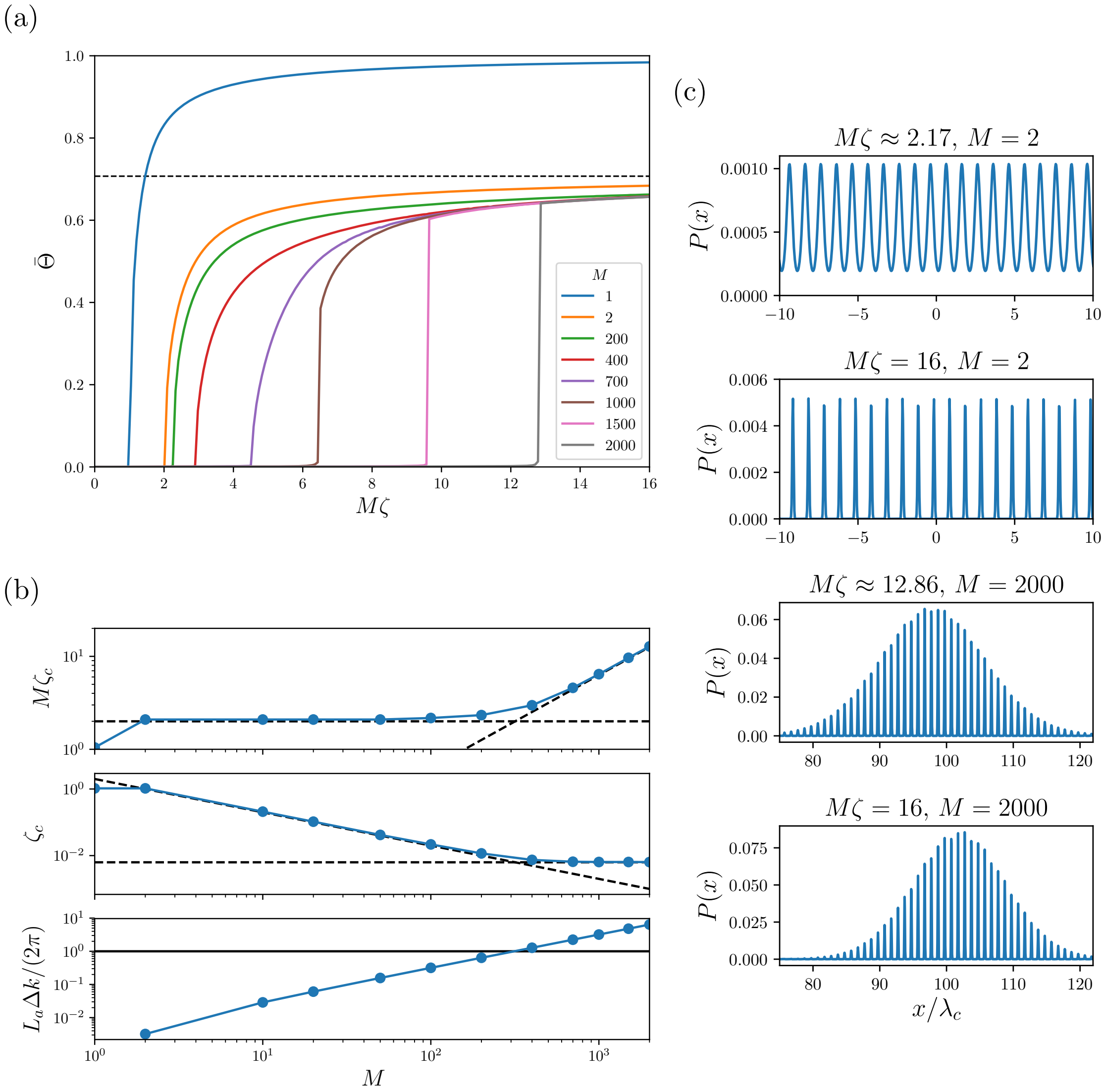

Figure 8.3.: Subfigure (a) depicts the total order parameter of the stationary distribution from the self-consistent iteration with temperature $k_\mathrm{B}T = \hbar\kappa/2$ for different total pump strengths $M\zeta$ after 1000 iterations. The black dashed line indicates the upper bound $\bar{\Theta} = \sqrt{2}/2$ for the multi-mode case. Subfigure (b) shows the thresholds where the order parameter becomes non-zero as extracted from (a). The mode distance δk is constant, thus the bandwidth $\Delta k = (M-1)\delta k$ increases with M, corresponding to the red path in Fig. 8.1. In the effective two-mode regime $M\zeta_c$ stays constant at a value of 2 (horizontal dashed line), while in the dephasing regime adding more modes leads to a linear increase $\approx M/158.7$ (tilted dashed line). Subfigure (c) depicts examples of stationary distributions for $M = 2$ (upper two plots) and $M = 2000$ (lower two plots), in each case one slightly and one far above threshold. Note that only a cutout of the distributions defined on $-150\lambda_c$ to $150\lambda_c$ is shown (the cutout interval for the latter case is the dephasing length $2\pi/\Delta k_r = 46.95\lambda_c$).

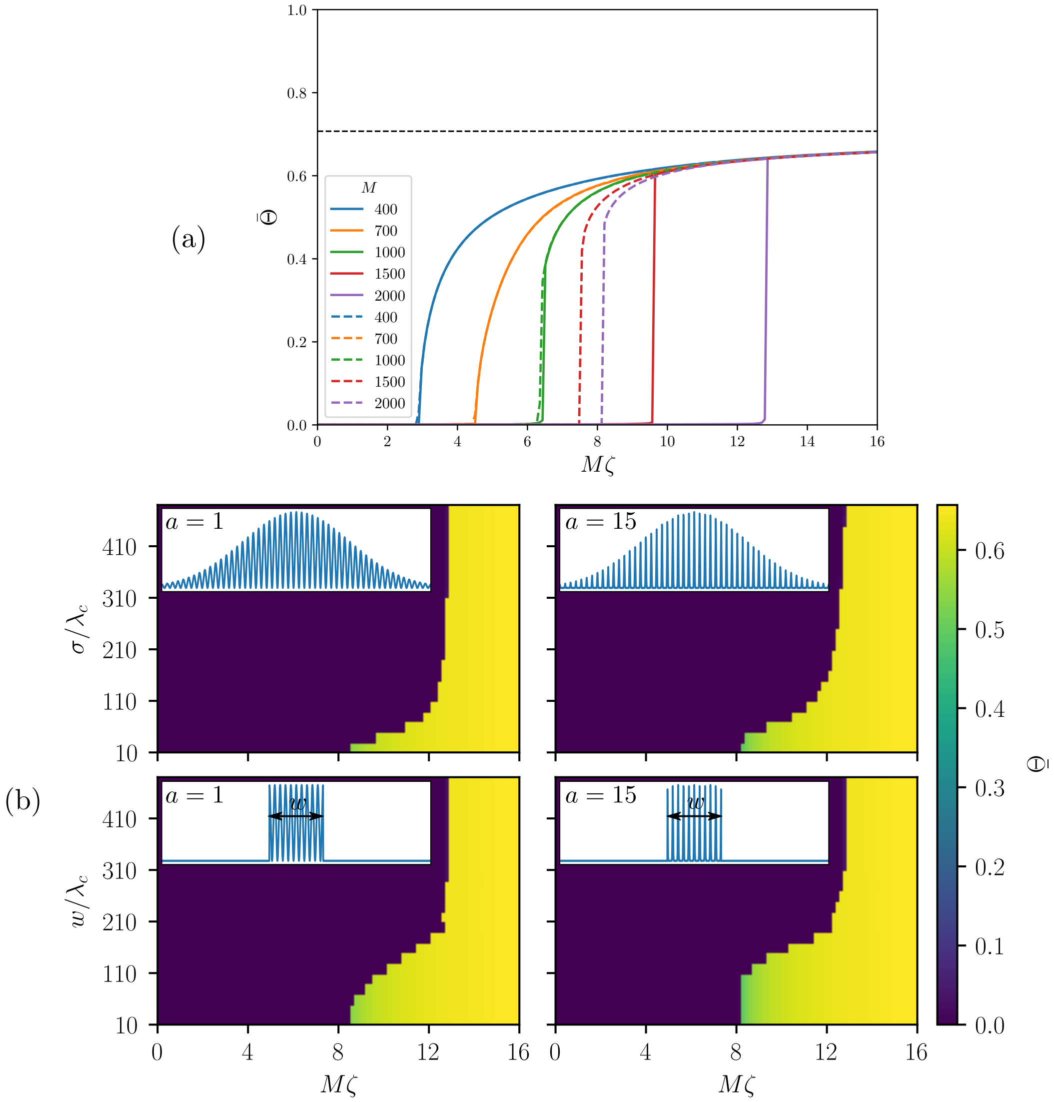

Figure 8.4.: Comparison of the self-consistent stationary order parameters for different initial distributions after 200 iterations for $k_\mathrm{B}T = \hbar\kappa/2$. The curves in (a) compare the results obtained using the model initial distribution with Gaussian envelope [Eqs. (8.15) and (8.16)] for $a = 15$ and $\sigma = 10\lambda_c$ with the homogeneous initial distribution from Fig. 8.3 for different bandwidths (or M). Subfigure (b) depicts the phase diagram of the order parameter for $M = 2000$ for different initial distributions shown in the inset. These have Gaussian envelopes in the upper row and rectangular envelopes in the lower row. The standard deviation σ and the width w both have the value $10\lambda_c$ for the example in the inset.

modes and thereby increasing the total input power does not help reducing the threshold anymore. This is because due to dephasing, the atoms cannot perfectly order to all modes, but only to an effective number of modes $M_{\text{eff}} = 1/\zeta_c$. This quantity grows like $M/2$ in the two-mode regime and stagnates at a certain value in the dephasing regime, which can be extracted from the numerical simulations as $M_{\text{eff}} \approx 158.7$ [see Fig. 8.3(b)]. In our case the transition takes place between $M = 200$ (where $L_a \Delta k/(2\pi) \approx 0.637$) and $M = 400$ (where $L_a \Delta k/(2\pi) \approx 1.277$).

Another qualitative difference between the two regimes is the form of the order parameter curves: In the two-mode regime the curves are continuous above threshold. In the dephasing regime there is a jump in the total order parameter, as in a first order phase transition. The difference is also manifest in the transition of the stationary distributions from the homogeneous to the ordered phase: The uppermost subplot for $M = 2$ in Fig. 8.3(c) slightly above threshold $M\zeta \approx 2.17$ suggests that here the stationary distribution continuously transforms from homogeneous to ordered for increasing ζ. This stands in contrast to the dephasing regime (see subplot for $M = 2000$ and $M\zeta \approx 12.86$, which is also slightly above the threshold).

8.3.2. Dependence on the initial distribution

For the non-continuous cases, we note that the stationary distribution found after a larger number of iterations depends on the initial distribution when using our self-consistent iteration algorithm. We now aim to qualitatively examine in which way. In order to reduce the analysis to few parameters, we choose model initial distributions which contain the main features of a stationary distribution above threshold: A periodic modulation with (approximately) λ_c and an envelope function $f_\nu(x)$. Specifically, we write

$$P_{\text{ini}}(x) \propto f_\nu(x) \cos^{2a}\left(\frac{k_c x}{2}\right) = f_\nu(x) \left(\frac{1 + \cos(k_c x)}{2}\right)^a \tag{8.15}$$

and for the envelope $f_\nu(x)$ we choose either a Gaussian with standard deviation (or Gaussian rms width) σ

$$f_{\text{G}}(x) = \exp\left(-\frac{x^2}{2\sigma^2}\right), \tag{8.16}$$

or a rectangle function with the width w

$$f_{\text{R}}(x) = \text{rect}\left(\frac{x}{w}\right) = \begin{cases} 1 & \text{for } -w/2 < x < w/2 \\ 0 & \text{otherwise.} \end{cases} \tag{8.17}$$

While the Gaussian closer resembles an actual stationary state, the rectangle function is practical due to its simplicity.

For $a = 1$ the modulation has a sine-form, while for larger $a \in \mathbb{N}$ it consists in recurring narrow peaks. For instance, the stationary solution in the uppermost subplot in Fig. 8.3(c) would be emulated by a small a, while the others have a larger a. Note that in the dense mode regime it does not matter if we take a sine or a cosine in the model distribution, since there are anyways always both in the vicinity k_c.

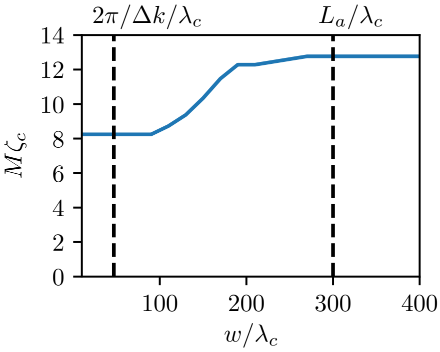

Figure 8.5.: The total multi-mode threshold $M\zeta_c$ for $M = 2000$ and different widths w of the rectangular initial distribution and $a = 15$ [extracted from Fig. 8.4(b)]. For $w < 2\pi/\Delta k$ it converges to $M\zeta_c^{\downarrow} = 8.24$ and for $w > L_a$ to $M\zeta_c \uparrow = 12.77$.

The results of the self-consistent iteration are shown in Fig. 8.4. In subplot (a) we see that for a fairly narrow Gaussian initial distribution with a standard deviation of $\sigma = 10\lambda_c$, the threshold for large mode numbers (bandwidths) is shifted to much lower pump strengths, while for small mode numbers (i.e. small bandwidth close to the effective two-mode regime) nothing changes. The transition from a localized distribution with small σ and a nearly flat cosine-like modulation for large σ is depicted in subplot (b) for $M = 2000$. As expected from the considerations above, we observe that the threshold goes to smaller values for smaller σ and approaches a value similar to that for the homogeneous initial distribution for large σ. A similar behavior can be seen for rectangular initial distributions with the width w, which suggests that qualitatively the results do not depend on details of the distribution other than the width of the envelope.

More insight can be gained by comparing the width of the initial distribution with the typical length scales of the system already mentioned in Fig. 8.2. Considering Fig. 8.5 we note that the threshold is constant when the width is within the in-phase region $w < 2\pi/\Delta k$ and has a lower value $M\zeta_c^{\downarrow} \approx 8.24$. For $w > L_a$ the initial distribution does not change anymore, so trivially also here the threshold is constant at a higher value $M\zeta_c^{\uparrow} \approx 12.77$. In between, for $2\pi/\Delta k < w < L_a$, the threshold increases with w. Note that this region only exists for $L_a > 2\pi/\Delta k$, i.e. in the dephasing regime, and not in the effective two-mode regime, where no jumps in the phase diagram occur. Finally, note that for the other model initial distributions these features are more washed out and the lower and upper value slightly differ from those given here.

8.3.3. Beyond the regime of high mode density

In this section we make a detour beyond the regime of high mode density, where modes have to be considered individually since even adjacent modes dephase. Technically, we take a subsection of modes where the bandwidth $\Delta k_r/k_c \approx 0.0213$ is fixed. The so-created interval is evenly filled up with M modes. Thus the mode distance goes inversely with the number of modes $\delta k = \Delta k_r/(M-1)$, i.e. $M_r = M$. Increasing M leads to the path through the mode regimes depicted by the green arrow in Fig. 8.1. Note that physically this is only possible when not pumping adjacent modes, i.e. for the case $p > 1$ (but still odd).

The results are plotted in Fig. 8.6. For small M we are in a regime where the modes have to be considered individually, since $L_a \delta k/\pi > 1$. Hence different mode configurations can lead to distinct behavior. For $M = 4$, $M = 6$ and $M = 10$, the random initial fluctuations on top of the homogeneous distribution drive the iteration into different meta-stable states having distinct potential energies, which explains the jumps of the order parameter between different values. The situation drastically changes for $M \gtrsim 15$ when leaving the individual mode regime and $L_a \delta k/\pi < 1$. The threshold then does not change much anymore by adding more modes, suggesting that it depends predominantly on the bandwidth Δk, which is constant. Reading off the figures, the transition takes place approximately between $M = 13$ (where $L_a \delta k/\pi \approx 1.07$) and $M = 15$ (where $L_a \delta k/\pi \approx 0.91$).

We also note that the upper bound of the rms order parameter $\sqrt{2}/2$ is not valid in the individual mode regime since the cosine-sine pair approximation in Eq. (8.14) cannot be made.

8.4. Simulation of the dynamics

In addition to the analytical and stationary considerations above, we now simulate the dynamics of the frequency comb set-up by numerical integration of the stochastic differential equations of motion given in Eqs. (3.11) with the order parameters Eq. (8.3).

Let us first define the quantities, which we depict in the following. As a measure of the order to all modes we again employ the total order parameter $\bar{\Theta}$ for each trajectory and calculate the trajectory average $\langle\bar{\Theta}\rangle$. Moreover, the total intra-cavity photon number $n = \sum_m |\alpha_m|^2$ is again approximated by its trajectory average $\langle n\rangle$. We define the kinetic energy as $E_{\text{kin}} = \langle p^2\rangle/(2m_a)$. Due to the equipartition theorem, it is related to the temperature by $E_{\text{kin}} = k_{\text{B}}T/2$.

Moreover, we aim to define a quantity which contains information about the atomic distribution. From a simple plot of the distribution one sees where the atoms are, but it is hard to tell where in space they are ordered, which would require to track the fast λ_c-oscillations. It is thus insightful to consider the averaged field distribution

$$F(x) = \frac{1}{M}\sum_m \Theta_m \cos(k_m x + \phi_m), \tag{8.18}$$

with the normalized spatial form of the mth cavity mode field $\Theta_m \cos(k_m x + \phi_m)$. Alternatively, this function can be interpreted as a projected particle density distribution by reading the order parameters as Fourier coefficients of the normalized particle distribution $P(x)$. They can be written as

$$\Theta_m = \begin{cases} \int_{-L}^{L} \mathrm{d}x\, P(x)\cos(k_m x) & m\,\text{odd} \\ -\int_{-L}^{L} \mathrm{d}x\, P(x)\sin(k_m x) & m\,\text{even}, \end{cases} \tag{8.19}$$

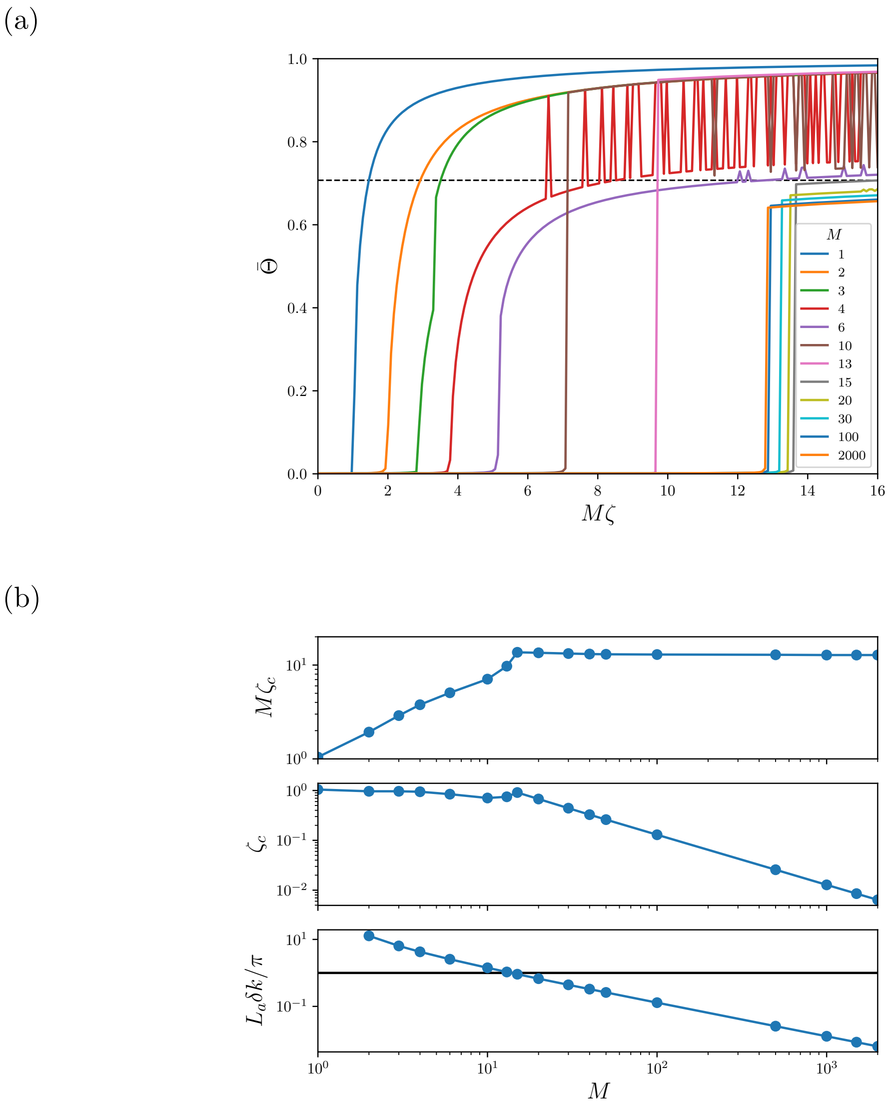

Figure 8.6.: (a) Steady-state order parameter from the self-consistent iteration for different mode numbers M for the temperature $k_{\mathrm{B}}T = \hbar\kappa/2$ and 1000 iterations. Here the bandwidth Δk is constant, thus the mode distance goes like $(M-1)^{-1}$. The black dashed line is at $\bar{\Theta} = \sqrt{2}/2$ indicates the upper bound for $L_a\delta k/\pi \ll 1$. (b) Thresholds as a function of the mode number. There are two different regimes depending on the parameter $L_a\delta k/\pi$.

noting that $\cos(x+\pi/2) = -\sin(x)$. Since the order parameters are defined for pumped modes ($m \in \mathcal{M}$) only, $F(x)$ is the truncated Fourier series of the particle distribution $P(x)$. $F(x)$ thus contains only those features of $P(x)$, which are relevant for scattering into the cavity or, in non-technical words, those features the apparatus "sees". Obviously, for a larger bandwidth more details can be resolved. Note that $F(x)$ is also proportional to the single-particle potential [Eq. (8.9)], when $\eta^2\Delta_c/(\Delta_c^2+\kappa^2)$ does not depend on m. Thus for $\Delta_c < 0$ the system favors placing an additional particle there, where it "assumes" that there are already atoms. Since this increases the photon number by super-radiant scattering, the apparatus can be interpreted as a light harvesting system.

The envelope of the fast λ_c-oscillations of the averaged field distribution $F(x)$ tells us where in space the atomic cloud is ordered. To extract it we use the root-mean-square envelope, which can be calculated by a convolution of F^2 and rectangle function with a width chosen as λ_c acting as a sliding window. The smoothed field distribution is then given by

$$\mathcal{F}(x) = \sqrt{F^2(x) * \mathrm{rect}\left(\frac{x}{\lambda_c}\right)}. \tag{8.20}$$

From our simulations we obtain the time evolution of the trajectory averaged order parameters $\langle\Theta_m\rangle(t)$, and thus one can consider the time evolution of the function $\mathcal{F}(x)$. Also experimentally, the order parameters can be indirectly measured via a homodyne measurement of the cavity output fields. When the dynamics of the cavity fields α_m is much faster than the one of the atoms, we can use the adiabatic approximation of the fields $\alpha_m \approx N\eta/(\Delta_c+i\kappa)\Theta_m$ to obtain an approximate expression for the order parameters

$$\Theta_m \approx \frac{\sqrt{\Delta_c^2+\kappa^2}}{N|\eta|}\tilde{\alpha}_m \tag{8.21}$$

in terms of the measurable field quadratures

$$\tilde{\alpha}_m = \mathrm{Re}\left[\alpha_m \exp\left(-i\mathrm{arg}[(\Delta_c+i\kappa)^{-1}]\right)\right]. \tag{8.22}$$

Figure 8.7 depicts an example time evolution of $\mathcal{F}(x)$, where the order parameters are approximated by trajectory averages either of the order parameters $\langle\Theta_m\rangle$ or the fields $\langle\alpha_m\rangle$ via Eq. (8.21). This demonstrates that the function $\mathcal{F}(x)$ is in principle constructable from measurements of the cavity fields.

8.4.1. Simulations of the self-ordering dynamics

We now compare the dynamics of $N = 100$ atoms and $M = 50$ modes for different pump strengths above and below the above obtained thresholds for the initial temperature $k_{\mathrm{B}}T = \hbar\kappa/2$. The initial spatial distribution is uniform on an interval of the width w, which we choose as either $20\lambda_c$ or $300\lambda_c$. The example parameters we consider are summarized by red crosses in Fig. 8.8, which are depicted within the phase diagram from the self-consistent iteration used in the previous section. Note that this is only for orientation: The situation in the dynamical case here is different since the particles

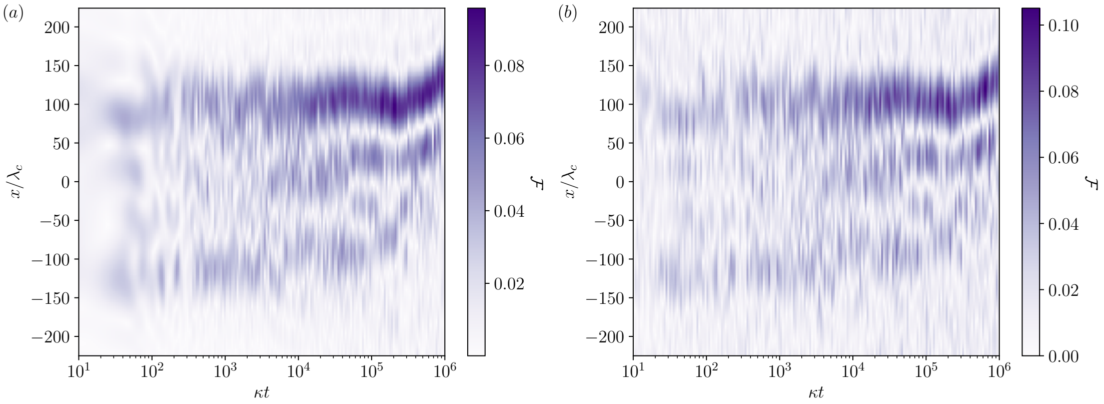

Figure 8.7.: The smoothed field distribution $\mathcal{F}(x)$ for the parameters in Fig. 8.14. (a) The order parameters come from averaged order parameters $\Theta_m \approx \langle \Theta_m \rangle$. (b) The order parameters are calculated from the measurable field quadratures via Eq. (8.21).

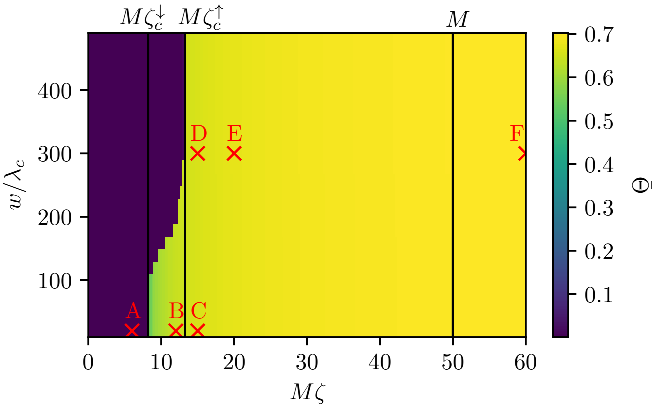

Figure 8.8.: Thresholds from the self-consistent iteration for $k_B T = \hbar\kappa/2$ for the bandwidth $\Delta k_r/k_c = 2.13\%$, $M = 50$ and a rectangular initial distribution with width w and $a = 15$. The phase diagram resembles the case for $M = 2000$ in Figs. 8.4 and 8.5, since the bandwidth is the same. The red crosses indicate the choice of initial width and pump strength for the dynamical simulations for orientation. The simulations with the initial width $w = 10\lambda_c$ are depicted in Figs. 8.10 (A), 8.11 (B) and 8.12 (C). The results for the initial width $w = 300\lambda_c$ are shown in Figs. 8.13 (D), 8.14 (E) and 8.15 (F).

can move out of the interval, which is not possible for the distribution used in the self-consistent iteration, and due to the relatively small particle number.

Again we choose the cavity parameters as $\kappa = 400\omega_{\mathrm{R}}^{k_c}$ and $\Delta_c = -\kappa$. As opposed to Sec. 8.3.1 we choose $M_r = 50$, i.e. 50 modes span the bandwidth $\Delta k_r/k_c = 2.13\%$. The mode spacing $\delta k/k_c = (94750 - 92750)/(93750(50-1)) = 4.35 \times 10^{-4}$ is larger, but still leads to the high mode density regime where adjacent modes do not dephase significantly, since $\delta k L_a/\pi \approx 0.26 \ll 1$ for $L_a = 300\lambda_c$ [see e.g. Fig. 8.6(b), where $M = 50$ is already in the flat part of the $M\zeta_c$ plot].

Figure 8.9 depicts the case of two modes for comparison. $\mathcal{F}(x)$ is uniform here, since the light fields do not contain any information about the absolute position. The total pump strength is $M\zeta = 15$ and the single-mode pump strength $\zeta = 7.5$. The latter is much larger than one and thus far above threshold. We see trapping in a translationally invariant potential and slow collective motion of the ordered atoms.

Figure 8.10 shows the multi-mode case ($M = 50$) for a pump below the lower threshold $\zeta_c^{\downarrow}$ and small initial width $w = 20\lambda_c$. Initially, the atoms order, which can be seen by the increase of the order parameter $\langle\bar{\Theta}\rangle$ and the photon number $\langle n\rangle$. Interestingly, the ordering is not sustained and falls apart. As usual in such systems, the kinetic energy rises initially since the atoms fall into their self-created potential, and gets slowly reduced on a longer time scale by cavity cooling. $\mathcal{F}(x)$ is not uniform anymore, but shows the localization on the dephasing length scale.

The pump strength $M\zeta = 15$ in Fig. 8.11 is above $\zeta_c^{\downarrow}$ but still below $\zeta_c^{\uparrow}$. This case strongly resembles the two-mode case: The ordering is stable and the values of $\langle\bar{\Theta}\rangle$ are similar. When an atom leaves the in-phase region, though, it is not trapped anymore, in contrast to the two-mode case. This is a consequence of the dephasing and the resulting decay of the interactions with distance. A very similar behavior can be seen for a pump strength slightly above $\zeta_c^{\uparrow}$ in Fig. 8.12.

When starting from a uniform distribution on a larger interval $L = 300\lambda_c$, the same pump strength above $\zeta_c^{\uparrow}$ as in Fig. 8.12 leads to strikingly different results as depicted in Fig. 8.13. The increase of the total order parameter is much lower compared to the small initial width. Ordering is stable in the early stage of the dynamics, but not in the late stage. From $\mathcal{F}(x)$ we see that the particles do not create one cluster, but rather order in several regions. Since the self-created potential is not as deep as before due to bad ordering, the initial increase of the kinetic energy is smaller, leading to faster cooling. We will examine this feature in more detail in the next section. Increasing the pump strength to $M\zeta = 20$ (see Fig. 8.14) leads to qualitatively similar results, but a higher fraction of ordered atoms. Also here it seems that the ordering becomes unstable on longer time scales than $\kappa t = 10^6$.

Finally, Fig. 8.15 shows results for high pump strengths of $M\zeta = 60$ and $\zeta = 1.2$ above the single-mode threshold. Since even a single-mode can sustain ordering here, the cloud organizes in some stable pattern. The particles still do not gather in an interval smaller than the dephasing length, but rather freeze close to their initial positions. While this leads to a low total order parameter, the total intensity is comparable to the well-ordered scenarios for small initial width of the distribution, e.g. Fig. 8.11, where the pump strength is much lower.

Summarizing, we find that the initial width of the distribution is the main factor deciding whether strong ordering to many modes occurs. Initial widths smaller than the dephasing length often result in ordering which can be stable on large time scales even below the multi-mode threshold $\zeta_c^{\downarrow}$ obtained using the self-consistent iteration. For initial widths larger than the dephasing length instead, the atoms do not find the multi-mode stationary state in the cases we considered and order only to few modes simultaneously. Even for pump strengths slightly above the multi-mode threshold $\zeta_c^{\uparrow}$ obtained before, the ordering is not large enough to be stable. By increasing the pump strength, the fraction of ordered atoms and thus the time of stable ordering increases. Finally, above the single-mode threshold, where one mode is sufficient to sustain ordering, the atoms freeze close to their current position and the state is definitely stable. A better ordering also in the case of wide initial distributions might be obtained by slowly ramping up the pump strength to its final value or by using higher initial temperatures as in Chapter 5.

8.4.2. Simulations from the cooling viewpoint

We now focus on the cooling capabilities for different mode configurations, i.e. the reduction of the kinetic energy. Here we add a harmonic trap, i.e. a restoring force $-D_{\mathrm{osc}}x$, such that the particles do not run away too far from the in-phase region when they are not trapped by the cavity potential. The constant is chosen as $D_{\mathrm{osc}}/(\hbar k_c \omega_{\mathrm{R}}^{k_c}) = 1/(150\lambda_c)$, while the width of the initial uniform atomic distribution is $300\lambda_c$. We take the same mode spacing as in the previous section, and by varying M the bandwidth $\Delta k = \delta k(M-1)$ grows linearly.

The results for 100 particles and different mode numbers are plotted in Fig. 8.16 on a linear and a logarithmic time scale. Analogously, the cases of 500 particles and 1000 particles are shown in Figs. 8.17 and 8.18, respectively.

All multi-mode simulations were done with $M\zeta = 4$, i.e. fixed total pump strength. Note that in course of varying M, the multi-mode threshold obtained in the previous section is traversed. Thus we observe self-organization for small M and no self-organization for large M by looking at the increase of the order parameter $\bar{\Theta}$. The same total pump strength $\zeta = 4$ in the single-mode case corresponds to a strong pump far above the single-mode threshold. Cooling is slower as compared to the multi-mode case. Interestingly, for the lower pump strength $\zeta = 2$, the cooling time decreases, but is still larger than in the multi-mode case[§].

Within the multi-mode case, we see that for a higher mode number M (or larger bandwidth Δk) the reduction of the kinetic energy is faster, while the increase of the order parameter is smaller, i.e. worse ordering is correlated with faster cooling. This is because for low mode numbers the system cools itself over the self-organization threshold, leading to substantial order parameters, while for higher mode numbers ($M = 20, 50$) this is not the case anymore, and the intra-cavity photon number stays nearly constant.

[§] Note that $M\zeta = 2$ for $M = 1$ leads to the same maximal (total) intra-cavity intensity as $M\zeta = 4$ (and $\zeta = 2$) for $M = 2$ since particles can only perfectly order to one of the two modes.

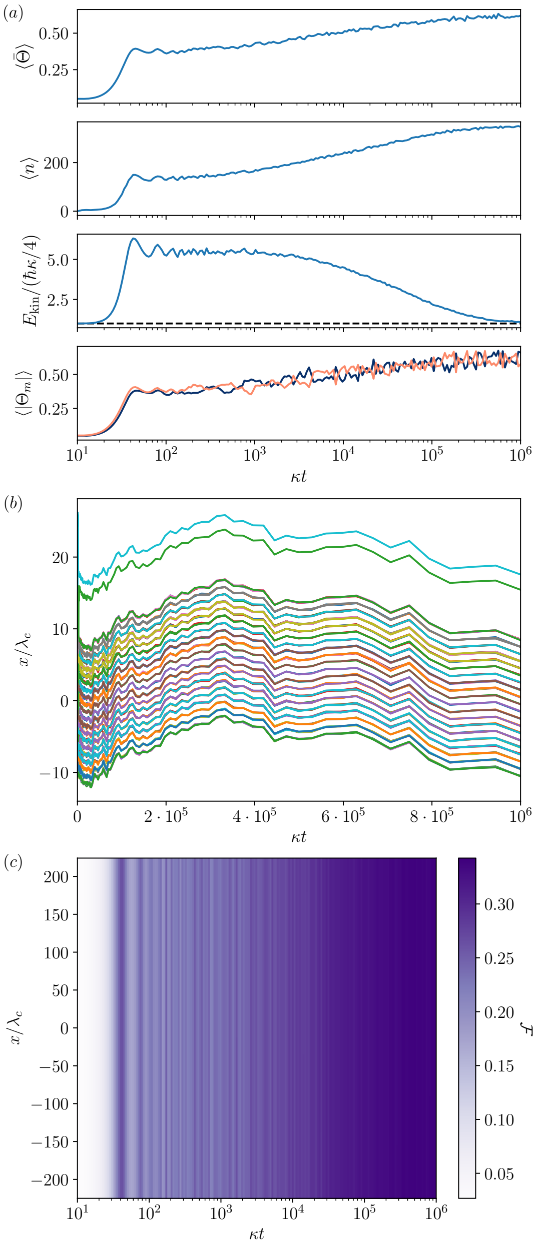

Figure 8.9.: Numerical simulation of the time evolution for $N = 100$ particles for two modes ($M = 2$) with equal wave number. The pump power is $M\zeta = 15$ and the initial distribution width $L_a = 20\lambda_c$. In (a) averages over 50 trajectories are depicted: The total order parameter $\langle\bar{\Theta}\rangle$, the total intracavity photon number $\langle n\rangle$, the kinetic energy E_{kin} and the individual order parameters $\langle|\Theta_m|\rangle$. An example trajectory of the particles' positions is shown in (b) on a linear time axis. Finally, subfigure (c) shows the function $\mathcal{F}(x)$ defined in Eq. (8.20) for the same example trajectory.

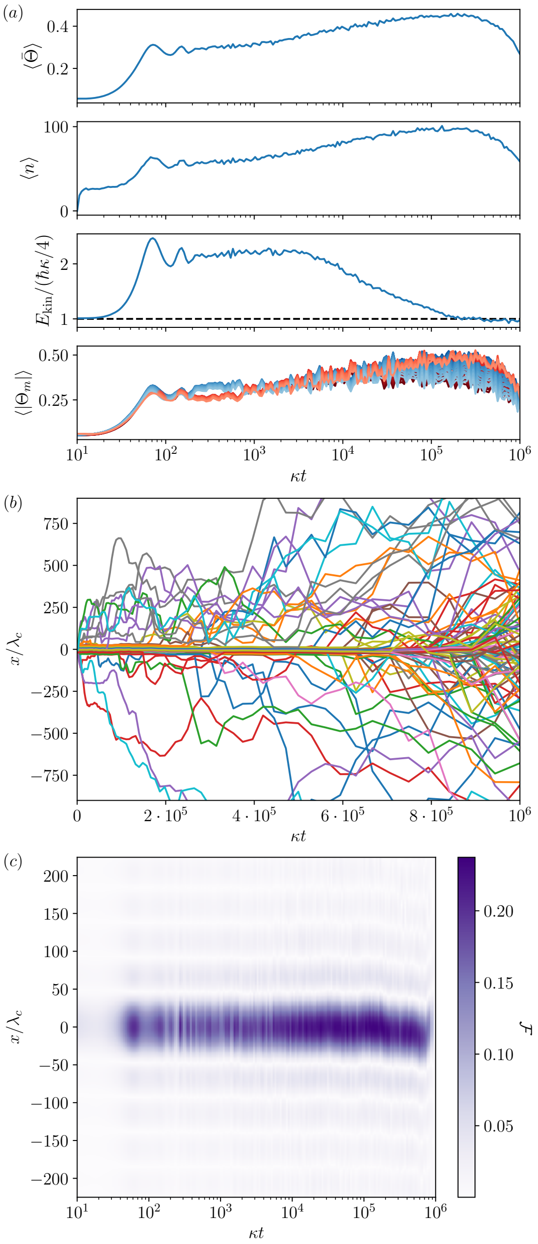

Figure 8.10.: Time evolution for $\zeta < \zeta_c^\downarrow$ and $w = 20\lambda_c$. The parameters are $M = 50$, $M\zeta = 6$ and $\zeta = 0.12$. See Fig. 8.9 for details.

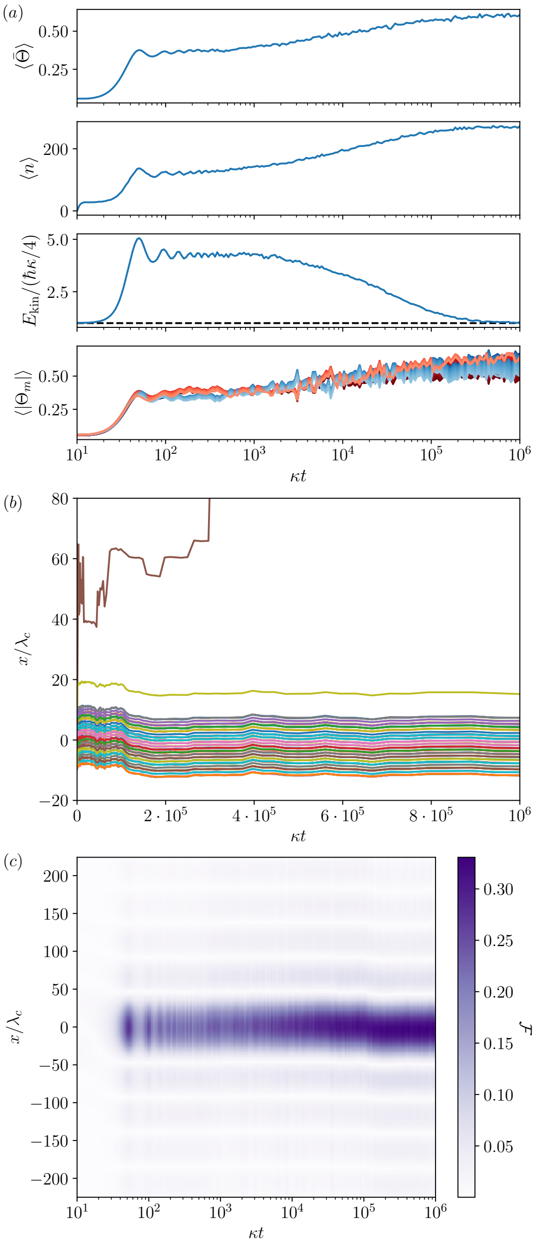

Figure 8.11.: Time evolution for $\zeta_c^\downarrow < \zeta < \zeta_c^\uparrow$ and $w = 20\lambda_c$. The parameters are $M = 50$, $M\zeta = 12$ and $\zeta = 0.24$. See Fig. 8.9 for details.

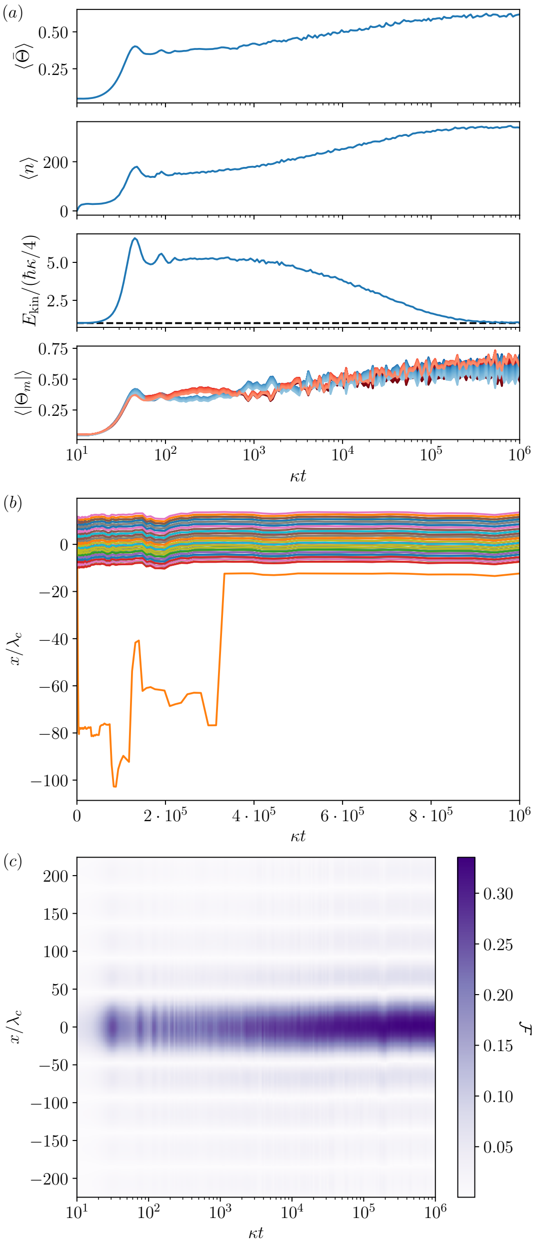

Figure 8.12.: Time evolution for $\zeta_c^{\uparrow} < \zeta < 1$ and $w = 20\lambda_c$. The parameters are $M = 50$, $M\zeta = 15$ and $\zeta = 0.3$. See Fig. 8.9 for details.

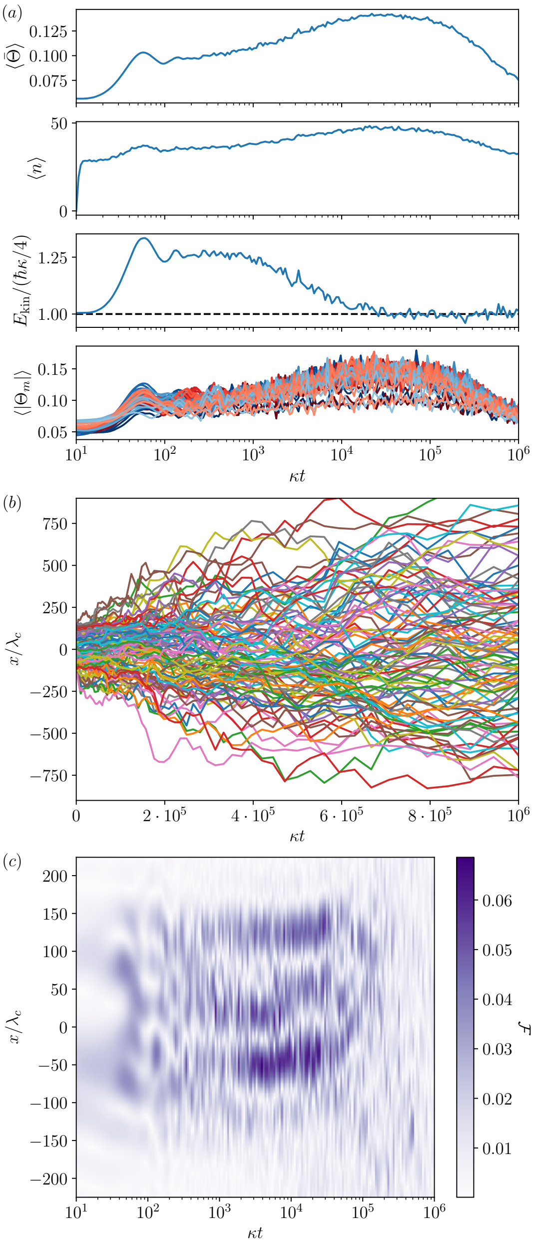

Figure 8.13.: Time evolution for $\zeta_c^{\uparrow} < \zeta < 1$ and $w = 300\lambda_c$. The parameters are $M = 50$, $M\zeta = 15$ and $\zeta = 0.3$. See Fig. 8.9 for details.

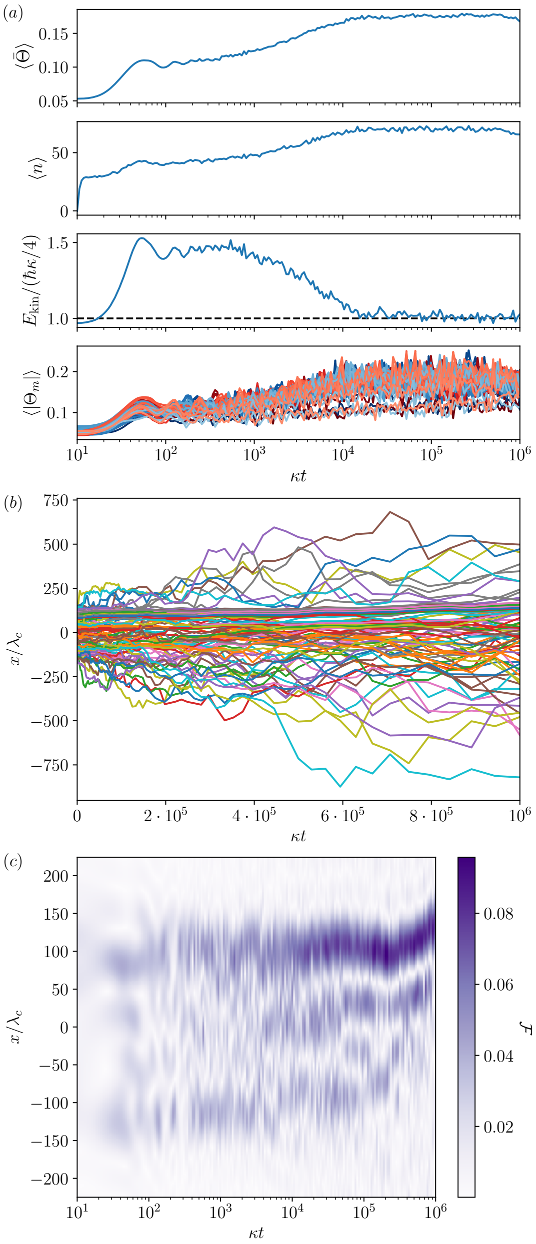

Figure 8.14.: Time evolution for $\zeta_c^{\uparrow} < \zeta < 1$ and $w = 300\lambda_c$. The parameters are $M = 50$, $M\zeta = 20$ and $\zeta = 0.4$. See Fig. 8.9 for details.

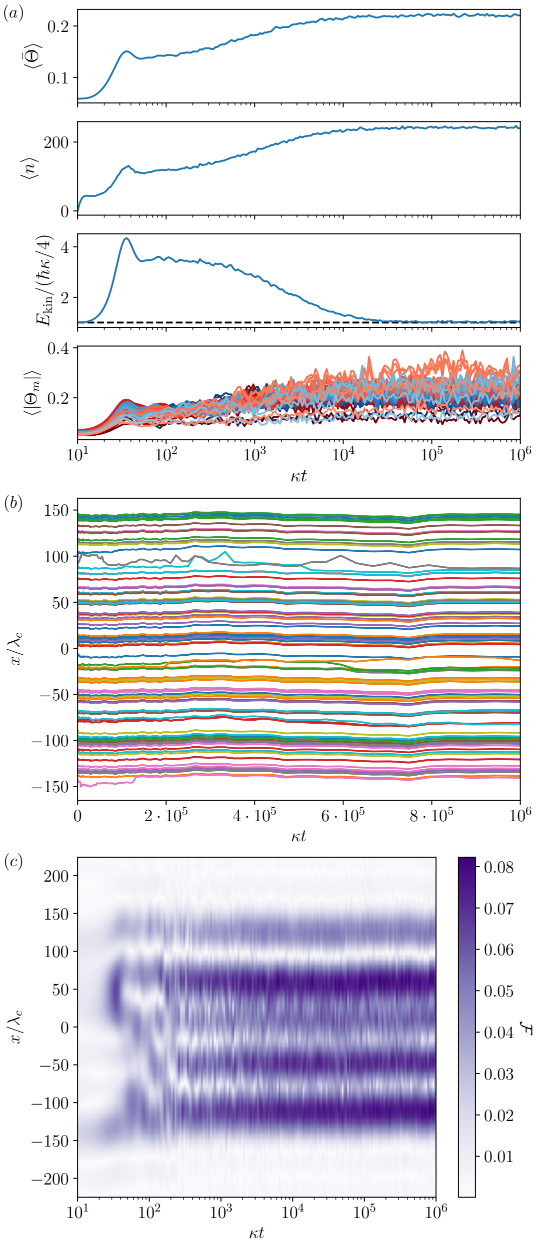

Figure 8.15.: Time evolution for $\zeta > 1$ and $w = 300\lambda_c$. The parameters are $M = 50$, $M\zeta = 60$ and $\zeta = 1.2$. See Fig. 8.9 for details.

The kinetic energy follows a damped oscillation. When the cloud does not organize fast enough, it expands freely and bounces back from the fixed harmonic trap, leading to the oscillations in the beginning. Since the atoms are less strongly trapped by the cavity field for larger M, the effect is more pronounced here. The oscillation frequency is independent of N.

Comparing different atom numbers we observe that cooling takes longer for a larger atom number N, which is consistent with previous results [8.4]. One has to note that this is due to the specific scaling we choose $\zeta \propto N$, which keeps the maximum potential depth constant.

Summarizing, from the point of view of cooling one benefits from more modes - it leads to faster cooling. The reason might be that for a similar total pump power the ordering is smaller for the many mode case (because it is difficult to adapt to many modes and each individual mode gets less power). This means that the initial increase in kinetic energy coming from the atoms falling into the potential well is much smaller.

Acknowledgments: This work was partly done in collaboration with Ivor Krešić and Ticijana Ban from the Institut za Fiziku in Zagreb, Croatia.

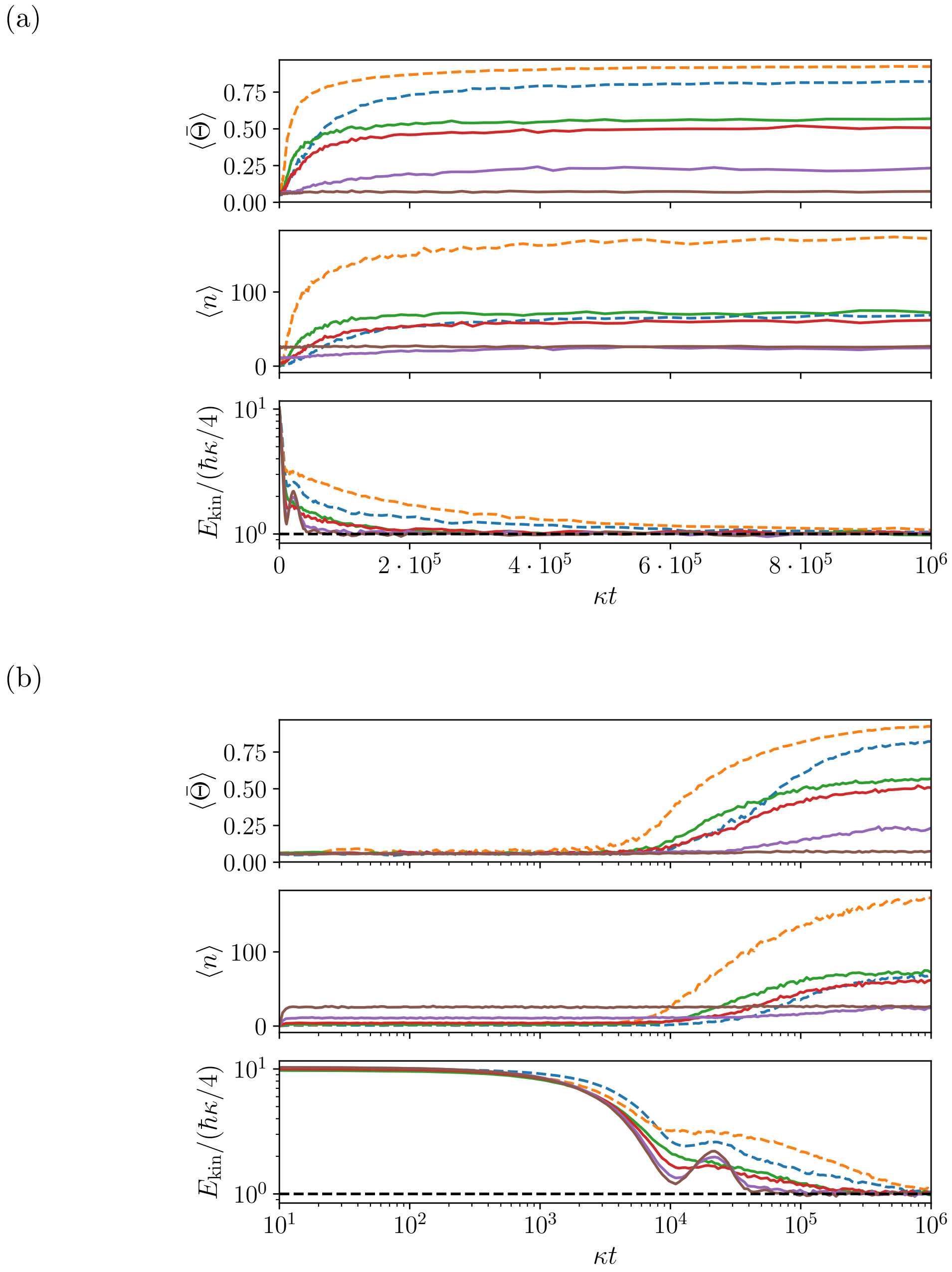

Figure 8.16.: Cooling dynamics of the averages over 50 trajectories of the total order parameter $\bar{\Theta}$, the total intra-cavity intensity $\sum_m |\alpha_m|^2$ and the kinetic energy E_{kin} for $N = 100$. The dashed blue curve was obtained for $M = 1$ and $M\zeta = 2$. All other curves have the same absolute pump strength $M\zeta = 4$ and different mode numbers $M = 1$ (dashed orange), $M = 2$ (green), $M = 6$ (red), $M = 20$ (purple) and $M = 50$ (brown). The data is depicted for (a) a linear and (b) a logarithmic time axis.

(a)

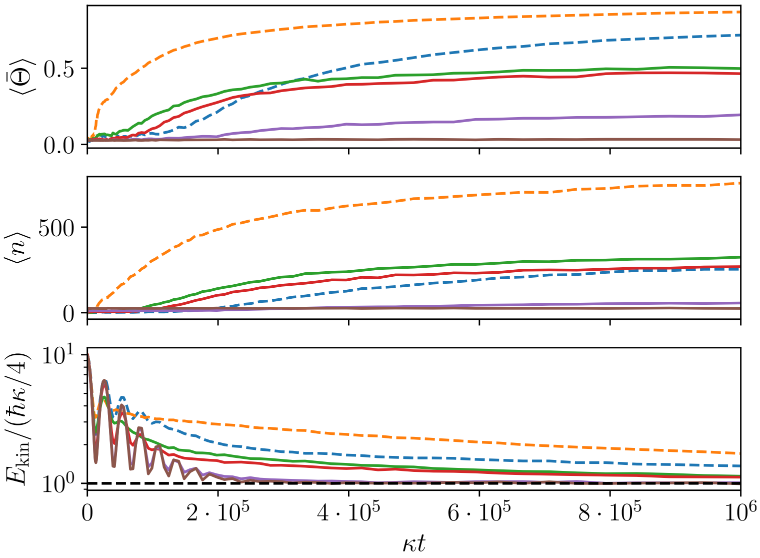

(b)

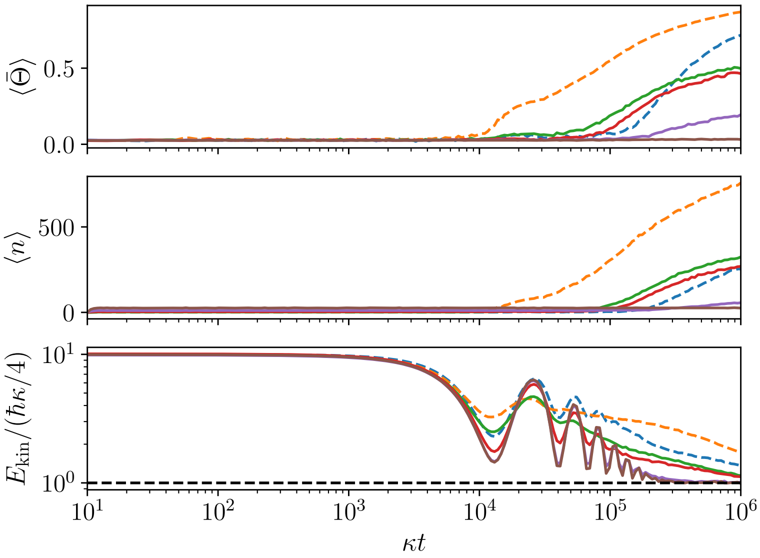

Figure 8.17.: Cooling dynamics for $N = 500$ with the same parameters as in Fig. 8.16.

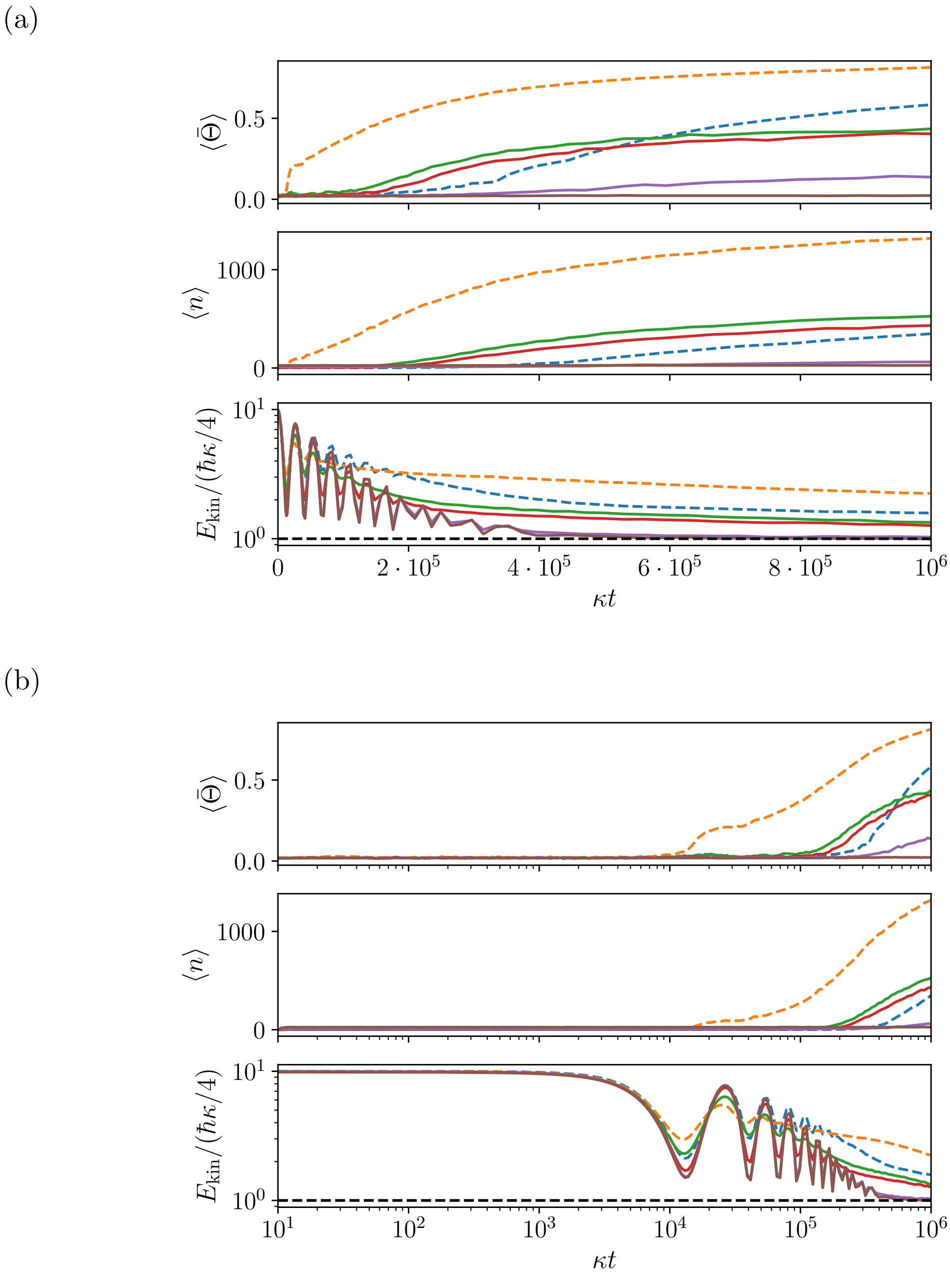

Figure 8.18.: Cooling dynamics for $N = 1000$ with the same parameters as in Fig. 8.16.

9. Conclusions

In this thesis we considered cold atoms in transversally pumped multi-mode optical resonators and their potential applications for solving real world optimization problems. Collective scattering of pump light into the resonator results in a complex coupled atom-field dynamics. For red cavity detuning, the time lag between atom and field dynamics results in cooling of the atomic motion. Above a pump intensity threshold, the atoms order according to their self-created trapping potential stemming from the interference of pump and cavity fields. An ordered configuration maximizes the light field in the resonator while minimizing the energy, for red detuning. Simultaneously pumping with several frequencies leads to a multitude of different optimal patterns and it is at first not clear which pattern or combination thereof the atoms attain [9.1]. When the dynamics of the light fields is much faster than the atomic motion, the self-trapping potentials can be seen as collective interaction potentials depending on all atom positions.

In order to simulate an optimization problem we first have to shape such an interaction potential (or cost function) such that the lowest energy state corresponds to the solution of the problem. In addition to that the system must dynamically attain this state to find the solution. Multi-mode resonators provide several unique features for realizing these requirements. Since all atoms interact with the same light fields, the interactions are infinite-range and couple all atoms. Multi-mode pumping allows for implementing conflicting constraints, which are always present in hard optimization problems. The manipulation of light is becoming more versatile every year [9.2], allowing for much flexibility in creating interference fields with different pump-cavity geometries. Finally, the light leaking out of the resonator gives insight about the atomic state and hence the measurement thereof yields information about the solution.

For classical atoms, a Langevin-type dynamics in the interaction potential emerges, where cavity cooling provides friction and photon loss leads to diffusion. We showed with extensive numerical simulations of a simple two mode model, that slowly increasing the pump strength lets the particles more probably find the global minimum of a potential landscape, a behavior analogous to thermal annealing. Starting with a higher temperature and cooling into the ordered phase results in a similar effect: higher initial temperatures lead to faster ordering according to the more stable phase, reminding of the Mpemba effect in water [9.3, 9.4]. Moreover, illuminating the atoms with a frequency comb can result in self-ordered clusters and faster cooling rates.

At nearly zero temperature the thermal fluctuations are superseded by emerging quantum fluctuations. Analogously, a slow increase of the pump strength implements a form of quantum annealing. The closed system performs coherent Hamiltonian dynamics instead of classical diffusion. In the framework of ultra-cold atoms in an optical lattice, we showed how to formally map the resulting cavity Hamiltonian to an Ising spin Hamiltonian with infinite-range interactions – the standard model of quantum annealing. With at least $N(N+1)/2$ pump-cavity mode pairs giving rise to sufficiently different interference fields, an arbitrary interaction matrix for an arbitrary problem can be created. We demonstrated how to obtain such a matrix for the example of a Hopfield network.

Special problems can be tackled with less resources, avoiding the N^2 overhead. In this vein we proposed a detailed implementation of a quantum simulator for the N-queens problem, where the task is to place N queens on an $N \times N$ chess board such they cannot attack each other according to chess rules. Variations of this problem were shown to be NP-complete and there exist hard instances for conventional classical algorithms for relatively small problem sizes. The problem is thus a promising candidate for testing if a quantum machine can do better than a classical one.

The implementation is based on a miniaturized chess board made from N ultra-cold atoms in an $N \times N$ optical lattice, where the tunneling of the atoms is frozen out in one direction. The chess rules are implemented by pumping from three directions with a frequency comb with only about N equidistant frequencies. One such beam invokes a repulsive interaction on lines, i.e. localized and translationally invariant in propagation direction and infinite-range perpendicular to the propagation direction. When the propagation directions are chosen accordingly, this energetically penalizes multiple occupation of diagonals and rows, as desired in the N-queens problem.

The solution state is again found via an adiabatic sweep by increasing the pump strength. During this sweep intermediate terms due to cavity-induced tunneling emerge, which cause highly non-local fluctuations. These typically cause problems for quantum Monte Carlo simulations of the quantum system, rendering our physical implementation hard to simulate on a classical device. Thus it is even more interesting to build the experiment and test for quantum advantage.

For future research it would be interesting to investigate the effect of cavity cooling in quantum annealing. For low enough steady state temperatures this could be used for ground state cooling and amend non-adiabatic errors during the sweep. Since cavity cooling only works for red cavity detuning, in our set-up we can only create attractive interactions. Thus it might be worthwhile to investigate the non-linearity due to the collective dispersive shift in the cavity as source of collective atom-atom interaction. Cooling in the open system is always accompanied by dephasing due to diffusion, which destroys coherent superpositions needed during the adiabatic sweep, which was already taken into account in Chapter 7. A better understanding of this interplay in the context of quantum simulation could lead to intriguing insights.

From the quantum simulation side a next step would be to check the effect of non-stoquasticity created by cavity-induced tunneling in the N-queens problem and other problems. For reliable theoretical predictions of quantum advantage one has to ask how the gap closes for larger system sizes and if this scales more favorably for large non-local fluctuations.

A. Additional material

A.1. Hermite-Gaussian modes

We consider a special case of a Fabry-Pérot resonator in three dimensions, namely two spherical mirrors with the same radius of curvature R at a distance L. The geometry of the resonator can be summarized by the so-called stability parameter

$$g = 1 - \frac{L}{R}. \tag{A.1}$$

There are stable modes for $-1 < g < 0$ and $0 < g < 1$ [A.1]. Special cases are therefore the confocal resonator ($g = 0$, $R = L$), the planar resonator ($g = 1$, $R \to \infty$) and the concentric resonator ($g = -1$, $R = L/2$). They are on the edge of the stability region, meaning that small deviations would lead to instabilities.

Assuming that the light travels into the z-direction, the field takes the form $\mathcal{G} = \tilde{\mathcal{G}}(x, y, z)e^{-ikz}$. The Helmholtz equation from Eq. (2.7) is then approximately given by

$$\frac{\partial^2 \tilde{\mathcal{G}}}{\partial x^2} + \frac{\partial^2 \tilde{\mathcal{G}}}{\partial y^2} - 2ik\frac{\partial \tilde{\mathcal{G}}}{\partial z} = 0 \tag{A.2}$$

where we neglected the term $\partial^2\tilde{\mathcal{G}}/\partial z^2$. This so-called paraxial approximation is valid when $|\partial^2\tilde{\mathcal{G}}/\partial z^2| \ll |k\partial\tilde{\mathcal{G}}/\partial z|$.

A complete set of solutions for this equation are the Hermite-Gaussian beams, which are given by [A.1]

$$\mathcal{G}_{lm}(x, y, z) = \mathcal{A}_{lm}(x, y, z)e^{-i\Phi_{lm}(x,y,z)} \tag{A.3}$$

with the amplitude and phase

$$\mathcal{A}_{lm}(x, y, z) = \frac{\mathcal{N}_{lm}}{w(z)} H_l\left(\sqrt{2}\frac{x}{w(z)}\right) H_m\left(\sqrt{2}\frac{y}{w(z)}\right) \exp\left(-\frac{x^2+y^2}{w^2(z)}\right) \tag{A.4a}$$

$$\Phi_{lm}(x, y, z) = kz + k\frac{x^2+y^2}{2\mathcal{R}(z)} - \phi_{lm}(z), \tag{A.4b}$$

where the H_l denote the Hermite polynomials. The beam waist w of the $l = m = 0$ beams, the radius of curvature $\mathcal{R}$ of the phase fronts and the Gouy phase shift ϕ_{lm} are given by

$$w(z) = w_0 \sqrt{1 + \left(\frac{z}{z_R}\right)} \tag{A.5}$$

$$\mathcal{R}(z) = z \left(1 + \left(\frac{z_R}{z}\right)^2\right) \tag{A.6}$$

$$\phi_{lm}(z) = (l + m + 1) \arctan\left(\frac{z}{z_R}\right) \tag{A.7}$$

with $w_0 = \sqrt{2z_R/k}$. The Rayleigh length z_R and the wave number k are the characteristic length scales. We choose $\mathcal{N}_{lm} = (2^{l+m} n! m!)^{-\frac{1}{2}} w_0$ such that the maximum is normalized to 1. The integers l and m parametrize the transversal modes, which are often denoted by TEM_{lm}.

Just as for the one-dimensional case in Sec. 2.2.2, we have to impose the boundary condition, which guarantees that the field is zero at the mirrors. Thereby we assume that the mirrors are placed at a distance $L \gg z_R$, where the phase fronts are spherical. Given a certain combination of length and mirror curvature, the boundary conditions fix the values of the Rayleigh length z_R and the resonant wave numbers k_{nlm}.

For the transversal shape, we impose that the curvature of mirrors and phase fronts coincide, thus $\mathcal{R}(L/2) = R$, which fixes the Rayleigh length $z_R = (L/2)\sqrt{2R/L - 1}$. Longitudinally, on the z-axis we know from the 1D considerations above, that the phase shift from one mirror to the other has to be a multiple of π for resonance [A.2]. The Gouy phase at the mirror positions takes the simple form

$$\begin{aligned} \phi_{lm}\left(\frac{L}{2}\right) &= (l + m + 1) \arctan \sqrt{\frac{L}{2R - L}} \\ &= (l + m + 1) \arctan \sqrt{\frac{1 - 1 + \frac{L}{R}}{1 + 1 - \frac{L}{R}}} \\ &= \frac{1}{2}(l + m + 1) \arccos(g), \end{aligned} \tag{A.8}$$

where we used the identity

$$\arccos(x) = 2 \arctan \sqrt{\frac{1 - x}{1 + x}}. \tag{A.9}$$

Noting that $\phi_{lm}(z) = -\phi_{lm}(-z)$ we get

$$\begin{aligned} \Phi_{nlm}(0, 0, L/2) - \Phi_{nlm}(0, 0, -L/2) &= n\pi \\ k\frac{L}{2} - \phi_{lm}\left(\frac{L}{2}\right) - \left\{-k\frac{L}{2} - \phi_{lm}\left(-\frac{L}{2}\right)\right\} &= n\pi \\ kL - 2\phi_{lm}\left(\frac{L}{2}\right) &= n\pi \\ kL - (l + m + 1) \arccos(g) &= n\pi. \end{aligned} \tag{A.10}$$

This condition results in the resonant wave numbers

$$k_{nlm} = (n\pi + (l+m+1)\arccos(g))/L. \tag{A.11}$$

In units of the free spectral range $\nu_0 = c/(2L)$, i.e. the frequency spacing between longitudinal modes, we get the resonant frequencies

$$\frac{\nu_{nlm}}{\nu_0} = \frac{ck_{nlm}}{2\pi\nu_0} = n + \frac{1}{\pi}(l+m+1)\arccos(g). \tag{A.12}$$

In a standing wave resonator where $z = 0$ is located at its center, even and odd modes then take the form of the real and imaginary part of $\mathcal{G}_{lm}$ with $k = k_{nlm}$, respectively, leading to

$$\mathcal{G}_{nlm} = \begin{cases} \frac{\mathcal{A}_{nlm}}{2}\cos(\Phi_{nlm}) \text{ for } n \,\text{odd} \\ \frac{\mathcal{A}_{nlm}}{2}\sin(\Phi_{nlm}) \text{ for } n \,\text{even.} \end{cases} \tag{A.13}$$

A.2. Steady state cavity fields in transversally pumped cavities

The aim of this section is a purely classical derivation of the steady state cavity field amplitudes for transversal pumping of a single atom or several atoms in a cavity. By using the value of the spontaneous emission rate obtained from quantum optics, we formally obtain the same expressions as in Chapter 3. This section follows Ref. [A.3], adapted to the notation in this thesis.

Classically in the limit of low saturation, an atom in an electromagnetic field E can be considered an oscillating dipole $d = \mathcal{P}E$ with the linear polarizability

$$\mathcal{P} = 6\pi\epsilon_0 c^3 \frac{2\gamma/\omega_a^2}{\omega_a^2 - \omega^2 - 2i(\omega^3/\omega_a^2)\gamma}. \tag{A.14}$$

It can be derived from a Lorentz oscillator model with a frequency dependent decay rate [A.3, A.4]. The imaginary part contributes to absorptive and the real part to dispersive effects.

Thereby ω_a is the atomic resonance frequency and γ the (amplitude) damping rate. Within the rotating wave approximation $\Delta_a = \omega - \omega_a \ll \omega_a$ we can use $\omega^2 - \omega_a^2 \approx 2\omega\Delta_a$ to simplify the expression. It can be even further simplified by going to the dispersive regime $|\Delta_a| \ll \gamma$. We obtain

$$\mathcal{P} \overset{\text{RWA}}{\approx} \frac{6\pi\epsilon_0}{k_a^3}\frac{-\Delta_a + i\gamma}{\Delta_a^2 + \gamma^2}\gamma \overset{\gamma\ll|\Delta_a|}{\approx} -\frac{6\pi\epsilon_0}{k_a^3}\frac{\gamma}{\Delta_a}. \tag{A.15}$$

Note that the absorptive imaginary part, and thus dissipation due to the atom, vanishes in the second approximation. Plugging in the result from quantum mechanics [A.5] for the damping rate $\gamma = k_a^3\mu^2/(6\pi\epsilon_0\hbar)$ yields $\mathcal{P} = -\mu^2/(\hbar\Delta_a)$, which is consistent with Sec. 2.3.2.

A.2.1. Scattering into a Gaussian mode

We are now interested in a dipole scattering from an incident field α_{in} into a Gaussian beam mode. The radiated mode amplitude in the far-field can be written in the simple form

$$\alpha_M = i\beta\alpha_{\text{in}} \tag{A.16}$$

with the parameter $\beta = k\mathcal{P}/(\pi w_0^2\epsilon_0)$. It is obtained by calculating the overlap between a Gaussian beam with waist w_0 and the dipole radiation pattern in the far-field known from classical electrodynamics [A.6]

$$\mathcal{E}_{\text{rad}} = \frac{k^2 \sin\theta}{4\pi\epsilon_0}\frac{e^{ikR}}{R}\mathcal{P}\mathcal{E}, \tag{A.17}$$

where θ is the angle between polarization and observation direction and R is the distance. Inserting the polarizability we get

$$\beta \overset{\text{RWA}}{\approx} \frac{6}{k^2w_0^2}\frac{-\Delta_a + i\gamma}{\Delta_a^2+\gamma^2}\gamma \overset{\gamma\ll|\Delta_a|}{\approx} -\frac{6}{k^2w_0^2}\frac{\gamma}{\Delta_a}. \tag{A.18}$$

In order to compare to quantum mechanical results, we plug in the value of γ from Wigner-Weisskopf theory and obtain

$$\beta = -\frac{\mu^2 k}{\pi w_0^2\epsilon_0\hbar\Delta_a}. \tag{A.19}$$

A.2.2. Scattering via atoms into an optical resonators

Now we consider the scattering of an atom sitting at an anti-node of a cavity mode, which is pumped with a field α_{in}. In order to obtain the resulting steady state cavity field, we consider the condition analogous to the one in Sec. 2.2.1

$$\alpha \overset{!}{=} r^2 e^{2ikL}\alpha + 2i\beta\alpha_{\text{in}} \tag{A.20}$$

with the pump term $2i\beta\alpha_{\text{in}}$. The factor 2 comes from the two scattering directions [A.3].

Solving for the cavity field yields analogously

$$\alpha_{\text{st}} = \frac{2i\beta\alpha_{\text{in}}}{1-r^2e^{2ikl}} \approx \frac{2i\beta\alpha_{\text{in}}}{q^2}\frac{1}{1-i\Delta_c/\kappa} = -\beta\frac{c}{L}\alpha_{\text{in}}\frac{1}{\Delta_c+i\kappa}, \tag{A.21}$$

where in the second step we performed the same approximation as in Sec. 2.2.1, which is valid close to a resonance [A.3]. Plugging in the value of β with the quantum mechanical expression for γ from Eq. (A.19) reveals the identity

$$-\beta\frac{c}{L} = \frac{\mu^2}{\hbar^2}\frac{\hbar\omega}{2V\epsilon_0}\frac{1}{\Delta_a} = \frac{\mu^2}{\hbar^2}\mathcal{E}_0^2\frac{1}{\Delta_a} = \frac{g^2}{\Delta_a} = U_0, \tag{A.22}$$

with the mode volume $V = L\pi w_0^2/2$. The effective mode area is thereby $A = \pi w_0^2/2$. Using $\eta = U_0\alpha_{\text{in}}$ as introduced in Sec. 3.1.1, Eq. (A.21) becomes

$$\alpha_{\text{st}} = \frac{U_0\alpha_{\text{in}}}{\Delta_c + i\kappa} = \frac{\eta}{\Delta_c + i\kappa}. \tag{A.23}$$

This corresponds the single-atom single-mode case of Eq. (3.20), when retardation effects and noise are neglected.

More realistically, the dipole is also driven by the cavity field itself. This can be taken into account by adding the corresponding terms in the steady state condition [A.3]

$$\alpha \overset{!}{=} r^2 e^{2ikL}\alpha + 2i\beta(\alpha_{\text{in}} + \alpha). \tag{A.24}$$

In a derivation analogous to the one above this leads to an effective shift in the detuning by U_0

$$\alpha_{\text{st}} = \frac{\eta}{\Delta_c - U_0 + i\kappa}. \tag{A.25}$$

Finally, when the cavity is filled with N atoms, it is the order parameter from Eq. (3.12) which quantifies how much light is scattered into the resonator. For a single mode it takes the form

$$\Theta = \frac{1}{N}\sum_j \mathcal{H}(x_j)\mathcal{G}^*(x_j). \tag{A.26}$$

Then the steady state condition analogous to Eq. (A.20) valid for $N|U_0| \ll |\Delta_c|$ becomes

$$\alpha \overset{!}{=} r^2 e^{2ikL}\alpha + 2i\beta N\Theta\alpha_{\text{in}} \tag{A.27}$$

and consequently

$$\alpha_{\text{st}} = \frac{\eta}{\Delta_c + i\kappa}N\Theta. \tag{A.28}$$

Compare again to Eq. (3.20) and Eq. (3.29).

A.3. Quantum Brownian motion of atoms in a cavity

In this section we present a quantum Brownian motion master equation for quantum particles in a transversally pumped optical resonator. Our motivation is to obtain a master equation without dynamical fields which still includes friction.

A.3.1. Motivation

We follow here a route analogous to the classical derivation in Sec. 3.2.1. In this vein, the master equation can be seen as the quantum analog to the Fokker-Planck equation in Eq. (3.25). It turns out, however, that it is not as straightforward as in the classical case.

To avoid unnecessary indices, we consider the single-mode case here (the extension to the non-cross-scattering multi-mode case is trivial). For $N|U_0| \ll |\Delta_c|$ and $|\mathcal{H}(x)|^2 = 1$, the corresponding Hamiltonian is given by

$$H = \sum_j \frac{\hat{p}_j^2}{2m_a} + \hbar N \eta \hat{\Theta}(a + a^\dagger) - \hbar \Delta_c a^\dagger a, \tag{A.29}$$

which is the single-mode case of Eq. (3.8) with the single-mode order operator

$$\hat{\Theta} = \frac{1}{N} \sum_j \mathcal{H}(\hat{x}_j) \mathcal{G}^*(\hat{x}_j). \tag{A.30}$$

Importantly, we consider the case for real interference fields $\mathcal{H}(x)\mathcal{G}^*(x) \in \mathbb{R}$, such that the order operator is Hermitian*. The full open-system dynamics is correspondingly given by the master equation

$$\dot{\rho} = -\frac{i}{\hbar}[H, \rho] + \kappa(2a\rho a^\dagger - a^\dagger a \rho - \rho a^\dagger a). \tag{A.31}$$

As described in Sec. 3.1.2, the open system can be described by the Langevin equations in Eqs. (3.10) for position $\hat{x}$, momentum $\hat{p}$ and field a. We now conduct the same elimination procedure as in the classical case in Sec. 3.2.1. Again taking into account linear friction only, we obtain the effective momentum equation

$$\begin{aligned}\dot{\hat{p}}_j = &- iN^2\eta^2 \frac{\Delta_c}{\Delta_c^2 + \kappa^2} \left([\hat{p}_j, \hat{\Theta}]\hat{\Theta} + \hat{\Theta}[\hat{p}_j, \hat{\Theta}] \right) \\ &- iN^2\eta^2 \frac{2\Delta_c \kappa}{(\Delta_c^2 + \kappa^2)^2} \left([\hat{p}_j, \hat{\Theta}]\dot{\hat{\Theta}} + \dot{\hat{\Theta}}[\hat{p}_j, \hat{\Theta}] \right) \\ &- iN\eta \sqrt{\frac{2\kappa}{\Delta_c^2 + \kappa^2}} \left([\hat{p}_j, \hat{\Theta}]\hat{\zeta} + \hat{\zeta}[\hat{p}_j, \hat{\Theta}] \right)\end{aligned} \tag{A.32}$$

with the Hermitian noise operator $\hat{\zeta} = (\hat{\xi} + \hat{\xi}^\dagger)/2$. This is the quantum analog to the momentum equation in Eq. (3.21).

While in the classical case the transformation to a Fokker-Planck equation is unique and straightforward, the transformation to a master equation in the quantum case is more involved and ambiguous, and further approximations have to be made. The problem thereby is the friction term containing $\dot{\hat{\Theta}}$. Ignoring this term, the corresponding master equation is of Lindblad form and was already presented in Eq. (3.30) and in several previous works such as Ref. [A.7]. In the single-mode case and for Hermitian order operators it is given by

$$\dot{\rho} = -\frac{i}{\hbar}[\tilde{H}, \rho] + N^2\eta^2 \frac{\kappa}{\Delta_c^2 + \kappa^2} \left(2\hat{\Theta}\rho\hat{\Theta} - \hat{\Theta}^2\rho - \rho\hat{\Theta}^2 \right) \tag{A.33}$$

---

[*] Note that a global x-independent phase would not change anything.

with

$$\tilde{H} = \sum_j \frac{\hat{p}_j^2}{2m_a} + \hbar N^2 \eta^2 \frac{\Delta_c}{\Delta_c^2 + \kappa^2} \hat{\Theta}^2. \tag{A.34}$$

This master equation, however, always converges to an infinite temperature steady state, as we will show later. From classical intuition this is clear, since the friction was totally neglected and thus cannot counteract the noise. The aim is now to include a linear friction term.

A.3.2. Quantum Brownian motion master equation

Reference [A.8] shows a detailed derivation of a quantum Langevin equation for a system operator Y of a system linearly coupling to a harmonic oscillator bath via the coupling operator X. Its general form after the first Markov approximation

$$\dot{Y} = \frac{i}{\hbar}[H_{\mathrm{sys}}, Y] - \frac{i}{2\hbar}\{[X, Y], \zeta(t) - \gamma \dot{X}\} \tag{A.35}$$

is exactly the same as Eq. (A.32). The curly brackets denote the anti-commutator.

Introducing a thermal bath with temperature T, a quantum master equation can be derived. The quantum Brownian motion master equation is given by [A.8]

$$\dot{\rho} = -\frac{i}{\hbar}[H_{\mathrm{sys}}, \rho] - \frac{i\gamma}{2\hbar}\left[X, \left\{\dot{X}, \rho\right\}\right] - \frac{\gamma k_{\mathrm{B}} T}{\hbar^2}[X, [X, \rho]] \tag{A.36}$$

with the temperature T and the damping rate $\mu = \gamma / m_a$. It is valid when the correlation time of the noise is much shorter than the time scale of the system dynamics and the damping, leading to the validity condition $\hbar\mu \ll k_{\mathrm{B}}T$. Thus it is capable of describing only the case of relatively high temperatures[†]. For a Brownian particle without any potential we have the coupling operator $X = \hat{x}$, and thus $\dot{X} = \hat{p}/m_a$. Note that this master equation does not have Lindblad form and is thus not guaranteed to preserve the positivity of the density operator.

For our system the quantum Brownian motion master equation takes the form [see Eq. (3.32)]

$$\begin{aligned} \dot{\rho} = &-\frac{i}{\hbar}[\tilde{H}, \rho] \\ &+ iN^2\eta^2 \frac{2\Delta_c \kappa}{(\Delta_c^2 + \kappa^2)^2}(\hat{\Theta}\rho\dot{\hat{\Theta}} - \dot{\hat{\Theta}}\rho\hat{\Theta} + \hat{\Theta}\dot{\hat{\Theta}}\rho - \rho\dot{\hat{\Theta}}\hat{\Theta}) \\ &+ N^2\eta^2 \frac{\kappa}{\Delta_c^2 + \kappa^2}(2\hat{\Theta}\rho\hat{\Theta} - \hat{\Theta}^2\rho - \rho\hat{\Theta}^2). \end{aligned} \tag{A.37}$$

[†] Note that this is not the well-known quantum optical master equation, which describes for instance the case of a cavity field coupled to the radiation modes outside the cavity, such as Eq. (A.31). In this case the system's motion is not assumed to be slow, while damping still is. Then the rotating wave approximation can be done, which simplifies the equations [A.8].

The temperature and the damping rate correspond to the classical values (see Sec. 3.2.1)

$$k_{\mathrm{B}}T = \hbar\frac{\Delta_c^2+\kappa^2}{-4\Delta_c} \tag{A.38}$$

$$\mu = -N^2\eta^2\frac{8\Delta_c\kappa}{(\Delta_c^2+\kappa^2)^2}\omega_{\mathrm{R}}. \tag{A.39}$$

As in the classical case, we need to assume $\Delta_c < 0$. Respecting the correct units, the coupling operator is $X = \hat{\Theta}/k$, where k^{-1} is a characteristic length scale of $\mathcal{H}(x)\mathcal{G}^*(x)$ (for instance we could have $\mathcal{H}(x)\mathcal{G}^*(x) = \cos(kx)$). Consistently, ignoring the central term containing the time derivative we get the master equation in Eq. (A.33). It is this term which gives rise to the desired friction.

Translating the validity of the master equation $\hbar\mu \ll k_{\mathrm{B}}T$ to our system parameters we obtain the condition

$$N\bar{n} \ll \frac{\Delta_c^2+\kappa^2}{4\Delta_c^2}\frac{\Delta_c^2+\kappa^2}{8\omega_{\mathrm{R}}\kappa} = \bar{n}_c\frac{(\Delta_c/\omega_{\mathrm{R}})^2+(\kappa/\omega_{\mathrm{R}})^2}{8\kappa/\omega_{\mathrm{R}}} = \bar{n}_c\frac{C^2+1}{8}\frac{\kappa}{\omega_{\mathrm{R}}} \tag{A.40}$$

with the maximum number of photons per particle $\bar{n} = N\eta^2/(\Delta_c^2+\kappa^2)$ and the classical threshold $\bar{n}_c = (\Delta_c^2+\kappa^2)/(4\Delta_c^2)$ [A.9]. We used the definition $\Delta_c = C\kappa$. That is, the description tends to be valid for weak pumping. Asking the question whether this still permits the self-ordered regime $\bar{n} > \bar{n}_c$ we get the condition

$$\frac{C^2+1}{8}\frac{\kappa}{\omega_{\mathrm{R}}} \gg N. \tag{A.41}$$

We see that entering the self-ordered regime while the master equation is valid is easier when $|C| \gg 1$ and thus $|\Delta_c| \gg \kappa$. It gets harder for large particle numbers N.

A.3.3. Ultra-cold atoms in optical lattices

Here we present a more detailed analysis of the Brownian motion master equation for the case of ultra-cold bosons in an optical lattice placed in a cavity, as introduced in Sec. 3.3. The Hamiltonian is given by [see Eq. (3.39)]

$$H_{\mathrm{L}} = -J\hat{B} + \hbar N\eta\hat{\Theta}_{\mathrm{L}}(a+a^\dagger) - \hbar\Delta_c a^\dagger a \tag{A.42}$$

with $\hat{B} = b_{i+1}^\dagger b_i + b_i^\dagger b_{i+1}$ and $\hat{\Theta}_{\mathrm{L}} = \sum_i (v_m^i \hat{n}_i + u_m^i \hat{B})/N$. The corresponding quantum Brownian motion master equation has the same form as Eq. (A.37), with the new definition of the order operator and the tunneling Hamiltonian as kinetic Hamiltonian, i.e.

$$\tilde{H}_{\mathrm{L}} = -J\hat{B} + \hbar(N\eta)^2\frac{\Delta_c}{\Delta_c^2+\kappa^2}\hat{\Theta}_{\mathrm{L}}^2. \tag{A.43}$$

We formulate the quantum Brownian motion master equation in the eigenbasis of the order operator defined by $\hat{\Theta}_{\mathrm{L}}|\nu\rangle = \theta_\nu|\nu\rangle$. Since $\hat{\Theta}_{\mathrm{L}}$ is assumed to be Hermitian here, the eigenvalues θ_ν are real. The time evolution of the density matrix elements $\rho_{\mu\nu} = \langle\mu|\rho|\nu\rangle$ is given by

$$\begin{aligned}
\dot{\rho}_{\mu\nu} =& -\left((N\eta)^2\frac{\kappa}{\Delta_c^2+\kappa^2}(\theta_\mu-\theta_\nu)^2 + i(N\eta)^2\frac{\Delta_c}{\Delta_c^2+\kappa^2}(\theta_\mu^2-\theta_\nu^2)\right)\rho_{\mu\nu} \\
&- i\frac{J}{\hbar}\sum_k\left[\left(1-i(N\eta)^2\frac{2\Delta_c\kappa}{(\Delta_c^2+\kappa^2)^2}(\theta_\mu-\theta_\nu)(\theta_\mu-\theta_k)\right)\left\langle\mu\left|\hat{B}\right|k\right\rangle\rho_{k\nu}\right. \\
&\qquad\left.-\left(1+i(N\eta)^2\frac{2\Delta_c\kappa}{(\Delta_c^2+\kappa^2)^2}(\theta_\mu-\theta_\nu)(\theta_k-\theta_\nu)\right)\left\langle k\left|\hat{B}\right|\nu\right\rangle\rho_{\mu k}\right] \\
=&(-\Gamma_{\mu\nu}-i\Omega_{\mu\nu})\rho_{\mu\nu} - i\frac{J}{\hbar}\sum_k\left((1-iK_{\mu k}^{\mu\nu})\left\langle\mu\left|\hat{B}\right|k\right\rangle\rho_{k\nu} - (1+iK_{k\nu}^{\mu\nu})\left\langle k\left|\hat{B}\right|\nu\right\rangle\rho_{\mu k}\right)
\end{aligned} \tag{A.44}$$

with the quantities

$$\Omega_{\mu\nu} = (N\eta)^2\frac{\Delta_c}{\Delta_c^2+\kappa^2}(\theta_\mu^2-\theta_\nu^2) \tag{A.45}$$

$$\Gamma_{\mu\nu} = (N\eta)^2\frac{\kappa}{\Delta_c^2+\kappa^2}(\theta_\mu-\theta_\nu)^2 \tag{A.46}$$

$$K_{kl}^{\mu\nu} = (N\eta)^2\frac{2\Delta_c\kappa}{(\Delta_c^2+\kappa^2)^2}(\theta_\mu-\theta_\nu)(\theta_k-\theta_l). \tag{A.47}$$

They describe the energy gaps, the dephasing rates and the friction, respectively. We will use later that

$$k_{\mathrm{B}}T = \hbar\frac{\Delta_c^2+\kappa^2}{-4\Delta_c} = -\frac{\hbar}{2}\frac{\Gamma_{\mu\nu}}{K_{\mu\nu}^{\mu\nu}}. \tag{A.48}$$

Note that in course of the derivation we applied the order operator to the left, which might be a problem when generalizing to non-Hermitian order operators.

Short times

For times much smaller than $\hbar J^{-1}$ we can assume that the J-term is constant and we obtain

$$\rho_{\mu\nu}(t) = \rho_{\mu\nu}(0)\exp\left(-\Gamma_{\mu\nu}t - i\Omega_{\mu\nu}t\right) \tag{A.49}$$

by integrating the first expression. The populations $\rho_{\nu\nu}$ do not get changed, but the coherences decay with a rate

$$\Gamma_{\mu\nu} = \kappa|\alpha_\mu-\alpha_\nu|^2 = (N\eta)^2\frac{\kappa}{\Delta_c^2+\kappa^2}(\theta_\mu-\theta_\nu)^2 = \kappa n_{\max}(\theta_\mu-\theta_\nu)^2. \tag{A.50}$$

Here $n_{\max}$ is the maximal photon number in the cavity. That is, the decay rate is given by the distance of the fields in phase space times the decay rate κ: The easier the fields can be distinguished, the faster the coherences vanish. This can be understood by thinking of the master equation as the average over many different quantum trajectories, where each trajectory corresponds to a different outcome of a continuous measurement of the field [A.10]. Thus if two states couple equally to the cavity, they do not dephase.

How does this affect the lifetime of quantum coherence of a lattice super-solid as observed in Ref. [A.11]? We consider the set-up in this experiment, where the pump laser has the same wave length as the lattice and is applied orthogonally, i.e. $\hat{\Theta}_\mathrm{L} = \sum_i (-1)^i \hat{n}_i$ (we fix the Wannier overlap to 1 here for simplicity). We consider one state where all N atoms scatter in phase and occupy every second site, and another state which has N_d defect atoms, i.e. atoms in the wrong well. This yields $(\theta_1 - \theta_2)^2 = (N/N - (N - 2N_d)/N)^2 = 4(N_d/N)^2$ and thus we get a dephasing rate

$$\Gamma = 4\kappa \left(\frac{N_d}{N}\right)^2 n_\mathrm{max}.$$

In experiments N is typically quite large, and if there are only few defect atoms the squared term can well compete with κ. Thus a small number of defect atoms does not lead to immediate dephasing. This was also observed in experiment, where the lattice super-solid was stable for typical experimental times [A.11].

Special case: 2 particles in double well

To gain more understanding let us solve the problem for one boson in a double well where $\hat{\Theta}_\mathrm{L} = \hat{n}_1 - \hat{n}_2$. The basis states are given by the occupation basis states $\{|1,0\rangle, |0,1\rangle\} \equiv \{|1\rangle, |2\rangle\}$, and the only non-zero matrix elements are $\langle 1|\hat{B}|2\rangle = \langle 2|\hat{B}|1\rangle = 1$. The density matrix elements follow the equations

$$\dot{\rho}_{11} = -i\frac{J}{\hbar}(\rho_{12}^* - \rho_{12}) = -2\frac{J}{\hbar}\mathrm{Im}(\rho_{12}) \tag{A.51a}$$

$$\dot{\rho}_{22} = i\frac{J}{\hbar}(\rho_{12}^* - \rho_{12}) = 2\frac{J}{\hbar}\mathrm{Im}(\rho_{12}) \tag{A.51b}$$

$$\dot{\rho}_{12} = -(\Gamma_{12} + i\Omega_{12})\rho_{12} - i\frac{J}{\hbar}(\rho_{22} - \rho_{11}) - \frac{J}{\hbar}K_{12}(\rho_{11} + \rho_{22}), \tag{A.51c}$$

where we note that $\rho_{11} + \rho_{22} = 1$, and the friction term forms an inhomogeneity. We use the short notation $K_{12} \equiv K_{12}^{12}$. It is useful to rewrite these equations with the variables $w = \rho_{22} - \rho_{11}$, $u = \mathrm{Re}(\rho_{12})$ and $v = \mathrm{Im}(\rho_{12})$ to obtain modified Bloch equations

$$\dot{w} = 4\frac{J}{\hbar}v \tag{A.52a}$$

$$\dot{u} = \Omega_{12}v - \Gamma_{12}u - \frac{J}{\hbar}K_{12} \tag{A.52b}$$

$$\dot{v} = -\Omega_{12}u - \Gamma_{12}v - \frac{J}{\hbar}w. \tag{A.52c}$$

By setting all the time-derivatives to zero, we can calculate the steady state values

$$w_\mathrm{st} = \frac{\Omega_{12}K_{12}}{\Gamma_{12}} \tag{A.53a}$$

$$u_\mathrm{st} = -\frac{J}{\hbar}\frac{K_{12}}{\Gamma_{12}} \tag{A.53b}$$

$$v_\mathrm{st} = 0. \tag{A.53c}$$

We rewrite the result using $K_{12}/\Gamma_{12} = -\hbar/(2k_\mathrm{B}T)$ to obtain the steady state populations

$$\begin{aligned}\rho_{11} =& \frac{1}{2} + \frac{1}{4}\frac{\hbar\Omega_{12}}{k_\mathrm{B}T} \\ \rho_{22} =& \frac{1}{2} - \frac{1}{4}\frac{\hbar\Omega_{12}}{k_\mathrm{B}T}.\end{aligned} \tag{A.54}$$

While without friction the steady state would be an equal population of both states, here we get a shift proportional to the ratio of the energy difference Ω_{12} over the self-consistent temperature. Their ratio corresponds to the Boltzmann factor up to first order in $\hbar|\Omega_{ij}|/(k_\mathrm{B}T)$, i.e.

$$\frac{\rho_{11}}{\rho_{22}} = \frac{1 + \frac{\hbar\Omega_{12}}{2k_\mathrm{B}T}}{1 - \frac{\hbar\Omega_{12}}{2k_\mathrm{B}T}} \approx \frac{\exp\left(\frac{\hbar\Omega_{12}}{2k_\mathrm{B}T}\right)}{\exp\left(-\frac{\hbar\Omega_{12}}{2k_\mathrm{B}T}\right)} = \exp\left(\frac{\hbar\Omega_{12}}{k_\mathrm{B}T}\right). \tag{A.55}$$

The steady state is thus the linear correction from the infinite temperature state and the master equation is confirmed to be valid only in the high-temperature limit. Note that for large $\hbar|\Omega_{ij}|/(k_\mathrm{B}T)$, the positivity of the density matrix is not preserved since ρ_{11} can become negative. This non-physical behavior comes from the non-Lindblad term.

We examine how this steady state is approached by assuming that u an v reach the steady state much faster than w. So by setting $\dot{u} = \dot{v} = 0$ we get the rate equation for the inversion

$$\dot{w} = 4\left(\frac{J}{\hbar}\right)^2 \frac{\Gamma_{12}}{\Gamma_{12}^2 + \Omega_{12}^2}\left(-w + \frac{\Omega_{12}K_{12}}{\Gamma_{12}}\right) \tag{A.56}$$

with the solution

$$w(t) = \left(w(0) - \frac{\Omega_{12}K_{12}}{\Gamma_{12}}\right)\exp\left(-4\left(\frac{J}{\hbar}\right)^2\frac{\Gamma_{12}}{\Gamma_{12}^2 + \Omega_{12}^2}t\right) + \frac{\Omega_{12}K_{12}}{\Gamma_{12}}. \tag{A.57}$$

Steady state

Let us now proceed to the general case. In the previous two sections we have seen that the matrix elements decay with the rate $\Gamma_{\mu\nu}$, and since $\Gamma_{\mu\mu} = 0$ only coherences decay. However, the friction term sustains some small coherence even in the steady state, as can be seen from Eqs. (A.53), which causes the linear thermal correction. $\Gamma_{\mu\nu}^{-1}$ is typically much smaller than the time needed to reach the steady state. Thus it makes sense to derive a rate equation for the populations only, which is valid on a coarse grained time scale where the coherences have already decayed. In principle one has to check in detail, however, if this is really valid for each case since the rates depend on the mode structure and can even become zero.

The master equation for the populations is given by [from Eq. (A.44)]

$$\dot{\rho}_\mu = -i\frac{J}{\hbar}\sum_{k\neq\mu}\langle\mu|\hat{B}|k\rangle(\rho_{k\mu} - \rho_{\mu k}), \tag{A.58}$$

where we use the notation $\rho_\mu \equiv \rho_{\mu\mu}$. The sum does not contain $k = \mu$ since $\langle \mu|\hat{B}|\mu\rangle = 0$. Thus populations are only coupled to coherences, and not directly among each other, which allows for separating populations and coherences.

We now consider the equations for $\dot{\rho}_{\mu\nu}$ in Eq. (A.44) for which $\mu \neq \nu$ and $\langle \mu|\hat{B}|\nu\rangle \neq 0$. These couple to populations ρ_{kk} on the one hand, but also to coherences ρ_{kl} $(k \neq l)$ with $\langle k|\hat{B}|l\rangle = 0$ on the other hand. We now make an approximation by ignoring these latter coherences with a tunneling matrix element equal to zero (this corresponds to an expansion in J). Then the remaining coherences couple to populations only:

$$\dot{\rho}_{\mu\nu} = (-\Gamma_{\mu\nu} - i\Omega_{\mu\nu})\rho_{\mu\nu} - i\frac{J}{\hbar}\langle \mu|\hat{B}|\nu\rangle \left[(\rho_\nu - \rho_\mu) - iK_{\mu\nu}(\rho_\nu + \rho_\mu)\right]. \tag{A.59}$$

Again we use $K_{\mu\nu} \equiv K^{\mu\nu}_{\mu\nu}$ since only those occur due to the approximation. In the case of two particles in a double well the approximation is exact since the only coherence ρ_{12} has $\langle 1|\hat{B}|2\rangle = 1 \neq 0$.

We now assume that they obtain a steady state before the populations change considerably and by setting $\dot{\rho}_{\mu\nu} = 0$ we obtain the steady state coherences

$$\rho_{\mu\nu} = -i\frac{J}{\hbar}\frac{1}{\Gamma_{\mu\nu} + i\Omega_{\mu\nu}}\langle \mu|\hat{B}|\nu\rangle \left[(\rho_\nu - \rho_\mu) - iK_{\mu\nu}(\rho_\nu + \rho_\mu)\right]. \tag{A.60}$$

Plugging this into the equation for the populations Eq. (A.58) yields the desired rate equation for the populations

$$\dot{\boldsymbol{\rho}} = M\boldsymbol{\rho} \tag{A.61}$$

where $\boldsymbol{\rho}$ is the vector containing the ρ_μ and where the matrix M is given by its components

$$M_{ij} = \begin{cases} -2\left(\frac{J}{\hbar}\right)^2 \sum_{k\neq i}\langle i|\hat{B}|k\rangle^2 \frac{\Gamma_{ik}}{\Gamma_{ik}^2+\Omega_{ik}^2}\left(1 + \frac{\Omega_{ik}K_{ik}}{\Gamma_{ik}}\right) & \text{for } i = j \\ -2\left(\frac{J}{\hbar}\right)^2 \langle i|\hat{B}|j\rangle^2 \frac{\Gamma_{ij}}{\Gamma_{ij}^2+\Omega_{ij}^2}\left(-1 + \frac{\Omega_{ij}K_{ij}}{\Gamma_{ij}}\right) & \text{for } i \neq j. \end{cases} \tag{A.62}$$

We note that $\Gamma_{ij} = \Gamma_{ji}$, $K_{ij} = K_{ji}$ and $\Omega_{ij} = -\Omega_{ji}$.

The steady state must fulfill

$$M\boldsymbol{\rho} = \sum_k M_{ik}\rho_k = -2\left(\frac{J}{\hbar}\right)^2 \sum_{k\neq i}\langle i|\hat{B}|k\rangle^2 \frac{\Gamma_{ik}}{\Gamma_{ik}^2 + \Omega_{ik}^2}\left(\rho_i - \rho_k + \frac{\Omega_{ik}K_{ik}}{\Gamma_{ik}}(\rho_i + \rho_k)\right) = 0 \tag{A.63}$$

and thus

$$\begin{aligned} \rho_i - \rho_j + \frac{\Omega_{ij}K_{ij}}{\Gamma_{ij}}(\rho_i + \rho_j) = 0 \\ \Rightarrow \quad \frac{\rho_i}{\rho_j} = \frac{1 - \frac{\Omega_{ij}K_{ij}}{\Gamma_{ij}}}{1 + \frac{\Omega_{ij}K_{ij}}{\Gamma_{ij}}} = \frac{1 + \frac{\hbar\Omega_{ij}}{2k_\mathrm{B}T}}{1 - \frac{\hbar\Omega_{ij}}{2k_\mathrm{B}T}} \approx \exp\left(\frac{\hbar\Omega_{ij}}{k_\mathrm{B}T}\right). \end{aligned} \tag{A.64}$$

The steady state corresponds again to a thermal state up to first order for high temperatures. As in the special case before, putting friction to zero $(K_{ij} = 0)$ yields a steady state with equal populations, which corresponds to the $T \to \infty$ limit. If two states couple equally to the modes, i.e. are degenerate eigenstates of $\hat{\Theta}_\mathrm{L}$, we get $\Gamma_{ij} = 0$, and the ratio of their populations is not determined at the steady state.

A.4. Non-adiabatic effects in a frequency-comb-pumped cavity

We consider the retardation part of the force from Eq. (8.4b) in Sec. 8.2, which contains only linear friction. This also captures cross-friction, i.e. friction felt by one atom caused by another. As before we consider the friction force for different mode configurations. For convenience, we define the single-particle damping rate $\mu_k = -8\omega_{\mathrm{R}}^k \frac{\eta^2\Delta_c\kappa}{(\Delta_c^2+\kappa^2)^2}$, which is positive for $\Delta_c < 0$. The recoil frequency $\omega_{\mathrm{R}}^k = \hbar k^2/(2m_a)$ is given for a certain wave number k.

Cosine mode

The retardation force on the jth particle is given by

$$F_{j,\mathrm{ret}} = -\mu_k \sin(kx_j) \sum_i p_i \sin(kx_i). \tag{A.65}$$

For one atom it simplifies to

$$F_{\mathrm{ret}} = -\mu_k p \sin^2(kx). \tag{A.66}$$

Since $\sin^2(kx) > 0$ this always results in friction for $\mu_k > 0$. Averaged over a uniform distribution, we get a reduction by a factor 1/2. Trapped particles spend much more time close to the zeros of the sine, and thus the reduction of friction due to the space dependence can become much larger.

We now switch to the case of two atoms. The force on atom 1 is given by

$$F_{1,\mathrm{ret}} = -\mu_k[p_1 \sin^2(kx_1) + p_2 \sin(kx_1)\sin(kx_2)]. \tag{A.67}$$

The first term is again the self-friction described above. The second term describes cross-friction, i.e. friction (or heating) of atom 1 due to atom 2.

The cross-friction term can be analyzed as follows (assuming $\mu_k > 0$): If both particles move into the same direction ($p_1p_2 > 0$), we get friction if $\sin(kx_1)\sin(kx_2) > 0$ and heating otherwise. For opposite directions ($p_1p_2 < 0$), there is friction for $\sin(kx_1)\sin(kx_2) < 0$. This cross-friction term is plotted in Figure A.1.

When the atoms are already trapped close to the potential minima, their motion can be described by two-particle oscillations with an oscillation frequency ω and the relative phase $\Delta\Phi$. They can be written as

$$x_1(t) = A\cos(\omega t - \Delta\Phi/2) \tag{A.68a}$$

$$x_2(t) = A\cos(\omega t + \Delta\Phi/2) \tag{A.68b}$$

or

$$x_{\mathrm{cm}}(t) = \frac{1}{2}(x_1(t) + x_2(t)) = A\cos(\omega t)\cos(\Delta\Phi/2) \tag{A.69a}$$

$$x_{\mathrm{rel}}(t) = \frac{1}{2}(x_1(t) - x_2(t)) = A\cos(\omega t)\sin(\Delta\Phi/2). \tag{A.69b}$$

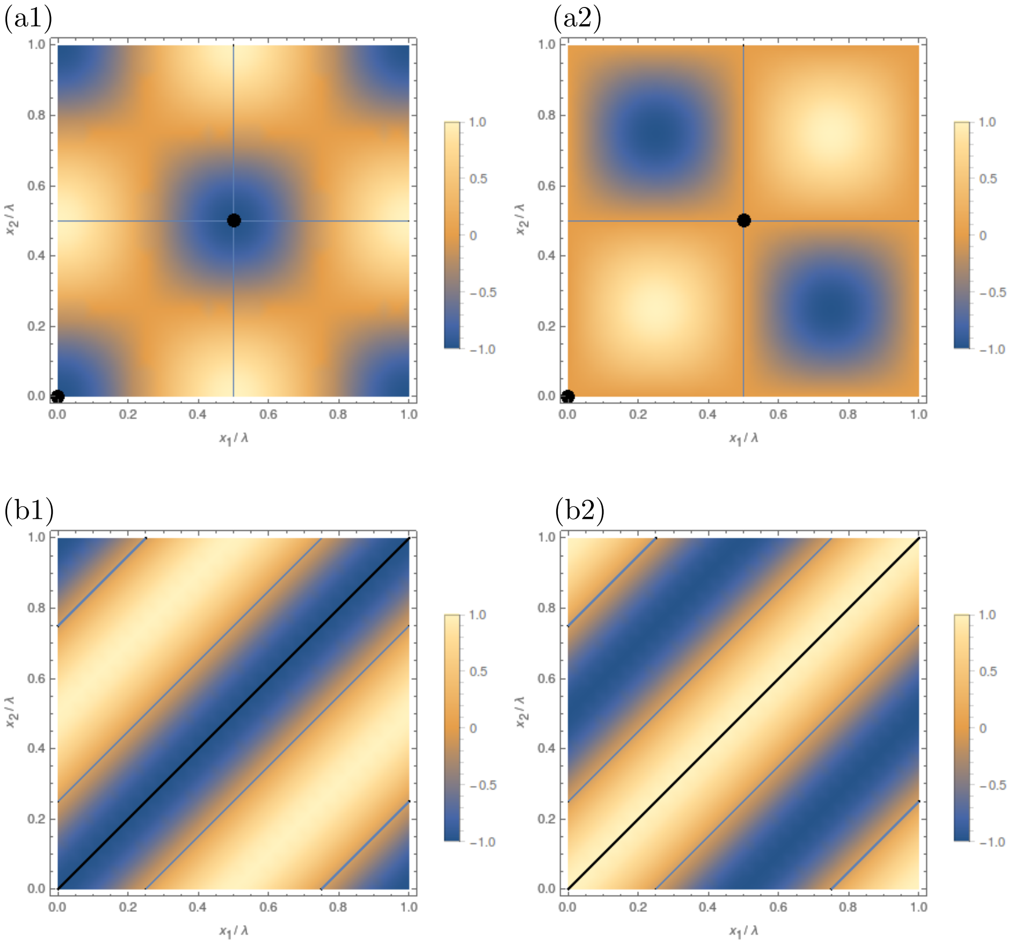

Figure A.1.: Collective potential and cross-friction in arbitrary units for two atoms at positions x_1 and x_2. Top: A single cosine mode yields (a1) the potential energy $-\cos(kx_1)\cos(kx_2)$ and (a2) the cross-friction $\sin(kx_1)\sin(kx_2)$. Bottom: A pair of cosine and sine modes gives rise to (b1) the potential energy $-\cos(k(x_1 - x_2))$ and (b2) the cross-friction $\cos(k(x_1 - x_2))$. The black lines and dots denote the minimum of the potential energy, while the blue lines denote the zeros of the potential energy.

The distinct oscillation modes are the center-of-mass (c-o-m) mode $\Delta\Phi = 0$, the relative mode $\Delta\Phi = \pi$ and the "plus" radial mode $\Delta\Phi = \pi/2$ and the "minus" radial mode $\Delta\Phi = -\pi/2$.

In the vicinity of the potential minima, the center-of-mass oscillations ($p_1 p_2 > 0$, $\Delta\Phi = 0$) through the minimum are in the area where $\sin(kx_1)\sin(kx_2) \geq 0$, and thus they are damped. In Fig. A.1 depicting the configuration space, the c-o-m mode corresponds to movement along the diagonal. Relative oscillations ($p_1 p_2 < 0$, $\Delta\Phi = \pi$) through the minimum are also damped, since $\sin(kx_1)\sin(kx_2) \leq 0$ along the anti-diagonal. The radial oscillation modes are heated by cross-friction, and at the vicinity of the minima they totally compensate self-friction, leaving the radial modes undamped. In Fig. A.1, they correspond to circular orbits around the trapping point. The heating due to cross-friction can be understood by the fact that atoms in radial modes move in the same direction ($p_1 p_2 > 0$) in the $\sin(kx_1)\sin(kx_2) < 0$ regions, while they move in opposite directions ($p_1 p_2 < 0$) in the $\sin(kx_1)\sin(kx_2) > 0$ regions. These undamped radial modes have also been observed in Ref. [A.12] for longitudinal pumping.

Cosine and sine mode

For a cosine and a sine mode with the same frequency, as described in Sec. 8.2, we get a retardation force depending on the distance only

$$F_{j,\mathrm{ret}} = -\mu_k \sum_i p_i \cos(k(x_i - x_j)). \tag{A.70}$$

For one atom this yields

$$F_{\mathrm{ret}} = -\mu_k p. \tag{A.71}$$

Compared to the single-mode case, the force on one atom is uniform in space. The averaged friction force is twice as strong as in the single-mode case. Note however, that we also pump two modes and thus we use twice as much pump power. The intra-cavity intensity, though, is the same as in the single-mode case.

For two atoms we obtain for the force on atom 1

$$F_{1,\mathrm{ret}} = -\mu_k [p_1 + p_2 \cos(k(x_1 - x_2))]. \tag{A.72}$$

Again, the cross-friction part $\cos(k(x_1 - x_2))$ is shown in Fig. A.1. Interestingly, it has the same form as the potential, in contrast to the single mode case. In the vicinity of the trapping region it is always 1. Going through the same arguments as for the single-mode case, we conclude that the center-of-mass motion is damped, while the relative oscillations are not damped. A similar result was obtained for a longitudinally pumped ring cavity [A.13]. The radial oscillations have no cross-friction contribution when averaged over one period, since atoms move as much together as against each other in one cycle. Thus only self-friction is left in this case.

Frequency comb

In the dense mode regime $L_a\delta k/(2\pi) \ll 1$ (see Sec. 8.2), the retardation force again resembles the two-mode case

$$F_{j,\mathrm{ret}} = -\mu_{k_0}\frac{1}{2}\sum_i p_i \sum_m m^2 \cos(k_m(x_i - x_j)) \tag{A.73}$$

with an additional sum. The summation again goes from 1 to M, thus the factor 1/2. The mode index $m = k_m/k_0$ does not vary much for $\Delta k/k_c \ll 1$, which is typically the case.

For one particle we obtain

$$F_{\mathrm{ret}} = -\mu_{k_0}\frac{1}{2}p\sum_m m^2 \approx -\mu_{k_c}\frac{M}{2}p, \tag{A.74}$$

neglecting corrections of the order $\mathcal{O}((\Delta k/k_c)^2)$. The self-friction is thus the same as in the two mode case for equal total pump strength.

For two particles, the force on particle 1 is

$$F_{1,\mathrm{ret}} = -\frac{\mu_{k_0}}{2}[p_1\sum_m m^2 + p_2\sum_m m^2\cos(k_m(x_1 - x_2))]. \tag{A.75}$$

Compared to the case of two modes, we see that the cross-friction coefficient decreases with the inter-atomic distance at a length scale $2\pi/\Delta k$ given by the bandwidth, comparable to the trapping potential.

B. Publication

Physical Review Letters **122**, 153603 (2019)

Ion-based quantum sensor for optical cavity photon numbers[*]

M. Lee[1], K. Friebe[1], D. A. Fioretto[1], K. Schüppert[1], F. R. Ong[1], D. Plankensteiner[2], V. Torggler[2], H. Ritsch[2], R. Blatt[1,3] and T. E. Northup[1]

[1]*Institut für Experimentalphysik, Universität Innsbruck, Technikerstraße 25, 6020 Innsbruck, Austria*

[2]*Institut für Theoretische Physik, Universität Innsbruck, Technikerstraße 21, 6020 Innsbruck, Austria*

[3]*Institut für Quantenoptik und Quanteninformation, Österreichische Akademie der Wissenschaften, Technikerstraße 21a, 6020 Innsbruck, Austria*

We dispersively couple a single trapped ion to an optical cavity to extract information about the cavity photon-number distribution in a nondestructive way. The photon-number-dependent ac Stark shift experienced by the ion is measured via Ramsey spectroscopy. We use these measurements first to obtain the ion-cavity interaction strength. Next, we reconstruct the cavity photon-number distribution for coherent states and for a state with mixed thermal-coherent statistics, finding overlaps above 99% with the calibrated states.

doi: 10.1103/PhysRevLett.122.153603

---

[*] Together with D. P., the main contribution of the author of this thesis were frequent discussions on the theoretical aspects of the experiment presented in the paper as well as some calculations.

B.1. Letter

Cavity quantum electrodynamics (cavity QED) provides a conceptually simple and powerful platform for probing the quantized interaction between light and matter [B.1]. Early experiments opened a window into the dynamics of coherent atom–photon interactions, first through observations of collective Rabi oscillations and vacuum Rabi splittings [B.2, B.3, B.4, B.5] and later at the single-atom level [B.6, B.7, B.8, B.9, B.10, B.11]. More recently, building on measurements of the cavity field via the atomic phase [B.12, B.13], cavity photon statistics have been analyzed in experiments with Rydberg atoms or superconducting qubits in microwave resonators [B.14, B.15, B.16, B.17], culminating in the generation and stabilization of nonclassical cavity field states [B.18, B.19, B.20, B.21, B.22, B.23, B.24]. These experiments operate in a dispersive regime, in which information about the cavity field can be extracted via the qubits with minimal disturbance to the field [B.1].

Dispersive experiments often operate in a regime in which one photon induces a significant atomic phase shift, the so-called strong pull regime [B.25]. However, interesting physical phenomena have also been explored with microwave cavities in the weak-pull regime, in which the small phase shift allows partial information about the atomic state to be acquired without collapse onto an eigenstate. Examples include the observation of quantum trajectories [B.26], the stabilization of Rabi oscillations via quantum feedback [B.27], and the entanglement of remote qubits [B.28].

In parallel, it was pointed out that the Jaynes-Cummings Hamiltonian that describes cavity QED also describes the interaction of light and ions in a harmonic trapping potential [B.29]. This interaction underpins the generation of nonclassical states of motion [B.30, B.31, B.32, B.33] and the implementation of gates between trapped ions [B.34]. In analogy to the phase shifts experienced by qubits due to the cavity field, ions experience quantized ac Stark shifts due to their coupling to the harmonic trap potential [B.35]. These shifts have been characterized using techniques similar to those introduced in Ref. [B.12]. Here, we have transferred the principle of dispersive measurement to an ion qubit coupled to a cavity. In contrast to experiments with flying Rydberg atoms, the ion is strongly confined; in contrast to both Rydberg and superconducting-qubit experiments, our cavity operates in the optical regime.

We employ a single trapped $^{40}\mathrm{Ca}^+$ ion as a quantum sensor [B.36] to extract information about cavity photons without destroying them. Via Ramsey spectroscopy of the ion, we measure the phase shift and dephasing of the ion's state, both of which result from the interaction of the ion with the cavity field. The mean phase shift is proportional to the mean cavity photon occupation number, due to the ac Stark effect, and the dephasing is due to the cavity photon state not being a pure number state. Reconstructing the cavity photon-number distribution from these measurements allows us to determine the mean and the width of the distribution and thus to distinguish between states with coherent photon statistics and mixed thermal-coherent statistics.

The ion is modelled as a three-level system in which two states, $|S\rangle \equiv |4^2\mathrm{S}_{1/2}, m_J = +1/2\rangle$ and $|D\rangle \equiv |3^2\mathrm{D}_{5/2}, m_J = +1/2\rangle$, comprise a qubit (Fig. 1). The cavity is dispersively coupled to the transition between $|D\rangle$ and the third state, $|P\rangle \equiv |4^2\mathrm{P}_{3/2}, m_J = +1/2\rangle$,

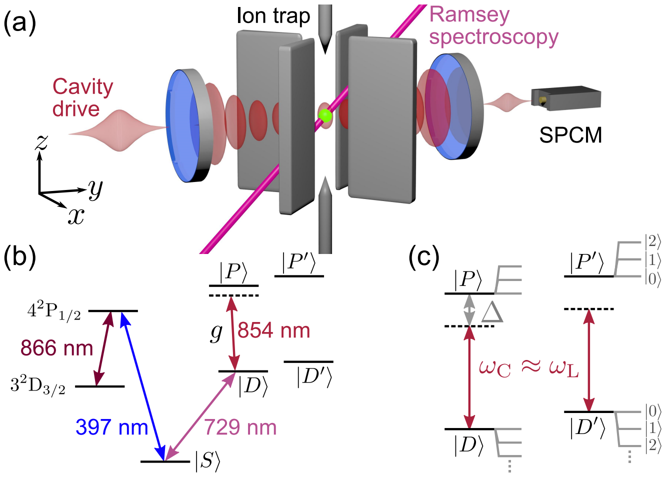

Figure B.1.: (a) Experimental set-up. A single ion is coupled to the cavity, which is driven by a weak laser field (cavity drive). The cavity drive laser (along $\hat{y}$) is polarized parallel to the quantization axis, in the direction $\hat{x} + \hat{z}$. The Ramsey spectroscopy laser propagates along $-(\hat{y} + \hat{z})$. Cavity output photons are detected by a single-photon-counting module (SPCM). (b) Energy level diagram of $^{40}\mathrm{Ca}^+$ with the relevant levels $|S\rangle$, $|D\rangle$, $|P\rangle$, $|D'\rangle \equiv |3^2\mathrm{D}_{5/2}, m_J = +3/2\rangle$ and $|P'\rangle \equiv |4^2\mathrm{P}_{3/2}, m_J = +3/2\rangle$ of the ion. The $4^2\mathrm{P}_{1/2}$ and $3^2\mathrm{D}_{3/2}$ manifolds are used for ion cooling and detection. (c) Levels $|D\rangle$, $|P\rangle$, $|D'\rangle$, and $|P'\rangle$ experience photon-number-dependent ac Stark shifts due to the cavity field, indicated in grey. The frequencies of the bare cavity and the drive laser are ω_C and ω_L, respectively, and Δ is the difference between ω_C and the transition frequency from $|D\rangle$ to $|P\rangle$.

with a detuning $\Delta = 2\pi \times 125$ MHz. The quantization axis is defined by a magnetic field of 4.06 G in the plane perpendicular to the cavity axis. The relevant ion-cavity parameters are given by $(g, \kappa, \gamma) = 2\pi \times (0.968,\ 0.068,\ 11.5)$ MHz, where g is the ion-cavity coupling strength calculated from the cavity properties and the atomic transition, κ is the cavity field decay rate, and γ is the atomic decay rate of state $|P\rangle$. Here, we assume that the ion is positioned at the waist and in an antinode of a TEM_{00} mode of the cavity [B.37, B.38]. The expected frequency shift of the cavity resonance induced by the dispersively coupled ion is $g^2/\Delta = 2\pi \times 7.50$ kHz, which is much smaller than κ, such that we operate in the weak-pull regime [B.25, B.26]; see Supplemental Material B.2 for further discussion of the choice of Δ. In this regime, the drive laser can be considered to be resonant with the cavity, irrespective of the state of the qubit.

In order to probe the cavity field, the ion is first Doppler-cooled and optically pumped to $|S\rangle$. As the first part of a Ramsey measurement, the qubit is then initialized in a superposition of $|S\rangle$ and $|D\rangle$ by a $\pi/2$-pulse of the Ramsey spectroscopy laser at 729 nm. Next, we drive the cavity with a weak laser field with wavelength $\lambda_\mathrm{L} = 854$ nm

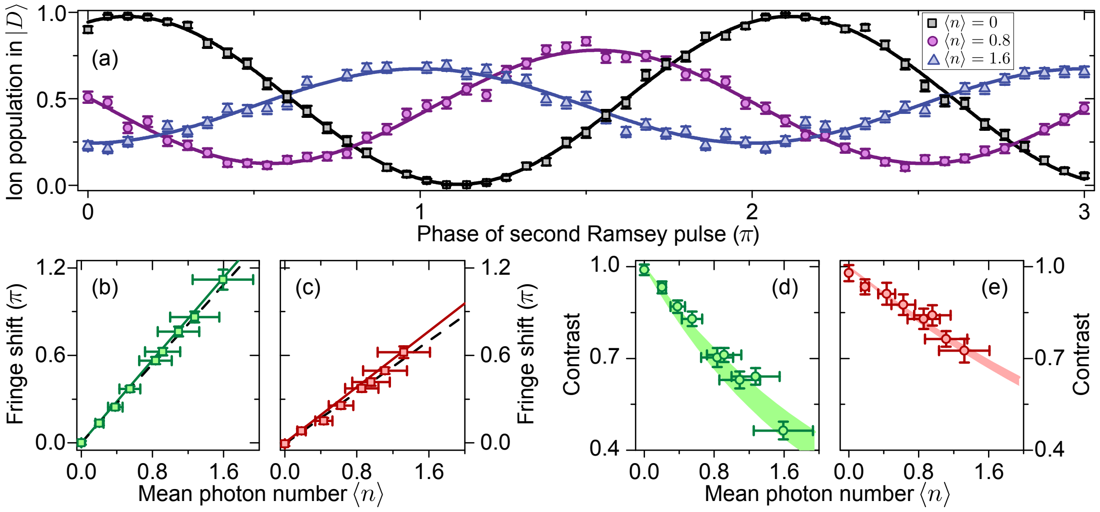

Figure B.2.: (a) Ramsey fringes for mean photon numbers $\langle n\rangle = 0$ (black squares), 0.8(2) (purple circles), and 1.6(3) (blue triangles). The solid lines are sinusoidal fits (see Supplemental Material B.2) and error bars denote quantum projection noise. (b) The phase shift of the Ramsey fringes as a function of $\langle n\rangle$ for the transition $|D\rangle - |P\rangle$. Squares are experimental data, while the solid line shows the theoretical model using the calculated coupling strength g. The dashed line is a linear fit to the data, from which g_{exp} is extracted (see main text). (c) Ramsey fringe phase shift as a function of $\langle n\rangle$ for the transition $|D'\rangle - |P'\rangle$ with $g' = 0.82\,g$. (d) Contrast of the Ramsey fringes as a function of $\langle n\rangle$ for the transition $|D\rangle - |P\rangle$. The shaded area shows the contrast expected from the theoretical model with g_{exp} as input, including its uncertainty. (e) Contrast vs. $\langle n\rangle$ for the transition $|D'\rangle - |P'\rangle$. For (b)-(e), the plotted uncertainties in $\langle n\rangle$ are statistical and systematic uncertainties from the calibration of the photon number. Systematic uncertainties in $\langle n\rangle$ are 20%. Error bars of fringe shift and contrast are uncertainties of the fits to the Ramsey fringes.

for $T = 50$ μs. Note that the interaction time T is much larger than the cavity photon lifetime of $\tau_{\mathrm{C}} = 1/(2\kappa) = 1.2$ μs, such that for a mean intracavity photon number of $\langle n\rangle$, $\langle n\rangle T/\tau_{\mathrm{C}}$ photons on average successively interact with the ion. Note also that T is much shorter than the coherence time of 950 μs on the $|S\rangle$–$|D\rangle$ transition [B.39]. The independently calibrated mean photon number $\langle n\rangle$ of the cavity field is set to a value between 0 and 1.6(3), and the drive laser frequency $\omega_{\mathrm{L}} = 2\pi c/\lambda_{\mathrm{L}}$ is resonant with the cavity frequency $\omega_{\mathrm{C}} + \langle\sigma_D\rangle g^2/\Delta$, where ω_{C} is the cavity resonance frequency when no ion is coupled to the cavity, and σ_D is the operator for the ion population in $|D\rangle$. Finally, a second $\pi/2$-pulse with variable phase ϕ completes the Ramsey measurement, after which the qubit state is detected using laser fields at 397 nm and 866 nm [B.39]. The measurement is repeated 250 times for each phase to obtain the ion population in

$|D\rangle$.

The mean population in $|D\rangle$ as a function of the phase ϕ is plotted in Fig. B.2(a) for three values of $\langle n\rangle$. As $\langle n\rangle$ is increased, two features emerge: the Ramsey fringe is shifted, and its contrast is reduced. The phase shift is directly proportional to $\langle n\rangle$, as shown in Fig. B.2(b), with proportionality factor Tg^2/Δ. For $\langle n\rangle = 0.8(2)$ and $1.6(3)$, the phase of the qubit is shifted by $0.57(3)\pi$ and $1.12(7)\pi$, respectively. A single photon only interacts with the ion during its time in the cavity, which has a mean value τ_{C}, corresponding to a phase shift of the ion by $\tau_{\mathrm{C}}\, g^2/\Delta = 0.018\pi$. The accumulated effect of all successive photons injected into the cavity accounts for the total phase shift of the qubit.

The measured phase shift as a function of $\langle n\rangle$ can be used to determine the ion-cavity coupling strength. This method is independent of the single-atom cooperativity and thus is valid also for systems in intermediate and even weak coupling regimes. In such regimes, observing the vacuum Rabi splitting is not possible, making it difficult to measure the coupling strength directly. As we have independently determined all ion-cavity parameters and calibrated the photo-detection efficiency, we fit a theoretical model to the data with the coupling strength as the only free parameter. In this way, we extract the experimental value of $g_{\mathrm{exp}} = 2\pi \times 0.96(4)$ MHz from the data displayed in Fig. B.2(b), in agreement with the theoretical value of $g = 2\pi \times 0.968$ MHz. We performed the same set of measurements on another $^{40}\mathrm{Ca}^+$ transition, using the states $|S\rangle$, $|D'\rangle \equiv |3^2\mathrm{D}_{5/2}, m_J = +3/2\rangle$, and $|P'\rangle \equiv |4^2\mathrm{P}_{3/2}, m_J = +3/2\rangle$ (Fig. B.2(c)); the coherence time for the transition $|S\rangle - |D'\rangle$ is 510 μs. For the transition $|D'\rangle - |P'\rangle$, we expect $g' = 2\pi \times 0.790$ MHz and extract $g'_{\mathrm{exp}} = 2\pi \times 0.77(4)$ MHz. From the two independent measurements on two transitions, we thus see that this new method determines the atom-cavity coupling strength in agreement with theory.

In Fig. B.2(d), the fringe contrast, defined as the peak-to-peak value of the fringe divided by twice the fringe offset, is plotted as a function of $\langle n\rangle$ for the transition $|D\rangle - |P\rangle$ and in Fig. B.2(e) for the transition $|D'\rangle - |P'\rangle$. This definition of the contrast takes into account that the midpoint of the fringe is not necessarily 0.5, due to spontaneous emission (see Supplemental Material B.2). For $|D\rangle - |P\rangle$, the contrast decreases from 0.99(2) to 0.46(3) as $\langle n\rangle$ increases from 0 to 1.6. This reduction reflects the fact that the intracavity photon number is inherently probabilistic, and in this case, for a coherent drive, follows a Poissonian distribution. The corresponding photon-number fluctuations in the cavity field lead to fluctuations of the qubit transition frequency through the photon-number-dependent ac Stark shift. Note that the observed reduction of contrast can, equivalently, be interpreted as a consequence of the qubit state being measured by the cavity field [B.14, B.25]: Intracavity photons interact dispersively with the qubit before leaking to the environment. The phase of the output photons thus carries information about the qubit state that could be accessed, e.g., with homodyne or heterodyne detection. All such quantum measurements imply some amount of backaction [B.25], which in our case takes the form of qubit decoherence. Note that in the absence of a cavity, photons would also induce an ac Stark shift of the ion's states, but due to the weakness of the free-space interaction, the effect would be too small to be measured at the single-photon level.

Spontaneous emission contributes to decoherence for both the cavity-drive measurement of Fig. B.2 and free-space measurements. We quantify this effect in a reference measurement using an "ion-drive" configuration: The cavity is translated by a few mm along $\hat{x}$ in order to decouple it from the ion. The ion is driven with a laser beam with frequency $\omega_\mathrm{L} = \omega_\mathrm{C}$. We perform Ramsey measurements with the cavity interaction replaced by the interaction of the ion with this ion-drive laser. The Ramsey fringe contrast is reduced due to off-resonant excitation of the population from $|D\rangle$ to $|P\rangle$, followed by spontaneous emission. Fig. B.3 compares the Ramsey fringe contrast as a function of the phase shift for both the ion-drive and cavity-drive measurements. A given phase shift corresponds to the same ac Stark shift at the ion in both measurements. The contrast of the cavity-drive data is smaller than that of the ion-drive data because in the former case, both spontaneous emission and decoherence induced by the cavity photons play a role. We therefore conclude from this reference measurement that decoherence is not just caused by spontaneous emission; rather, a significant contribution to decoherence of the ion qubit stems from interaction with the cavity field via the backaction of the cavity photons on the ion.

Next, we reconstruct the cavity photon number distribution with a maximum likelihood algorithm (see Supplemental Material B.2). This algorithm finds the photon number distribution that is most likely to have interacted with the ion. It is based on a model, in which the coherent cavity drive with mean photon number n_coh is described by an amplitude $\eta = \kappa\sqrt{n_\mathrm{coh}}$, and additional number fluctuations are described by a thermal bath with mean photon number n_th corresponding to an incoherent contribution to the driving [B.40]. The photon number distribution of the intracavity field is then determined by the two parameters η and n_th. The result of the reconstruction is shown in Fig. B.4. For the three Ramsey fringes measured on the $|D\rangle - |P\rangle$ transition, displayed in Fig. B.2(a), the reconstruction yields a squared statistical overlap (SSO) $\left(\sum_n \sqrt{p_\mathrm{rec}(n) p_\mathrm{cal}(n)}\right)^2$ between the reconstructed distribution $p_\mathrm{rec}(n)$ and the independently calibrated input state distribution $p_\mathrm{cal}(n)$ above 99% (Figs. B.4(a)-(c)). The reconstructed state shown in Fig. B.4(a) corresponds to the vacuum state, and the states in Fig. B.4(b) and (c) are coherent states, with Mandel Q parameters $Q = \left(\langle n^2\rangle - \langle n\rangle^2\right) / \langle n\rangle - 1$ of $0.00^{+0.02}_{-0.01}$, $-0.03(7)$, and $0.04(5)$, respectively [B.41]. The uncertainty of the reconstructed distribution is dominated by quantum projection noise in the Ramsey measurement (see Supplemental Material B.2).

This reconstruction method is also applied to a fourth state which is generated by applying amplitude noise to the cavity drive laser via an acousto-optic modulator. The noise has a bandwidth of 10 MHz $\gg 2\kappa$ and can therefore be considered as white noise. The reconstructed state, shown in Fig. B.4(d), can be described by mixed coherent and thermal statistics: From the calibration of the added noise (see Supplemental Material B.2), a value of $Q = 0.64(6)$ is expected, while the reconstruction yields $Q = 0.70^{+0.07}_{-0.10}$. The result thus shows super-Poissonian intracavity photon statistics caused by the added thermal noise and is clearly distinct from the statistics of a coherent state. Note that our sensing technique is nondestructive because the dispersive interaction with the ion does not annihilate the measured intracavity photons.

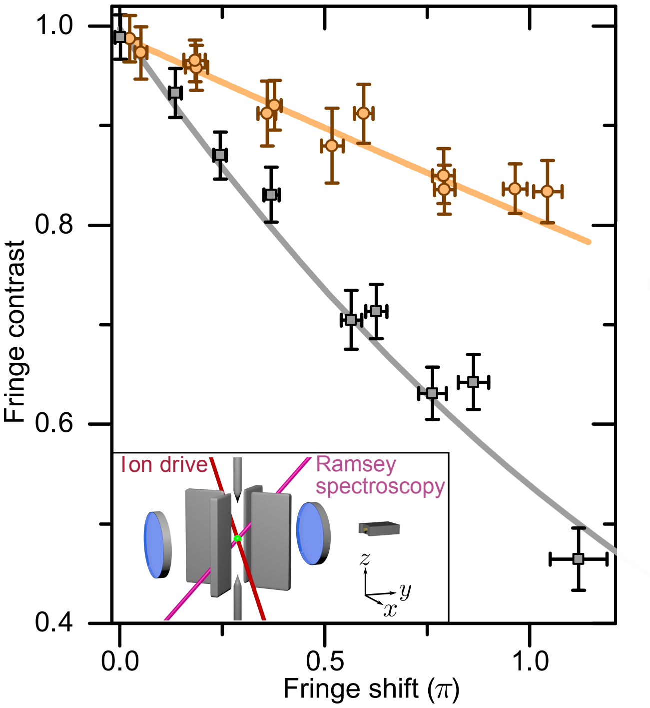

Figure B.3.: Ramsey fringe contrast as a function of phase shift for ion-drive (orange circles) and cavity-drive (black squares; same data as in Fig. B.2(b) and (d)) measurements on the $|D\rangle$–$|P\rangle$ transition. The lines are theory curves, using g_{exp} for the cavity-drive data. The inset shows the ion-drive beam, which propagates along $\hat{x} - \hat{z}$ and is polarized along $\hat{x} + \hat{z}$, along with the Ramsey spectroscopy beam. The ion is decoupled from the cavity for the ion-drive measurement.

An extension of this work would be to reconstruct the full density matrix of arbitrary states of the cavity field. For this purpose, we require a displacement operation of the cavity field, as has been demonstrated in microwave cavities [B.18]. With the target field to be measured populating the cavity, a second field as a local oscillator would be sent to the cavity. The total field interacting with the ion would be the sum of the known (local oscillator) and unknown (target) fields, and by varying the known field and measuring the state of the ion, one would be able to extract the full target field density matrix.

We have focused here on measuring the ion's state to extract information about the cavity field. However, the scenario can be reversed: quantum nondemolition measurements of the ion's state become possible in our setup via heterodyne measurement of the cavity output field, allowing single quantum trajectories of the ion's electronic state to be monitored and the qubit state to be stabilized, as demonstrated with superconducting qubits [B.27, B.26]. Furthermore, the strong-pull regime ($g^2/\Delta > \kappa$) would be accessible with a higher finesse cavity [B.25, B.26] (see Supplemental Material B.2). In this regime, the qubit spectrum splits into several lines, each corresponding to a differ-

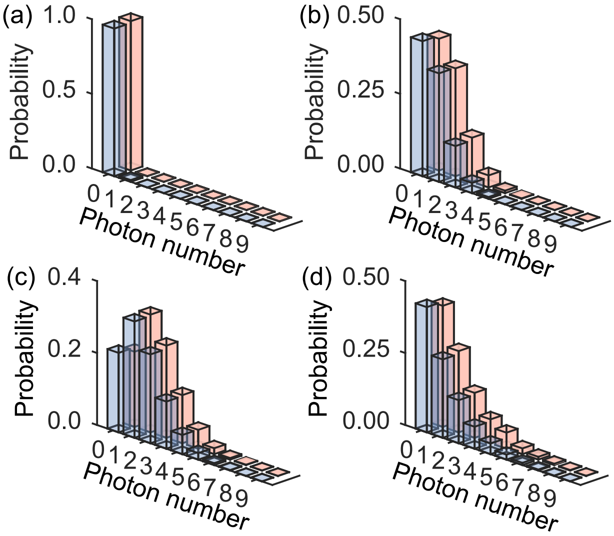

Figure B.4.: Photon number distributions reconstructed from the measured Ramsey fringes for intracavity mean photon numbers of (a) 0, (b) 0.8(2), and (c) 1.6(3) (blue bars), and the expected distributions (pink bars). The reconstructed distributions yield mean photon numbers of $0.01^{+0.05}_{-0.02}$, 0.84(8), and $1.49^{+0.05}_{-0.06}$. (d) Reconstructed distribution when the cavity is driven with light of mixed coherent-thermal statistics with mean photon number $\langle n \rangle = 1.05^{+0.07}_{-0.11}$, yielding a reconstructed mean photon number of $\langle n \rangle = 1.12^{+0.14}_{-0.15}$. The squared statistical overlap between the reconstructed distributions and the expected distributions is higher than 0.99 for (a)-(d).

ent photon-number component [B.15, B.42], providing a route to engineer nonclassical cavity-field states in the optical domain. Other possible extensions include increasing the sensitivity of the measurement by using several ions via their collective coupling to the cavity [B.43] or via their entanglement [B.44].

In summary, we have implemented an ion-based analyzer for the statistics of optical photons that does not destroy the photons. Information about the intracavity photon number is imprinted onto the state of an ion qubit via a dispersive interaction. Ramsey spectroscopy and the maximum likelihood method are used to reconstruct the intracavity photon statistics, yielding results in excellent agreement with the expected distributions. Our work represents the first such nondestructive probing of cavity photon distributions in the optical domain, providing tools for the generation of nonclassical optical states.

This work has been financially supported by the Austrian Science Fund (FWF) through Projects F4019, V252, M1964, W1259-N27, and F4013-N23; by the Army Research Laboratory's Center for Distributed Quantum Information via the project SciNet: Scalable Ion-Trap Quantum Network, Cooperative Agreement No. W911NF15-2-0060; and by the European Union's Horizon 2020 research program through the Marie Skłodowska-Curie Actions, Grant No. 656195.

M.L. and K.F. contributed equally to this work.

B.2. Supplemental material

B.2.1. Modelling the system

Atomic levels

In order to calculate the theory lines in Fig. 2(b)-(e) in the main text, we consider the following atomic basis states: $|S\rangle = |4^2\mathrm{S}_{1/2}, m_J = +1/2\rangle$, $|D\rangle = |3^2\mathrm{D}_{5/2}, m_J = +1/2\rangle$, $|P\rangle = |4^2\mathrm{P}_{3/2}, m_J = +1/2\rangle$, and $|S'\rangle$ (see Fig. B.5), where $|S'\rangle$ is a dark state, which collects spontaneous emission from $|P\rangle$ to the second ground state $|4^2\mathrm{S}_{1/2}, m_J = -1/2\rangle$, as well as to the states $|3^2\mathrm{D}_{5/2}, m_J = -1/2\rangle$, $|3^2\mathrm{D}_{5/2}, m_J = +3/2\rangle$, and the states in the $3^2\mathrm{D}_{3/2}$ manifold. $|S'\rangle$ does not participate in the ion-cavity interaction and is not coupled to the Ramsey spectroscopy laser. The manifolds involved in the process are displayed in Fig. B.5(a). The total decay rate of state $|P\rangle$ is $\Gamma_P = \Gamma_{\mathrm{PS}} + \Gamma_{\mathrm{PD}} + \Gamma_{\mathrm{PD}_{3/2}} = 2\pi \times 23$ MHz, with values $\Gamma_{\mathrm{PS}} = 2\pi \times 21.4$ MHz for decay from $4^2\mathrm{P}_{3/2}$ to $4^2\mathrm{S}_{1/2}$, $\Gamma_{\mathrm{PD}} = 2\pi \times 1.34$ MHz for decay from $4^2\mathrm{P}_{3/2}$ to $3^2\mathrm{D}_{3/2}$, and $\Gamma_{\mathrm{PD}_{3/2}} = 2\pi \times 0.152$ MHz for decay from $4^2\mathrm{P}_{3/2}$ to $3^2\mathrm{D}_{3/2}$. Taking into account the Clebsch-Gordan coefficients, the decay rates are $\Gamma_{|S\rangle} = 2/3\,\Gamma_{\mathrm{PS}} = 2\pi \times 14.3$ MHz from $|P\rangle$ to $|S\rangle$, $\Gamma_{|S'\rangle} = 1/3\,\Gamma_{PS} + 3/5\,\Gamma_{PD} + \Gamma_{PD_{3/2}} = 2\pi \times 8.1$ MHz from $|P\rangle$ to $|S'\rangle$, and $\Gamma_{|D\rangle} = 2/5\,\Gamma_{PD} = 2\pi \times 0.54$ MHz from $|P\rangle$ to $|D\rangle$.

Hamiltonian

The Hamiltonian of the system is given by

$$\begin{aligned} H_S/\hbar =& \omega_D \sigma_D + (\omega_D + \omega_P)\,\sigma_P + \omega_{\mathrm{C}} a^\dagger a + g\,(\sigma_{PD} a + \mathrm{h.c.}) \\ &+ \left(\eta a^\dagger e^{-i\omega_{\mathrm{L}} t} + \mathrm{h.c.}\right) + \left(\Omega \sigma_{SD} e^{-i\omega_{\mathrm{R}} t} + \mathrm{h.c.}\right). \end{aligned}$$

Here, ω_D corresponds to the energy of the level $|D\rangle$, ω_P to that of $|P\rangle$, $\sigma_{D(P)}$ is the projection operator onto the state $|D\rangle$ ($|P\rangle$), ω_{C} is the cavity frequency, a is the annihilation operator of the cavity mode, g is the ion-cavity coupling strength, $\sigma_{PD} = \sigma_{DP}^\dagger$ is the transition operator between states $|P\rangle$ and $|D\rangle$, η is the amplitude of the drive laser in the cavity drive term, ω_{L} is the frequency of the cavity drive laser, Ω is the Rabi frequency of the laser on the $|S\rangle$–$|D\rangle$ qubit transition, $\sigma_{SD} = \sigma_{DS}^\dagger$ is the transition operator between states $|S\rangle$ and $|D\rangle$, and ω_{R} is the frequency of the Ramsey spectroscopy laser. The energy of the ground state $|S\rangle$ is chosen as the energy reference. Fig. B.5(b) shows the relevant states, frequencies and decay channels. This Hamiltonian is transformed into a rotating frame via

$$H_I = i\hbar \dot{U} U^\dagger + U H_S U^\dagger,$$

with a unitary operator

$$U = \exp\left[i\left(\omega_{\mathrm{R}}\sigma_D + (\omega_s + \omega_P)\sigma_P + \omega_P a^\dagger a\right) t\right].$$

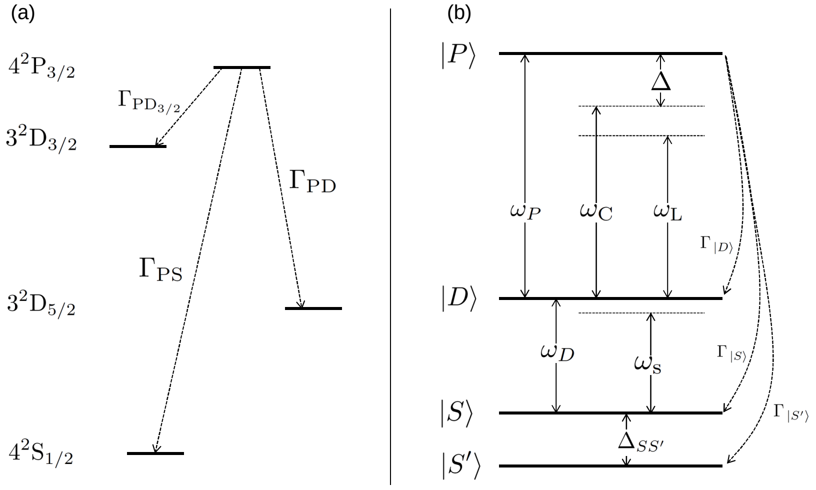

Figure B.5.: Definition of the involved levels and transitions. (a) Levels and decay channels considered in the model. Note that decay to $4^2\mathrm{S}_{1/2}$ from $3^2\mathrm{D}_{5/2}$ is not included, since the lifetime of the latter level of 1 s is much longer than the duration of one experimental cycle. (b) Definition of the levels, energies, detunings and decay constants in the model. Note that the decay from $|P\rangle$ to $|S'\rangle$ combines decay channels ending in $4^2\mathrm{S}_{1/2}$, $3^2\mathrm{D}_{5/2}$, and $3^2\mathrm{D}_{3/2}$.

We thus obtain the Hamiltonian in the interaction picture as

$$
\begin{aligned}
H_I/\hbar = & \Delta_{D\mathrm{R}}\sigma_D + (\Delta_{P\mathrm{L}} + \Delta_{\mathrm{CL}} + \Delta_{D\mathrm{R}})\sigma_P + \Delta_{SS'}\sigma_{S'} \\
& + \Delta_{\mathrm{CL}}\, a^\dagger a \\
& + g\left(\sigma_{PD}\, a + \sigma_{DP}\, a^\dagger\right) + \eta(a + a^\dagger) \\
& + \Omega\left(\sigma_{SD} + \sigma_{DS}\right).
\end{aligned}
\tag{B.1}
$$

Here, $\Delta_{D\mathrm{R}} = \omega_D - \omega_{\mathrm{R}}$ is the detuning between the Ramsey spectroscopy laser and the $|D\rangle$–$|S\rangle$ transition, $\Delta_{P\mathrm{L}} = \omega_P - \omega_{\mathrm{L}}$ is the detuning between the cavity drive laser and the $|P\rangle$–$|D\rangle$ transition, $\Delta_{\mathrm{CL}} = \omega_{\mathrm{C}} - \omega_{\mathrm{L}}$ is the detuning between the cavity drive laser and the cavity mode, and $\Delta_{SS'}$ is the detuning between state $|S\rangle$ and the dark state $|S'\rangle$. In the cavity drive term, the drive amplitude η for coherent driving on resonance, i.e., for $\Delta_{\mathrm{CL}} = 0$, is given by $\eta = \kappa\sqrt{n_{\mathrm{coh}}}$ with n_{coh} the mean photon number and 2κ the decay rate of the cavity photons. This relation can be derived from the Heisenberg-Langevin equation for the cavity field a in steady state (cf. section I.C). The value of η used in the simulation stems from the calibration of the mean photon number.

In the dispersive regime $\Delta_{P\mathrm{L}} \gg g$, the Hamiltonian can be approximated: Using the transformation

$$U = e^{\frac{g}{\Delta_{\mathrm{PL}}}\left(\sigma_{PD} a - a^{\dagger}\sigma_{DP}\right)}$$

and the Baker-Campbell-Hausdorff formula, and truncating the series at first order in $g/\Delta_{P\mathrm{L}}$, one finds the transformed Hamiltonian

$$\begin{aligned}
UHU^{\dagger}/\hbar \approx &\left(\Delta_{\mathrm{DR}} - 2\frac{g^2}{\Delta_{\mathrm{PL}}} a^{\dagger}a\right)\sigma_D \\
&+ \left(\Delta_{P\mathrm{L}} + \Delta_{\mathrm{CL}} + \Delta_{D\mathrm{R}} + 2\frac{g^2}{\Delta_{P\mathrm{L}}}\left(a^{\dagger}a + 1\right)\right)\sigma_P \\
&+ \Delta_{\mathrm{CL}} a^{\dagger}a + \eta\left(a + a^{\dagger}\right) + \Omega\left(\sigma_{SD} + \sigma_{DS}\right) \\
&+ \frac{\eta g}{\Delta_{PL}}\left(\sigma_{DP} + \sigma_{PD}\right) \\
&+ \frac{\Omega g}{\Delta_{PL}}\left(a^{\dagger}\sigma_{SP} + \sigma_{PS} a\right).
\end{aligned}$$

The first two lines of this equation describe the ac Stark shift of the states $|D\rangle$ and $|P\rangle$, with the magnitude of the shift dependent on the dispersive shift per photon $g^2/\Delta_{P\mathrm{L}}$ and the photon number operator $a^{\dagger}a$. The energy shift of the state $|D\rangle$, when time-integrated during the interaction time, leads to the phase shift of the Ramsey fringe. The detuning between cavity and atom $\Delta_{P\mathrm{L}}$ is denoted by Δ in the main text and the remainder of the supplemental material.

Master equation

The system evolution is calculated by numerically integrating the following master equation in Python, using QuTiP [B.45, B.46]. The master equation consists of four terms, describing unitary evolution, atomic decay, cavity decay with rate κ, and incoherent cavity driving, derived from a stochastic drive term [B.47, B.40]:

$$\begin{aligned}
\frac{d\rho}{dt} = &-\frac{i}{\hbar}\left[\rho, H_I\right] \\
&+ \sum_{i=D,S,S'} \frac{\Gamma_i}{2}\left(2\sigma_i^{-}\rho\sigma_i^{+} - \rho\sigma_i^{+}\sigma_i^{-} - \sigma_i^{+}\sigma_i^{-}\rho\right) \\
&+ \frac{\kappa}{2}\left(2a\rho a^{\dagger} - \rho a^{\dagger}a - a^{\dagger}a\rho\right) \\
&+ \delta n\left(\left[\left[a,\rho\right], a^{\dagger}\right] + \left[\left[a^{\dagger},\rho\right], a\right]\right)
\end{aligned} \tag{B.2}$$

The photons are described by a Fock state basis, truncated at $n = 9$. This number is sufficient, since for the measured coherent states the mean photon number is below two, which would correspond to a population of below $2 \cdot 10^{-4}$ for the Fock state $|n = 9\rangle$. In the experiment, the incoherent drive is implemented by adding white amplitude noise to the RF-amplitude for the acousto-optic modulator of the cavity drive beam. The bandwidth of the frequency generator used for generating the noise reaches from DC to 10 MHz. Since the full cavity linewidth is only $2\kappa = 2\pi \times 136$ kHz, this can be considered white noise.

Expanding the last term of Eq. B.2 and combining it with the cavity-decay term, we get:

$$\begin{aligned}&\frac{\kappa + \delta n}{2}\left(2a\rho a^\dagger - \rho a^\dagger a - a a^\dagger \rho\right)\\ +&\frac{\delta n}{2}\left(2a^\dagger \rho a - \rho a a^\dagger - a a^\dagger \rho\right),\end{aligned}$$

which corresponds to thermal driving of the cavity [B.48] with a thermal bath with mean photon number $n_{\mathrm{th}} = \delta n/\kappa$. Since the coherent and incoherent drive do not interfere, the total mean photon number is given by the sum of the coherent and incoherent contributions as $\langle n\rangle = n_{\mathrm{coh}} + n_{\mathrm{th}}$.

Second transition $|D'\rangle$–$|P'\rangle$

For simulating the second transition, (data in Fig. 2(c) and (e) of the main text), the following parameters need to be changed: g is replaced by g', and due to the different Clebsch-Gordan coefficients, only the following decay channels exist: $\Gamma_{|S'\rangle} = 11/15\,\Gamma_{\mathrm{PD}}$ for decay from $|P'\rangle$ to the dark state $|S'\rangle$, and $\Gamma_{|S\rangle} = \Gamma_{\mathrm{PS}}$ for decay from $|P'\rangle$ to $|S\rangle$. $\Gamma_{|D\rangle}$ is replaced with $\Gamma_{|D'\rangle} = 4/15\,\Gamma_{\mathrm{PD}}$ for decay from $|P'\rangle$ to $|D'\rangle$. Note that for this transition, $|P'\rangle$ has no allowed decay to the second ground state $|4^2\mathrm{S}_{1/2}, m_J = -1/2\rangle$. In Eq. B.1, D is replaced by D' and P by P'. Note also that the photon polarization is the same for both transitions $|D\rangle$–$|P\rangle$ and $|D'\rangle$–$|P'\rangle$.

B.2.2. Reconstruction algorithm

In order to reconstruct the photon number distribution in the cavity (Fig. 4 in the main text), we first define a likelihood function [B.49] as

$$\begin{aligned}L(\eta, \delta n) = \prod_{k=1}^{N} &\left[P_k(\eta, \delta n)\right]^{f_k}\\ &\times \left[1 - P_k(\eta, \delta n)\right]^{1-f_k} \times \mathrm{const}.\end{aligned} \tag{B.3}$$

In this formula, $N = 51$ is the number of points per Ramsey fringe, f_k is the measured probability to find the ion in $|D\rangle$ for point k in the fringe, P_k is the excitation probability expected from solving the master equation with the cavity drive parameters η and δn as input, and const is a scaling factor. The quantity L describes the likelihood to observe the measured result (given by f_k) for certain parameters $(\eta, \delta n)$, based on the model of the system (given by $P_k(\eta, \delta n)$). The parameters that best describe the data are obtained by maximizing the likelihood or its logarithm

$$\begin{aligned}\log\left[L\left(\eta,\delta n\right)\right]=&\sum_{k=1}^{N}\big(f_k\log\left[P_k\left(\eta,\delta n\right)\right]\\&+\left(1-f_k\right)\log\left[1-P_k\left(\eta,\delta n\right)\right]\big)+\text{const.}\end{aligned}\tag{B.4}$$

In order to obtain P_k for a given set $(\eta,\delta n)$, we numerically integrate the master equation Eq. B.2. The number N was chosen such that there are a sufficient number of points for the sinusoidal fits to the Ramsey fringes.

The iterative algorithm for maximizing the likelihood function runs as follows:

1. Integrate Eq. B.2 for given values of η and δn.
2. Calculate the likelihood function using Eq. B.4.
3. Change η and δn and repeat.

This sequence is iterated until the maximum value of the likelihood has been found in a Nelder-Mead simplex optimization. The corresponding values of η_{opt} and δn_{opt} are the most likely ones to explain the measured data, and the reconstructed photon number distribution is given by the corresponding diagonal elements $p(n)$ of the cavity density matrix obtained from integrating the master equation with η_{opt} and δn_{opt} as input.

B.2.3. Photon number calibration

We independently calibrated the intracavity mean photon number to be able to compare the reconstructed photon number distribution with the expected values. Given the probability for a photon to leave the cavity through the output mirror of $p_{\text{out}}=11(2)\%$, which corresponds to a total photon detection efficiency $\varepsilon=p_{\text{out}}\times\zeta=4(1)\%$ (including detector efficiency and optical loss in the path efficiency ζ), we calculate an expected count rate of $2\kappa\times p_{\text{out}}\times\zeta=38(8)$ kHz for the single-photon counting module (SPCM) at the cavity output for a mean photon number of $\langle n\rangle=1$ in the cavity. This rate corresponds to an expected number of counts of $C_0=475(100)$ during the interaction time of $\tau=50$ μs. We take the cavity field build-up time into account by including a correction factor $c=0.922$, extracted from a simulation, and accordingly get a number of counts of $C_1=C_0/c=515(108)$ for the calibration. By measuring the output counts C, we are thus able to calibrate the mean photon number in the cavity field for a given input power as $\langle n\rangle=C/C_1$.

B.2.4. Fit model

For analyzing the Ramsey fringes, we use a fit model of the following form:

$$E(\phi)=B+A\cdot\cos\left(\pi\left(\phi-\phi_0\right)\right)$$

Here, $E(\phi)$ stands for the excitation of the ion to the state $|D\rangle$ (or $|D'\rangle$), ϕ for the phase of the second Ramsey pulse with respect to the first one, A is the amplitude of the fringe, ϕ_0 the fringe shift, and B is the offset of the fringe. The contrast is calculated as $2A/(2B)$, with $2A$ the peak-to-peak value of the fringe and $2B$ the maximum possible peak-to-peak value. This definition takes into account that spontaneous emission reduces the fringe offset to $B < 0.5$, leading to a maximum possible peak-to-peak value of the fringe of $2B$, as the minimum value is zero and the midpoint of the fringe is B. We include the spontaneous emission from the excited state $|P\rangle$ by making the offset B dependent on the off-resonant excitation to state $|P\rangle$ (or $|P'\rangle$). B therefore has to be recalculated for each value of $\langle n\rangle$ as

$$B = B_{\langle n\rangle=0} \cdot \exp\left(-\Gamma_{|S'\rangle} p_{P^{(\prime)}} \langle n\rangle \, \tau\right)$$

Here, $p_{P^{(\prime)}} = 2g^2\langle n\rangle / \left(\Gamma^2_{|D^{(\prime)}\rangle} + \Delta^2\right)$ is the probability to off-resonantly excite the ion from $|D\rangle$ ($|D'\rangle$) to state $|P\rangle$ ($|P'\rangle$), and $B_{\langle n\rangle=0} = 0.4915$ is the maximum offset achievable for the given coherence time and $\langle n\rangle = 0$. This number is half of the maximum achievable excitation of a single Doppler-cooled ion.

The phase offset of $-0.12(1)\pi$ for $\langle n\rangle = 0$, obtained from the fit, is due to an ac Stark shift of the ion levels, caused by the non-zero spatial overlap of the ion wave packet and a laser field at 783 nm used to actively stabilize the cavity length; this field populates a TEM_{01} cavity mode [B.50].

B.2.5. Uncertainty analysis of the reconstructed photon statistics

The uncertainties of the reconstructed photon number distributions are determined by quantum projection noise [B.51] in the Ramsey measurement. The following method is used to estimate the uncertainties of the reconstructed states shown in Fig. 4 of the main text.

1. For a given Ramsey fringe, the maximum likelihood method returns the parameter set (η_{opt}, δn_{opt}), which determines the corresponding photon number distribution.
2. A Monte-Carlo simulation is executed to obtain a random Ramsey fringe which takes into account the quantum projection noise: The ion populations of this fringe are based on the measured ion populations with additional noise following a binomial distribution with 250 cycles used in the experiment.
3. We reconstruct (η_i, δn_i) from the Ramsey fringe obtained in Step 2. The index i indicates the iteration number in the Monte Carlo simulation.
4. Steps 2 and 3 are repeated until the standard deviations of all calculated numbers (η_i, δn_i) have converged according to the criterion that the standard deviation as a function of the number of samples varies less than 5%. The uncertainties ($\Delta\eta$, $\Delta\delta n$) are then set to the values of the standard deviations. The mean of the obtained η_i and δn_i is η_{opt} and δn_{opt}.
5. The upper limit of the reconstructed distribution is given by ($\eta + \Delta\eta$, $\delta n + \Delta\delta n$), and the lower limit by ($\eta - \Delta\eta$, $\delta n - \Delta\delta n$). The uncertainties of the mean photon numbers $\langle n\rangle$ and Mandel Q parameters are calculated by propagating these values.

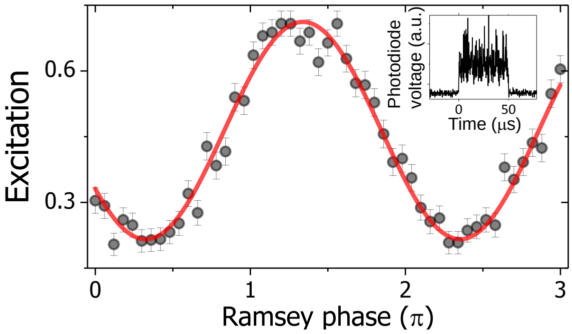

Figure B.6.: Ramsey fringe when the cavity is driven with a coherent field with additional white noise. The black circles are data points and the red line is a sinusoidal fit to the data. From the fit, a phase shift of $0.71(2)\pi$ and a contrast of $0.57(3)$ are extracted. The error bars are quantum projection noise. (inset) Photodiode measurement of the cavity input field.

B.2.6. Driving the cavity with additional amplitude noise

We estimate the intracavity field from a calibration measurement of the cavity drive beam (inset of Fig. B.6) with a photodiode. In the photodiode signal, there is a contribution from the coherent statistics, which is calibrated independently (see Sec. B.2.3), and a noise contribution with thermal statistics. The coherent statistics is determined by the coherent amplitude η, while the thermal part is described via the mean thermal photon number $n_{\text{th}} = \delta n/\kappa$. By dividing the voltage on the photodiode into the offset part (coherent statistics) and oscillations on top (thermal part), we can calibrate δn as a function of the amplitude V_{AC} of the oscillations: we first extract the conversion factor S_{V} between photodiode voltage and SPCM counts, as $C = S_{\text{V}} \cdot V_{\text{DC}}$, where C is the number of measured counts in the SPCM and V_{DC} is the voltage measured on the photodiode for coherent driving. Next, we can calculate the noise contribution via $\delta n = \kappa S_{\text{V}} V_{\text{AC}}/C_1$, using the fact that the number of SPCM counts originating from the thermal part is proportional to V_{AC}. In this way, we calculate the mean coherent and thermal photon numbers of the expected as $n_{\text{coh}} = 0.64(14)$ and $n_{\text{th}} = 0.44(9)$, both of which agree with the reconstructed values $n_{\text{coh, rec}} = 0.68(16)$ and $n_{\text{th,rec}} = 0.47(15)$.

B.2.7. Phase resolution of the Ramsey measurements

The phase resolution $\delta\phi$ of our Ramsey measurement is limited by quantum projection noise [B.51] in the measurement of the ion's state. In order to estimate $\delta\phi$, we start by simulating a single reference fringe for a mean photon number $\langle n \rangle = 1$ with N phase values, by numerically solving the master equation Eq. B.2. Using the excitation probability Q_k for a given phase ϕ_k in this fringe, we draw a random sample m_k with a probability Π_k given by the binomial distribution

$$\Pi_k(m_k) = \binom{M}{m_k} Q_k^M \left(1 - Q_k\right)^{M-m_k},$$

where $M = 250$ is the number of repetitions for measuring the ion excitation and m_k is the number of times that the ion is found in the excited state $|D\rangle$ out of M trials. The excitation of the ion to state $|D\rangle$ is then calculated as $p_k = m_k/M$ (corresponding to the values f_k in Eq. B.4). This is repeated for all N phase values ϕ_k used in the real measurement. Next, we extract the phase shift of this simulated fringe, by fitting a sinusoidal function to the simulated data p_k vs. ϕ_k. This procedure is repeated $50,000$ times and we obtain a distribution of extracted phase values with a standard deviation σ_ϕ. We define the phase resolution as $\delta\phi = 2\sigma_\phi$, since this is the minimum distance between two phase distributions that are distinguishable. A value of $\delta\phi = 0.011\,\pi$ is found. Translating this result into a resolution of the mean photon number via

$$\delta\phi = \frac{g^2}{\Delta}\tau\,\delta\bar{n},$$

we find values of $\delta\bar{n}_{PD} = 0.013(5)$ for the $|D\rangle$–$|P\rangle$ transition and $\delta\bar{n}_{P'D'} = 0.020(8)$ for the $|D'\rangle$–$|P'\rangle$ transition. In other words, it is possible to distinguish the phase shift of the qubit Bloch vector for cavity field states, whose mean photon number is different by just $\delta\bar{n}_{PD}$ or $\delta\bar{n}_{P'D'}$, respectively.

B.2.8. Choice of experiment parameters

The detuning Δ and interaction time τ are chosen in the following way:

1. First, τ is fixed. We require τ to be short enough that the measured Ramsey fringe contrast is not significantly reduced due to noise sources that become significant on this time scale, but long enough that we can consider the cavity field to be in steady state, that is, longer than the build-up time of the cavity field. In our case, $\tau = 50$ μs is chosen to be much shorter than the coherence time of 950 μs of the ion qubit (due to magnetic field fluctuations) and much longer than the cavity build-up time of 1.7 μs, extracted from a numerical simulation of our cavity. For this value of τ, we observe a Ramsey fringe contrast of 99(2)% with no photons in the cavity.

2. Next, the maximum intracavity photon number $\langle n\rangle_{\max}$ is chosen for the planned set of measurements. Here, we wanted to observe the contrast reduction and phase shift at the single-photon level up to values beyond $\langle n\rangle = 1$, so we chose $\langle n\rangle_{\max} = 1.5$.

3. Finally, Δ is fixed. For a given value of $\langle n\rangle$, as Δ is reduced, the Ramsey fringe contrast is also reduced due to the increased rates of measurement-induced dephasing and spontaneous emission. If Δ is too small, it will not be possible to distinguish the contrast for $\langle n\rangle_{\max}$ from noise. On the other hand, increasing Δ extends the range of observable photon numbers, but at the cost of reduced sensitivity to changes in contrast and phase as a function of photon number. We chose the detuning $\Delta = 2\pi\cdot 125$ MHz, corresponding to a contrast of 0.5 for $\langle n\rangle_{\max} = 1.5$.

Note that in our experiment, uncertainties in the measured Ramsey fringe contrasts and phase shifts stem from quantum projection noise [B.51]. For each phase in the Ramsey fringe of Fig. 2(a) in the main text, the measurement was repeated 250 times, corresponding to a total data acquisition time of several hours. With these statistics, the signal-to-noise ratio (SNR) of the Ramsey fringe, defined as the ratio of the root-mean-square of the ion excitation data in the fringe to the mean quantum projection noise, decreases from 30 for the fringe with $\langle n\rangle = 0$ to 16 for the fringe with $\langle n\rangle = 1.6$. Our choice of a contrast of 0.5 for the maximum mean photon number was therefore conservative: We could have chosen a lower value for Δ and accepted a lower SNR. Also, acquiring more data to reduce the statistical uncertainty would have given us even more room to reduce Δ. However, this approach becomes more challenging for longer measurement times in view of experimental drifts.

It is also worth noting that the ratio of the spontaneous emission rate $\gamma_{\text{sp}} = \gamma\langle n\rangle g^2/\Delta^2$ and the rate of measurement-induced dephasing in the weak-pull regime [B.25] $\gamma_{\text{m}} \propto \langle n\rangle g^4/(\kappa\Delta^2)$ is independent of Δ and proportional only to the mean photon number and the cooperativity: $\gamma_{\text{m}}/\gamma_{\text{sp}} \propto \langle n\rangle g^2/(\kappa\gamma)$. For this reason, increasing Δ does not enhance the relative strength of the measurement-induced dephasing effect with respect to the contrast reduction due to spontaneous emission.

B.2.9. Strong-pull regime in an optical cavity

We estimate that it would be possible to reach the strong-pull regime ($g^2/\Delta > \kappa$) in the optical domain with state-of-the-art mirrors. Ref. [B.52] reports a measurement of high-reflectivity mirrors with transmission $T = 5\cdot 10^{-7}$ and scattering and absorption loss of $A = 1.1\cdot 10^{-6}$ per mirror for wavelengths near 850 nm, corresponding to a finesse of $2\cdot 10^6$. For a cavity with such mirrors and the length of our cavity of 19.98 mm, a photon lifetime of $\tau_{\text{c}} = 42\ \mu\text{s}$ is expected, while the one-sided output coupling $T/(2T + 2A) = 16\%$ is comparable to that of our cavity.

In this regime, we would need to modify the procedure of Sec. B.2.8 because our experimental goal would be different. The goal of the measurements presented in the main text is to observe the evolution of the Ramsey fringe contrast and phase shift over a range of intracavity photon numbers. In contrast, the strong pull regime offers a setting in which one could resolve a splitting of the qubit transition corresponding to the different photon number states in the cavity field [B.25]. In this way, it would be possible to project the cavity field onto a particular number state via measurement of the ion state.

The question then becomes: For given values of g and κ corresponding to a particular experimental implementation, what values of Δ satisfy the strong-pull condition while allowing the dispersive frequency shift $\chi = g^2/\Delta$ to be resolved via qubit spectroscopy within the cavity lifetime?

We consider that an ion is initially prepared in $|S\rangle$ and is coupled to the cavity field on the $|P\rangle - |D\rangle$ transition for an interval τ_1. During this interval, the ion is driven by a classical laser field (which we refer to as a spectroscopy laser) on the $|S\rangle - |D\rangle$ transition. Subsequently, for an interval τ_2, state detection with 397 nm and 866 nm laser fields is used to determine whether the ion is in $|S\rangle$ or $|D\rangle$. Performing this measurement for different detunings of the spectroscopy laser would allow one to resolve the photon number-state splitting.

For a projective measurement that collapses the cavity field onto a nonclassical state, the total interval $\tau_1 + \tau_2$ must be shorter than the cavity lifetime. As an initial estimate, we neglect τ_2 and choose the longest possible interval for the ion interaction with the cavity field, that is, by setting $\tau_1 = \tau_c = 42$ μs. The frequency resolution of the spectroscopy laser is then given by $2\pi/\tau_1 = 2\pi \cdot 24$ kHz. This frequency resolution must be narrower than χ, thus constraining our choice of Δ: $\Delta < \frac{g^2 \tau_1}{2\pi}$. A second bound corresponds to the strong-pull condition: $\Delta < \frac{g^2}{\kappa}$.

Table B.1 lists values for g corresponding to both the $^{40}\mathrm{Ca}^+$ transition used in the main text and to the D2 line in neutral $^{133}\mathrm{Cs}$. In $^{133}\mathrm{Cs}$, the qubit would be comprised of the states $|6^2\mathrm{S}_{1/2}, F = 3, m_F = 3\rangle$ and $|6^2\mathrm{S}_{1/2}, F = 4, m_F = 4\rangle$, and a microwave field or an optical Raman transition would be used to probe the qubit transition. Here, we assume that the cavity lifetime is τ_c and that the mirror radii of curvature are identical to those of our current cavity, yielding the same mode volume. We see that the first bound corresponds to $\Delta < 2\pi \cdot 39$ MHz for $^{40}\mathrm{Ca}^+$ and to $\Delta < 2\pi \cdot 164$ MHz for $^{133}\mathrm{Cs}$. The second bound corresponds to $\Delta < 2\pi \cdot 490$ MHz for $^{40}\mathrm{Ca}^+$ and to $\Delta < 2\pi \cdot 2$ GHz for $^{133}\mathrm{Cs}$. In both cases, the first bound is the infimum and thus the relevant bound. This bound also corresponds to an optimum point for experiments, since decreasing Δ further will increase the effective spontaneous emission rate, broadening the spectroscopic signal. Note that g can be further enhanced by taking advantage of collective atom-cavity coupling.

Finally, we return to the question of ion state detection in the interval τ_2. Detecting the state of the ion was achieved with current technology in 10.5 μs with 99% readout fidelity [B.53, B.54]; the detection time can be made faster or slower depending on the fidelity requirement. We thus see that including realistic values for τ_2 in the estimate above will lower the upper bound on Δ by about 25%.

Table B.1.: Estimation for the strong-pull regime in atom-cavity systems. For $^{40}\mathrm{Ca}^+$, the $|D\rangle - |P\rangle$ transition from the main text was considered, while for $^{133}\mathrm{Cs}$ we considered the transition $|6^2\mathrm{S}_{1/2}, F = 4, m_F = 4\rangle - |6^2\mathrm{P}_{3/2}, F' = 5, m'_F = 5\rangle$.

Species	$^{40}\mathrm{Ca}^+$	$^{133}\mathrm{Cs}$
Wavelength (nm)	854	852
$g/2\pi$ (MHz)	0.968	2.0
$\gamma/2\pi$ (MHz)	11.5	2.6
$\kappa/2\pi$ (kHz)	1.9	1.9
$\Delta/2\pi$ (MHz)	39	164

Bibliography

References for Chapter 1

[1.1] M. Planck, “Zur Theorie des Gesetzes der Energieverteilung im Normalspectrum,” *Verhandlungen der Deutschen Physikalischen Gesellschaft*, vol. 2, no. 237, 1900.

[1.2] A. Einstein, “Über einen die Erzeugung und Verwandlung des Lichtes betreffenden heuristischen Gesichtspunkt,” *Annalen der Physik*, vol. 322, no. 6, pp. 132–148, 1905.

[1.3] A. Einstein, “Quantentheorie des einatomigen idealen Gases,” *Sitzungsberichte der Preussischen Akademie der Wissenschaften Sitzung der phys.-math. Klasse vom 29. Januar*, 1925.

[1.4] E. Schrödinger, “An undulatory theory of the mechanics of atoms and molecules,” *Physical Review*, vol. 28, no. 6, p. 1049, 1926.

[1.5] P. A. M. Dirac, “The quantum theory of the emission and absorption of radiation,” *Proceedings of the Royal Society of London. Series A, Containing Papers of a Mathematical and Physical Character*, vol. 114, no. 767, pp. 243–265, 1927.

[1.6] E. Fermi, “Quantum theory of radiation,” *Reviews of Modern Physics*, vol. 4, no. 1, p. 87, 1932.

[1.7] R. P. Feynman, “Mathematical formulation of the quantum theory of electromagnetic interaction,” *Physical Review*, vol. 80, no. 3, p. 440, 1950.

[1.8] J. P. Gordon, H. J. Zeiger, and C. H. Townes, “The maser – new type of microwave amplifier, frequency standard, and spectrometer,” *Physical Review*, vol. 99, no. 4, p. 1264, 1955.

[1.9] A. L. Schawlow and C. H. Townes, “Infrared and optical masers,” *Physical Review*, vol. 112, no. 6, p. 1940, 1958.

[1.10] T. H. Maiman, “Stimulated optical radiation in ruby,” *Nature*, vol. 187, no. 493, 1960.

[1.11] C. N. Cohen-Tannoudji, “Nobel lecture: Manipulating atoms with photons,” *Reviews of Modern Physics*, vol. 70, pp. 707–719, Jul 1998.

[1.12] R. J. Glauber, “Nobel lecture: One hundred years of light quanta,” *Reviews of Modern Physics*, vol. 78, no. 4, p. 1267, 2006.

[1.13] D. Meschede, H. Walther, and G. Müller, "One-atom maser," *Physical Review Letters*, vol. 54, no. 6, p. 551, 1985.

[1.14] S. Haroche, "Nobel lecture: Controlling photons in a box and exploring the quantum to classical boundary," *Reviews of Modern Physics*, vol. 85, no. 3, p. 1083, 2013.

[1.15] M. H. Anderson, J. R. Ensher, M. R. Matthews, C. E. Wieman, and E. A. Cornell, "Observation of Bose–Einstein condensation in a dilute atomic vapor," *Science*, vol. 269, no. 5221, pp. 198–201, 1995.

[1.16] K. B. Davis, M.-O. Mewes, M. R. Andrews, N. J. van Druten, D. S. Durfee, D. Kurn, and W. Ketterle, "Bose–Einstein condensation in a gas of sodium atoms," *Physical Review Letters*, vol. 75, no. 22, p. 3969, 1995.

[1.17] D. Jaksch, C. Bruder, J. I. Cirac, C. W. Gardiner, and P. Zoller, "Cold bosonic atoms in optical lattices," *Physical Review Letters*, vol. 81, no. 15, p. 3108, 1998.

[1.18] I. Bloch, "Ultracold quantum gases in optical lattices," *Nature Physics*, vol. 1, no. 1, pp. 23–30, 2005.

[1.19] R. P. Feynman, "Simulating physics with computers," *International Journal of Theoretical Physics*, vol. 21, no. 6, pp. 467–488, 1982.

[1.20] A. Einstein, "Zur Quantentheorie der Strahlung," *Physikalische Zeitschrift*, vol. 18, pp. 121–128, 1917.

[1.21] R. Grimm, M. Weidemüller, and Y. B. Ovchinnikov, "Optical dipole traps for neutral atoms," in *Advances in atomic, molecular, and optical physics*, vol. 42, pp. 95–170, Elsevier, 2000.

[1.22] T. W. Hänsch and A. L. Schawlow, "Cooling of gases by laser radiation," *Optics Communications*, vol. 13, no. 1, pp. 68–69, 1975.

[1.23] E. T. Jaynes and F. W. Cummings, "Comparison of quantum and semiclassical radiation theories with application to the beam maser," *Proceedings of the IEEE*, vol. 51, no. 1, pp. 89–109, 1963.

[1.24] P. Pinkse, T. Fischer, P. Maunz, and G. Rempe, "Trapping an atom with single photons," *Nature*, vol. 404, no. 6776, p. 365, 2000.

[1.25] P. Domokos and H. Ritsch, "Mechanical effects of light in optical resonators," *Journal of the Optical Society of America B*, vol. 20, no. 5, pp. 1098–1130, 2003.

[1.26] P. Horak, G. Hechenblaikner, K. M. Gheri, H. Stecher, and H. Ritsch, "Cavity-induced atom cooling in the strong coupling regime," *Physical Review Letters*, vol. 79, no. 25, p. 4974, 1997.

[1.27] P. Maunz, T. Puppe, I. Schuster, N. Syassen, P. W. Pinkse, and G. Rempe, "Cavity cooling of a single atom," *Nature*, vol. 428, no. 6978, p. 50, 2004.

[1.28] C. Hood, M. Chapman, T. Lynn, and H. Kimble, "Real-time cavity QED with single atoms," *Physical Review Letters*, vol. 80, no. 19, p. 4157, 1998.

[1.29] P. Horak, H. Ritsch, T. Fischer, P. Maunz, T. Puppe, P. Pinkse, and G. Rempe, "Optical kaleidoscope using a single atom," *Physical Review Letters*, vol. 88, no. 4, p. 043601, 2002.

[1.30] R. Bonifacio, L. De Salvo, L. Narducci, and E. D'Angelo, "Exponential gain and self-bunching in a collective atomic recoil laser," *Physical Review A*, vol. 50, no. 2, p. 1716, 1994.

[1.31] D. Kruse, C. von Cube, C. Zimmermann, and P. W. Courteille, "Observation of lasing mediated by collective atomic recoil," *Physical Review Letters*, vol. 91, no. 18, p. 183601, 2003.

[1.32] P. Domokos and H. Ritsch, "Collective cooling and self-organization of atoms in a cavity," *Physical Review Letters*, vol. 89, no. 25, p. 253003, 2002.

[1.33] A. T. Black, H. W. Chan, and V. Vuletić, "Observation of collective friction forces due to spatial self-organization of atoms: from Rayleigh to Bragg scattering," *Physical Review Letters*, vol. 91, no. 20, p. 203001, 2003.

[1.34] J. Asbóth, P. Domokos, H. Ritsch, and A. Vukics, "Self-organization of atoms in a cavity field: Threshold, bistability, and scaling laws," *Physical Review A*, vol. 72, no. 5, p. 053417, 2005.

[1.35] V. Torggler and H. Ritsch, "Adaptive multifrequency light collection by self-ordered mobile scatterers in optical resonators," *Optica*, vol. 1, no. 5, pp. 336–342, 2014.

[1.36] K. Baumann, C. Guerlin, F. Brennecke, and T. Esslinger, "Dicke quantum phase transition with a superfluid gas in an optical cavity," *Nature*, vol. 464, no. 7293, p. 1301, 2010.

[1.37] C. Maschler and H. Ritsch, "Cold atom dynamics in a quantum optical lattice potential," *Physical Review Letters*, vol. 95, no. 26, p. 260401, 2005.

[1.38] R. Landig, L. Hruby, N. Dogra, M. Landini, R. Mottl, T. Donner, and T. Esslinger, "Quantum phases from competing short-and long-range interactions in an optical lattice," *Nature*, vol. 532, no. 7600, p. 476, 2016.

[1.39] J. Larson, B. Damski, G. Morigi, and M. Lewenstein, "Mott-insulator states of ultracold atoms in optical resonators," *Physical Review Letters*, vol. 100, no. 5, p. 050401, 2008.

[1.40] Y. Li, L. He, and W. Hofstetter, "Lattice-supersolid phase of strongly correlated bosons in an optical cavity," *Physical Review A*, vol. 87, no. 5, p. 051604, 2013.

[1.41] S. F. Caballero-Benitez and I. B. Mekhov, "Quantum optical lattices for emergent many-body phases of ultracold atoms," *Physical Review Letters*, vol. 115, no. 24, p. 243604, 2015.

[1.42] S. F. Caballero-Benitez, G. Mazzucchi, and I. B. Mekhov, "Quantum simulators based on the global collective light-matter interaction," *Physical Review A*, vol. 93, no. 6, p. 063632, 2016.

[1.43] I. B. Mekhov and H. Ritsch, "Quantum optics with quantum gases: Controlled state reduction by designed light scattering," *Physical Review A*, vol. 80, no. 1, p. 013604, 2009.

[1.44] S. Inouye, A. Chikkatur, D. Stamper-Kurn, J. Stenger, D. Pritchard, and W. Ketterle, "Superradiant Rayleigh scattering from a Bose–Einstein condensate," *Science*, vol. 285, no. 5427, pp. 571–574, 1999.

[1.45] S. Ostermann, F. Piazza, and H. Ritsch, "Spontaneous crystallization of light and ultracold atoms," *Physical Review X*, vol. 6, no. 2, p. 021026, 2016.

[1.46] I. Dimitrova, W. Lunden, J. Amato-Grill, N. Jepsen, Y. Yu, M. Messer, T. Rigaldo, G. Puentes, D. Weld, and W. Ketterle, "Observation of two-beam collective scattering phenomena in a Bose–Einstein condensate," *Physical Review A*, vol. 96, no. 5, p. 051603, 2017.

[1.47] T. Grießer and H. Ritsch, "Light-induced crystallization of cold atoms in a 1d optical trap," *Physical Review Letters*, vol. 111, no. 5, p. 055702, 2013.

[1.48] D. Holzmann, M. Sonnleitner, and H. Ritsch, "Synthesizing variable particle interaction potentials via spectrally shaped spatially coherent illumination," *New Journal of Physics*, vol. 20, no. 10, p. 103009, 2018.

[1.49] I. P. Gent, C. Jefferson, and P. Nightingale, "Complexity of n-queens completion," *Journal of Artificial Intelligence Research*, vol. 59, pp. 815–848, 2017.

[1.50] D. Wales, *Energy landscapes: Applications to clusters, biomolecules and glasses.* Cambridge University Press, 2003.

[1.51] A. R. Kan, C. G. E. Boender, and G. T. Timmer, "A stochastic approach to global optimization," in *Computational mathematical programming*, pp. 281–308, Springer, 1985.

[1.52] S. Kirkpatrick, C. D. Gelatt, and M. P. Vecchi, "Optimization by simulated annealing," *Science*, vol. 220, no. 4598, pp. 671–680, 1983.

[1.53] N. Metropolis, A. W. Rosenbluth, M. N. Rosenbluth, A. H. Teller, and E. Teller, "Equation of state calculations by fast computing machines," *The Journal of Chemical Physics*, vol. 21, no. 6, pp. 1087–1092, 1953.

[1.54] S. Geman and D. Geman, "Stochastic relaxation, Gibbs distributions, and the Bayesian restoration of images," *IEEE Transactions on pattern analysis and machine intelligence*, no. 6, pp. 721–741, 1984.

[1.55] T. Kadowaki and H. Nishimori, "Quantum annealing in the transverse ising model," *Physical Review E*, vol. 58, p. 5355, Nov 1998.

[1.56] E. Farhi, J. Goldstone, S. Gutmann, and M. Sipser, "Quantum computation by adiabatic evolution," *quant-ph/0001106*, 2000.

[1.57] T. Albash and D. A. Lidar, "Adiabatic quantum computation," *Reviews of Modern Physics*, vol. 90, no. 1, p. 015002, 2018.

[1.58] M. A. Nielsen and I. Chuang, *Quantum computation and quantum information.* Cambridge University Press, 2010.

[1.59] M. Johnson, M. Amin, S. Gildert, T. Lanting, F. Hamze, N. Dickson, R. Harris, A. Berkley, J. Johansson, P. Bunyk, *et al.*, "Quantum annealing with manufactured spins," *Nature*, vol. 473, no. 7346, pp. 194–198, 2011.

[1.60] S. Boixo, T. F. Rønnow, S. V. Isakov, Z. Wang, D. Wecker, D. A. Lidar, J. M. Martinis, and M. Troyer, "Evidence for quantum annealing with more than one hundred qubits," *Nature Physics*, vol. 10, no. 3, pp. 218–224, 2014.

[1.61] S. V. Isakov, G. Mazzola, V. N. Smelyanskiy, Z. Jiang, S. Boixo, H. Neven, and M. Troyer, "Understanding quantum tunneling through quantum Monte Carlo simulations," *Physical Review Letters*, vol. 117, no. 18, p. 180402, 2016.

[1.62] T. Keller, S. B. Jäger, and G. Morigi, "Phases of cold atoms interacting via photon-mediated long-range forces," *Journal of Statistical Mechanics: Theory and Experiment*, vol. 2017, no. 6, p. 064002, 2017.

[1.63] T. Keller, V. Torggler, S. B. Jäger, S. Schütz, H. Ritsch, and G. Morigi, "Quenches across the self-organization transition in multimode cavities," *New Journal of Physics*, vol. 20, no. 2, p. 025004, 2018.

[1.64] V. Torggler, S. Krämer, and H. Ritsch, "Quantum annealing with ultracold atoms in a multimode optical resonator," *Physical Review A*, vol. 95, no. 3, p. 032310, 2017.

[1.65] V. Torggler, P. Aumann, H. Ritsch, and W. Lechner, "A Quantum N-Queens Solver," *Quantum*, vol. 3, p. 149, June 2019.

[1.66] M. Lee, K. Friebe, D. A. Fioretto, K. Schüppert, F. R. Ong, D. Plankensteiner, V. Torggler, H. Ritsch, R. Blatt, and T. E. Northup, "Ion-based quantum sensor for optical cavity photon numbers," *Physical Review Letters*, vol. 122, no. 15, p. 153603, 2019.

References for Chapter 2

[2.1] S. Dutra, *Cavity Quantum Electrodynamics: The Strange Theory of Light in a Box.* Wiley Series in Lasers and Applications, Wiley, 2005.

[2.2] H. Tanji-Suzuki, I. D. Leroux, M. H. Schleier-Smith, M. Cetina, A. T. Grier, J. Simon, and V. Vuletić, "Interaction between atomic ensembles and optical resonators: classical description," in *Advances in atomic, molecular, and optical physics*, vol. 60, pp. 201–237, Elsevier, 2011.

[2.3] A. Siegman, *Lasers.* University Science Books, 1986.

[2.4] H. Kogelnik and T. Li, "Laser beams and resonators," *Applied Optics*, vol. 5, no. 10, pp. 1550–1567, 1966.

[2.5] C. Gerry and P. Knight, *Introductory Quantum Optics.* Cambridge University Press, 2004.

[2.6] J. D. Jackson, *Classical electrodynamics.* John Wiley & Sons, 2012.

[2.7] E. T. Jaynes and F. W. Cummings, "Comparison of quantum and semiclassical radiation theories with application to the beam maser," *Proceedings of the IEEE*, vol. 51, no. 1, pp. 89–109, 1963.

[2.8] C. W. Gardiner and P. Zoller, *Quantum Noise: A Handbook of Markovian and Non-Markovian Quantum Stochastic Methods with Applications to Quantum Optics.* Springer Series in Synergetics, Springer, 2004.

[2.9] P. Domokos and H. Ritsch, "Mechanical effects of light in optical resonators," *Journal of the Optical Society of America B*, vol. 20, no. 5, pp. 1098–1130, 2003.

[2.10] V. Weisskopf and E. Wigner, "Berechnung der natürlichen Linienbreite auf Grund der Diracschen Lichttheorie," *Zeitschrift für Physik*, vol. 63, no. 1-2, pp. 54–73, 1930.

[2.11] D. Jaksch, C. Bruder, J. I. Cirac, C. W. Gardiner, and P. Zoller, "Cold bosonic atoms in optical lattices," *Physical Review Letters*, vol. 81, no. 15, p. 3108, 1998.

[2.12] I. Bloch, "Ultracold quantum gases in optical lattices," *Nature Physics*, vol. 1, no. 1, pp. 23–30, 2005.

[2.13] W. Niedenzu, *Microscopic description and simulation of ultracold atoms in optical resonators.* PhD thesis, Universität Innsbruck, 2012.

[2.14] W. Kohn, "Analytic properties of Bloch waves and Wannier functions," *Physical Review*, vol. 115, no. 4, p. 809, 1959.

[2.15] D. Jaksch and P. Zoller, "The cold atom Hubbard toolbox," *Annals of Physics*, vol. 315, no. 1, pp. 52–79, 2005.

[2.16] M. P. Fisher, P. B. Weichman, G. Grinstein, and D. S. Fisher, “Boson localization and the superfluid-insulator transition,” *Physical Review B*, vol. 40, no. 1, p. 546, 1989.

[2.17] M. Greiner, O. Mandel, T. Esslinger, T. W. Hänsch, and I. Bloch, “Quantum phase transition from a superfluid to a Mott insulator in a gas of ultracold atoms,” *Nature*, vol. 415, no. 6867, p. 39, 2002.

[2.18] F. Meinert, M. J. Mark, E. Kirilov, K. Lauber, P. Weinmann, M. Gröbner, A. J. Daley, and H.-C. Nägerl, “Observation of many-body dynamics in long-range tunneling after a quantum quench,” *Science*, vol. 344, no. 6189, pp. 1259–1262, 2014.

References for Chapter 3

[3.1] H. Ritsch, P. Domokos, F. Brennecke, and T. Esslinger, “Cold atoms in cavity-generated dynamical optical potentials,” *Reviews of Modern Physics*, vol. 85, no. 2, p. 553, 2013.

[3.2] H. Breuer and F. Petruccione, *The Theory of Open Quantum Systems.* Oxford University Press, 2002.

[3.3] C. W. Gardiner and P. Zoller, *Quantum Noise: A Handbook of Markovian and Non-Markovian Quantum Stochastic Methods with Applications to Quantum Optics.* Springer Series in Synergetics, Springer, 2004.

[3.4] P. Domokos, P. Horak, and H. Ritsch, “Semiclassical theory of cavity-assisted atom cooling,” *Journal of Physics B*, vol. 34, no. 2, p. 187, 2001.

[3.5] W. Niedenzu, T. Grießer, and H. Ritsch, “Kinetic theory of cavity cooling and self-organisation of a cold gas,” *Europhysics Letters*, vol. 96, no. 4, p. 43001, 2011.

[3.6] R. Landig, L. Hruby, N. Dogra, M. Landini, R. Mottl, T. Donner, and T. Esslinger, “Quantum phases from competing short-and long-range interactions in an optical lattice,” *Nature*, vol. 532, no. 7600, p. 476, 2016.

[3.7] D. Nagy, P. Domokos, A. Vukics, and H. Ritsch, “Nonlinear quantum dynamics of two BEC modes dispersively coupled by an optical cavity,” *The European Physical Journal D*, vol. 55, no. 3, p. 659, 2009.

[3.8] P. Domokos and H. Ritsch, “Mechanical effects of light in optical resonators,” *Journal of the Optical Society of America B*, vol. 20, no. 5, pp. 1098–1130, 2003.

[3.9] S. Schütz, H. Habibian, and G. Morigi, “Cooling of atomic ensembles in optical cavities: Semiclassical limit,” *Physical Review A*, vol. 88, no. 3, p. 033427, 2013.

[3.10] S. B. Jäger, S. Schütz, and G. Morigi, “Mean-field theory of atomic self-organization in optical cavities,” *Physical Review A*, vol. 94, no. 2, p. 023807, 2016.

[3.11] T. Keller, V. Torggler, S. B. Jäger, S. Schütz, H. Ritsch, and G. Morigi, "Quenches across the self-organization transition in multimode cavities," *New Journal of Physics*, vol. 20, no. 2, p. 025004, 2018.

[3.12] H. Risken and T. Frank, *The Fokker-Planck Equation: Methods of Solution and Applications.* Springer Series in Synergetics, Springer Berlin Heidelberg, 1996.

[3.13] T. Keller, S. B. Jäger, and G. Morigi, "Phases of cold atoms interacting via photon-mediated long-range forces," *Journal of Statistical Mechanics: Theory and Experiment*, vol. 2017, no. 6, p. 064002, 2017.

[3.14] C. Maschler, I. B. Mekhov, and H. Ritsch, "Ultracold atoms in optical lattices generated by quantized light fields," *The European Physical Journal D*, vol. 46, no. 3, pp. 545–560, 2008.

[3.15] A. Vukics, C. Maschler, and H. Ritsch, "Microscopic physics of quantum self-organization of optical lattices in cavities," *New Journal of Physics*, vol. 9, no. 8, p. 255, 2007.

[3.16] C. Maschler and H. Ritsch, "Cold atom dynamics in a quantum optical lattice potential," *Physical Review Letters*, vol. 95, no. 26, p. 260401, 2005.

[3.17] M. R. Bakhtiari, A. Hemmerich, H. Ritsch, and M. Thorwart, "Nonequilibrium phase transition of interacting bosons in an intra-cavity optical lattice," *Physical Review Letters*, vol. 114, no. 12, p. 123601, 2015.

[3.18] J. Larson, B. Damski, G. Morigi, and M. Lewenstein, "Mott-insulator states of ultracold atoms in optical resonators," *Physical Review Letters*, vol. 100, no. 5, p. 050401, 2008.

[3.19] S. F. Caballero-Benitez and I. B. Mekhov, "Quantum optical lattices for emergent many-body phases of ultracold atoms," *Physical Review Letters*, vol. 115, no. 24, p. 243604, 2015.

[3.20] P. Domokos and H. Ritsch, "Collective cooling and self-organization of atoms in a cavity," *Physical Review Letters*, vol. 89, no. 25, p. 253003, 2002.

References for Chapter 4

[4.1] S. Kirkpatrick, C. D. Gelatt, and M. P. Vecchi, "Optimization by simulated annealing," *Science*, vol. 220, no. 4598, pp. 671–680, 1983.

[4.2] H. Risken and T. Frank, *The Fokker-Planck Equation: Methods of Solution and Applications.* Springer Series in Synergetics, Springer Berlin Heidelberg, 1996.

[4.3] S. Geman and C.-R. Hwang, "Diffusions for global optimization," *SIAM Journal on Control and Optimization*, vol. 24, no. 5, pp. 1031–1043, 1986.

[4.4] B. Gidas, "Global optimization via the Langevin equation," in *1985 24th IEEE Conference on Decision and Control*, pp. 774–778, IEEE, 1985.

[4.5] N. Metropolis, A. W. Rosenbluth, M. N. Rosenbluth, A. H. Teller, and E. Teller, "Equation of state calculations by fast computing machines," *The Journal of Chemical Physics*, vol. 21, no. 6, pp. 1087–1092, 1953.

[4.6] S. Geman and D. Geman, "Stochastic relaxation, Gibbs distributions, and the Bayesian restoration of images," *IEEE Transactions on pattern analysis and machine intelligence*, no. 6, pp. 721–741, 1984.

[4.7] P. Rossky, J. Doll, and H. Friedman, "Brownian dynamics as smart Monte Carlo simulation," *The Journal of Chemical Physics*, vol. 69, no. 10, pp. 4628–4633, 1978.

[4.8] H. A. Kramers, "Brownian motion in a field of force and the diffusion model of chemical reactions," *Physica*, vol. 7, no. 4, pp. 284–304, 1940.

[4.9] P. Domokos and H. Ritsch, "Mechanical effects of light in optical resonators," *Journal of the Optical Society of America B*, vol. 20, no. 5, pp. 1098–1130, 2003.

[4.10] W. Niedenzu, T. Grießer, and H. Ritsch, "Kinetic theory of cavity cooling and self-organisation of a cold gas," *Europhysics Letters*, vol. 96, no. 4, p. 43001, 2011.

[4.11] V. Torggler and H. Ritsch, "Adaptive multifrequency light collection by self-ordered mobile scatterers in optical resonators," *Optica*, vol. 1, no. 5, pp. 336–342, 2014.

[4.12] A. Das and B. K. Chakrabarti, "Colloquium: Quantum annealing and analog quantum computation," *Reviews of Modern Physics*, vol. 80, no. 3, p. 1061, 2008.

[4.13] H. Ritsch, P. Domokos, F. Brennecke, and T. Esslinger, "Cold atoms in cavity-generated dynamical optical potentials," *Reviews of Modern Physics*, vol. 85, no. 2, p. 553, 2013.

[4.14] T. Albash and D. A. Lidar, "Adiabatic quantum computation," *Reviews of Modern Physics*, vol. 90, no. 1, p. 015002, 2018.

[4.15] L. Stella, G. E. Santoro, and E. Tosatti, "Optimization by quantum annealing: Lessons from simple cases," *Physical Review B*, vol. 72, no. 1, p. 014303, 2005.

[4.16] P. Hauke, H. G. Katzgraber, W. Lechner, H. Nishimori, and W. D. Oliver, "Perspectives of quantum annealing: Methods and implementations," *arXiv:1903.06559*, 2019.

[4.17] S. V. Isakov, G. Mazzola, V. N. Smelyanskiy, Z. Jiang, S. Boixo, H. Neven, and M. Troyer, "Understanding quantum tunneling through quantum Monte Carlo simulations," *Physical Review Letters*, vol. 117, no. 18, p. 180402, 2016.

[4.18] L. Hormozi, E. W. Brown, G. Carleo, and M. Troyer, “Nonstoquastic Hamiltonians and quantum annealing of an Ising spin glass,” *Physical Review B*, vol. 95, no. 18, p. 184416, 2017.

References for Chapter 5

[5.1] T. Keller, S. B. Jäger, and G. Morigi, “Phases of cold atoms interacting via photon-mediated long-range forces,” *Journal of Statistical Mechanics: Theory and Experiment*, vol. 2017, no. 6, p. 064002, 2017.

[5.2] P. Horak, G. Hechenblaikner, K. M. Gheri, H. Stecher, and H. Ritsch, “Cavity-induced atom cooling in the strong coupling regime,” *Physical Review Letters*, vol. 79, no. 25, p. 4974, 1997.

[5.3] P. Domokos and H. Ritsch, “Mechanical effects of light in optical resonators,” *Journal of the Optical Society of America B*, vol. 20, no. 5, pp. 1098–1130, 2003.

[5.4] A. T. Black, H. W. Chan, and V. Vuletić, “Observation of collective friction forces due to spatial self-organization of atoms: from Rayleigh to Bragg scattering,” *Physical Review Letters*, vol. 91, no. 20, p. 203001, 2003.

[5.5] K. Baumann, C. Guerlin, F. Brennecke, and T. Esslinger, “Dicke quantum phase transition with a superfluid gas in an optical cavity,” *Nature*, vol. 464, no. 7293, p. 1301, 2010.

[5.6] J. Asbóth, P. Domokos, H. Ritsch, and A. Vukics, “Self-organization of atoms in a cavity field: Threshold, bistability, and scaling laws,” *Physical Review A*, vol. 72, no. 5, p. 053417, 2005.

[5.7] S. Schütz and G. Morigi, “Prethermalization of atoms due to photon-mediated long-range interactions,” *Physical Review Letters*, vol. 113, no. 20, p. 203002, 2014.

[5.8] S. Schütz, S. B. Jäger, and G. Morigi, “Thermodynamics and dynamics of atomic self-organization in an optical cavity,” *Physical Review A*, vol. 92, no. 6, p. 063808, 2015.

[5.9] D. H. J. O’Dell, S. Giovanazzi, and G. Kurizki, “Rotons in gaseous Bose–Einstein condensates irradiated by a laser,” *Physical Review Letters*, vol. 90, p. 110402, Mar 2003.

[5.10] P. Münstermann, T. Fischer, P. Maunz, P. W. H. Pinkse, and G. Rempe, “Observation of cavity-mediated long-range light forces between strongly coupled atoms,” *Physical Review Letters*, vol. 84, pp. 4068–4071, May 2000.

[5.11] V. Vuletić and S. Chu, “Laser cooling of atoms, ions, or molecules by coherent scattering,” *Physical Review Letters*, vol. 84, no. 17, p. 3787, 2000.

[5.12] S. Schütz, S. B. Jäger, and G. Morigi, “Dissipation-assisted prethermalization in long-range interacting atomic ensembles,” *Physical Review Letters*, vol. 117, no. 8, p. 083001, 2016.

[5.13] S. B. Jäger, S. Schütz, and G. Morigi, “Mean-field theory of atomic self-organization in optical cavities,” *Physical Review A*, vol. 94, no. 2, p. 023807, 2016.

[5.14] S. Schütz, H. Habibian, and G. Morigi, “Cooling of atomic ensembles in optical cavities: Semiclassical limit,” *Physical Review A*, vol. 88, no. 3, p. 033427, 2013.

[5.15] P. Domokos, P. Horak, and H. Ritsch, “Semiclassical theory of cavity-assisted atom cooling,” *Journal of Physics B*, vol. 34, no. 2, p. 187, 2001.

[5.16] V. Torggler and H. Ritsch, “Adaptive multifrequency light collection by self-ordered mobile scatterers in optical resonators,” *Optica*, vol. 1, no. 5, pp. 336–342, 2014.

[5.17] F. Brennecke, T. Donner, S. Ritter, T. Bourdel, M. Köhl, and T. Esslinger, “Cavity QED with a Bose–Einstein condensate,” *Nature*, vol. 450, no. 7167, pp. 268–271, 2007.

[5.18] R. Landig, L. Hruby, N. Dogra, M. Landini, R. Mottl, T. Donner, and T. Esslinger, “Quantum phases from competing short-and long-range interactions in an optical lattice,” *Nature*, vol. 532, no. 7600, p. 476, 2016.

[5.19] J. Léonard, A. Morales, P. Zupancic, T. Esslinger, and T. Donner, “Supersolid formation in a quantum gas breaking a continuous translational symmetry,” *Nature*, vol. 543, no. 7643, pp. 87–90, 2017.

[5.20] J. Dalibard and C. Cohen-Tannoudji, “Atomic motion in laser light: connection between semiclassical and quantum descriptions,” *Journal of Physics B*, vol. 18, no. 8, p. 1661, 1985.

[5.21] A. Campa, T. Dauxois, and S. Ruffo, “Statistical mechanics and dynamics of solvable models with long-range interactions,” *Physics Reports*, vol. 480, no. 3, pp. 57–159, 2009.

[5.22] T. N. Teles, F. P. d. C. Benetti, R. Pakter, and Y. Levin, “Nonequilibrium phase transitions in systems with long-range interactions,” *Physical Review Letters*, vol. 109, no. 23, p. 230601, 2012.

[5.23] A. Pikovsky, S. Gupta, T. N. Teles, F. P. d. C. Benetti, R. Pakter, Y. Levin, and S. Ruffo, “Ensemble inequivalence in a mean-field X Y model with ferromagnetic and nematic couplings,” *Physical Review E*, vol. 90, no. 6, p. 062141, 2014.

[5.24] D. Auerbach, “Supercooling and the Mpemba effect: When hot water freezes quicker than cold,” *American Journal of Physics*, vol. 63, no. 10, pp. 882–885, 1995.

[5.25] J. D. Brownridge, “When does hot water freeze faster then cold water? a search for the Mpemba effect,” *American Journal of Physics*, vol. 79, no. 1, pp. 78–84, 2011.

[5.26] Y. Tao, W. Zou, J. Jia, W. Li, and D. Cremer, “Different ways of hydrogen bonding in water-why does warm water freeze faster than cold water?,” *Journal of Chemical Theory and Computation*, vol. 13, no. 1, pp. 55–76, 2017.

[5.27] J. Jin and W. A. Goddard III, “Mechanisms underlying the Mpemba effect in water from molecular dynamics simulations,” *Journal of Physical Chemistry C*, vol. 119, no. 5, pp. 2622–2629, 2015.

[5.28] X. Zhang, Y. Huang, Z. Ma, Y. Zhou, J. Zhou, W. Zheng, Q. Jiang, and C. Q. Sun, “Hydrogen-bond memory and water-skin supersolidity resolving theMpemba paradox,” *Physical Chemistry Chemical Physics*, vol. 16, no. 42, pp. 22995–23002, 2014.

[5.29] W. Niedenzu, T. Grießer, and H. Ritsch, “Kinetic theory of cavity cooling and self-organisation of a cold gas,” *Europhysics Letters*, vol. 96, no. 4, p. 43001, 2011.

[5.30] T. Grießer, W. Niedenzu, and H. Ritsch, “Cooperative self-organization and sympathetic cooling of a multispecies gas in a cavity,” *New Journal of Physics*, vol. 14, no. 5, p. 053031, 2012.

[5.31] H. Habibian, A. Winter, S. Paganelli, H. Rieger, and G. Morigi, “Bose-glass phases of ultracold atoms due to cavity backaction,” *Physical Review Letters*, vol. 110, no. 7, p. 075304, 2013.

[5.32] S. Krämer and H. Ritsch, “Self-ordering dynamics of ultracold atoms in multicolored cavity fields,” *Physical Review A*, vol. 90, no. 3, p. 033833, 2014.

[5.33] C. Maschler, H. Ritsch, A. Vukics, and P. Domokos, “Entanglement assisted fast reordering of atoms in an optical lattice within a cavity at t= 0,” *Optics Communications*, vol. 273, no. 2, pp. 446–450, 2007.

[5.34] V. Torggler, S. Krämer, and H. Ritsch, “Quantum annealing with ultracold atoms in a multimode optical resonator,” *Physical Review A*, vol. 95, no. 3, p. 032310, 2017.

References for Chapter 6

[6.1] H. Ritsch, P. Domokos, F. Brennecke, and T. Esslinger, “Cold atoms in cavity-generated dynamical optical potentials,” *Reviews of Modern Physics*, vol. 85, no. 2, p. 553, 2013.

[6.2] A. T. Black, H. W. Chan, and V. Vuletić, “Observation of collective friction forces due to spatial self-organization of atoms: from Rayleigh to Bragg scattering,” *Physical Review Letters*, vol. 91, no. 20, p. 203001, 2003.

[6.3] S. Slama, G. Krenz, S. Bux, C. Zimmermann, and P. W. Courteille, “Cavity-enhanced superradiant Rayleigh scattering with ultracold and Bose–Einstein condensed atoms,” *Physical Review A*, vol. 75, no. 6, p. 063620, 2007.

[6.4] P. Treutlein, D. Hunger, S. Camerer, T. W. Hänsch, and J. Reichel, “Bose–Einstein condensate coupled to a nanomechanical resonator on an atom chip,” *Physical Review Letters*, vol. 99, no. 14, p. 140403, 2007.

[6.5] S. Gupta, K. L. Moore, K. W. Murch, and D. M. Stamper-Kurn, “Cavity nonlinear optics at low photon numbers from collective atomic motion,” *Physical Review Letters*, vol. 99, no. 21, p. 213601, 2007.

[6.6] K. Baumann, C. Guerlin, F. Brennecke, and T. Esslinger, “Dicke quantum phase transition with a superfluid gas in an optical cavity,” *Nature*, vol. 464, no. 7293, p. 1301, 2010.

[6.7] K. Arnold, M. Baden, and M. Barrett, “Self-organization threshold scaling for thermal atoms coupled to a cavity,” *Physical Review Letters*, vol. 109, no. 15, p. 153002, 2012.

[6.8] H. Keßler, J. Klinder, M. Wolke, and A. Hemmerich, “Steering matter wave superradiance with an ultranarrow-band optical cavity,” *Physical Review Letters*, vol. 113, no. 7, p. 070404, 2014.

[6.9] A. J. Kollár, A. T. Papageorge, K. Baumann, M. A. Armen, and B. L. Lev, “An adjustable-length cavity and Bose–Einstein condensate apparatus for multimode cavity QED,” *New Journal of Physics*, vol. 17, no. 4, p. 043012, 2015.

[6.10] P. Domokos and H. Ritsch, “Collective cooling and self-organization of atoms in a cavity,” *Physical Review Letters*, vol. 89, no. 25, p. 253003, 2002.

[6.11] J. Keeling, M. Bhaseen, and B. Simons, “Fermionic superradiance in a transversely pumped optical cavity,” *Physical Review Letters*, vol. 112, no. 14, p. 143002, 2014.

[6.12] F. Piazza and P. Strack, “Umklapp superradiance with a collisionless quantum degenerate fermi gas,” *Physical Review Letters*, vol. 112, no. 14, p. 143003, 2014.

[6.13] Y. Chen, Z. Yu, and H. Zhai, “Superradiance of degenerate Fermi gases in a cavity,” *Physical Review Letters*, vol. 112, no. 14, p. 143004, 2014.

[6.14] K. Hepp and E. H. Lieb, “On the superradiant phase transition for molecules in a quantized radiation field: The Dicke Maser model,” *Annals of Physics*, vol. 76, no. 2, pp. 360–404, 1973.

[6.15] R. Landig, L. Hruby, N. Dogra, M. Landini, R. Mottl, T. Donner, and T. Esslinger, “Quantum phases from competing short-and long-range interactions in an optical lattice,” *Nature*, vol. 532, no. 7600, p. 476, 2016.

[6.16] Y. Li, L. He, and W. Hofstetter, "Lattice-supersolid phase of strongly correlated bosons in an optical cavity," *Physical Review A*, vol. 87, no. 5, p. 051604, 2013.

[6.17] M. R. Bakhtiari, A. Hemmerich, H. Ritsch, and M. Thorwart, "Nonequilibrium phase transition of interacting bosons in an intra-cavity optical lattice," *Physical Review Letters*, vol. 114, no. 12, p. 123601, 2015.

[6.18] S. Krämer and H. Ritsch, "Self-ordering dynamics of ultracold atoms in multicolored cavity fields," *Physical Review A*, vol. 90, no. 3, p. 033833, 2014.

[6.19] V. Torggler and H. Ritsch, "Adaptive multifrequency light collection by self-ordered mobile scatterers in optical resonators," *Optica*, vol. 1, no. 5, pp. 336–342, 2014.

[6.20] S. Gopalakrishnan, B. L. Lev, and P. M. Goldbart, "Emergent crystallinity and frustration with Bose–Einstein condensates in multimode cavities," *Nature Physics*, vol. 5, no. 11, pp. 845–850, 2009.

[6.21] S. Gopalakrishnan, B. L. Lev, and P. M. Goldbart, "Frustration and glassiness in spin models with cavity-mediated interactions," *Physical Review Letters*, vol. 107, no. 27, p. 277201, 2011.

[6.22] S. Gopalakrishnan, B. L. Lev, and P. M. Goldbart, "Exploring models of associative memory via cavity quantum electrodynamics," *Philosophical Magazine*, vol. 92, no. 1-3, pp. 353–361, 2012.

[6.23] H. Habibian, A. Winter, S. Paganelli, H. Rieger, and G. Morigi, "Bose-glass phases of ultracold atoms due to cavity backaction," *Physical Review Letters*, vol. 110, no. 7, p. 075304, 2013.

[6.24] I. B. Mekhov and H. Ritsch, "Quantum nondemolition measurements and state preparation in quantum gases by light detection," *Physical Review Letters*, vol. 102, no. 2, p. 020403, 2009.

[6.25] S. F. Caballero-Benitez and I. B. Mekhov, "Quantum optical lattices for emergent many-body phases of ultracold atoms," *Physical Review Letters*, vol. 115, no. 24, p. 243604, 2015.

[6.26] A. J. Kollár, A. T. Papageorge, V. D. Vaidya, Y. Guo, J. Keeling, and B. L. Lev, "Supermode-density-wave-polariton condensation with a Bose–Einstein condensate in a multimode cavity," *Nature Communications*, vol. 8, p. 14386, 2017.

[6.27] P. Hauke, L. Bonnes, M. Heyl, and W. Lechner, "Probing entanglement in adiabatic quantum optimization with trapped ions," *Frontiers of Physics*, vol. 3, p. 21, 2015.

[6.28] M. Johnson, M. Amin, S. Gildert, T. Lanting, F. Hamze, N. Dickson, R. Harris, A. Berkley, J. Johansson, P. Bunyk, *et al.*, "Quantum annealing with manufactured spins," *Nature*, vol. 473, no. 7346, pp. 194–198, 2011.

[6.29] V. Choi, “Minor-embedding in adiabatic quantum computation: I. The parameter setting problem,” *Quantum Information Processing*, vol. 7, no. 5, pp. 193–209, 2008.

[6.30] W. Lechner, P. Hauke, and P. Zoller, “A quantum annealing architecture with all-to-all connectivity from local interactions,” *Science Advances*, vol. 1, no. 9, p. e1500838, 2015.

[6.31] T. Kadowaki and H. Nishimori, “Quantum annealing in the transverse ising model,” *Physical Review E*, vol. 58, p. 5355, Nov 1998.

[6.32] E. Farhi, J. Goldstone, S. Gutmann, J. Lapan, A. Lundgren, and D. Preda, “A quantum adiabatic evolution algorithm applied to random instances of an NP-complete problem,” *Science*, vol. 292, no. 5516, pp. 472–475, 2001.

[6.33] R. M. Sandner, W. Niedenzu, F. Piazza, and H. Ritsch, “Self-ordered stationary states of driven quantum degenerate gases in optical resonators,” *Europhysics Letters*, vol. 111, no. 5, p. 53001, 2015.

[6.34] S. Santra, O. Shehab, and R. Balu, “Ising formulation of associative memory models and quantum annealing recall,” *Physical Review A*, vol. 96, no. 6, p. 062330, 2017.

[6.35] C. Maschler, I. B. Mekhov, and H. Ritsch, “Ultracold atoms in optical lattices generated by quantized light fields,” *The European Physical Journal D*, vol. 46, no. 3, pp. 545–560, 2008.

[6.36] C. Maschler and H. Ritsch, “Cold atom dynamics in a quantum optical lattice potential,” *Physical Review Letters*, vol. 95, no. 26, p. 260401, 2005.

[6.37] I. B. Mekhov and H. Ritsch, “Quantum optics with ultracold quantum gases: towards the full quantum regime of the light–matter interaction,” *Journal of Physics B*, vol. 45, no. 10, p. 102001, 2012.

[6.38] D. Jaksch, C. Bruder, J. I. Cirac, C. W. Gardiner, and P. Zoller, “Cold bosonic atoms in optical lattices,” *Physical Review Letters*, vol. 81, no. 15, p. 3108, 1998.

[6.39] W. Kohn, “Analytic properties of Bloch waves and Wannier functions,” *Physical Review*, vol. 115, no. 4, p. 809, 1959.

[6.40] D. Nagy, P. Domokos, A. Vukics, and H. Ritsch, “Nonlinear quantum dynamics of two BEC modes dispersively coupled by an optical cavity,” *The European Physical Journal D*, vol. 55, no. 3, p. 659, 2009.

[6.41] M. Wolke, J. Klinner, H. Keßler, and A. Hemmerich, “Cavity cooling below the recoil limit,” *Science*, vol. 337, no. 6090, pp. 75–78, 2012.

[6.42] F. Mila and K. P. Schmidt, “Strong-coupling expansion and effective Hamiltonians,” in *Introduction to Frustrated Magnetism*, pp. 537–559, Springer, 2011.

[6.43] B. Paredes, A. Widera, V. Murg, O. Mandel, S. Fölling, I. Cirac, G. V. Shlyapnikov, T. W. Hänsch, and I. Bloch, “Tonks–Girardeau gas of ultracold atoms in an optical lattice,” *Nature*, vol. 429, no. 6989, pp. 277–281, 2004.

[6.44] G. E. Santoro and E. Tosatti, “Optimization using quantum mechanics: quantum annealing through adiabatic evolution,” *Journal of Physics A*, vol. 39, no. 36, p. R393, 2006.

[6.45] S. Boixo, T. F. Rønnow, S. V. Isakov, Z. Wang, D. Wecker, D. A. Lidar, J. M. Martinis, and M. Troyer, “Evidence for quantum annealing with more than one hundred qubits,” *Nature Physics*, vol. 10, no. 3, pp. 218–224, 2014.

[6.46] B. Heim, T. F. Rønnow, S. V. Isakov, and M. Troyer, “Quantum versus classical annealing of Ising spin glasses,” *Science*, vol. 348, no. 6231, pp. 215–217, 2015.

[6.47] H. G. Katzgraber, F. Hamze, Z. Zhu, A. J. Ochoa, and H. Munoz-Bauza, “Seeking quantum speedup through spin glasses: The good, the bad, and the ugly,” *Physical Review X*, vol. 5, no. 3, p. 031026, 2015.

[6.48] T. Kato, “On the adiabatic theorem of quantum mechanics,” *Journal of the Physical Society of Japan*, vol. 5, no. 6, pp. 435–439, 1950.

[6.49] J. J. Hopfield, “Neural networks and physical systems with emergent collective computational abilities,” *Proceedings of the national academy of sciences*, vol. 79, no. 8, pp. 2554–2558, 1982.

[6.50] J. J. Hopfield, “Neurons with graded response have collective computational properties like those of two-state neurons,” *Proceedings of the national academy of sciences*, vol. 81, no. 10, pp. 3088–3092, 1984.

[6.51] D. O. Hebb, *The organization of behavior: A neuropsychological theory.* Psychology Press, 2005.

[6.52] D. J. Amit, H. Gutfreund, and H. Sompolinsky, “Statistical mechanics of neural networks near saturation,” *Annals of Physics*, vol. 173, no. 1, pp. 30–67, 1987.

References for Chapter 7

[7.1] A. W. Harrow and A. Montanaro, “Quantum computational supremacy,” *Nature*, vol. 549, no. 7671, pp. 203–209, 2017.

[7.2] J. I. Cirac and P. Zoller, “Goals and opportunities in quantum simulation,” *Nature Physics*, vol. 8, pp. 264–266, apr 2012.

[7.3] R. Blatt and C. F. Roos, “Quantum simulations with trapped ions,” *Nature Physics*, vol. 8, no. 4, pp. 277–284, 2012.

[7.4] I. Bloch, J. Dalibard, and S. Nascimbene, “Quantum simulations with ultracold quantum gases,” *Nature Physics*, vol. 8, pp. 267–276, apr 2012.

[7.5] A. Aspuru-Guzik and P. Walther, “Photonic quantum simulators,” *Nature Physics*, vol. 8, no. 4, pp. 285–291, 2012.

[7.6] S. De Léséleuc, S. Weber, V. Lienhard, D. Barredo, H. P. Büchler, T. Lahaye, and A. Browaeys, “Accurate mapping of multilevel Rydberg atoms on interacting spin-1/2 particles for the quantum simulation of Ising models,” *Physical Review Letters*, vol. 120, no. 11, p. 113602, 2018.

[7.7] A. A. Houck, H. E. Türeci, and J. Koch, “On-chip quantum simulation with superconducting circuits,” *Nature Physics*, vol. 8, no. 4, pp. 292–299, 2012.

[7.8] I. M. Georgescu, S. Ashhab, and F. Nori, “Quantum simulation,” *Reviews of Modern Physics*, vol. 86, pp. 153–185, Mar 2014.

[7.9] M. Saffman, “Quantum computing with atomic qubits and Rydberg interactions: progress and challenges,” *Journal of Physics B*, vol. 49, no. 20, p. 202001, 2016.

[7.10] J. Preskill, “Quantum computing in the NISQ era and beyond,” *Quantum*, vol. 2, p. 79, 2018.

[7.11] S. Boixo, S. V. Isakov, V. N. Smelyanskiy, R. Babbush, N. Ding, Z. Jiang, M. J. Bremner, J. M. Martinis, and H. Neven, “Characterizing quantum supremacy in near-term devices,” *Nature Physics*, vol. 14, no. 6, p. 595, 2018.

[7.12] J. Preskill, “Quantum computing and the entanglement frontier,” *arXiv:1203.5813*, 2012.

[7.13] H. Bernien, S. Schwartz, A. Keesling, H. Levine, A. Omran, H. Pichler, S. Choi, A. S. Zibrov, M. Endres, M. Greiner, *et al.*, “Probing many-body dynamics on a 51-atom quantum simulator,” *Nature*, vol. 551, no. 7682, p. 579, 2017.

[7.14] K. Kim, M.-S. Chang, S. Korenblit, R. Islam, E. E. Edwards, J. K. Freericks, G.-D. Lin, L.-M. Duan, and C. Monroe, “Quantum simulation of frustrated ising spins with trapped ions,” *Nature*, vol. 465, no. 7298, pp. 590–593, 2010.

[7.15] P. Schauß, M. Cheneau, M. Endres, T. Fukuhara, S. Hild, A. Omran, T. Pohl, C. Gross, S. Kuhr, and I. Bloch, “Observation of spatially ordered structures in a two-dimensional Rydberg gas,” *Nature*, vol. 491, no. 7422, pp. 87–91, 2012.

[7.16] T. Kadowaki and H. Nishimori, “Quantum annealing in the transverse ising model,” *Physical Review E*, vol. 58, p. 5355, Nov 1998.

[7.17] E. Farhi, J. Goldstone, S. Gutmann, and M. Sipser, “Quantum computation by adiabatic evolution,” *quant-ph/0001106*, 2000.

[7.18] T. Albash and D. A. Lidar, “Adiabatic quantum computation,” *Reviews of Modern Physics*, vol. 90, no. 1, p. 015002, 2018.

[7.19] A. Lucas, “Ising formulations of many NP problems,” *Frontiers of Physics*, vol. 2, p. 5, 2014.

[7.20] S. Boixo, T. F. Rønnow, S. V. Isakov, Z. Wang, D. Wecker, D. A. Lidar, J. M. Martinis, and M. Troyer, “Evidence for quantum annealing with more than one hundred qubits,” *Nature Physics*, vol. 10, no. 3, pp. 218–224, 2014.

[7.21] P. Hauke, H. G. Katzgraber, W. Lechner, H. Nishimori, and W. D. Oliver, “Perspectives of quantum annealing: Methods and implementations,” *arXiv:1903.06559*, 2019.

[7.22] W. Lechner, P. Hauke, and P. Zoller, “A quantum annealing architecture with all-to-all connectivity from local interactions,” *Science Advances*, vol. 1, no. 9, p. e1500838, 2015.

[7.23] V. Choi, “Minor-embedding in adiabatic quantum computation: I. The parameter setting problem,” *Quantum Information Processing*, vol. 7, no. 5, pp. 193–209, 2008.

[7.24] H. Ritsch, P. Domokos, F. Brennecke, and T. Esslinger, “Cold atoms in cavity-generated dynamical optical potentials,” *Reviews of Modern Physics*, vol. 85, no. 2, p. 553, 2013.

[7.25] C. Maschler and H. Ritsch, “Cold atom dynamics in a quantum optical lattice potential,” *Physical Review Letters*, vol. 95, no. 26, p. 260401, 2005.

[7.26] R. Landig, L. Hruby, N. Dogra, M. Landini, R. Mottl, T. Donner, and T. Esslinger, “Quantum phases from competing short-and long-range interactions in an optical lattice,” *Nature*, vol. 532, no. 7600, p. 476, 2016.

[7.27] I. B. Mekhov and H. Ritsch, “Quantum optics with ultracold quantum gases: towards the full quantum regime of the light–matter interaction,” *Journal of Physics B*, vol. 45, no. 10, p. 102001, 2012.

[7.28] S. F. Caballero-Benitez, G. Mazzucchi, and I. B. Mekhov, “Quantum simulators based on the global collective light-matter interaction,” *Physical Review A*, vol. 93, no. 6, p. 063632, 2016.

[7.29] J. Bell and B. Stevens, “A survey of known results and research areas for n-queens,” *Discrete Mathematics*, vol. 309, no. 1, pp. 1–31, 2009.

[7.30] I. P. Gent, C. Jefferson, and P. Nightingale, “Complexity of n-queens completion,” *Journal of Artificial Intelligence Research*, vol. 59, pp. 815–848, 2017.

[7.31] I. Hen, “Realizable quantum adiabatic search,” *Europhysics Letters*, vol. 118, no. 3, p. 30003, 2017.

[7.32] I. Hen and F. M. Spedalieri, "Quantum annealing for constrained optimization," *Physical Review Applied*, vol. 5, no. 3, p. 034007, 2016.

[7.33] P. Domokos and H. Ritsch, "Collective cooling and self-organization of atoms in a cavity," *Physical Review Letters*, vol. 89, no. 25, p. 253003, 2002.

[7.34] A. T. Black, H. W. Chan, and V. Vuletić, "Observation of collective friction forces due to spatial self-organization of atoms: from Rayleigh to Bragg scattering," *Physical Review Letters*, vol. 91, no. 20, p. 203001, 2003.

[7.35] V. D. Vaidya, Y. Guo, R. M. Kroeze, K. E. Ballantine, A. J. Kollár, J. Keeling, and B. L. Lev, "Tunable-range, photon-mediated atomic interactions in multimode cavity QED," *Physical Review X*, vol. 8, no. 1, p. 011002, 2018.

[7.36] S. Gupta, K. L. Moore, K. W. Murch, and D. M. Stamper-Kurn, "Cavity nonlinear optics at low photon numbers from collective atomic motion," *Physical Review Letters*, vol. 99, no. 21, p. 213601, 2007.

[7.37] S. Gopalakrishnan, B. L. Lev, and P. M. Goldbart, "Frustration and glassiness in spin models with cavity-mediated interactions," *Physical Review Letters*, vol. 107, no. 27, p. 277201, 2011.

[7.38] S. Gopalakrishnan, B. L. Lev, and P. M. Goldbart, "Exploring models of associative memory via cavity quantum electrodynamics," *Philosophical Magazine*, vol. 92, no. 1-3, pp. 353–361, 2012.

[7.39] S. Krämer and H. Ritsch, "Self-ordering dynamics of ultracold atoms in multicolored cavity fields," *Physical Review A*, vol. 90, no. 3, p. 033833, 2014.

[7.40] V. Torggler, S. Krämer, and H. Ritsch, "Quantum annealing with ultracold atoms in a multimode optical resonator," *Physical Review A*, vol. 95, no. 3, p. 032310, 2017.

[7.41] I. B. Mekhov and H. Ritsch, "Quantum nondemolition measurements and state preparation in quantum gases by light detection," *Physical Review Letters*, vol. 102, no. 2, p. 020403, 2009.

[7.42] V. Choi, "Minor-embedding in adiabatic quantum computation: Ii. Minor-universal graph design," *Quantum Information Processing*, vol. 10, no. 3, pp. 343–353, 2011.

[7.43] A. Rocchetto, S. C. Benjamin, and Y. Li, "Stabilizers as a design tool for new forms of the Lechner-Hauke-Zoller annealer," *Science Advances*, vol. 2, no. 10, p. e1601246, 2016.

[7.44] A. W. Glaetzle, R. M. van Bijnen, P. Zoller, and W. Lechner, "A coherent quantum annealer with Rydberg atoms," *Nature Communications*, vol. 8, p. 15813, 2017.

[7.45] W. Vinci and D. A. Lidar, “Scalable effective-temperature reduction for quantum annealers via nested quantum annealing correction,” *Physical Review A*, vol. 97, no. 2, p. 022308, 2018.

[7.46] L. Hormozi, E. W. Brown, G. Carleo, and M. Troyer, “Nonstoquastic Hamiltonians and quantum annealing of an Ising spin glass,” *Physical Review B*, vol. 95, no. 18, p. 184416, 2017.

[7.47] T. Albash, “Role of nonstoquastic catalysts in quantum adiabatic optimization,” *Physical Review A*, vol. 99, no. 4, p. 042334, 2019.

[7.48] S. V. Isakov, G. Mazzola, V. N. Smelyanskiy, Z. Jiang, S. Boixo, H. Neven, and M. Troyer, “Understanding quantum tunneling through quantum Monte Carlo simulations,” *Physical Review Letters*, vol. 117, no. 18, p. 180402, 2016.

[7.49] J. Klassen and B. M. Terhal, “Two-local qubit Hamiltonians: when are they stoquastic?,” *Quantum*, vol. 3, p. 139, May 2019.

[7.50] M. Marvian, D. A. Lidar, and I. Hen, “On the computational complexity of curing non-stoquastic Hamiltonians,” *Nature Communications*, vol. 10, no. 1, p. 1571, 2019.

[7.51] I. Bloch, “Ultracold quantum gases in optical lattices,” *Nature Physics*, vol. 1, no. 1, pp. 23–30, 2005.

[7.52] F. Meinert, M. J. Mark, E. Kirilov, K. Lauber, P. Weinmann, M. Gröbner, A. J. Daley, and H.-C. Nägerl, “Observation of many-body dynamics in long-range tunneling after a quantum quench,” *Science*, vol. 344, no. 6189, pp. 1259–1262, 2014.

[7.53] P. Domokos and H. Ritsch, “Mechanical effects of light in optical resonators,” *Journal of the Optical Society of America B*, vol. 20, no. 5, pp. 1098–1130, 2003.

[7.54] C. Maschler, I. B. Mekhov, and H. Ritsch, “Ultracold atoms in optical lattices generated by quantized light fields,” *The European Physical Journal D*, vol. 46, no. 3, pp. 545–560, 2008.

[7.55] D. Jaksch, C. Bruder, J. I. Cirac, C. W. Gardiner, and P. Zoller, “Cold bosonic atoms in optical lattices,” *Physical Review Letters*, vol. 81, no. 15, p. 3108, 1998.

[7.56] W. Kohn, “Analytic properties of Bloch waves and Wannier functions,” *Physical Review*, vol. 115, no. 4, p. 809, 1959.

[7.57] D. Nagy, P. Domokos, A. Vukics, and H. Ritsch, “Nonlinear quantum dynamics of two BEC modes dispersively coupled by an optical cavity,” *The European Physical Journal D*, vol. 55, no. 3, p. 659, 2009.

[7.58] H. Habibian, A. Winter, S. Paganelli, H. Rieger, and G. Morigi, “Bose-glass phases of ultracold atoms due to cavity backaction,” *Physical Review Letters*, vol. 110, no. 7, p. 075304, 2013.

[7.59] W. S. Bakr, J. I. Gillen, A. Peng, S. Fölling, and M. Greiner, "A quantum gas microscope for detecting single atoms in a Hubbard-regime optical lattice," *Nature*, vol. 462, no. 7269, p. 74, 2009.

[7.60] J. F. Sherson, C. Weitenberg, M. Endres, M. Cheneau, I. Bloch, and S. Kuhr, "Single-atom-resolved fluorescence imaging of an atomic mott insulator," *Nature*, vol. 467, no. 7311, p. 68, 2010.

[7.61] H. Carmichael, *An Open Systems Approach to Quantum Optics: Lectures Presented at the Université Libre de Bruxelles, October 28 to November 4, 1991.* No. Bd. 18 in An Open Systems Approach to Quantum Optics: Lectures Presented at the Université Libre de Bruxelles, October 28 to November 4, 1991, Springer Berlin Heidelberg, 1993.

[7.62] M. Wolke, J. Klinner, H. Keßler, and A. Hemmerich, "Cavity cooling below the recoil limit," *Science*, vol. 337, no. 6090, pp. 75–78, 2012.

[7.63] R. Jha, D. Das, A. Dash, S. Jayaraman, B. K. Behera, and P. K. Panigrahi, "A novel quantum N-queens solver algorithm and its simulation and application to satellite communication using IBM quantum experience," *arXiv:1806.10221 [quant-ph]*, 2018.

[7.64] S. Krämer, D. Plankensteiner, L. Ostermann, and H. Ritsch, "QuantumOptics.jl: A Julia framework for simulating open quantum systems," *Computer Physics Communications*, pp. –, 2018.

References for Chapter 8

[8.1] J. Asbóth, P. Domokos, H. Ritsch, and A. Vukics, "Self-organization of atoms in a cavity field: Threshold, bistability, and scaling laws," *Physical Review A*, vol. 72, no. 5, p. 053417, 2005.

[8.2] W. Niedenzu, T. Grießer, and H. Ritsch, "Kinetic theory of cavity cooling and self-organisation of a cold gas," *Europhysics Letters*, vol. 96, no. 4, p. 43001, 2011.

[8.3] S. Schütz and G. Morigi, "Prethermalization of atoms due to photon-mediated long-range interactions," *Physical Review Letters*, vol. 113, no. 20, p. 203002, 2014.

[8.4] P. Horak and H. Ritsch, "Scaling properties of cavity-enhanced atom cooling," *Physical Review A*, vol. 64, no. 3, p. 033422, 2001.

References for Chapter 9

[9.1] V. Torggler and H. Ritsch, "Adaptive multifrequency light collection by self-ordered mobile scatterers in optical resonators," *Optica*, vol. 1, no. 5, pp. 336–342, 2014.

[9.2] S. De Léséleuc, S. Weber, V. Lienhard, D. Barredo, H. P. Büchler, T. Lahaye, and A. Browaeys, "Accurate mapping of multilevel Rydberg atoms on interacting spin-1/2 particles for the quantum simulation of Ising models," *Physical Review Letters*, vol. 120, no. 11, p. 113602, 2018.

[9.3] E. B. Mpemba and D. G. Osborne, "Cool?," *Physics Education*, vol. 4, no. 3, p. 172, 1969.

[9.4] Y. Tao, W. Zou, J. Jia, W. Li, and D. Cremer, "Different ways of hydrogen bonding in water-why does warm water freeze faster than cold water?," *Journal of Chemical Theory and Computation*, vol. 13, no. 1, pp. 55–76, 2017.

References for Chapter A

[A.1] A. Siegman, *Lasers.* University Science Books, 1986.

[A.2] H. Kogelnik and T. Li, "Laser beams and resonators," *Applied Optics*, vol. 5, no. 10, pp. 1550–1567, 1966.

[A.3] H. Tanji-Suzuki, I. D. Leroux, M. H. Schleier-Smith, M. Cetina, A. T. Grier, J. Simon, and V. Vuletić, "Interaction between atomic ensembles and optical resonators: classical description," in *Advances in atomic, molecular, and optical physics*, vol. 60, pp. 201–237, Elsevier, 2011.

[A.4] R. Grimm, M. Weidemüller, and Y. B. Ovchinnikov, "Optical dipole traps for neutral atoms," in *Advances in atomic, molecular, and optical physics*, vol. 42, pp. 95–170, Elsevier, 2000.

[A.5] V. Weisskopf and E. Wigner, "Berechnung der natürlichen Linienbreite auf Grund der Diracschen Lichttheorie," *Zeitschrift für Physik*, vol. 63, no. 1-2, pp. 54–73, 1930.

[A.6] J. D. Jackson, *Classical electrodynamics.* John Wiley & Sons, 2012.

[A.7] C. Maschler, I. B. Mekhov, and H. Ritsch, "Ultracold atoms in optical lattices generated by quantized light fields," *The European Physical Journal D*, vol. 46, no. 3, pp. 545–560, 2008.

[A.8] C. W. Gardiner and P. Zoller, *Quantum Noise: A Handbook of Markovian and Non-Markovian Quantum Stochastic Methods with Applications to Quantum Optics.* Springer Series in Synergetics, Springer, 2004.

[A.9] T. Keller, V. Torggler, S. B. Jäger, S. Schütz, H. Ritsch, and G. Morigi, "Quenches across the self-organization transition in multimode cavities," *New Journal of Physics*, vol. 20, no. 2, p. 025004, 2018.

[A.10] H. Carmichael, *An Open Systems Approach to Quantum Optics: Lectures Presented at the Université Libre de Bruxelles, October 28 to November 4, 1991*. No. Bd. 18 in An Open Systems Approach to Quantum Optics: Lectures Presented at the Université Libre de Bruxelles, October 28 to November 4, 1991, Springer Berlin Heidelberg, 1993.

[A.11] R. Landig, L. Hruby, N. Dogra, M. Landini, R. Mottl, T. Donner, and T. Esslinger, "Quantum phases from competing short-and long-range interactions in an optical lattice," *Nature*, vol. 532, no. 7600, p. 476, 2016.

[A.12] J. K. Asbóth, P. Domokos, and H. Ritsch, "Correlated motion of two atoms trapped in a single-mode cavity field," *Physical Review A*, vol. 70, no. 1, p. 013414, 2004.

[A.13] M. Gangl and H. Ritsch, "Cold atoms in a high-Q ring cavity," *Physical Review A*, vol. 61, no. 4, p. 043405, 2000.

References for Chapter B

[B.1] S. Haroche and J. M. Raimond, *Exploring the Quantum: Atoms, Cavities and Photons*. New York: Oxford University Press, 2006.

[B.2] Y. Kaluzny, P. Goy, M. Gross, J. M. Raimond, and S. Haroche, "Observation of self-induced Rabi oscillations in two-level atoms excited inside a resonant cavity: The ringing regime of superradiance," *Physical Review Letters*, vol. 51, pp. 1175–1178, Sept. 1983.

[B.3] M. G. Raizen, R. J. Thompson, R. J. Brecha, H. J. Kimble, and H. J. Carmichael, "Normal-mode splitting and linewidth averaging for two-state atoms in an optical cavity," *Physical Review Letters*, vol. 63, pp. 240–243, July 1989.

[B.4] F. Bernardot, P. Nussenzveig, M. Brune, J. M. Raimond, and S. Haroche, "Vacuum Rabi splitting observed on a microscopic atomic sample in a microwave cavity," *Europhysics Letters*, vol. 17, p. 33, 1992.

[B.5] R. J. Brecha, L. Orozco, M. G. Raizen, M. Xiao, and H. J. Kimble, "Observation of oscillatory energy exchange in a coupled atom-cavity system," *Journal of the Optical Society of America B*, vol. 12, p. 2329, 1995.

[B.6] R. J. Thompson, G. Rempe, and H. J. Kimble, "Observation of normal-mode splitting for an atom in an optical cavity," *Physical Review Letters*, vol. 68, pp. 1132–1135, Feb. 1992.

[B.7] M. Brune, F. Schmidt-Kaler, A. Maali, J. Dreyer, E. Hagley, J. M. Raimond, and S. Haroche, "Quantum Rabi oscillation: A direct test of field quantization in a cavity," *Physical Review Letters*, vol. 76, pp. 1800–1803, Mar. 1996.

[B.8] J. J. Childs, K. An, M. S. Otteson, R. R. Dasari, and M. S. Feld, "Normal-mode line shapes for atoms in standing-wave optical resonators," *Physical Review Letters*, vol. 77, pp. 2901–2904, Sept. 1996.

[B.9] C. J. Hood, M. S. Chapman, T. W. Lynn, and H. J. Kimble, "Real-time cavity QED with single atoms," *Physical Review Letters*, vol. 80, pp. 4157–4160, May 1998.

[B.10] A. Boca, R. Miller, K. M. Birnbaum, A. D. Boozer, J. McKeever, and H. J. Kimble, "Observation of the vacuum Rabi spectrum for one trapped atom," *Physical Review Letters*, vol. 93, p. 233603, Dec. 2004.

[B.11] P. Maunz, T. Puppe, I. Schuster, N. Syassen, P. W. H. Pinkse, and G. Rempe, "Normal-mode spectroscopy of a single-bound-atom–cavity system," *Physical Review Letters*, vol. 94, no. 3, p. 033002, 2005.

[B.12] M. Brune, P. Nussenzveig, F. Schmidt-Kaler, F. Bernardot, A. Maali, J. M. Raimond, and S. Haroche, "From Lamb shift to light shifts: Vacuum and subphoton cavity fields measured by atomic phase sensitive detection," *Physical Review Letters*, vol. 72, pp. 3339–3342, May 1994.

[B.13] P. Bertet, A. Auffeves, P. Maioli, S. Osnaghi, T. Meunier, M. Brune, J. M. Raimond, and S. Haroche, "Direct measurement of the Wigner function of a one-photon Fock state in a cavity," *Physical Review Letters*, vol. 89, p. 200402, Oct 2002.

[B.14] D. I. Schuster, A. Wallraff, A. Blais, L. Frunzio, R.-S. Huang, J. Majer, S. M. Girvin, and R. J. Schoelkopf, "AC Stark Shift and Dephasing of a Superconducting Qubit Strongly Coupled to a Cavity Field," *Physical Review Letters*, vol. 94, p. 123602, Mar. 2005.

[B.15] D. I. Schuster, A. A. Houck, J. A. Schreier, A. Wallraff, J. M. Gambetta, A. Blais, L. Frunzio, J. Majer, B. Johnson, M. H. Devoret, S. M. Girvin, and R. J. Schoelkopf, "Resolving photon number states in a superconducting circuit," *Nature*, vol. 445, no. 7127, pp. 515–518, 2007.

[B.16] C. Guerlin, J. Bernu, S. Deléglise, C. Sayrin, S. Gleyzes, S. Kuhr, M. Brune, J. M. Raimond, and S. Haroche, "Progressive field-state collapse and quantum non-demolition photon counting," *Nature*, vol. 448, no. 7156, pp. 889–893, 2007.

[B.17] B. R. Johnson, M. D. Reed, A. A. Houck, D. I. Schuster, L. S. Bishop, E. Ginossar, J. M. Gambetta, L. DiCarlo, L. Frunzio, S. M. Girvin, and R. J. Schoelkopf, "Quantum non-demolition detection of single microwave photons in a circuit," *Nature Physics*, vol. 6, pp. 663–667, June 2010.

[B.18] S. Deleglise, I. Dotsenko, C. Sayrin, J. Bernu, M. Brune, J. M. Raimond, and S. Haroche, "Reconstruction of non-classical cavity field states with snapshots of their decoherence," *Nature*, vol. 455, pp. 510–514, Sept. 2008.

[B.19] M. Hofheinz, H. Wang, M. Ansmann, R. C. Bialczak, E. Lucero, M. Neeley, A. D. O'Connell, D. Sank, J. Wenner, J. M. Martinis, and A. N. Cleland, "Synthesizing arbitrary quantum states in a superconducting resonator," *Nature*, vol. 459, no. 7246, pp. 546–549, 2009.

[B.20] C. Sayrin, I. Dotsenko, X. Zhou, B. Peaudecerf, T. Rybarczyk, S. Gleyzes, P. Rouchon, M. Mirrahimi, H. Amini, M. Brune, J. M. Raimond, and S. Haroche, "Real-time quantum feedback prepares and stabilizes photon number states," *Nature*, vol. 477, pp. 73–77, Sept. 2011.

[B.21] B. Vlastakis, G. Kirchmair, Z. Leghtas, S. E. Nigg, L. Frunzio, S. M. Girvin, M. Mirrahimi, M. H. Devoret, and R. J. Schoelkopf, "Deterministically encoding quantum information using 100-photon Schrödinger cat states," *Science*, vol. 342, no. 6158, pp. 607–610, 2013.

[B.22] R. W. Heeres, B. Vlastakis, E. Holland, S. Krastanov, V. V. Albert, L. Frunzio, L. Jiang, and R. J. Schoelkopf, "Cavity state manipulation using photon-number selective phase gates," *Physical Review Letters*, vol. 115, p. 137002, Sept. 2015.

[B.23] E. T. Holland, B. Vlastakis, R. W. Heeres, M. J. Reagor, U. Vool, Z. Leghtas, L. Frunzio, G. Kirchmair, M. H. Devoret, M. Mirrahimi, and R. J. Schoelkopf, "Single-photon-resolved cross-Kerr interaction for autonomous stabilization of photon-number states," *Physical Review Letters*, vol. 115, p. 180501, Oct. 2015.

[B.24] C. Wang, Y. Y. Gao, P. Reinhold, R. W. Heeres, N. Ofek, K. Chou, C. Axline, M. Reagor, J. Blumoff, K. M. Sliwa, L. Frunzio, S. M. Girvin, L. Jiang, M. Mirrahimi, M. H. Devoret, and R. J. Schoelkopf, "A Schrödinger cat living in two boxes," *Science*, vol. 352, no. 6289, pp. 1087–1091, 2016.

[B.25] J. Gambetta, A. Blais, D. I. Schuster, A. Wallraff, L. Frunzio, J. Majer, M. H. Devoret, S. M. Girvin, and R. J. Schoelkopf, "Qubit-photon interactions in a cavity: Measurement-induced dephasing and number splitting," *Physical Review A*, vol. 74, no. 4, p. 042318, 2006.

[B.26] K. W. Murch, S. J. Weber, C. Macklin, and I. Siddiqi, "Observing single quantum trajectories of a superconducting quantum bit," *Nature*, vol. 502, pp. 211–214, Oct. 2013.

[B.27] R. Vijay, C. Macklin, D. H. Slichter, S. J. Weber, K. W. Murch, R. Naik, A. N. Korotkov, and I. Siddiqi, "Stabilizing Rabi oscillations in a superconducting qubit using quantum feedback," *Nature*, vol. 490, pp. 77–80, Oct. 2012.

[B.28] N. Roch, M. E. Schwartz, F. Motzoi, C. Macklin, R. Vijay, A. W. Eddins, A. N. Korotkov, K. B. Whaley, M. Sarovar, and I. Siddiqi, "Observation of measurement-induced entanglement and quantum trajectories of remote superconducting qubits," *Physical Review Letters*, vol. 112, p. 170501, Apr 2014.

[B.29] C. A. Blockley, D. F. Walls, and H. Risken, “Quantum collapses and revivals in a quantized trap,” *Europhysics Letters*, vol. 17, no. 6, p. 509, 1992.

[B.30] J. I. Cirac, R. Blatt, A. S. Parkins, and P. Zoller, “Preparation of Fock states by observation of quantum jumps in an ion trap,” *Physical Review Letters*, vol. 70, pp. 762–765, Feb. 1993.

[B.31] D. M. Meekhof, C. Monroe, B. E. King, W. M. Itano, and D. J. Wineland, “Generation of nonclassical motional states of a trapped atom,” *Physical Review Letters*, vol. 76, pp. 1796–1799, Mar. 1996.

[B.32] C. Monroe, D. M. Meekhof, B. E. King, and D. J. Wineland, “A “Schrödinger Cat” Superposition State of an Atom,” *Science*, vol. 272, pp. 1131–1136, 1996.

[B.33] D. Kienzler, H.-Y. Lo, B. Keitch, L. de Clercq, F. Leupold, F. Lindenfelser, M. Marinelli, V. Negnevitsky, and J. P. Home, “Quantum harmonic oscillator state synthesis by reservoir engineering,” *Science*, vol. 347, pp. 53–56, 2015.

[B.34] H. Häffner, C. Roos, and R. Blatt, “Quantum computing with trapped ions,” *Physics Reports*, vol. 469, no. 4, pp. 155–203, 2008.

[B.35] F. Schmidt-Kaler, H. Häffner, S. Gulde, M. Riebe, G. Lancaster, J. Eschner, C. Becher, and R. Blatt, “Quantized AC-Stark shifts and their use for multiparticle entanglement and quantum gates,” *Europhysics Letters*, vol. 65, pp. 587–593, 2004.

[B.36] C. L. Degen, F. Reinhard, and P. Cappellaro, “Quantum sensing,” *Reviews of Modern Physics*, vol. 89, p. 035002, 2017.

[B.37] C. Russo, H. G. Barros, A. Stute, F. Dubin, E. S. Phillips, T. Monz, T. E. Northup, C. Becher, T. Salzburger, H. Ritsch, P. O. Schmidt, and R. Blatt, “Raman spectroscopy of a single ion coupled to a high-finesse cavity,” *Applied Physics B*, vol. 95, pp. 205–212, 05 2009.

[B.38] A. Stute, B. Casabone, B. Brandstätter, D. Habicher, P. O. Schmidt, T. E. Northup, and R. Blatt, “Toward an ion-photon quantum interface in an optical cavity,” *Applied Physics B*, vol. 107, no. 4, pp. 1145–1157, 2012.

[B.39] P. Schindler, D. Nigg, T. Monz, J. T. Barreiro, E. Martinez, S. X. Wang, S. Quint, M. F. Brandl, V. Nebendahl, C. F. Roos, M. Chwalla, M. Hennrich, and R. Blatt, “A quantum information processor with trapped ions,” *New Journal of Physics*, vol. 15, no. 12, p. 123012, 2013.

[B.40] C. Gardiner and P. Zoller, *Quantum Noise: A Handbook of Markovian and Non-Markovian Quantum Stochastic Methods with Applications to Quantum Optics.* Springer Series in Synergetics, Berlin: Springer-Verlag Berlin Heidelberg, 2004.

[B.41] R. J. Glauber, *Optical Coherence and Photon Statistics.* Wiley-VCH Verlag GmbH & Co. KGaA, 2007.

[B.42] I. B. Mekhov, C. Maschler, and H. Ritsch, "Probing quantum phases of ultracold atoms in optical lattices by transmission spectra in cavity quantum electrodynamics," *Nature Physics*, vol. 3, pp. 319–323, 2007.

[B.43] S. Begley, M. Vogt, G. K. Gulati, H. Takahashi, and M. Keller, "Optimized multi-ion cavity coupling," *Physical Review Letters*, vol. 116, p. 223001, May 2016.

[B.44] D. Leibfried, E. Knill, S. Seidelin, J. Britton, R. B. Blakestad, J. Chiaverini, D. B. Hume, W. M. Itano, J. D. Jost, C. Langer, R. Ozeri, R. Reichle, and D. J. Wineland, "Creation of a six-atom "Schrodinger cat" state," *Nature*, vol. 438, pp. 639–642, 2005.

[B.45] J. R. Johansson, P. D. Nation, and F. Nori, "QuTiP: An open-source Python framework for the dynamics of open quantum systems," *Computer Physics Communications*, vol. 183, pp. 1760–1772, 2012.

[B.46] J. R. Johansson, P. D. Nation, and F. Nori, "QuTiP 2: A Python framework for the dynamics of open quantum systems," *Computer Physics Communications*, vol. 184, p. 1234, 2013.

[B.47] C. W. Gardiner and A. S. Parkins, "Driving atoms with light of arbitrary statistics," *Physical Review A*, vol. 50, pp. 1792–1806, Aug 1994.

[B.48] H. J. Carmichael, *Statistical Methods in Quantum Optics 1: Master Equations and Fokker-Planck Equations.* Springer-Verlag Berlin Heidelberg, 1999.

[B.49] A. I. Lvovsky and M. G. Raymer, "Continuous-variable optical quantum-state tomography," *Reviews of Modern Physics*, vol. 81, pp. 299–332, Mar 2009.

[B.50] A. Stute, *A Light-Matter Quantum Interface: Ion-Photon Entanglement and State Mapping.* PhD thesis, Leopold-Franzens-Universität Innsbruck, 2012.

[B.51] W. M. Itano, J. C. Bergquist, J. J. Bollinger, J. M. Gilligan, D. J. Heinzen, F. L. Moore, M. G. Raizen, and D. J. Wineland, "Quantum projection noise: Population fluctuations in two-level systems," *Physical Review A*, vol. 47, pp. 3554–3570, May 1993.

[B.52] G. Rempe, R. J. Thompson, H. J. Kimble, and R. Lalezari, "Measurement of ultralow losses in an optical interferometer," *Optics Letters*, vol. 17, pp. 363–365, March 1992.

[B.53] A. H. Myerson, D. J. Szwer, S. C. Webster, D. T. C. Allcock, M. J. Curtis, G. Imreh, J. A. Sherman, D. N. Stacey, A. M. Steane, and D. M. Lucas, "High-fidelity readout of trapped-ion qubits," *Physical Review Letters*, vol. 100, p. 200502, May 2008.

[B.54] R. Noek, G. Vrijsen, D. Gaultney, E. Mount, T. Kim, P. Maunz, and J. Kim, "High speed, high fidelity detection of an atomic hyperfine qubit," *Optics Letters*, vol. 38, pp. 4735–4738, Nov 2013.

List of publications

Publications during the PhD studies

- V. Torggler, P. Aumann, H. Ritsch, and W. Lechner, "A quantum N-queens solver", *Quantum* **3**, 149 (2019).
- M. Lee, K. Friebe, D. A. Fioretto, K. Schüppert, F. R. Ong, D. Plankensteiner, V. Torggler, H. Ritsch, R. Blatt, and T. E. Northup, "Ion-based quantum sensor for optical cavity photon numbers", *Phys. Rev. Lett.* **122**, 153603 (2019).
- T. Keller, V. Torggler, S. B. Jäger, S. Schütz, H. Ritsch, and G. Morigi, "Quenches across the self-organization transition in multimode cavities", *New. J. Phys.* **20**, 025004 (2018).
- V. Torggler, S. Krämer, and H. Ritsch, "Quantum annealing with ultracold atoms in a multimode optical resonator", *Phys. Rev. A* **95**, 032310 (2017).

Publications before starting the PhD studies

- V. Torggler, H. Ritsch, "Adaptive multifrequency light collection by self-ordered mobile scatterers in optical resonators", *Optica* **1**, 5, 336-342 (2014).

Talks

- "Self-ordering and quantum optimization of cold atoms in a multi-mode cavity", *Seminar talk at the Institut za Fiziku*, Zagreb, Croatia, July 24, 2019.
- "Quantum annealing with ultracold atoms in multimode resonators", *57th Cracow School of Theoretical Physics*, Zakopane, Poland, June 15, 2017.
- "Optimization with multi-mode cavities", *D-A-CH project meeting*, Saarbrücken, Germany, October 5, 2016.
- "Optimization with multi-mode cavities", *Seminar of the group of T. Esslinger at ETH Zürich*, Zurich, Switzerland, July 5, 2016.
- "Multi-frequency self-organization", *Seminar of the group of G. Morigi at Universität des Saarlandes*, Saarbrücken, Germany, December 7, 2015.

- “Adaptive dynamics of scatterers in multi-frequency light fields in optical resonators”, *D-A-CH project meeting*, Innsbruck, Austria, September 23, 2015.
- “Adaptive multifrequency light collection by self-ordered mobile scatterers in optical resonators”, 28th SFB-FoQuS Meeting, Vienna, Austria, December 11, 2014.
- “Multi-frequency self-organisation of atoms in a cavity”, *Young European Scientist Meeting 2014 (YES)*, Zams, Austria, March 25, 2014.

Poster presentations

- “A Quantum N-Queens Solver”, Coauthors: P. Aumann, H. Ritsch, W. Lechner, *Adiabatic Quantum Computing conference (AQC 2019)*, Innsbruck, Austria, June 26, 2019.
- “A Quantum N-Queens Solver”, Coauthors: P. Aumann, H. Ritsch, W. Lechner, *43rd SFB-FoQuS Meeting*, Innsbruck, Austria, October 19, 2018.
- “Quantum annealing with ultracold atoms in a multimode optical resonator”, Coauthors: S. Krämer, H. Ritsch, *International Conference on Quantum Optics 2018*, Obergurgl, Austria, March 1, 2018.
- “Quantum annealing with ultracold atoms in a multimode optical resonator”, Coauthors: S. Krämer, H. Ritsch, *Okinawa School in Physics: Coherent Quantum Dynamics CQD 2017*, Okinawa, Japan, September 29, 2017.
- “Quantum annealing with ultracold atoms in a multimode optical resonator”, Coauthors: S. Krämer, H. Ritsch, *DK-ALM Summer School*, Pertisau, Austria, July 5, 2017.
- “Quantum annealing with ultracold atoms in a multimode optical resonator”, Coauthors: S. Krämer, H. Ritsch, *35th SFB-FoQuS Meeting*, Vienna, Austria, December 15, 2016.
- “Quantum annealing with ultracold atoms in a multimode optical resonator”, Coauthors: S. Krämer, H. Ritsch, *Quantum gases and quantum coherence (BEC 2016)*, Salerno, Italy, September 2, 2016.
- “Multi-frequency self-organization in optical lattices in cavities”, Coauthor: H. Ritsch, *31st SFB-FoQuS Meeting*, Vienna, Austria, December 17, 2015.
- “Adaptive multifrequency light collection by self-ordered mobile scatterers in optical resonators”, Coauthor: H. Ritsch, *Joint 2015 Annual Meeting of the Austrian Physical Society and the Swiss Physical Society*, Vienna, Austria, September 1, 2015.

- “Adaptive multifrequency light collection by self-ordered mobile scatterers in optical resonators”, Coauthor: H. Ritsch, *Young Atom Opticians Conference (YAO 2015)*, Zurich, Switzerland, April 22, 2015.

- “Adaptive particle dynamics in multi-frequency cavity light”, Coauthor: H. Ritsch, *Winterschool on Non-Equilibrium Quantum Systems: Theory and Experimental Implementation*, Obergurgl, Austria, April 7, 2015.